METABOLIC REMODELLING DEFINES CELLULAR SUBTYPES OF HUMAN NEURONAL PROGENITORS AND THEIR SUSCEPTIBILITY TO ZIKA VIRUS REPLICATION



Javier Andrés Gilbert Jaramillo

Linacre College

A thesis submitted for the degree of *Doctor of Philosophy*

Hilary 2022

ACKNOWLEDGMENTS

The work presented in this thesis was completed over four years and was possible thanks to the funding of The Ecuadorian National Government - SENESCYT and the Sir Dunn School of Pathology. I would like to firstly thank my supervisors Professor William Siward James and Professor Zoltán Molnár for their inputs, advice, and support during my DPhil. Also, to Professor Kieran Clarke and Professor Patricia Garcez for the support at the start of my project.

There was no better motivation during this DPhil than the “not too scientific” discussions with friends: Dr. Sharat Warrier et al. (ShAlbha), Indra Rudiansyah et al., Ujang Purnama et al., Auguste Valdisiute, Dr. Matthew Kerr.

Thanks go to my friends Dr. Michael Knight and Dr. Maeva Dupont with whom I shared my SARS-CoV-2 work throughout the ongoing COVID-19 pandemic. Michael, thanks for all the times in the CL3 working with something we didn’t know what it was, you truly made great times out of a pandemic.

Special thanks go to Catriona Rooney a.k.a. CHERooney, Eli, Cat, not just for her amazing support but for the helpful scientific discussions, data analysis debates, and the grammatical corrections that facilitated the completion of this thesis.

I would also like to mention colleagues and superiors in the James lab, Molnár group and the CMRG: Maria et al., Alun, Cathy, Jane, Vicky, Claudia, Becky, Marcos, Dr. Cher-Rin Chong, Dr. Rita Alonaizan, Dr. Shuichi Hayashi, Dr. Kourosh Ebrahimi, Becky, Adam, the minions I supervised, Old Rosie and to the dumbbells.

Finally, I wish to thank my beloved family, madre, padre y hermanos, sin ustedes esto no hubiese sido posible. Enana, desde arriba me ves y me bendices – esta fue por ti y la he cumplido…

TABLE OF CONTENTS

ABBREVIATIONS ..... *vi*

COVID-19 IMPACT STATEMENT *1*

ABSTRACT *3*

1. INTRODUCTION *5*

1.1 Zika virus and the metabolic dysregulations in fetal brain cells 5

1.2 Thesis aims for the ZIKV work 16

2. METHODS *18*

2.1 Viral propagation and quantification 18

2.2 Cell culture 22

2.3 Viral challenges 31

2.4 Immunofluorescence analysis 34

2.5 Metabolic measurements 42

2.6 Transmission Electron Microscopy (TEM) 46

2.7 Molecular biology analysis 47

2.8 Physiological measurements: Muscle motion recording 48

2.9 Transfection in hi-NPCs 49

2.10 Statistical analysis and software 49

3. METABOLIC REMODELLING DISTINGUISHES SUBTYPES OF HUMAN iPSC-DERIVED CORTICAL NEURONAL PROGENITOR CELLS (hi-NPCS) *50*

3.1 ABSTRACT 50

3.2 INTRODUCTION 52

3.3 AIMS 57

3.4 METHODS 58

3.5 RESULTS 60

3.6 DISCUSSION 67

3.7 CONCLUSION 72

4. ZIKA VIRUS-INDUCED BIRTH DEFECTS DURING FIRST TRIMESTER MAY RESULT FROM THE DIFFERENTIAL METABOLIC DYSFUNCTION INDUCED BY INFECTION OF EARLY VERSUS LATE NEURONAL PROGENITORS *74*

4.1 ABSTRACT 74

4.2 INTRODUCTION 76

4.3 AIMS 79

4.4 METHODS 80

4.5 RESULTS 82

4.6 DISCUSSION 95

4.7 CONCLUSION 102

5. IMMUNE-METABOLISM OF MACROPHAGES PREVENTS ZIKV INFECTION AND FACILITATES THE DISSEMINATION OF VIRIONS IN THE FETAL BRAIN ***105***

5.1 ABSTRACT 105

5.2 INTRODUCTION 107

5.3 AIMS 111

5.4 METHODS 112

5.5 RESULTS 115

5.6 DISCUSSION 127

5.7 CONCLUSION 132

6. GENERAL DISCUSSION ***135***

6.1 *In vitro* hiPSC neuronal differentiation produce subtypes of cortical neuronal progenitors 137

6.2 Increased glycolytic capacity is imposed during ZIKV optimal replication 139

6.3 ZIKV dissemination in the fetal brain is an indirect effect of macrophage immune-metabolic control of glycolysis 141

6.4 Limitations of the current research 144

6.5 Conclusion and future work 146

7. MACROPHAGES PHAGOCYTIZE SARS-CoV-2 VIRIONS AND DECREASE VIRAL REPLICATION IN INFECTED IN VITRO TISSUE MODELS ***148***

7.1 ABSTRACT 148

7.2 INTRODUCTION 150

7.3 AIMS 158

7.4 METHODS 159

7.5 RESULTS 162

7.6 DISCUSSION 177

7.7 CONCLUSION 181

7.8 Limitations of the current research 182

7.9 Conclusion and future work 182

8. ADDITIONAL MATERIALS ***184***

8.1 FIGURES 184

8.2 TABLES 188

8.3 SCIENTIFIC CONTRIBUTIONS DURING MY DPHIL 189

8.4 FOOTNOTES 195

9. BIBLIOGRAPHY ***196***

TABLE OF FIGURES

FIGURE 1. NT50 AND NT90 VALUES OF CLINICAL SAMPLES (OXFORD-ASTRAZENECA CLINICAL TRIAL) 2
FIGURE 1.1. GLUCOSE RECEPTORS IN THE EMBRYONIC MOUSE BRAIN. 7
FIGURE 1.2. GLUCOSE METABOLISM IN ASTROCYTES AND NEURONAL CELLS. 8
FIGURE 1.3. HYPOTHESISED KEY ROLE OF GLYCOLYSIS AND NEUROINFLAMMATION IN CONGENITAL ZIKV SYNDROME. 12
FIGURE 1.4. TIMELINE OF HUMAN MICROGLIAL DEVELOPMENT 13
FIGURE 3.1. NEUROGENESIS IN THE MOUSE CORTEX 53
FIGURE 3.2. SCHEMATIC ILLUSTRATION OF NEUROGENESIS IN THE MAMMALIAN NEOCORTEX 54
FIGURE 3.3. CORTICAL DIFFERENTIATION FROM HIPSCS PRODUCES PHENOTYPICALLY DISTINCT NEURONAL PROGENITORS (HI-NPCS) 61
FIGURE 3.4. CORTICAL DIFFERENTIATION FROM HIPSCS PRODUCES PHENOTYPICALLY DISTINCT NEURONAL PROGENITORS (HI-NPCS) 62
FIGURE 3.5. METABOLIC REMODELLING DISTINGUISHES HI-NPC SUBTYPES 64
FIGURE 3.6. EARLY HI-NPCS EXHIBIT HIGHER GLYCOLYTIC CAPACITY 66
FIGURE 4.1. LATE HI-NPCS EXHIBIT LARGER ACCUMULATION OF INTRACELLULAR NON-ASSEMBLED ZIKV PARTICLES 83
86
FIGURE 4.2. LATE HI-NPCS EXHIBIT A LARGER INCREASE IN THE GLYCOLYTIC CAPACITY DURING ZIKV REPLICATION 87
FIGURE 4.3. ZIKV INDUCES HI-NPC SUBTYPE-SPECIFIC MITOCHONDRIAL STRESS 90
91
FIGURE 4.4. ZIKV REPLICATION IMPOSES HIGHER DEMANDS ON THE METABOLISM OF LIPIDS IN EARLY HI-NPCS 91
FIGURE 4.5. INFECTED EARLY HI-NPCS ACCUMULATE LIPID DROPLETS DURING EARLY STAGES OF ZIKV REPLICATION 94
FIGURE 4.6. OVERALL METABOLIC ALTERATIONS IN ZIKV-INFECTED NEURONAL PROGENITOR SUBTYPES 104
FIGURE 5.1. ZIKV INFECTION PATHOGENESIS IN PREGNANCY 108
FIGURE 5.2. KEY STEPS IN THE DEVELOPMENT OF EMBRYONIC MICROGLIA. 109
FIGURE 5.3. A DEFINED-SOURCE, SERUM-FREE CULTURE MEDIA SUPPORTS THE DIFFERENTIATION OF HI-NPC SUBTYPES 117
FIGURE 5.4. DIFFERENTIATION OF HIPSC-DERIVED CORTICAL BRAIN ORGANOIDS USING A DEFINED-SOURCE, SERUM-FREE CULTURE MEDIA 118
FIGURE 5.5. LONG-TERM COCULTURE OF PROLIFERATIVE NEURONAL AND TISSUE-RESIDENT-LIKE MACROPHAGE PRECURSORS AS A MODEL OF THE EARLY FETAL BRAIN 120
FIGURE 5.6. ZIKV PRODUCTIVELY INFECT TISSUE-RESIDENT-LIKE MACROPHAGES AT LOW LEVELS 124
125
FIGURE 5.7. MACROPHAGES DISSEMINATE ZIKV IN THE FETAL BRAIN 125
FIGURE 5.8. CYTOSOLIC METABOLISM OF GLUCOSE FACILITATES ZIKV INFECTION IN HIPSC-MPH 126
FIGURE 5.9. IMMUNE-METABOLIC CONTROL IN MACROPHAGES MAY HIGHLIGHT MECHANISMS OF ZIKV DISSEMINATION CAUSING MICROCEPHALY IN NEW-BORNS 134
FIGURE 7.1. SARS-COV-2 INFECTION OF LUNGS LEADING TO CYTOKINE STORM RESULTING IN MULTI-ORGAN FAILURE 152
FIGURE 7.2. POSSIBLE PATHWAYS CONTRIBUTING TO HYPERACTIVATION OF MONOCYTE-DERIVED MACROPHAGES AND HYPERINFLAMMATION IN COVID-19. 155
FIGURE 7.3. SARS-COV-2 DOES NOT PRODUCTIVELY INFECT MONOCYTE-DERIVED MACROPHAGES 165

FIGURE 7.4. DETECTION OF MACROPHAGE-INTERNALIZED VIRIONS DECREASE IN A TIME-DEPENDENT MANNER 167
FIGURE 7.5. INTERNALIZED SARS-COV-2 VIRIONS ARE TARGETED FOR PHAGOLYSOSOME DEGRADATION 168
169
FIGURE 7.6. MACROPHAGES ARE NOT PER MISSIVE TO SARS-COV-2 INFECTION UNDER COCULTURE CONDITIONS WITH SUSCEPTIBLE VERO CELLS 170
FIGURE 7.7. SARS-COV-2 VIRIONS ARE INTERNALIZED BY HIPSC-MPH 172
FIGURE 7.8. MACROPHAGE INTERACTIONS WITH VERO CCL-81 SHOW CELLULAR AGGREGATION 173
FIGURE 7.9. SARS-COV-2 INFECTED HIPSC-DERIVED CARDIOMYOCYTES DO NOT REPRESENT A ROUTE FOR CELL-TO-CELL TRANSFER OF VIRIONS TO MACROPHAGES 176
SUPPLEMENTARY FIGURE 1. ZIKV INFECTION CAUSES NUCLEAR DAMAGE IN EARLY HI-NPCS 184
SUPPLEMENTARY FIGURE 2. ZIKV SHOW PERINUCLEAR REPLICATION SITES IN INFECTED LATE HI-NPCS 185
SUPPLEMENTARY FIGURE 3. HUMAN ZIKV SEROPOSITIVE SAMPLES VALIDATE A LARGE-SCALE HIGH-THROUGHPUT METHOD FOR THE QUANTIFICATION OF ZIKV 186
SUPPLEMENTARY FIGURE 4. U87 ASTROCYTOMA CELLS DO NOT UPTAKE KETONE BODY BETA-HYDROXYBUTYRATE (BHB) 187
SUPPLEMENTARY TABLE 1. 188

ABBREVIATIONS

ACACA	Acetyl-CoA carboxylase alpha
ACADM	Acyl-CoA Dehydrogenase Medium Chain
ACE2	Angiotensin-converting enzyme 2
ADAM17	Disintegrin and metalloprotease 17
ADRS	Acute respiratory syndrome
AM	Alveolar macrophages
Ang	Angiotensin
ANOVA	Analysis of variance
ATP	Adenosine triphosphate
AXL	AXL Receptor Tyrosine Kinase
β-HB	Beta hydroxybutyrate
BSA	Bovine serum albumin
CCK-8	Cell counting kit-8
CD	Cluster of differentiation
cDNA	Complementary Deoxyribonucleic acid
CMC	Carboxymethyl cellulose
COVID-19	Coronavirus disease
CPE	Cytopathic effect
CPM	Counts per minute
DAPI	4′,6-diamidino-2-phenylindole
DAPT	N-[N-(3,5-difluorophenacetyl)-L-alanyl]-S-phenylglycine t-butyl ester
DENV	Dengue virus
dH2O	Deionized water

DMEM	Dulbecco's Modified Eagle Medium
DS	Donkey serum
EBs	Embryoid bodies
ELISpot	Enzyme-linked ImmunoSpot assay
Env	Envelope protein
ER	Endoplasmic reticulum
FACs	Fluorescence-activated cell sorting
FASN	Fatty acid synthase
FBS	Fetal bovine serum
FCS	Fetal calf serum
FGF	Fibroblast growth factor
FFU	Focus-forming unit
GAPDH	Glyceraldehyde-3-Phosphate Dehydrogenase
GFR	Growth factor reduced
GLUT	Glucose transporter
GW	Gestational week
h.p.i.	Hours post-infection
HADHA	Hydroxyacyl-CoA dehydrogenase trifunctional multienzyme complex subunit alpha.
HCMV	Human cytomegalovirus
HCV	Hepatitis C virus
HEK	Human Embryonic Kidney Cells
hi-NPCs	Human induced pluripotent stem cell-derived neuronal progenitor cells
hiPSC	Human induced pluripotent stem cell(s)

hiPSC-CM	Human induced pluripotent stem cell-derived cardiomyocytes
hiPSC-MPh	Human induced pluripotent stem cell-derived macrophages
HIV	Human immunodeficiency virus
HK-1	Hexokinase 1
HRP	Horseradish peroxidase
IF	Immunofluorescence
IFN	Interferon
IgG	Immunoglobulin G
iPSC	Induced pluripotent stem cell(s)
KO	Gene knockout
LAMP	Lysosomal-associated membrane proteins
LDH	Lactate dehydrogenase
LN_2	Liquid nitrogen
M.O.I.	Multiplicity of infection
M1	Macrophage typing 1
M2	Macrophage typing 2
MAP2	Microtubule-associated protein 2
MDCK	Madin-Darby canince kidney cells
MDM	Monocyte derived macrophages
MERS-CoV	Middle East respiratory syndrome coronavirus
mRNA	Messenger ribonucleic acid
NAD	Nicotinamide adenine dinucleotide
NAD(H)	Nicotinamide adenine dinucleotide (reduced)
NADPH	Nicotinamide adenine dinucleotide phosphate
Nestin	Neuroepithelial stem cell protein

NeuN	Neuronal nuclear protein
Ni	Non-infected
NIM	Neuronal induction media
NK	Natural killer
NMM	Neuonal maintenance media
NPCs	Neuronal progenitor cells
NS	Non-structural protein
NT50	Half-maximal neutralization titre
OA	Oleic acid
OCT	Optimal cutting temperature
ODM	Organoid differentiation media
p-H3	Phospho-histone 3
Pax6	Paired Box 6
PBMC	Peripheral blood mononuclear cells
PBS	Phosphate buffered saline
PDK	Pyruvate dehydrogenase kinase isoform
PFA	Paraformaldehyde
PFU	Plaque forming unit
pH	Potential of hydrogen
PHE	Public Health England
PreMac	Macrophage precursor
Protein N	Nucleocapsid protein
P/S	Penicillin / streptavidin
qPCR	Quantitative polymerase chain reaction
Rab	Ras-associated binding proteins

RBD-Fc	Receptor binding domain fragment crystallizable region
RCF	Relative centrifugal force
RIPA	Radio-Immunoprecipitation Assay
RNA	Ribonucleic acid
ROCKi	Rho-kinase inhibitors
ROS	Reactive oxygen species
RPMI	Roswell Park Memorial Institute
RSAD2	Radical S-Adenosyl Methionine Domain Containing 2
RT	Room temperature
S100B	Calcium-binding protein B
SARS-CoV (2)	Severe acute respiratory syndrome coronavirus (2)
Sox2	Sex determining region Y -box 2
ssRNA	single-stranded RNA
TAM	Tumour-associated macrophages
Tbr2	T-box protein
TCA	Tricarboxylic acid cycle
TEM	Transmission electron microscopy
TMRPSS2	Transmembrane protease serine 2
TGF	Transforming growth factor
UV	Ultraviolet radiation
V-ATPases	Vacuolar-type ATPases
VCC	Vesicle-containing compartment
YF	Yellow fever virus
ZIKV	Zika virus

COVID-19 IMPACT STATEMENT

This thesis was originally designed to elucidate the metabolic intermediates required to support productive ZIKV replication and how the manipulation of their intracellular levels may serve for therapeutical purposes. To do this, I proposed the study of the changes in glucose and lipid metabolism (main fuel sources of the brain), during ZIKV infection, using relevant models of the embryonic and early fetal brain. To avoid potential undesired side effects on the cellular metabolism by drug administration, I aimed to use a CRISPR-KO edited cell line, available in the James lab biobank. RSAD2-CRISPR-KO cells reflect immune-metabolic compromised responses specifically at the levels of GAPDH in the glycolytic pathway thus, they were selected as the model to reveal potential differences in the metabolic demands, during ZIKV replication, between non-immune and immune cells of the fetal brain.

The COVID-19 pandemic impacted this research by forcing it to a stop at the stage of investigation into the potential metabolic alterations by ZIKV in non-immune cells of the early fetal brain. The original funding body, The Ecuadorian National Government, could not provide funds for an extension of this work. Due to my training with level II pathogens and techniques for viral counting and neutralization experiments, I joined the efforts of my supervisor Prof. William James in providing a platform to investigate the therapeutic potential of neutralizing compounds and vaccines for SARS-CoV-2.

Early in the 2020 pandemic, there was the need for large scale readouts of these compounds thus, under the supervision of Prof. James, I led a group of students implementing a microneutralization foci forming unit assay (fast high-throughput

method for viral quantification). This assay was validated in June 2020 with samples from the Oxford-AstraZeneca phase1/2 clinical trial, provided by Prof. Sarah Gilbert, University of Oxford. The results obtained (Figure 1) mirrored those of the reported by Public Health England in Folegatti *et al.,* 2020[1].

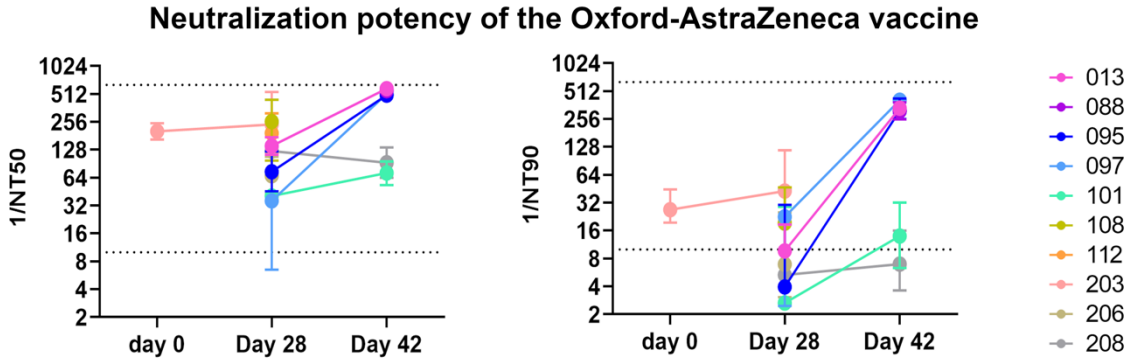


Figure 1. NT50 and NT90 values of clinical samples (Oxford-AstraZeneca clinical trial)
Dot plots showing the NT50 and NT90 values of the *in house* microneutralization assay performed in trial participants (Oxford-AstraZeneca phase 1/2 clinical trial) at day 0 and, at 28- and 42-days post-booster. Bars display mean ± SD. n = 3 technical replicates per sample.

This microneutralization assay was further used as part of the Oxford response to the global pandemic by providing a platform for estimating the neutralization of live viruses by several compounds[2–8] and to confirm the efficacy of several vaccine types and boosters against SARS-CoV-2 variants of concerns[9–13] (collaborations are listed in the Appendix of this thesis – 8.3). Thus, over the last 1.5 years of my DPhil, in addition to testing the efficacy of COVID-19 vaccines and neutralizing compounds, I conducted a small research study aiming to examine the role of macrophages in the pathogenesis of SARS-CoV-2. The data generated is included as the fourth result chapter in this DPhil thesis.

ABSTRACT

Maternal infections by Zika virus (ZIKV) during the first trimester of pregnancy result in either abortion or severe damage to the developing brain in 8-12% of cases. However, the route of ZIKV to the developing brain remains unclear. Emerging work suggests ZIKV replication imposes energetic demands on the developing brain that overwrite the highly orchestrated energetic processes required for normal cellular growth, proliferation, and differentiation. Energetic dysfunction could be attributed as the main cause for ZIKV-induced detrimental brain damage in new-borns yet, there is no clear evidence on the altered energetic pathway(s) and/or substrate(s) required to sustain ZIKV replication.

The work presented in this thesis showed the characterization of 2D *in vitro* cultures of cortical neuronal progenitor cells (hi-NPCs) and tissue-resident-like macrophages (hiPSC-MPh) derived from human pluripotent stem cells as models of the early fetal brain to better understand the pathogenesis of ZIKV. Analysis of the preferred energetic pathway in hi-NPCs distinguished two distinct subtypes of brain progenitors resembling populations with characteristics of quiescent radial-glia-like cells or proliferative intermediate neuronal progenitors. ZIKV infection in hi-NPCs revealed a subtype-specific permissibility to infection with metabolic implications resulting in reprogramming towards an increased cytosolic glucose metabolism. This was not observed in hiPSC-MPh as these cells showed less permissibility to ZIKV infection than hi-NPCs yet, the low rates of viral production in hiPSC-MPh were sufficient to disseminate virions to hi-NPCs, highlighting a potential route for maternal-fetal transmission of ZIKV. Further analysis using immune-metabolic compromised RSAD2-KO hiPSC-MPh showed that cytosolic

glycolysis may underlie mechanisms for high rates of ZIKV replication. However, more research and validation of the current results are required to clearly elucidate whether energy intermediates can diminish ZIKV replication for potential therapeutics. These were not explored in detail due to the disruptions caused by the COVID-19 pandemic, instead this thesis includes an isolated chapter on SARS-CoV-2 because of the change in research projects.

The small research on SARS-CoV-2 hypothesises that macrophages do not negatively contribute to severe COVID-19 by the triggering the cytokine storm but have a dual role by decreasing SARS-CoV-2 replication kinetics by the degradation of circulating virions. Herein, I showed that macrophages, both peripheral (MDM) and hiPSC-MPh, were not productively infected by SARS-CoV-2 virions after direct (cell-free) or indirect exposure (cell-to-cell transfer). Instead, these cells phagocytized virions for phagolysosome degradation and decreased the viral replication kinetics by reducing the amount of output virions that can infect susceptible cells. This suggested a potential protective role of macrophages against the dissemination of SARS-CoV-2 within infected tissues.

1. INTRODUCTION

1.1 Zika virus and the metabolic dysregulations in fetal brain cells

The Flavirirus genus comprises epidemic mosquito-borne positive single-stranded RNA viruses [(+)ssRNA] such as Dengue virus (DENV), Yellow fever (YF) and Zika virus (ZIKV)[14]. ZIKV, firstly isolated in 1947 from a febrile rhesus macaque in Uganda, became a major public health concern worldwide in 2016[15–17] due to the outbreaks in infections being correlated with brain damage in new-borns and Guillain-Barre syndrome in adults[17–21]. The most severe consequence of ZIKV infections in new-borns is exhibited by a microcephalic brain. This is mostly correlated with maternal ZIKV infections during the first trimester of pregnancy[22–24]. ZIKV-mediated cell death of brain cell types, particularly neuronal progenitors, may partially explain the reduction of the brain mass that precedes the microcephalic phenotypes.

Moreover, microcephaly in new-borns has been reported in cases of genetic mutations and energy impairment during neurodevelopment[25,26]. Brain deficiency of the main glucose receptor, GLUT-1, causes microcephaly and highlights the importance of sufficient energy supply for the correct development and function of the brain[27–30]. Thus, the energetic demands imposed by ZIKV and potential metabolic dysregulations due to the requirements for viral assembly may underpin the death of neuronal progenitors.

To date, as there is no approved vaccine for ZIKV, efforts are invested in designing and repurposing drugs that may prevent viral replication in susceptible cells. However, understanding how ZIKV populates the developing fetus may improve drug targeting and efficacy. Maternal-fetal transmission of pathogens has been

previously reported for Hepatitis B and the Japanese encephalitis virus. The productive infection of macrophages by these viruses signifies a route of maternal-fetal transcytosis; the migration and release of infectious particles by cells that act as carriers[31,32]. Thus, as the developing fetal brain, during early stages, is invaded by yolk-sac-derived native immune cells (tissue-resident macrophages)[33,34], ZIKV infection in these cells may be a route for maternal-fetal transmission. Most of the work described in this thesis will focus on elucidating specific metabolic dysregulations in neuronal progenitors during ZIKV replication and how the potential reduction of ZIKV replication in fetal macrophages via native-immune metabolic control may indirectly drive viral dissemination in the early developing brain.

1.1.1 Metabolic substrates of the fetal and adult brain

The developing cortex depends on the precise replication, expansion, and migration of cells from the radial glial progenitors[35]. Energy metabolism may orchestrate these processes, during the fetal life, by providing a pool of metabolites, substrates, and ATP[36]. Little is known about fetal brain metabolism but, studies of the adult brain suggest that the different brain cell types have distinct requirements for energy substrates, particularly during activation[37,38]. For example, the metabolism of neurons is potentially more dependent on oxygen than that of astrocytes and oligodendrocytes[39,40]. Glucose entry is mediated by the superfamily of GLUT proteins which are expressed across the placenta, blood-brain barrier, neuronal progenitors, differentiated neuronal tissue, and microglia[41,42] (Figure 1.1). Therefore, glucose is considered to be the primary energy source for the brain and its correct development during embryonic life[43]. Mature neurons can convert glucose into Acetyl-CoA for the production of substrates and the generation of ATP

by oxidative phosphorylation, whereas glial cells, even in the presence of oxygen, preferentially convert glucose to lactate via cytosolic metabolism ("Warbug effect")[37,44]; resembling metabolic characteristics of cancerous cells. Therefore, it is plausible that brain circulating lactate can also be metabolised by differentiated neurons for mitochondrial respiration and generation of ATP (Figure 1.2); potentially in a preferable way to glucose[39]. Metabolic flexibility and substrate exchange between brain cells also includes glutamate[27,45,46], ketone bodies[47], and fatty acids[44,48,49].

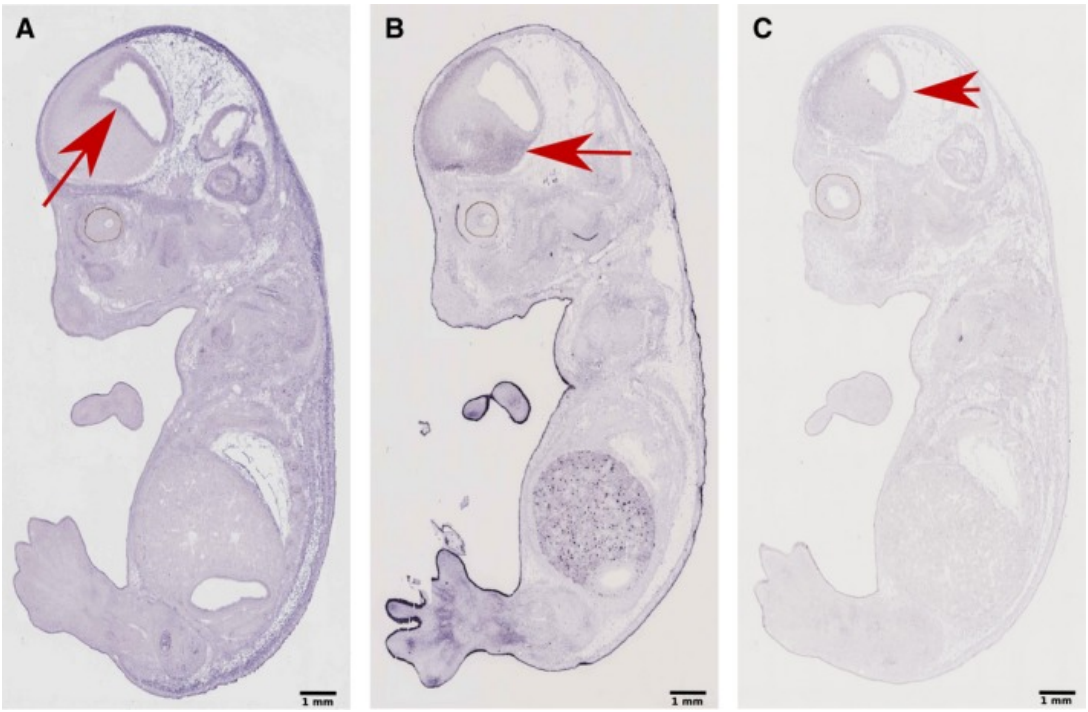


Figure 1.1. Glucose receptors in the embryonic mouse brain
GENEPAINT sagittal plane sectioning image data of E14.5 Strain C57BL/6. (A) *In situ* hybridisation of the solute carrier family 2 (facilitated glucose transporter) member 1 (SLC2A1), mainly located in the ventricular zone at the neural progenitor region of the cerebral cortex and the ganglionic eminence (red arrow) (GENEPAINT set ID: EH739). (B) *In situ* hybridisation of the solute carrier family 2 (facilitated glucose transporter) member 3 (SLC2A3) mainly located in postmitotic and differentiated neuronal populations in the primordial plexiform zone or preplate of the cortex and the striatum (red arrow) (GENEPAINT set ID: EH4603). (C) *In situ* hybridisation of the solute carrier family 2 (facilitated glucose transporter) member 5 (SLC2A5) widely spread across the brain (red arrow) (GENEPAINT set ID: EH4766). Scale bar: 1 mm. Obtained from Gilbert-Jaramillo et al., 2019[36].

During neonate life, while breastfeeding, mammalians are exposed to a particular condition where carbohydrates, previously supplied by the maternal circulation, become restricted, and the diet is mainly constituted on fats and their derivatives[50,51].

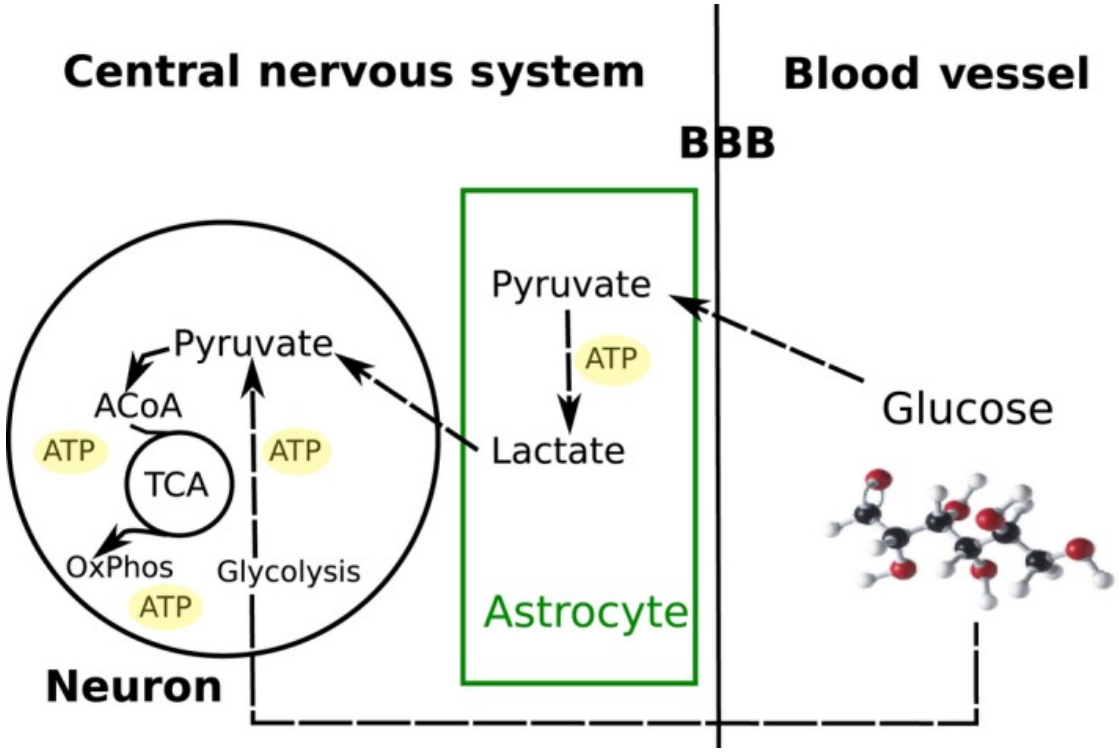


Figure 1.2. Glucose metabolism in astrocytes and neuronal cells
Glucose molecules available in the blood vessels cross the blood-brain barrier (BBB) and are taken up by astrocytes and neurons. Astrocytes use aerobic glycolysis, despite the presence of oxygen, to produce ATP and Lactate (Warburg-like effect). Neurons take up glucose directly from the bloodstream, which is converted to pyruvate via glycolysis. Lactate shuttled by astrocytes is also taken up by neurons and converted into pyruvate. Pyruvate inside the neuronal cytosol is converted into Acetyl-CoA and enters the Krebs cycle, releasing by-products for OxPhos to produce sufficient ATP, required for neuronal activity. Obtained from Gilbert-Jaramillo et al., 2019[36].

This may highlight the relevance of non-glucose sources to support brain energy homeostasis. Altogether, it is known that utilization of glucose and fatty acids are the main energetic substrates in the brain[44,52–57]. Research focused on the metabolism of glucose and fatty acids has emphasized their role as the two main nutrients in neuronal progenitor cells (NPCs)[58,59]. The shift between glucose

metabolism to fatty acid oxidation in the mitochondria is potentially implicated in determining the maturation of NPCs[60]. These distinctions in the preferred metabolic pathway among the different cell types in the early developing brain[61] may be correlated with the differences exhibited in native immune responses[62,63].

1.1.2 ZIKV infection and damage of the developing fetal brain

The clinical symptomatology of ZIKV infection including generalised mild fever, myalgia, arthralgia, headache, rash and conjunctivitis[21,64–66] is reported only in the minority of the patients (~20% of ZIKV +ve cases)[66]. Despite the symptomatology being close to that of common viral infections such as influenza virus, ZIKV reaches different tissues including the decidua, fetal placenta, the umbilical cord and the brain[67–74]. The infection of these cells supports the hypothesis of vertical maternal-fetal transmission as a route of infection to the developing fetus[75–78].

ZIKV preferential tropism for neural stem cells and progenitors is more marked than for other flaviviruses[67,71,79–83], potentially explaining why the detrimental damage to the fetus is not reflected to similar extent in the adult symptomatology[79,84]. ZIKV-derived microcephaly and eye malformations are the most detrimental phenotypes in new-borns[85–88]. Microcephaly includes the reduction of the head circumference of 2 standard deviation smaller than the local average. The clinical severity of microcephaly differs broadly in the loss of brain mass and morphology[26,89]. This suggests potential differences by severe neuronal loss in the cerebral cortex[88,90] and/or reduction in the population of glial cells[91]. Primary microcephaly, as a disease caused by genetic mutations and maternal viral infections[25,26,83,88], has an estimated rate of 2–12 cases per 10,000 births. This rate increased up to ~ 20-fold in early 2016 in Brazil due to ZIKV infections[21,77,86,92,93], yet there were few

neurological complications in infected new-borns in other countries[24,94–96]. This is potentially related to dysregulations in cellular metabolism as the microcephalic reports mainly corresponded to areas of poverty and malnutrition[97].

Since the 2016 outbreak in Brazil, ZIKV research has showed that infection downregulates different genes related to neuronal differentiation, neuronal growth, cellular metabolic function, and cell survival[17,72,74,83,91,98,99]. Moreover, ZIKV-derived eye malformations are yet to be fully determined due to the poor knowledge of the full spectrum of ocular lesions[100,101]. Nevertheless, several abnormalities such as focal pigment mottling of the retina, atrophy in the chorioretina, alteration in the retinal vasculature, optic nerve abnormalities, bilateral iris coloboma and lens subluxation[101,102] and, in the fetus, loss of retinal epithelium, thin choroid, perivascular choroidal inflammatory infiltrate and atrophy of the optic nerve[103] have been reported.

1.1.3 Cellular metabolic stress imposed during ZIKV replication

ZIKV dysregulation of cellular and molecular homeostasis showed several biological processes potentially underpinning the neurological damage with changes in cellular metabolism as a common feature[72,88]. Similar to DENV, ZIKV replication potentially activates early glycolysis[104,105] and late fatty acid β-oxidation[106], yet it remains unclear why there are highly contradictory results from different cellular and animal models[107–111]. As a consensus, ZIKV replication primarily dysregulates the metabolism of glucose and fatty acids[112–114] which potentially occurs at different times that may correlate to the viral replication stage.

In 2016, Edward Blonz hypothesised that brain energetic failure may cause the detrimental damage observed in the new-borns[115] by the alteration in the uptake of glucose in brain cells potentially by the interaction between ZIKV proteins and GLUT-1 receptors[115]. In this context, research has shown that activation of the glycolytic pathway may be used to produce energy to support optimal ZIKV replication[107]. Increased glycolysis evokes cellular energy impairment, which contributes to ER stress[116], mitochondrial dysfunction and the production of reactive oxygen species (ROS) [117,118]; processes reported in models of ZIKV infection and that may all contribute to neurodegeneration.

The elevated ROS production in the brain has been reported to contribute to lipid droplet accumulation, particularly in glial cells[119]. Lipid droplets are intracellular organelles involved in fatty acid trafficking, energy homeostasis and antiviral immunity[120–122]. ZIKV potentially triggers lipid droplet accumulation for viral encapsidating and/or to increase the ATP availability, via beta-oxidation of fatty acids[108,112,113], to support the increased energetic cellular requirements during viral replication. This, potentially underlies the impaired autophagy observed in ZIKV infection models[17,36,71,107,123,124]. Altogether, the consequences of interconnected dysregulation of glucose and lipid metabolism may explain cellular features of ZIKV infection such as dysregulated autophagy, elevated ROS, ER stress, and neuroinflammation (Figure 1.3).

Moreover, geographical distribution can play a role in congenital ZIKV syndrome, with the highest prevalence of the epidemic being observed in the North-East region of Brazil, a population characterised by poverty[93,97]. In these populations, malnutrition is a prevalent comorbidity[97]. Therefore, specific dysregulation of the cellular metabolic pathways might play an important role in the susceptibility or

protection against ZIKV virulence with relevance for pathophysiological and clinical implications.

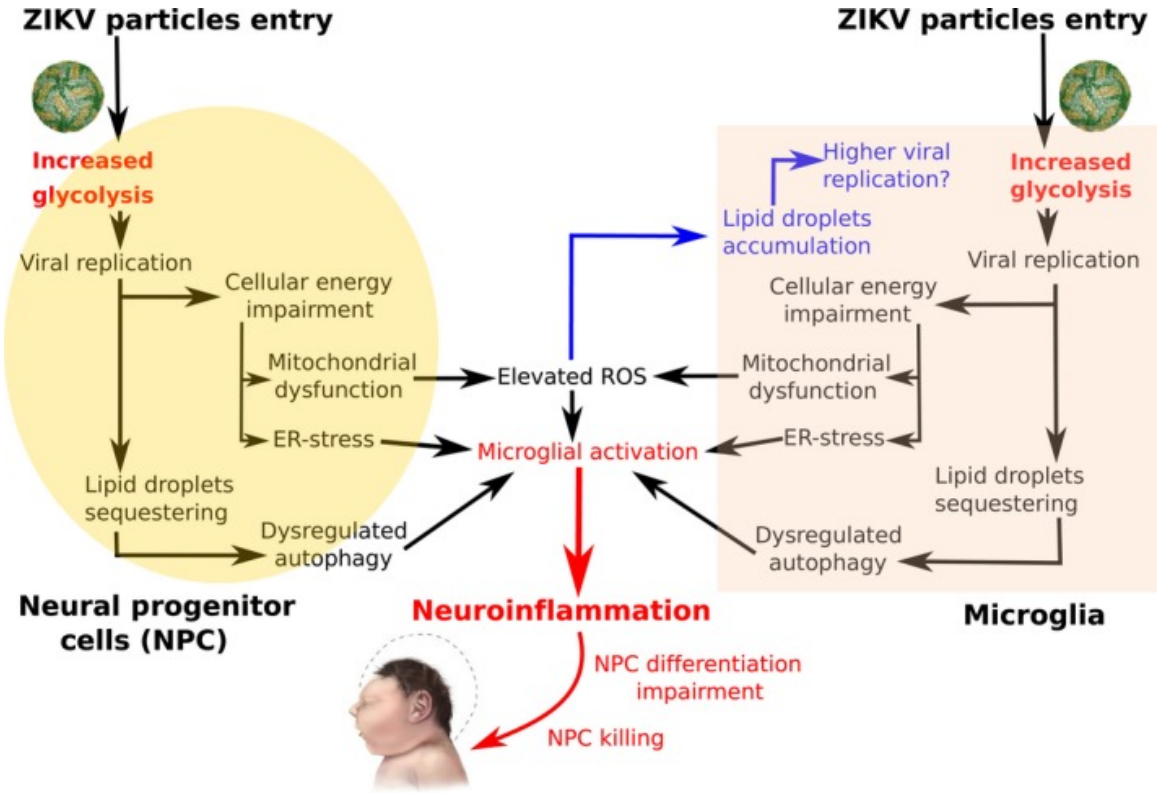


Figure 1.3. Hypothesised key role of glycolysis and neuroinflammation in congenital ZIKV syndrome
Increased glycolysis following ZIKV infection and replication in the endoplasmic reticulum (ER) of both neural progenitor (NPC) and microglial cells potentially causes (1) cellular energy impairment with further mitochondrial dysfunction and ER stress, and (2) sequestration of cytoplasmic lipid droplets required for final replication (pathways highlighted in black). Elevated reactive oxygen species (ROS) due to mitochondrial dysfunction cause an accumulation of lipid droplets in microglia, potentially favouring a higher viral replication rate than in neurons (pathway highlighted in blue). (3) Microglial activation by dysregulated autophagy, ER stress and elevated ROS contribute to neuroinflammation, impairing NPC differentiation and promoting NPC killing mechanisms (pathway highlighted in red); a possible explanation for brain growth impairment and congenital ZIKV syndrome. Obtained from Gilbert-Jaramillo et al., 2019[36].

1.1.4 Macrophage immune-metabolism and ZIKV dissemination

During early development, the rapid growth of the yolk sac, among other extraembryonic tissues, occurs upon embryo implantation[125]. Tissue-resident macrophages, originated from the yolk sac[126], migrate, and populate the developing

brain between gestational weeks 4 and 24[125,127,128]. These cells will constitute the microglia of the brain (Figure 1.4). After the embryonic stage (GW 8.5), viral invasion of the developing brain involves, prior contact to the immune responses of microglial cells, the dissemination through two main barriers, the placental and the blood brain barrier, which shield and protect the developing brain against pathogens[129,130].

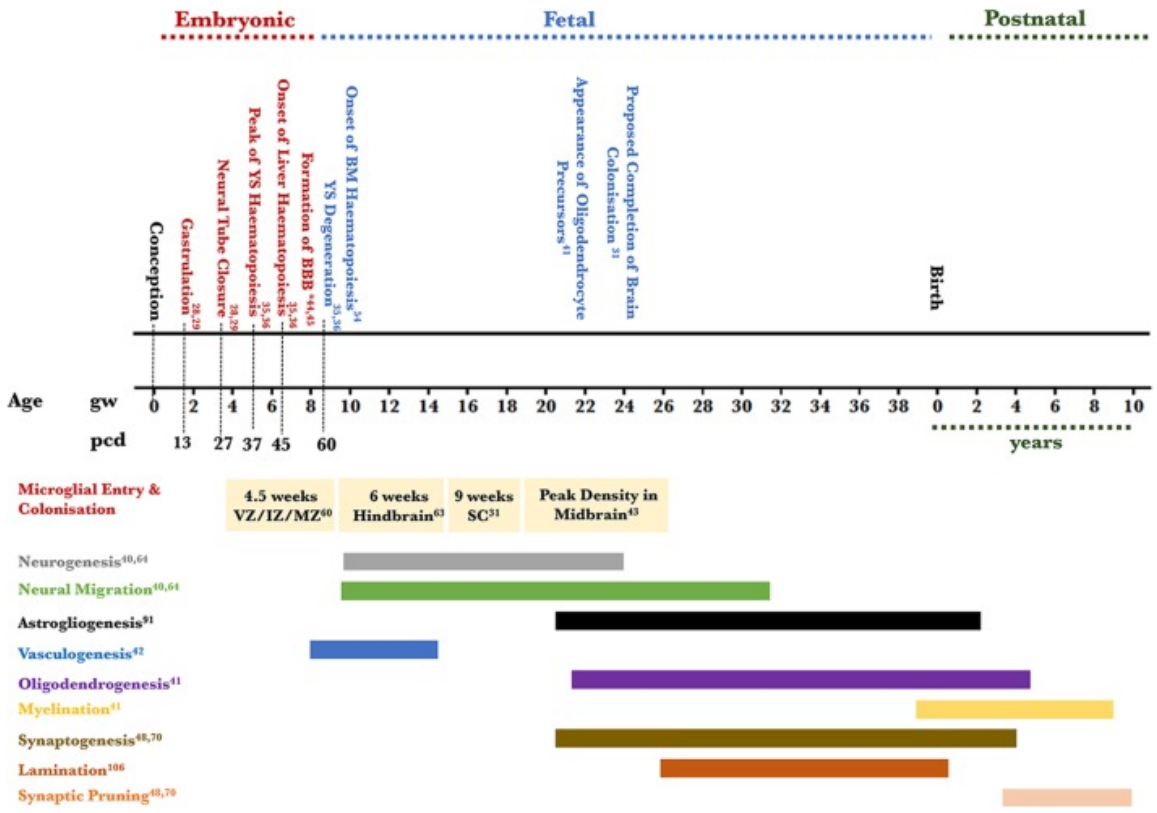


Figure 1.4. Timeline of human microglial development
This figure places microglial entry into developing brain areas in the context of the approximate co-ocurrence of cortical developmental events. Microglia are detected in the ameboid state in the telencephalic ventricular, intermediate, and MZs and not the cortical plate at 4.5 weeks of gestation; microglia are detected in the ramified state in the hindbrain by 6 weeks; amoeboid microglia are detected in the SC by 9 weeks of gestation; the density of amoeboid microglia is the highest in the mesencephalon (midbrain) by 22 weeks of gestation. *Two barriers are included here: the BBB proper at the levels of the endothelium of the cerebral blood vessels and the blood-CSF barrier at the level of the choroid plexus epithelial cells. The CSF-brain barrier is detected as early as 16 days through the appearance of strap junctions and is not shown on the timeline. Abbreviations: BBB, blood-brain barrier; BM, bone marrow; CSF, cerebrospinal fluid; IZ, intermediate zone; MZ, marginal zone; PCD, post conceptional days; GW, gestational weeks; SC, spinal cord; YS, yolk sac. Obtained from Menassa and Gomez-Nicola, 2018[131].

Permissiveness of macrophages to infection may transform them into viral reservoirs for the dissemination into different tissues[77]. Viral infections such as HIV, HCV, HCMV and Japanese encephalitis virus have been reported to reach, stress, and infect brain cells. This is mediated by the productive infection of infiltrating peripheral macrophages and microglia[132–139]. Viral productive infection of these cells may involve a persistent productive viral replication, time limited productive replication / partial replication or a restricted / short-term non-productive replication[140]. Thus, it is hypothesised that productive ZIKV infection of yolk-sac derived tissue-resident macrophages underpin a potential route for vertical transmission during pregnancy[77,141].

Differential viral infection among cell types correlates to different entry mechanisms[142]. Receptor-mediated entry modulates infection levels and underpin the activation of different native-immune recognition pathways[143,144]. ZIKV, like other arboviruses, infects cells by receptor-mediated entry mechanisms[143,144]. Therefore, the abundance of specific receptors relevant for ZIKV entry could display differences between brain radial glial-borne cells and microglia. AXL receptors have been highlighted to mediate the entry of ZIKV virus however, ZIKV can infect cells by other routes that remain unclear[81,145–153]. Thus, different cell types could exhibit differences in the permissibility to entry and infection of ZIKV. In addition, the infectivity of ZIKV could differ by biological differences of the host cells such as differences native immune responses.

ZIKV, as a potential evolutionary advantage strategy, downregulates the expression of immunological genes in infected cells[154]. In macrophages, activation of interferons (IFN) in response to infection plays the major role in the viral recognition and during the restriction of viral replication[155,156]. Macrophages are plastic cells

capable of adapting their cellular metabolism in response to pathogens. The metabolic shift towards cytosolic glycolysis and lactate production is a known feature of macrophage polarization and activation towards M1 phase[157–159]. ZIKV infection has been correlated with a downregulation of the mRNA levels of the IFN-I receptor, IFNAR1, and upregulation of several genes involved in the glycolytic pathway[72,154] as a potential mechanism to facilitate viral replication. Viperin, also known as Radical S-Adenosyl Methionine Domain Containing 2 (RSAD2), is inducible dependent and independent of IFN type I and II signalling. This protein has a key role in the modulation of cellular metabolism by native immunity[160–163]. Thus, the study of cellular metabolism of RSAD2-KO and wild-type macrophages, under ZIKV infection, may exhibit specific substrate(s), involved in the metabolic control, as potential requirement(s) for a persistent productive viral replication, with implications for therapeutics.

1.2 Thesis aims for the ZIKV work

The work described in this thesis intends to examine potential metabolic disparities caused by ZIKV infection on the two main substrates (glucose and lipids) of the cells present during early fetal brain development: radial-glial progenitors, intermediate progenitors, and yolk-sac macrophages. This potential cell-type specific dysregulation of cellular metabolism may reveal disparities in ZIKV replication rates, ZIKV-induced cell death, ZIKV dissemination and, metabolic stress underpinning the differences in brain damage observed when infection occurs at different trimesters of pregnancy. It will further investigate specific energy metabolic intermediates, using wild-type and immune metabolic compromised yolk-sac-like macrophages, required for sustained ZIKV replication. Thus, this research may reveal compounds with therapeutic potential by the activation of secondary energy pathways which may not provide the bulk of intermediates required for the correct assembly and replication of ZIKV virions but promote cell survival.

This will be achieved by three result chapters focusing on:

1. Differentiating and characterizing subtypes of cortical neuronal progenitor cells from human induced pluripotent stem cells (hi-NPCs)
2. Investigating the dysregulation of energy metabolism (glucose, lipid and, mitochondrial homeostasis) in ZIKV-infected hi-NPC subtypes as the main cells involved in the expansion of the fetal cortex
3. Determining the susceptibility of yolk-sac-like macrophages (hiPSC-MPh) to ZIKV infection and their contribution to ZIKV dissemination in the fetal brain

4. Determining the role of energy metabolism in the susceptibility of hiPSC-MPh to be productively infected by ZIKV virions
5. Elucidating specific metabolic intermediates that influence ZIKV infection in hiPSC-MPh and hi-NPCs
6. Examining the potential therapeutics of metabolic modulation by nutritional and/or pharmaceutical intervention in hiPSC-MPh and hi-NPCs

2. METHODS

2.1 Viral propagation and quantification

2.1.1 Propagation of ZIKV stocks

ZIKV stock was produced from a vial of ZIKV strain (MP1751) obtained from the James laboratory. Initial vial, [2x10^6 PFU/ml] was kindly provided by Public Health England. Details of the isolate are included in the worldwide virus collection database[164,165]. For viral propagation, 100 µL of the initial stock were added to a T175 flask containing ~90% confluency of Vero cells (ATCC CCL-81) passages 56 to 62 and incubated for five minutes at room temperature. After incubation, 20 mL of Dulbecco's Modified Eagle Medium (DMEM, Sigma; D6429-500ML) high glucose supplemented with 1% FBS (Sigma; F9665-500ML) and 1% Glutamax (Life Technologies; 35050-038) were added. Cells were further incubated with the viral inoculum for 1.3 h at room temperature (RT) on a rocker at 20 cycles/minute (Biometra ROCKY®). Cells were then kept at 37 °C, 5% carbon dioxide for ~4 days. The inoculated cells were checked twice daily, and the supernatant was collected, in 15 mL falcon tubes, upon evident cytopathic effect (CPE). Cell debris present in the supernatants were pelleted by centrifugation at 10.000 rcf for five minutes. Media-containing virus was obtained by collecting the supernatant cleared from cell debris. One mL aliquots of virus-containing media were prepared and kept at -80 °C.

2.1.2 Titration of ZIKV

Virus titration was conducted by plaque assay. 100 µL of media-containing virus was added onto three wells on a 24-well plate. Serial 10^{-1} dilutions of the media-

containing virus were prepared and ran in triplicates. Plates were inverted 180 degrees and 500 µL of Vero cell suspension at a density of 5 x 10^5 cells/mL was added. Plates were then incubated for 2 h at 37 °C, 5% carbon dioxide after which 500 µL of 1.5% carboxymethyl cellulose overlay (CMC low viscosity, BDH Laboratory supplies; 276494N) were added to prevent viral spread. Plates were further incubated for 80 h at 37 °C, 5% carbon dioxide. After incubation, media was aspirated, and cells were washed once with PBS. 500 µL of Amido black stain (To 925.6 mL of dH2O: 1 g Napthol blue-black powder, 60 mL acetic acid glacial (Sigma; A6283-1), 13.6 g sodium acetate anhydrous (Sigma; S5636-500G) was added for 30 minutes at RT to fix the cells and reveal viral plaques. Amido black stains proteins thus, lack of staining (plaques) corresponds to sites of infection and cell death; debris removed during washing process. Plates were dried out on paper towels and imaged using a Molecular Imaging ChemiDoc™ XRS+ (Bio-Rad; 721BR03173). Plaque forming units (p.f.u.) were calculated as follows: $p.f.u. = (n/0.1)/D$ where n = average number of plaques, 0.1 is the volume of virus added in mL, and D = dilution factor. For the preparation of serial dilutions, cell suspensions and CMC, high glucose DMEM supplemented with 1% FBS and 1% Glutamax was used.

2.1.3 Microtitration of ZIKV

Microtitration of ZIKV was done by a foci-forming unit (FFU) assay, developed by the detection of 50 and 100 FFU using several dilutions of the mouse anti-flavivirus envelope protein antibody 4G2. 20 µL of media-containing virus were added to the respective wells of a 96-well plate. 100 µL/well of Vero CCL-81 suspension at a density of 4.5x10^5 cells/mL was added to each well. Plates were then incubated for 2 h at 37 °C, 5% carbon dioxide. After incubation, to prevent satellite focus formation, 100 µL of CMC overlay per well were added and plates were further

incubated for 28 h under the same conditions. CMC overlay and medium were then removed, and each well was washed with 180 µL of PBS. Cells were then fixed using 100 µL of 4% paraformaldehyde (PFA, AlfaAesar; J61899) for 30 minutes. After incubation, PFA was removed and 100 µL 1% ethanolamine (Sigma; E0135) in PBS were added per well to quench excess aldehydes and prevent potential loss of epitopes. For foci reveal, ethanolamine was discarded, and cells were permeabilized for 30 minutes at 37°C, 5% carbon dioxide with 100 µL/well of 2% Triton X-100 (Sigma; T9284-100ML) in PBS. Wells were further washed three times with 100 µL wash buffer (0.1% Tween-20, Sigma; P7949-500ML in PBS) and tapped out to dry. 50 µL of 1:125 dilution of 4G2, in wash buffer, was added over 6 technical replicates. Plates were incubated for 1 hour at RT on a rocker before washing and drying as detailed before. 50 µL of 1:1000 anti-mouse IgG HRP-linked secondary antibody (Sigma; A9917-1ML) were added to each well for 1 hour then plates washed and dried as before. Wells were further incubated for 10 minutes with 50 µL of TrueBlue peroxidase substrate (Seracare Life Sciences Inc.; 5510-0030). To stop HRP-peroxidase reaction, wells were incubated for 5 minutes with 100 µL of dH2O. Plates were dried out on paper towels and imaged using an ELISpot reader (AID – Autoimmun Diagnostika GMBH).

2.1.4 Production of SARS-CoV-2 stocks

The work was conducted in the containment level 3 facility of the University of Oxford, operating under the license from the Health and Safety Authority, UK, on the basis of an agreed code of practice, risk assessments (under the Advisory Committee on Dangerous Pathogens guidance) and standard operating procedures. SARS-CoV-2 isolates: Victoria/01/2020[166], B.1.1.7 H204820430 (alfa),

2/UK/VUI/1/2020[167] and, B.1.351 (20I/501.V2.HV001) (beta)[168], provided by Public Health England (PHE), were propagated in Vero cells. Victoria strain, used at passages 5 and 6, was propagated in Vero CCL-81. SARS-CoV-2 alfa and beta variants, used at passage P4, were propagated in Vero E6 / TMPRSS2 (NIBSC reference 100978). All the isolates were deep sequenced at the Wellcome Trust Centre for Human Genetics, University of Oxford. More details on the origin of the isolates and their respective access number are detailed in Skelly and Harding et al., 2021[12].

2.1.5 Microtitration of SARS-CoV-2

Microtitration of SARS-CoV-2 was done by FFU assay. SARS-CoV-2 was quantified by titrating 20 µL of undiluted and diluted media-containing virus in quadruplicates. 100 µL/well of Vero CCL-81 ($4.5x10^5$ cells/mL) were added to each well followed by 2 h incubation at 37 °C, 5% carbon dioxide. To prevent satellite focus formation, 100 µL of CMC overlay per well were added, after the initial incubation, and plates were further incubated for 23 h (Victoria and alfa variant) and 18 h (beta variant) under the same conditions. Washing and fixing steps were conducted as detailed for ZIKV virus (section 2.1.3). Primary antibody solutions comprised monoclonal antibodies (mAbs) anti-N EY 2A and anti-S EY $6A^9$, both used at 1 ug/mL, for the respective detection of Victoria and beta and, alfa variants. Anti-human IgG HRP-linked secondary antibody 1:5000 (Sigma; A0170-1ML) was used as secondary antibody. Plates were dried imaged using an ELISpot reader (AID – Autoimmun Diagnostika GMBH).

2.1.6 Viral thermostability (ZIKV and SARS-CoV-2)

Thermostability of viruses was done at 37 °C, 5% carbon dioxide. 500 µL of media-containing virus were added to wells of a 24-well plate, each corresponding to a specific time point. 350 µL of media were collected and kept at -80 °C. Media was thawed, mixed and, 20 µL were titrated using the respective FFU assay.

2.2 Cell culture

2.2.1 Culture of cancerous cells

2.2.1.1 Culture of Vero CCL-81 cells

Vero CCL-81 cells were cultured at 37 °C, 5% carbon dioxide in DMEM high glucose supplemented with 10% FBS. Vero cells were passaged every 2-3 days. Prior to passages and for the preparation for plaque assay / microtitration experiments, media from Vero cells was replaced for DMEM high glucose supplemented with 1% FBS and 1% Penicillin-Streptomycin (P/S) (Gibco; 15140122) (low serum DMEM). Cell passage was done at ~90% confluency. To do this, cells were washed once with PBS and incubated with TrypLE™ Express Enzyme (Gibco; 12604013) for 1 minute at RT followed by 5 minutes at 37 ^{o}C. Cells were percussed and resuspended in 1:10 (low serum DMEM:TrypLE™). All cells were pelleted by centrifugation at 400g for 5 minutes at 4^{o}C prior to resuspension.

2.2.1.2 Culture of U87 astrocytoma cells

U87 astrocytoma cells were thawed in DMEM high glucose supplemented with 10% FBS. Cells were passaged every ~5 days in DMEM high glucose supplemented with 1% FBS. Cells were serum deprived overnight before replating. Cells were lifted as detailed for Vero cells in section 2.2.1.1. Cell pellets were resuspended in DMEM

(ThermoFisher; 21063029), supplemented with 1% Glutamax and either 2 mM or 5 mM glucose, counted and plated. Cells were cultured and maintained at 37 °C, 5% carbon dioxide

2.2.2 Differentiation of cell types from hiPSCs

2.2.2.1 Donors' cell lines

2.2.2.1.1 Human induced pluripotent stem cells (hiPSCs)

The hiPSC lines used in this thesis project have been reported elsewhere: SFC840-03-03[169], SFC841-03-01[170] and, SFC856-03-04[171]. Cell lines were derived from dermal fibroblasts from disease-free donors recruited through StemBANCC[172] and the Oxford Parkinson's Disease Centre: participants were recruited to this study having given signed informed consent, which included derivation of hiPSC lines from skin biopsies (Ethics Committee: National Health Service, Health Research Authority, NRES Committee South Central, Berkshire, UK, who specifically approved this part of the study (REC 10/H0505/71)). Non-sendai reprogramming (Cytotune, Life Technologies) was used to reprogram fibroblast cells into hiPSCs. In addition to these cells, iPSC derived from IMR-90 (fibroblast from healthy lung tissue) commercial line were also used. hiPSCs were cultured in an *in house*, defined, open-source medium termed OXE8[173]. Vials containing 1 ml were diluted in 10 ml of Advanced-DMEM/F12 (Gibco; 12634028), spun at 400 rcf for 5 min and resuspended in OXE8 supplemented with 10μM Y-27632 (ROCKi; Abcam, ab120129). Cells, resuspended as clumps, were plated onto Geltrex™ precoated plates and cultured at 37 °C, 5% carbon dioxide. Media changes were done every 24 h using not supplemented OXE8. At ~90% confluency, cells were passaged. Cells were passaged every 2-3 days and, after passage 4, cells were either

differentiated or stored in liquid nitrogen (LN_2). Passaging as clumps[170] was achieved by using 0.5 mM EDTA (Invitrogen; 15575-038) in PBS in Geltrex™ (Gibco; A1413302) precoated plates. Single cell suspension was achieved by TrypLE™ incubation for 3-5 minutes whilst clumps by 2-4 minutes with 0.5mM EDTA in PBS. Both incubations were conducted 37 °C, 5% carbon dioxide

2.2.2.1.2 Human derived samples

Leukocyte cones from healthy donors were provided by the NHS Blood and Transplant services (Oxford, UK) under contract 17/WM/0333. Informed consent was obtained from each donor before blood collection. Isolation of peripheral blood mononuclear cells (PBMC) was done by gradient centrifugation at RT on HistoPaque®-1077 (Sigma;10771). Further centrifugations of the collected pass-through solution were done at 20 °C. After this, red blood cells were lysed using ACK lysis buffer (ThermoFisher; A1049201). Cell suspension was allowed to adhere to 10 cm^2 petri-dishes (Corning) at 150 × 10^6 cells/dish in warm RPMI-1640 medium (GIBCO™; 11875093) and incubated for 2 h at 37 °C, 5% carbon dioxide. Monocytes were then differentiated into macrophages or stored in -80 °C.

2.2.2.2 Generation and culture of cortical progenitor cells (hi-NPCs)

hiPSC passaged twice post-thawing at a confluency of ~95% were induced to neuronal lineages using a modification of a protocol reported elsewhere[174]. For neuronal differentiation, 6-7 days incubation in neuronal induction media (NIM) were required. Media was replaced daily, and cells were observed under the microscope to assess the formation of a neuroepithelium-like sheet. If detachment (normally occurring after day 6), cells were washed once with PBS and incubated with 0.5mM EDTA in PBS for 5 minutes at 37 °C, 5% carbon dioxide. Cells were resuspended,

using a p1000, in 10 ml of Advanced-DMEM/F12 and spun at 300 rcf for 3 min. Cell pellet was resuspended, as clumps, in neuronal maintenance media (NMM) supplemented with 10μM ROCKi, using a 5 ml stripette. Cell suspension was distributed, drop wise, on Geltrex™ precoated plates and incubated at 37 °C, 5% carbon dioxide. Media was replaced daily with NMM. After 5 days, cells were replated (split 1:2) as detailed before. Following 3 extra days in culture, cells were either replated (split 1:2) or stored in LN_2 (early hi-NPCs). Two additional passages, each of 3 days, were conducted. Cells from the final passage were replated as single cells; a step required for the differentiation of late hi-NPCs. To note, as the cells cultured in the *in house* media showed greater adherence, during passages after neuronal induction, the incubation times with 0.5mM EDTA in PBS were ~9-10 minutes whilst for cells cultured in commercial media, ~5-7 minutes. For long term storage in LN_2, cells were resuspended in freezing media composed of NMM supplemented with 10% DMSO and 5 μM ROCKi. After long term storage, cells were thawed on a water bath at 37 °C, resuspended in 10 ml of Advanced-DMEM/F12, spun at 300 rcf for 3 min and plated on Geltrex™ precoated plates using NMM supplemented with 10μM ROCKi for 24 h. Early hi-NPCs were plated as clumps and late hi-NPCs were plated as single cells. See Table 1 below for details on media composition and volumes of preparation.

Components	Final concentration	Commercial NIM	*In house* NIM	Commercial NMM	*In house* NMM
Neurobasal (Life Technologies; 21103049)	N/A	24.4 mL	-	24.4 mL	-
DMEM:F12 (Life Technologies; 21331020)	N/A	24.4 mL	-	24.4 mL	-
Advanced DMEM:F12	N/A	-	49.5 mL	-	49.5 mL
Glutamax (100x)	2 mM	0.5 mL	0.5 mL		0.5 mL
LDN193189 (Sigma; SML0559)	100 nM	50 µL	50 µL	N/A	N/A
SB431542 (Cambridge Bioscience; ZRD-SB-50)	10 µM	5 µL	5 µL	N/A	N/A
B-27™ Supplement (50X), serum free (Life Technologies; 17504-044)	N/A	0.5 mL	-	0.5 mL	-
N-2 Supplement (100X) (Life Technologies; 17502-048)	N/A	0.25 mL	-	0.25 mL	-
Triiodothyronine	3 nM	-	0.5 µL	-	0.5 µL
D-galactose [0.1 M]	33.5 µM	-	16.75 µL	-	16.75 µL

*Table 1. Volumes represented on the table are to prepare 50 mL of each medium.

2.2.2.3 Generation and culture of fetal-like macrophages (hiPSC-MPhs)

Macrophages were differentiated from hiPSC following the protocol detailed in Vaughan-Jackson et al., 2021[173]. In brief, hiPSC passaged two-three times were

resuspended in EB medium (OXE8 media with 50ng/mL BMP4 (Peprotech; PHC9534), 50ng/mL VEGF (Peprotech; PHC9394), and 20ng/mL SCF (Miltenyi Biotec; 130-096-695)) supplemented with 10μM ROCKi and plated on AggreWell™ 800 plates (Stemcell technologies; 34815) at a density of $4x10^6$ cells/well. Aggrewell plates were previously rinsed with 0.5mL Anti-Adherence Rinsing solution (Stemcell technologies; 07010) and centrifugation at 3000 rcf for 3 minutes at 15ºC to remove bubbles from the microwells. The AggreWell™ plate-containing cells was spun at 100 rcf for 3 minutes at 4 ºC. Cells were then incubated for 4 days at 37ºC, carbon dioxide with daily media change. EBs were lifted from the plate using a Pasteur pipette and divided evenly into 2xT175 flasks before adding 20 mL of differentiation medium (Advanced DMEM:F12 supplemented with 2mM Glutamax, 15 mM HEPES (Gibco; 15630080), 5 μg/mL Human recombinant insulin solution (Sigma; I9278-5ML), 15 μM Tropolone (Sigma; T89702-1G), 25 ng/mL IL-3 (Invitrogen; PHC0033), 50 ng/mL M-CSF (Invitrogen; PHC9501), and 1% P/S. These differentiation cultures were incubated at 37ºC, 5% carbon dioxide, with weekly feeding of an additional 10 mL until the production of macrophage precursors (PreMacs). PreMacs were collected weekly, and an equal volume of the media collected was replaced into the differentiation cultures. Harvested PreMacs were spun at 400 rcf for 5 minutes and resuspended in macrophage medium (Advanced DMEM:F12 supplemented with 2mM Glutamax, 15 mM HEPES, and 50 ng/mL M-CSF. These cells were terminally differentiated into macrophages for 7 days with a 50% media change on day 4.

2.2.2.4 Generation and culture of cardiomyocytes (hiPSC-CMs)

hiPSC at a confluency of ~90% were dissociated with ReLeSR™ (STEMCELL Technologies; 100-0484) and transferred to Growth Factor Reduced (GFR) Matrigel® Matrix (FisherScientific; 354234) precoated plates for differentiation into

cardiomyocytes[175]. Plates were incubated for 24 h at 37 ºC, 5% carbon dioxide. Media was then replaced for RPMI supplemented with 1% B-27™ minus insulin (Gibco™; 1895601) and 6 µM CHIR99201 (Tocris Bioscience; 4423) and incubated for 2 days. For the next 24 h, media was replaced for RPMI with 1% B27 minus insulin until the addition of fresh RPMI with 1% B-27™ minus insulin supplemented with 2.5 µM Wnt-C59 (Tocris Bioscience; 5148). Cells were kept in this media for 48 h. On days 5, 7 and 9, media was replaced for RPMI with 1% B-27™ minus insulin. At day 11 and 13, cells were depleted from glucose by media change to RPMI no glucose (Gibco™; 11879020) supplemented with 1% B-27™ minus insulin. Cells were then fed every 2 days with RPMI supplemented with B-27™. hiPSC-CMs were washed twice with PBS and incubated for 8 minutes, at 37 ºC with TrypLE. Cells were resuspended in PBS and spun for 4 minutes at 1500 rpm. Pellets were resuspended and replated in RPMI supplemented with B-27™.

2.2.3 Generation and culture of 3D cortical organoids

EBs were formed by replating 100 µL of cell suspension (1.25 cells/mL) on a U-bottom 96-well plate in EB formation media with 10µM ROCKi. This media consisted in the modification of OXE8 reported in Vaughan-Jackson et al., 2021[173]. Modifications consisted of a decrease in the FGF-2 concentration to 4 ng/mL and no addition of TGF-beta. Plates were incubated at 37ºC, 5% carbon dioxide for 11 days. 50 µL of EB medium were added on day 1 of feeding. 75% media change was done daily (d2 – d4). At d5, d7 and d9, 75% media change to 3D NIM was done. At d11, several EBs were fixed in 4% PFA for 2 h at RT and stored at 4C in PBS. The remaining EBs were embedded in Matrigel for 1 h at 37ºC, 5% carbon dioxide and then fed with organoid differentiation media (ODM) for 24 h. After incubation, using a Pasteur pipette, 6 organoids were transferred per well on a 6-well plate and fed

with ODM. Organoids were fed every other day, collected, and stored on days 18, 24, 31, 38, 45 and 59, as detailed before. Commercial NIM and ODM were prepared as reported in Lancaster et al., 2013[176]. *In house* 3D NIM consisted of a modified EB formation media (no HEPES, 10 µM Tropolone, 0.02 µM progesterone, and 0.1 mM putrescene) whilst *in house* ODM consisted of a supplementation of the NIM version (0.22 mM D-galactose and 3 nM triiodothyronine).

2.2.4 Coculture models of the fetal brain

2.2.4.1 Coculture of early hi-NPCs with PreMacs

Early hi-NPCs and PreMacs were resuspended in brain coculture media (defined-source NMM supplemented with 15 mM HEPES and 50 ng/mL M-CSF) supplemented with 10 µM ROCKi. Cells were plated at a 1:4 ratio (PreMac : early hi-NPCs) and incubated for 24 h at 37ºC, 5% carbon dioxide on Geltrex™ precoated plates. In the case of pre-plated conditions, cells were let to attach for 24 h in the desire plate format prior to coculture. 100% media change was done on day 1, followed by 50% media change every other day. Cells were passaged every ~3 days when confluency reach over 100%. At each passage, cells were replated using coculture media with 10µM ROCKi for 24 h to ensure optimal cell survival. For resuspension, cells were washed once with PBS and incubated with StemPro™ Accutase™ (Gibco; A1110501) for 3 minutes at 37 ºC. Cells were further diluted 1:10 in Advanced DMEM:F12 and spun at 300 rcf for 3 minutes. For collection, cells were fixed with 4% PFA for 15 minutes at RT or stained prior to fixation. Cells were stored in FACs buffer (PBS supplemented with 1% FBS, 10 µg/mL human-IgG (Sigma; I8640-100MG), and 0.01% Sodium azide) at 4C.

2.2.4.2 Coculture of early hi-NPCs with hiPSC-MPhs

hiPSC-MPhs, differentiated for 7 days in macrophage medium, were resuspended, and replated in brain coculture medium. hiPSC-MPhs were either plated on Geltrex™ precoated plates or on overnight preplated hi-NPCs to a 1:4 ratio (hiPSC-MPh : early hi-NPCs). Cocultures were conducted in 96-well plates and incubated at 37°C, 5% carbon dioxide prior to ZIKV infection. hiPSC-MPhs plated on precoated plates were exposed to hi-NPCs 2 h post-plating and further incubated for the remaining 22 h.

2.2.5 Differentiation and culture of human MDMs

Monocytes, obtained from PBMC gradient centrifugation, were terminally differentiated into macrophages. Adherent cells were washed once with PBS and media was replaced with complete RPMI (10% FCS, 1% P/S, 1% HEPES) supplemented with 10 ng/mL of human recombinant M-CSF (10 ng/mL, Life Technologies; PHC9501). Media change was conducted every 3 days during differentiation (7 – 10 days). After terminal differentiation, macrophages were washed once with PBS and incubated for 10 minutes with StemPro™ Accutase™ for resuspension. Cells were resuspended and diluted 1:10 mL in PBS, spun at 400 rpm for 5 minutes and, cell pellets were resuspended for final plating in complete RPMI.

2.2.6 Coculture of Vero CCL-81 and macrophages

Macrophage precursors were replated at a density of $5.6x10^3$ per well (96-well plate) and terminally differentiated for seven days (see sections 2.2.2.3 and 2.2.5). At d7, freshly resuspended Vero cells, cultured in DMEM high glucose 1% FBS for 24 h prior to coculture, were added to wells containing macrophages at a density of

$16.8x10^3$ per well (Vero 3:1 macrophage ratio). Cells were incubated for 72 h at 37°C, 5% carbon dioxide. Cells were washed and either fed or infected with SARS-CoV-2. When coculturing cells on a different plate format (e.g., 24-well plate), ratio of cells was estimated based on the area of the wells. Macrophage medium was used for the coculture of hiPSC-MPh whilst for MDMs, DMEM high glucose (1% P/S, 1% FBS) medium was used.

2.2.7 Coculture of hiPSC-CMs and hiPSC-MPhs

Differentiated hiPSC-CMs were replated on matrigel precoated plates in cardiomyocyte media and incubated at 37°C, 5% carbon dioxide for 48 h until contractibility was regained. Terminally differentiated hiPSC-MPh were resuspended in cardiomyocyte coculture media (macrophage media supplemented with oleic acid (OA) bounded to albumin (Sigma; O3008-5ML)) and replated on cardiomyocyte-containing wells. Cocultures were then incubated for 72 h prior to infection. A ratio of 2.5:1 (hiPSC-CM:hiPSC-MPh) was optimal for the coculture.

2.3 Viral challenges

2.3.1 ZIKV challenge in monocultures

For hi-NPC viral challenge, NMM media containing ROCKi was changed in thawed/replated hi-NPCs for NMM without ROCKi. hi-NPCs were incubated for 2 h at 37 °C, 5% carbon dioxide with media-containing ZIKV. Viral dilutions were prepared on ice. ZIKV challenges were done at an M.O.I. of 1 for 2 h at 37 °C, 5% carbon dioxide. Media-containing virus was then removed, and cells were washed once with PBS before adding fresh NMM and incubated under the same conditions. For hiPSC-MPh, cultured in macrophage medium, challenge experiments were

conducted over 4 h at M.O.I. of 0.01, 0.1 and 1, following the steps detailed before. Mock challenges were done by exposing cells to supernatants of Vero cells cultured for 72 h. For infection of U87 cells, these cells were cultured overnight in serum-free media composed of DMEM no glucose (ThermoFisher; 21063029) supplemented with 2.0 mM glucose, 0.5 mM fructose and 1% GlutaMax. Prior to infection, media was replaced for either same media or media supplemented with 2.5 mM D-BHB and cells were incubated for 2 h at 37 ^{o}C. After this time, cells were exposed to media-containing ZIKV and incubated at 37 ^{o}C for 3 h. Cells were then washed once with PBS and incubated in BHB-containing or control media until sampling.

2.3.2 ZIKV challenge in cocultures

hiPSC-MPh were challenged with ZIKV at an M.O.I. of 1. Cells were incubated for 4 h at 37 ^{o}C, 5% carbon dioxide before washed once with PBS and, either cocultured with early hi-NPCs or replated onto pre-plated hi-NPCs. Replated macrophages were detached with accutase (3 minutes incubation at 37 ^{o}C). Control conditions were exposed to supernatants of Vero cells cultured for 72 h. Infection was conducted in five replicates. 90 µL of media were collected at the respective time-points and stored at -80 ^{o}C for further microtitration. hi-NPCs used as controls were directly infected for 4 h at an M.O.I. of 1.

2.3.3 SARS-CoV-2 challenge in monocultures

Cell cultures were transported to the containment level 3 facility and let to settle down for ~15 minutes at 37 ^{o}C, 5% carbon dioxide. Stocks of SARS-CoV-2 with known concentrations were thawed, and dilutions were made up at RT. Cells were challenged to either media-containing virus or fresh media. hiPSC-CMs and Vero

cells were challenged for 2 h at 37 ºC, 5% carbon dioxide whilst macrophages were challenged for 4 h under the same conditions. After incubation, media was collected and stored at – 80 ºC until microtitration, cells were washed once with PBS and either fed with fresh media or fixed for 30 minutes with 4% PFA, 50 mM sucrose in PBS. For colocalization experiments, before fixation as detailed before, macrophages were either incubated for 15 minutes, 30 minutes, 1 h, 2 h, 4 h and 6 h or incubated for 5 h, resuspended with accutase (10 minutes at 37 ºC) using a Cell scrapper, Med,2-POS blade (Sarstedt; 83.3951) and pelleted by centrifugation at 400 rpm for 5 minutes. Upon experiments, hiPSC-CMs were challenged at M.O.I. of 0.01, 0.1 and 1, Vero cells were challenged at M.O.I. of 0.01, 0.1, 1 and 2 and, Macrophages were challenged at M.O.I. of 2.

2.3.4 SARS-CoV-2 challenge in cocultures

Like monocultures, cocultures were transported to the containment level 3 facility and let to settle down for ~15 minutes at 37 ºC, 5% carbon dioxide before infection. Viral dilutions were made up at RT and challenge experiments were conducted for 2 h at 37 ºC, 5% carbon dioxide. Media was collected and stored at – 80 ºC until microtitration. Cocultures were then wash once with PBS and either fixed with 4% PFA for 30 minutes or fed with fresh medium until the respective collection time-point. All the cocultures experiments were conducted at an M.O.I. of 0.01. Internal controls composed of Vero-only and hiPSC-CM-only were infected following the same methodology.

2.4 Immunofluorescence analysis

2.4.1 Immunofluorescence in hi-NPC cultures

2.4.1.1 Confocal microscopy

For detection of neuronal markers, cells were washed once with PBS and fixed with 2% PFA for 30 minutes. Fixed cells were permeabilized for 10 minutes in permeabilization buffer (PBS with 0.1% Trition X-100). Cells were washed once and then blocked for 2 h at RT in blocking buffer (permeabilization buffer with 10% donkey serum (DS, Cat No)). Cells were incubated overnight with primary antibodies in PBS with 0.3% triton X-100 and 5% DS (incubating solution) at 4 ^{o}C. Antibodies dilutions were as follow: anti-Pax6 (1:200, Biolegend; Poly19013), anti-Pax6 (1:200, GeneTex; GTX113241), anti-Tbr2 (1:50, AbCam; Ab23345), anti-Tuj1 (1:1000, Biolegend; 801202), anti-Sox2 (1:150, Merck; Ab5603), anti-Iba1 (1:500, AbCam; Ab5076), anti-MAP2 (1:100, Sigma; M4403), anti-Nestin (1:100, AbCam; Ab93666), anti-NeuN (1:150, Merck; MAB377) and, anti-pH-3 (1:50, Abcam; ab14955). Antibodies were discarded, cells were washed three times, each for 10 minutes, with permeabilization buffer. Cells incubated for 2 h at RT with secondary antibodies in incubating solution. Secondary antibodies were diluted 1:500 and corresponded to: goat anti-mouse and goat anti-rabbit Alexa Fluor 488, Alexa Fluor 546, Alexa Fluor 555, Alexa Fluor 647 and, Alexa Fluor 750, or donkey anti-goat Alexa Fluor 488 and Alexa Fluor 647 (all from Invitrogen). Cells were incubated for 5 minutes with 1:10.000 dilution of DAPI in PBS and then washed three times and as detailed before. Coverslips (Marienfield; 0117520) were mounted on a glass slide (ThermoScientific; 12404070) using Fluorescence Mounting Medium (Dako; S3023). Slides were visualized with a Zeiss LSM710 confocal microscope. Immunostaining of primary conjugated antibodies comprised anti-SSEA-4 (BD

Biosciences; 560796), anti-CD56 (BD Biosciences; 555516) and anti-CD271 (Miltenyi Biotec; 130-098-112). For staining of mitochondrial membrane potential, live hi-NPCs were incubated with 130 nM MitoTracker™ Red CMXRos (ThermoFisher; M7512) for 30 minutes in the dark at 37 °C, 5% carbon dioxide. Cells were then washed once with PBS and fixed with 2% PFA for 30 minutes. After fixation, cells were incubated with 1% ethanolamine in PBS for 5 minutes and then permeabilized and blocked in FACs buffer with 0.01% saponin (Merck; 47036) for 30 minutes at RT. hi-NPCs were incubated with anti-ZIKV Envelope (1:50, GeneTex; GTX133314) overnight at 4 °C. Antibody solution was removed, cells were washed three times, each 5 minutes with FACs buffer with 0.01% saponin, and stained for 1 h at RT with secondary antibody solution (FACs buffer with 0.01% saponin) containing 1:2000 DAPI, 1:5000 BODIPY™ 493/503 (ThermoFisher; D3922) and goat anti-rabbit Alexa Fluor 647. Cells were washed three times and mounted on glass slides as detailed above. Image acquisitions with a Zeiss LSM710 confocal microscope were performed in five random fields captured under 63x magnification, 1.2 zoom of six sections per image, each section of 5 µm. Images were processed and/or quantified using Fiji-ImageJ2 version 2.3.0/1.53f.

2.4.1.2 Flow cytometry

Adhered hi-NPCs were detached with accutase (5-10 minutes incubation at 37 °C, 5% carbon dioxide) and stained for 15 minutes at RT with LIVE/DEAD™ Fixable Violet Dead Cell Stain Kit (ThermoFisher; L34955) following the manufacturer's procedure. Cells were then fixed with 2% PFA in PBS for 15 minutes or live stained with markers of brain cell types prior to fixation. Fixed cells were stored at 4 °C in a V-bottom 96-well plate with FACs buffer. Cells were spun at 400 rpm for 5 minutes and pellets were resuspended in permeabilization solution (0.3% saponin FACs) for

1 h at RT. 2X primary antibody solutions in permeabilization buffer were added to a final 1X concentration and incubated overnight at 4 ^{o}C. Primary antibodies: anti-Pax6 (1:75, GeneTex; GTX113241), anti-Tbr2 (1:50, AbCam; Ab23345), anti-Sox2 (1:35, Merck; Ab5603), anti-MAP2 (1:50, Sigma; M4403), anti-Nestin (1:35, AbCam; Ab93666), anti-NeuN (1:100, Merck; MAB377), anti-Ki67 (1:275, Abcam; ab16667) and anti-S100B (1:15, Sigma; S2532). Cells were spun at 500 rpm for 5 minutes and washed once with permeabilization buffer for 10 minutes before spun and resuspended in secondary antibody solution (permeabilization buffer with 1:2000 goat anti-rabbit Alexa Fluor 555 and goat anti-mouse Alexa Fluor 647, both from Invitrogen). Incubation with secondary antibodies was done at RT for 1 h. Cells were then washed twice with permeabilization buffer and resuspended in PBS. Live staining of markers of brain cell types was conducted following the manufacturer's procedure (BD Biosciences Human Neural Cell Sorting Kit; 562271). Shortly, after live/dead staining, cells were filtered through a 70 µm cell strainer (Greiner; 542-070) and resuspended in media containing 5 mM EDTA. Cells were then stained with either primary conjugated antibodies or isotype controls for 30 minutes at 4 ^{o}C. Finally, cells were washed once (centrifuged at 400 rpm for 3 minutes) and resuspended in 1% PFA in FACs buffer for 30 minutes. Data acquisition was done with Cytoflex LX (Beckman Coulter) CytExpert software. Data analysis was performed using FlowJo V10.8.1.

2.4.1.3 Fluorescence imaging

For nuclear imaging, hi-NPCs plated on 96-well plates (PerkinElmer; 6055302) were fixed with 2% PFA for 15 minutes at RT and stained with 1:10.000 DAPI dilution in PBS for 10 minutes. Cells were washed three times, each for 10 minutes, and images with an EVOSFL Auto (Life technologies). Nuclear size and shape, of at

least 300 nuclei per condition, were calculated. Images were processed and/or quantified using Fiji-ImageJ2 version 2.3.0/1.53f.

2.4.1.4 Imaging flow cytometry (Imagestream®)

Adhered hi-NPCs were detached with accutase (5-10 minutes incubation at 37 °C, 5% carbon dioxide) and live stained for mitochondrial membrane potential as detailed in section 2.4.1.1. After staining and wash, cells were fixed with 2% PFA in PBS for 30 minutes at RT. Cells were washed and kept in FACs buffer at 4 °C. Cells were permeabilized for 30 minutes with FACs buffer 0.3% saponin prior to overnight incubation at 4 °C with primary antibody solution A (FACs buffer 0.1% saponin, 1:100 anti-NS4A (GeneTex; GTX133704) and 1:100 anti-NS1 (Abcam; ab214337). Cells were washed once with permeabilization buffer and stained for 1 h with 1:1000 goat anti-mouse Alexa Fluor 546 and goat anti-rabbit Alexa Fluor 750.

Cells were washed and stained with primary antibody solution B (FACs buffer 0.1% saponin, 1:100 anti-Envelope) for 3 h at RT. Secondary antibody detection with goat anti-rabbit Alexa Fluor 647 was conducted in parallel with 1:10.000 Bodipy™ staining for 1 h at RT. Cells were stained for 5 minutes with 1:10.000 DAPI in FACs buffer and washed as before. Cells were kept in PBS and data acquisition was done with an Amnis® ImageStream®X MkII (Luminex) Inspire 10 software. Data analysis was performed using IDEAS software V6.2.

2.4.2 Immunofluorescence in 3D cortical brain organoids

d10 brain organoids were washed once with washing solution (0.05% Tween-20 in PBS) for 5 minutes and blocked for 2 h at RT in 10% DS, 3% Triton X-100 in PBS prior to antibody staining. Primary antibodies were incubated overnight at 4 °C: anti-Pax6 (1:100, Biolegend; Poly19013), anti-Tuj1 (1:1000, Biolegend; 801202) and

anti-Iba1 (1:500, AbCam; Ab5076) in 5% DS, 3% Triton X-100 in PBS, shaking at 450 rpm. Brain organoids were washed three times, 10 minutes each, with washing solution and then stained for 2.5 h at RT with 1:500 secondary antibodies: donkey anti-goat Alexa Fluor 568, donkey anti-rabbit Alexa Fluor 488 and, donkey anti-mouse Alexa Fluor 647 (all from Invitrogen) in 10% DS, 3% Triton X-100 in PBS. After incubation, cells were washed three times with PBS as detailed before, incubated for 10 minutes with 1:10.000 DAPI in PBS and washed again for three times before imaging. Image acquisitions, at a depth of ~20 µm either by slices with thickness of 1 or 5 µm, were captured with a Zeiss LSM710 confocal microscope under 20x, 40x and 63x magnification. For staining of matrigel^{TM} embedded organoids of more than 10 days, samples were cryo-sectioned. Organoids were dried-out by sucrose gradient. Organoids were placed in PBS 10% and 20% sucrose, each incubation for 1 h. Organoids were then placed in 30% sucrose overnight at 4 ^{o}C. Samples were immersed in optimal cutting temperature (OCT) compound on dry ice until frozen. 20 µm sections were collected on glass slides and dried at RT for 4 h. For staining, slides were immersed in PBS for 10 minutes, immediately rinsed in dH2O and dried on paper towels. Slides were blocked for 2 h at RT with 20% goat serum, 0.3% Triton X-100 in PBS. Primary antibody staining was done overnight at 4 ^{o}C in 5% goat serum, 0.3% Triton X-100 in PBS. (Primary antibodies: anti-Ki67 (1:275, Abcam; ab16667) and anti-S100B (1:15, Sigma; S2532), anti-Nestin (1:500, AbCam; Ab93666), anti-NeuN (1:500, Merck; MAB377), anti-Sox2 (1:500, Merck; Ab5603), anti-MAP2 (1:500, Sigma; M4403), anti-Pax6 (1:100, GeneTex; GTX113241) and anti-Tbr2 (1:1000, Millipore; AB15894)). Three washes of 15 minutes each were conducted in PBS and secondary staining, over 2 h at RT, in 5% goat serum, 0.3% Triton X-100 in PBS comprised 1:500 goat anti-

rabbit Alexa Fluor 633 and goat anti-mouse Alexa Fluor 488 both from Invitrogen. Slides were then washed three times, each for 15 minutes, in PBS before 5 minutes incubation with 1:10.000 DAPI and finally washed three more times. Z-stack image acquisitions, with a Zeiss LSM710 confocal microscope were captured under 5x, 10x and 20x magnification, corresponding zoom of 0.6, 1 and 1. All the images were processed using Fiji-ImageJ2 version 2.3.0/1.53f.

2.4.3 Immunostaining of ZIKV challenged hiPSC-MPhs

Fixed cells were incubated for 5 minutes with 1% Ethanolamine in PBS before permeabilization in FACs buffer 0.3% Triton X-100 for 30 minutes at RT. Cells were then incubated overnight at 4 ^{o}C with primary conjugated 1:50 anti-CD9 (BD Pharmingen; 555371) and 1:100 anti-Envelope in FACs buffer 0.1% saponin. Cells were washed three times, 10 minutes each, with FACs buffer 0.1% saponin and stained with secondary antibody solution for 2 h at RT (FACs buffer 0.1% saponin with 1:500 goat anti-mouse Alexa Fluor 488 (to enhance CD9 signal), 1:800 goat anti-rabbit Alexa Fluor 657 and 1:500 Alexa Fluor 555 Phalloidin (ThermoFisher; A34055)). Cells were washed three times as before, followed by 10 minutes incubation with 1:10000 DAPI in PBS and three washes with PBS. Cells were imaged using a Zeiss LSM710 confocal microscope. 20x magnification, Z-stack projections of 5µm, corresponding zoom of 1. All the images were processed using Fiji-ImageJ2 version 2.3.0/1.53f.

2.4.4 Immunostaining of membrane-bound ACE2

Pre-plated MDM (three donors' cell lines) and hiPSC-MPh (two donors' cell lines) were detached using cell scrappers after 10 minutes incubation with accutase at 37 ^{o}C, 5% carbon dioxide. Live cells were stained using 1:1000 LIVE/DEAD^{TM} staining

(ThermoFisher; L23102) for 15 minutes at RT. Cells were washed once with PBS and spun at 400 rpm for 5 minutes. Cell pellets were resuspended in blocking solution (FACs buffer with 1:100 human Fc Block (BioLegend; 422302)) for 5 minutes. Cells were further incubated for 30 minutes with several dilutions of an *in house* biotinylated RBF-Fc in FACs buffer (details of the synthesizing procedure are available on Deimel et al., 2022 - manuscript under submission). Cells were washed as before and resuspended in FACs buffer containing 1:2000 Streptavidin, AlexaFluor™ 647 conjugate (ThermoFisher; S21374) for 30 minutes at RT. Cells were washed and fixed in 2% PFA in FACs buffer for 10 minutes at RT. PFA was washed and cells were spun at 1000 rpm for 5 minutes and resuspended in PBS. ACE2 expression controls were done by using MDCK and ACE2 transiently expressing MDCK-ACE2. Data acquisition was done with Cytoflex LX (Beckman Coulter) CytExpert software. The percentage of positive cells was calculated by normalization to secondary-only controls. Data analysis was performed using FlowJo V10.8.1.

2.4.5 Immunofluorescence analysis of SARS-CoV2 challenged cells

2.4.5.1 Super-resolution Airyscan microscopy

Fixed cells were rinsed three times with PBS, incubated for 2 minutes with NH_4Cl and rinsed three more times with PBS. Cells were then permeabilized for 10 minutes (0.3% Triton X-100 in PBS). Cells were rinsed as detailed before and blocked for 45 minutes in 5% BSA in PBS prior to extra 20 minutes incubation in blocking solution (5% BSA, 1:200 human Fc block in PBS). Cells were rinsed three times and incubated for 1 h at RT in primary antibody solution (0.015% Triton X-100 blocking solution with 1:400 anti-Rab5A (Cell Signalling Technology; 46449), 1:100 anti-Rab7 (Abcam; ab137029), 1:700 anti-protein N EY2A antibody[9]. Cells were

washed three times with PBS, each for 5 minutes, and stained for 45 minutes at RT with 1:1000 goat anti-mouse or goat anti-rabbit Alexa Fluor 647 (Cell Signalling Technology), 1:400 Alexa Fluor 555 Phalloidin and 1:1000 Streptavidin. Cells were then stained for 5 minutes at RT with DAPI and washed three times. For the immunostaining of the cocultures, MDM were pre-stained with 1:1000 CellTracker™ RedCMTPX Dye (ThermoFisher; C34552) whilst hiPSC-MPh were stained, post-fixation, with 1:500 anti-Iba1 (FUJIFILM Wako; 019-19741). Coverslips were mounted on a glass slide using Fluorescence Mounting Medium and visualized with an 880 Airyscan confocal microscope (Zeiss). Images were quantified, using home-made macros, with Fiji-ImageJ2 version 2.3.0/1.53f. For colocalization, images were segmented and masked to generate constructs of cell pose. This was done using the free online algorithms from Cellpose – Omnipose (2D) (Cellpose_2D_ZeroCostDL4Mic.ipynb). More than 300 cells per condition in at least three independent donors were quantified.

2.4.5.2 Imaging flow cytometry (Imagestream®)

Fixed pellets were resuspended in permeabilization buffer (0.015% Triton X-100, 5% BSA, 1:100 human Fc block in PBS) for 10 minutes at 4 °C. 2X Primary antibody solution (permeabilization buffer with anti-protein N 1:500 EY2A or 1:350 biotinylated EY2A antibodies[9]) was then added for 30 minutes at 4 °C. Cells were diluted 1:15 in permeabilization buffer and spun at 500 rpm for 5 minutes. Cell pellets were resuspended in secondary antibody solution (permeabilization buffer with 1:700 Streptavidin Alexa Fluor 488 or 1:1000 goat anti-human Alexa Fluor 488) and incubated for 30 minutes 4 °C. Cells were washed as indicated before and an additional wash with 1:10 dilution in PBS (spun at 600 rpm for 2 min) was conducted.

Cell pellets were finally resuspended in PBS and data acquisition was done with Amnis® ImageStream®X MkII (Luminex) Inspire 10 software. Data analysis was performed using IDEAS software V6.2.

2.5 Metabolic measurements

2.5.1 Radioactive measurements

2.5.1.1 Glycolytic flux

hi-NPC pre-plated for 10 hours (5 h post-attachment) were fed with culture medium containing 5-^{3}H-glucose and incubated at 37 ^{o}C, 5% carbon dioxide. 5-^{3}H-glucose is converted via glycolysis into fructose-6-phosphate releasing $^{3}H_2O$ into the culture medium. Culture media was composed of no glucose DMEM (Thermo Fischer; 11966025) supplemented with 5 mM glucose and 0.2 µCi/mL or 0.00074 MBq/mL of glucose, D-[5-^{3}H(N)] (PerkinElmer). Cells were incubated for 4 and 6 h after which cell supernatants from duplicate plates were collected at each respective time-point and stored at -20 °C. Released $^{3}H_2O$ required to be separated from unconverted 5-^{3}H-glucose. The separation process was done using the ion-exchange chromatography separation (Dowex) method. Dowex solution was prepared by mixing 250 g AmberChrom® 1X4 chloride form, 100-200 mesh (Sigma; 428590) with 1.25 M NaOH and 1.61 M boric acid. The mixture was mixed gently and repeatedly washed with dH_2O pH 7.5 was reached. Dowex soltion was added to glass Pasteur pipettes (VWR 612-1701, Avantor; 612-1701) containing glass wool. 200 µl of the media were added to the Dowex column and incubated for 15 mins allowing ^{3}H glucose to bind to the column. $^{3}H_2O$ was eluted to the vials by two rinsing them twice with dH_2O. Radioactivity was measured using Tri-Carb 2800TR Liquid

Scintillation Analyzer (Perkin Elmer). 0.2 mL medium at time point 0 was used as a control to determine the specific activity of the buffer.

2.5.1.2 Glucose oxidation

Glucose oxidation was measured using a protocol modification[177] of the original $^{14}CO_2$ capture method by Collins et al., 1998[178]. hi-NPCs pre-plated for 10 h in a 24-well plate were washed once with PBS and fed with no glucose DMEM supplemented with 12 mM glucose containing 0.2µCi/mL [D-[14C(U) glucose: 1mCi-37MBq]. The released $^{14}CO_2$ was trapped in KOH-soaked filter papers. To kill the cells and allow the released of $^{14}CO_2$, cells were incubated with perchloric acid (Merck; 244252) for 1 h after 2 and 4 h post-feeding. Filter paper containing trapped $^{14}CO_2$ were analyzed using a scintillation counter and the radiation counts per minute (CPM) were measured. 0.01 mL medium at time point 0 was used as a control to determine the specific activity of the buffer.

2.5.1.3 Oleic acid oxidation

Radioactive tracing of oleic acid oxidation was based on the detection of $^{3}H_2O$ produced from ^{3}H oleate in the electron transport chain, as reported elsewhere[175]. hi-NPCs pre-plated for 10 h were fed for 4 and 6 h at 37 °C, 5% carbon dioxide with no glucose DMEM, 2% BSA, 0.3 mM oleate and 0.2µCi/mL of oleate, [9,10-3H(N): 1mCi-37MBq] (PerkinElmer). For media preparations, oleate was heated to melt them down and, was simultaneously added with ^{3}H oleate to the BSA to ensure the same binding. Folch extraction method[179], modified and reported by Malandraki-Miller, S. et al., 2019[180] was used to separate the $^{3}H_2O$ from the ^{3}H oleate. 0.5 mL of perfusate was pipetted in 15 mL falcon tube containing 1.88 mL of chloroform:methanol (1:2 v/v) solution, 625 µl chloroform and 625 µl KCL-HCl

solution (2 M KCl, 0.4 M HCl). The solution was then rotated on a laboratory stuart rotator SB3 at 40 rpm for 1 h. After rotation, top aqueous layer was collected, and bottom organic layer was discarded. The aqueous layer was then exposed to 1 mL chloroform, 1 mL methanol and 0.9 mL KCL-HCL and rotated for 1 h at 40 rpm. 0.5 mL the top aqueous layer was used to count the radioactivity using a Tri-Carb 2800TR Liquid Scintillation Analyzer (Perkin Elmer). 0.5 mL medium at time point 0 was used as a control to determine the specific activity of the buffer.

2.5.2 Glycolytic capacity

2.5.2.1 Extracellular glucose measurements

For extracellular measurements of glucose consumption, the concentration of glucose in the culture media was detected using a miniaturization of a commercial protocol (Merck; GAHK20). 100 µL of culture media were diluted 1:10 and 1:20 in dH2O (dilutions depended on the initial level of glucose). 20 µL of each dilution were added per well on a F-bottom 96-well plate. Glucose solution was freshly made up by resuspending the vial in 20 mL of dH_2O and 100ul of Glucose solution to each sample. Plates were incubated at 35 °C for 15 min inside a SpectraMax M5 plate reader (Molecular devices). NADH absorbance was read at 340 nm wavelength. A standard curve from known concentrations of glucose (0.3, 0.5, 0.8, 1.0, 1.5, 2.0, 2.5 mM) was run per plate and glucose values from the samples were calculated by curve fitting. For readouts of glucose from cells exposed to ZIKV, media was kept at 4 °C for 96 h prior to measure to allow for the decay in viral infectivity.

2.5.2.2 Extracellular lactate measurements

Lactate from the culture media was detected using an *in house* method based on the NADH absorbance at 340 nm wavelength. The accuracy of the lactate measurements was assessed by comparing the real absorbance at 340 nm to the expected absorbance estimated based on the extinction coefficient of the NADH ($A= \varepsilon_1 C$). 5µL of sample were added per well and incubated with 100 µL of freshly made running buffer solution for 20 minutes at 37 °C inside a SpectraMax M5 plate reader. Like the glucose protocol, NADH absorbance was read at 340 nm wavelength. A standard curve from known concentrations of sodium L-lactate (Merck; L7022) was run per plate (0.09, 0.17, 0.34, 0.49, 0.70, 1.00, 2.00, 4.00 mM). Lactate concentration was calculated by curve fitting. For readouts of lactate from cells exposed to ZIKV, media was kept at 4 °C for 96 h prior to measure to allow for the decay in viral infectivity. Running buffer consisted of a mixture of 3.5 mL of glycine buffer with 6.5 dH_2O, 10 mg of NAD (N0632) and 165 µL of 1000 units/mL LDH (Sigma; L3916). For 100 mL of glycine buffer, 4.5 g of glycine [0.6 M] (Merck; G8898), 1.3 mL of 50-60% purity hydrazine hydrate (Sigma; 225819) were mixed with 95 mL of dH_2O. Solution was buffered to a pH of 9.2 by the addition of 600 µL of KOH [10 M].

2.5.3 Cell survival measurements

Cell survival was estimated by their metabolic activity using the CCK-8 assay (Sigma; 96992). Manufacturers' procedure was followed with minimal modifications. The CCK-8 assay uses a water-soluble tetrazolium salt that is reduced by cellular dehydrogenases to produce an orange formazan dye. In brief, cells were washed once with PBS and incubated for 2 h at 37 °C, 5% carbon dioxide with 100 µL fresh medium containing 10 µL of CCK-8 (96-well plate format). After incubation, 100 µL

were collected and absorbance was read at 460 nm wavelength. Cells were washed once with PBS and further incubated with fresh media for further measurements or disposed.

2.6 Transmission Electron Microscopy (TEM)

Macrophages challenged for 5 h with SARS-CoV-2 or mock-controls were washed once with PBS. For transmission electron microscopy, cells were fixed for 1 h at RT with 4% PFA, 2.5% glutaraldehyde (Merck; G5882) in 0.1 M PIPES buffer (pH 7.2) and further incubated overnight at 4 °C. Cells were washed with freshly made 0.1 M PIPES buffer followed by a 15 minute wash in 50 mM glycine in 0.1 M PIPES buffer and a last 10 minutes wash in 0.1 M PIPES buffer. Cells were further incubated for 1 hr at 4 °C in 1% osmium tetroxide, 1.5% potassium ferrocyanide in 0.1 M PIPES buffer with vigorous agitation. Cells were then washed 5 times in ultra-pure water and incubated overnight at 4 °C in 0.5% uranyl acetate. Samples were washed with water and dehydrated through a graded series of ice-cold ethanol solutions (from 30–95%) for 15 min each followed by a final incubation in 100% ice-cold ethanol for 90 min. Samples were then infiltrated with 25% Agar 100 resin (Agar Scientific) in ethanol for 3 h and then 50% resin overnight, followed by 75% and 100% resin each for 3 h and then 100% resin overnight. The samples were embedded in flat-dish moulds and polymerized at 60 °C for 48 h. Ultrathin (90-nm) sections were cut with a Diatome diamond knife using a Leica UC7 ultramicrotome and post-stained for 5 min with lead citrate. Sections were viewed on a FEI Tecnai 12 TEM operated at 120 kV equipped with a Gatan OneView digital camera

2.7 Molecular biology analysis

2.7.1 RNA extraction and cDNA conversion

Cell were detached with accutase (5 – 10 minutes at 37 °C), spun at 400 rpm for 5 minutes and pellets were frozen dry at -80 °C. Cell pellets were thawed on ice and RNA extraction was done using the RNeasy Mini Kit (QIAGEN; 74104). Before RNA elution in 35-50µL RNAse free water, samples were DNAse treated RNAse-Free DNase Set; QIAGEN, 79254). RNA concentration was quantified using a Nanodrop 2000c. RNA was reversed transcribed into complementary DNA (cDNA) using the High-Capacity RNA-to-cDNA™ Kit (ThermoFisher; 4387406). For cDNA conversion, samples were diluted, and equal concentration of RNA was added for the reaction.

2.7.2 Quantitative polymerase chain reaction

Gene expression was determined using the double stranded DNA binding dye SYBR™ Green. Primers efficiency was determined by SYBR green qPCR across 5x3-fold dilutions of cDNA and calculated in Microsoft Excel as $Efficiency = (10\text{^}(-1/Slope) - 1) * 100$ where slope is calculated for the plot of average Ct against Log(sample quantity) - primers' efficiency for qPCR of non-published primers is included in Table 2. qPCR reactions comprised of 1 volume of sample cDNA to 3 volumes mastermix (Power SYBR™Green PCR Master Mix (ThermoFisher; 4367659), forward and reverse primer mix, and nuclease free water at a ratio of 5µL : 1µL : 1.5µL respectively). Reactions were in run in five replicates in either 96-well format, 20 µL/sample, or 384-well format, 10 µL/sample. The threshold cycle ($2^{-\Delta\Delta Ct}$) method of comparative PCR was used to analyze the results. $2^{-\Delta Ct}$ was calculated by the normalization of the sample Ct value to the

average Ct value of two housekeeper genes, UBC and TBP. $2^{-\Delta\Delta Ct}$ analysis was done by the further normalisation of the samples against a 0 h control. For the quantification of ZIKV transcripts, Ct values were also normalized against UBC and TBP and further normalised against untreated controls, displaying results as $2^{-\Delta Ct}$ and $2^{-\Delta\Delta Ct}$.

Gene	Forward Primer	Reverse Primer	Efficiency (%)
ZIKV	AGGATCATAGGTGATGAAGAAAAGT	CCTGACAACACTAAGATTGGTGC	102.19
PDK-2	GCCGCTTGGATCTTTGTGGA	CCAGCTCCTTCTATCCTCCCTT	121.94
UCP2	GTCCGGTTACAGATCCAAGGAG	GGCAACCAGCCCATTGTAGA	96.57
HK-1	GCAGCTCCTGGCCTATTACT	TGGCATAGAGATACTTGTCAATCT	86.63
ACACA	ACCTGTAGTAGCTGCTGGTG	TCCAGGGCATACTTGGTAGC	102.02
HADHA	CCAGAAGATAGTGGACCGGC	AGGGCTGTTAGCATGGTCAG	101.12
FASN	GTCTCTGAAGGGCATCCTGG	GAGACAGTTCACCAAGCCCA	111.14
ACADM	GTGGAAGCAGATACCCCAGG	GCAGCTACTACAGGTCTGGT	102.10

*Table 2. Primers were concentrated at 100 nM and the annealing temperature at 64 °C.

2.8 Physiological measurements: Muscle motion recording

Video recordings, of 15-30 seconds duration at 60X magnification, of hiPSC-CMs were taken with a Canon EOS 100D camera. The videos were converted into 50 frames per second tiff sequence images using the pre-defined code: *for i in *.*; do ffmpeg -i "$i" -pix_fmt nv12 -f avi -c:v rawvideo "${i%.*}.avi "; done.* The videos were then processed using pre-defined macros plug-in Muscle Motion software v.1 in FIJI/ImageJ as reported elsewhere[181,182]. Processed data was further analyzed with Fiji-ImageJ2 version 2.3.0/1.53f and Microsoft® Excel for Mac Version 16.51 to calculate the parameters of muscle motion: amplitude, peak-to-peak time, time to peak, relaxation time, and peak amplitude.

2.9 Transfection in hi-NPCs

NS4A transfection in hi-NPCs was attempted using FuGENE HD. hi-NPCs pre-plated for 24 h at 37 °C, 5% carbon dioxide or in suspension were washed/resuspended in Opti-MEM™. Cells were then exposed to pre-incubated (30 minutes at RT) transfection mixtures (FuGENE HD 1 : 1 DNA mixture (pcDNA3.1 and NS4A-2K-2B) in Opti-MEM™ reduced serum medium (ThermoFisher; 31985070)). Transfection was allowed for 6 h at 37 °C, 5% carbon dioxide prior to media change for fresh NMM. After 56 h post-transfection, cells were resuspended, fixed with 4% PFA for 15 minutes at RT, and stained with anti-NS4 and anti-V5 antibodies. Secondary staining with anti-mouse AlexaFluor 488 and anti-rabbit AlexaFluor 647 (both from Sigma) was conducted. Cell pellets were finally resuspended in PBS and data acquisition was done with Cytoflex LX (Beckman Coulter). Data analysis was performed using FlowJo V10.8.1.

2.10 Statistical analysis and software

This thesis was written using Microsoft® Word for Mac version 16.51 (2021). Detailed information on the versions of each software used for data analysis and the respective statistical tests is available on the method section within each chapter.

3. METABOLIC REMODELLING DISTINGUISHES SUBTYPES OF HUMAN iPSC-DERIVED CORTICAL NEURONAL PROGENITOR CELLS (hi-NPCS)

3.1 ABSTRACT

The adult brain is comprised of millions of neurons, glia, ependyma and microglia. The normal fetal brain development requires the production of these diverse cell types from various progenitor subtypes with distinct relative abundance. Neuronal progenitors can be classified based on their relative position to the basement membrane (apical or basal), morphology, gene expression or interkinetic nuclear migration. Neuronal progenitor subtypes have distinct fate restrictions that is regulated by time-dependent gene expression patterns and activation of specific energetic pathways during differentiation. Understanding the causal relationships in changes in cell cycle parameters and fate determination of the produced cells is one of the central issues in *in vitro* developmental neurobiology. Here, I showed morphological and physiological characterization of 2D *in vitro* cultures of hiPSC-derived neuronal progenitor cells (hi-NPCs) obtained at two different stages during cortical neuronal differentiation. These cultures had different populations of neuronal progenitors that metabolically resemble two distinct progenitor subtypes in the forebrain: radial-glia progenitors (early hi-NPCs) and intermediate progenitors (late hi-NPCs). I showed that both early and late hi-NPCs express markers of human neuronal progenitor cells, and that both cultures inherit similar ratios of neuronal and non-neuronal cells. Importantly, when measured by short- and long-term metabolic tracing, late hi-NPCs show significantly higher rates of fatty acid

oxidation and lower glycolytic flux. In addition, this chapter highlights the advantage of metabolic measurements as a tool to overcome some of the limitations associated with morphological characterization for the subtyping of neuronal progenitor cells cultured *in vitro*. Lastly, the physiological characterization and distinction of human induced neuronal progenitor (hi-NPCs) subtypes of the forebrain during *in vitro* cortical differentiation provides a powerful tool to study mechanisms of fetal development as well as disease modelling of fetal pathogenesis such as Zika virus-mediated brain abnormalities.

3.2 INTRODUCTION

Intrauterine development during the first trimester of pregnancy includes a series of orchestrated cellular processes, mainly cell division and differentiation, which give origin to primitive tissue and organs[183]. The brain develops from a neural plate that forms a tube. The inner lining of this tube contains the germinal zone where most of the progenitor cells are situated. This surface is next to the ventricles thus, it is called ventricular surface. Since the basal lamina is at the outside surface, it is referred to as basal, whereas the ventricular surface as apical[184–186]. These principles apply to the entire developing nervous system. The progenitors in the ventricular surface (such as radial glia) are also referred to as apical progenitors, whereas the intermediate progenitors with no contacts to the ventricular surface are also referred to as basal or intermediate progenitors[184–186] (Figure 3.1).

At early stages, the cortical expansion of the brain take place from self-renewing divisions that will eventually switch to proliferative divisions[187]. The switch between these stages is reflected in the combinatorial transcription factor expression and the change in nucleokinesis during division[186] (Figure 3.2). Proliferative divisions require nutrient supply and gas exchange. These processes are controlled by the primitive permeable blood brain barrier[188–190]. It is debated what time the blood brain barrier is fully functional and whether the foetal blood brain barrier is less mature compared to the adult brain[191–193]. However, the vasculature specific susceptibility to hypoxia and metabolic changes[191–193], potentially underlies a higher sensitivity of the developing brain to external insults[194].

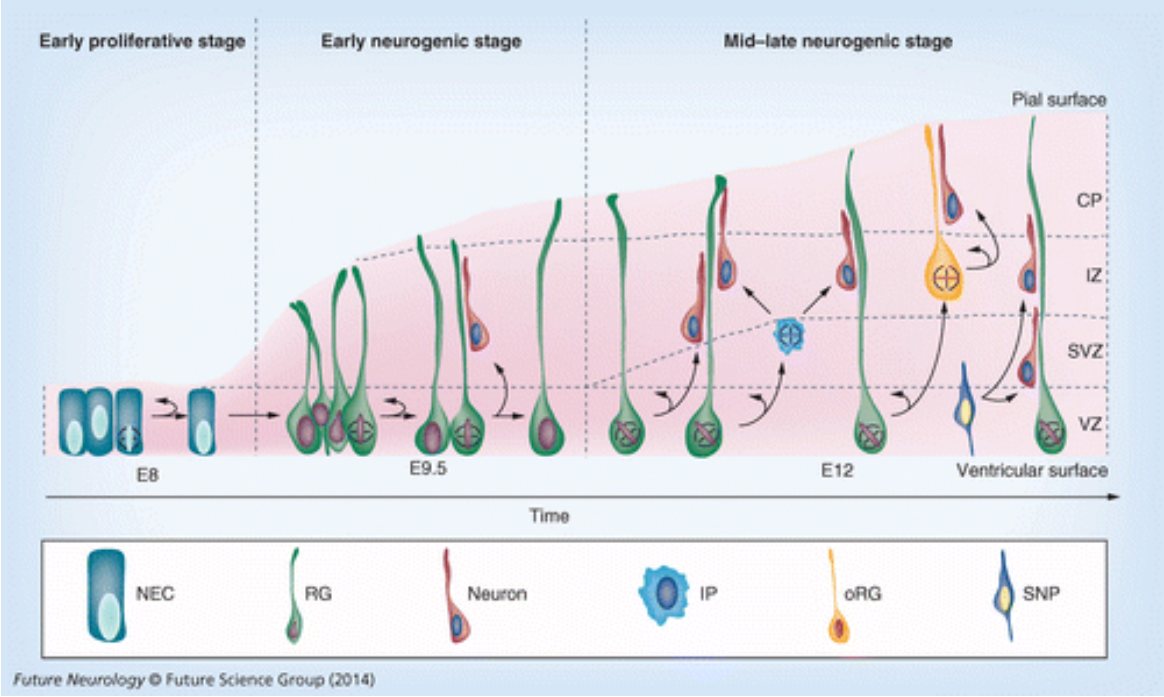


Figure 3.1. Neurogenesis in the mouse cortex
Neural stem cells (NECs) initially divide symmetrically to expand their pool and progressively transform into radial glia progenitor (RGP) cells. RGPs divide symmetrically, and asymmetrically to produce neurons that migrate radially to form the cortical plate (CP). At earlier stages, RGPs divide asymmetrically to produce neurons directly, then switch to indirect neurogenesis through intermediate progenitors (IPs) or outer subventricular zone radial glia progenitors (oSVZ oRGs). oRGs divide asymmetrically to produce neurons in mice, or transient amplifying cells in humans. IPs mostly populate the SVZ while oRGs translocate into the intermediate zone (IZ) for neurogenesis. Short neural precursors (SNPs) are located in the VZ, where they divide symmetrically to produce neurons. Obtained from Postiglioni & Hippenmeyer, 2014[187].

The diversity of the cells that are produced in progenitors are regulated by the space and time of the production. The same progenitor can have very different properties at different stages of development[186] (Figure 3.2). Progenitors at different sectors of the neuroepithelum has different combinatorial gene expression patterns[195,196]. Moreover, lineage tracing from selected progenitors revealed the changing properties of the generated cells[197,198]. Changes in protein expression and/or the presence/absence of certain cellular receptors facilitates the differentiation of neuronal subtypes yet, the main distinctions for these subtypes are their migration characteristics and final alignment into different brain regions[186,199–201]. In summary, brain development involves the division and differentiation of several subtypes of

neuronal and non-neuronal cells, some of which originated from the same progenitors[202,203] (Figures 3.1 and 3.2).

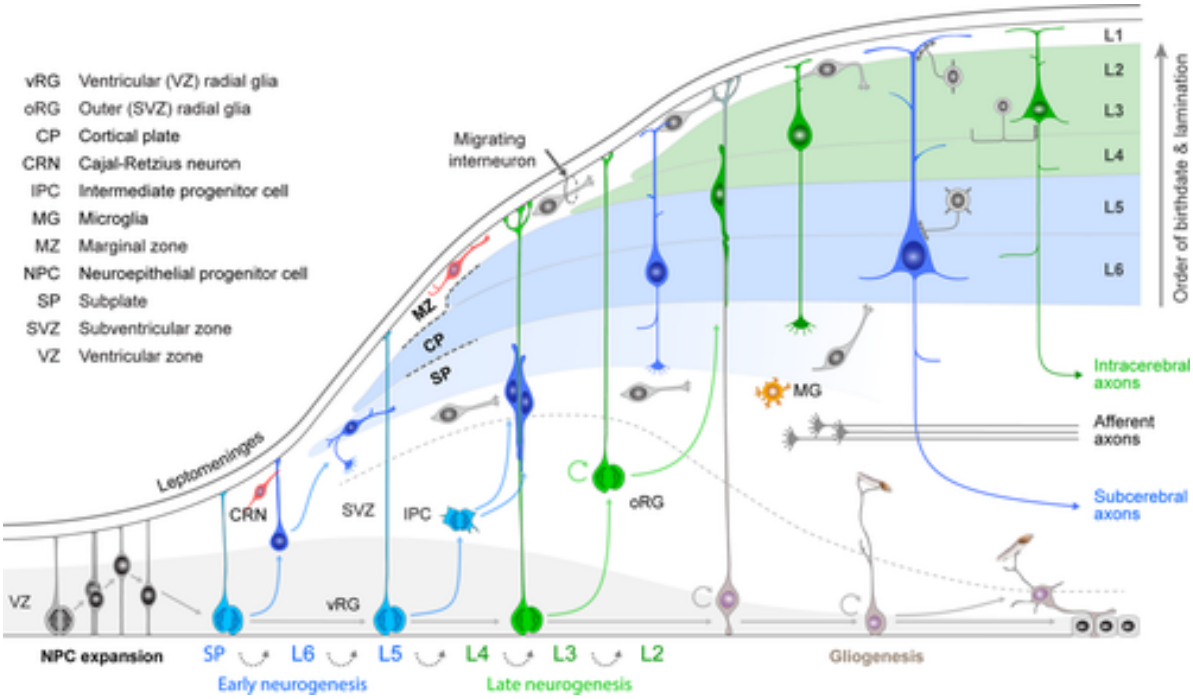


Figure 3.2. Schematic illustration of neurogenesis in the mammalian neocortex
Neuroepithelial cells (NPCs) undergo symmetric cell division to produce an initial pool of cortical progenitors that later transform into ventricular radial glia cells (vRGCs). vRGCs begin asymmetric cell division to generate another vRGC and a nascent projection neuron. The neuron then migrates radially from the ventricular zone (VZ) along the basal process of a RGC into the cortical plate (CP). The earliest born neurons migrate to form the preplate. Later migrating neurons split the preplate into the marginal zone (MZ) and subplate (SP). As neurogenesis proceeds, diverse subtypes of neurons are generated through the successive asymmetric division of RGCs. Early-born nascent projection neurons settle in the deep layers (Layers 5 and 6; red layers), and later-born projection neurons settle in towards mid-neurogenesis stage. Additionally, some populations of RGC daughter cells become intermediate progenitor cells (IPCs) or outer radial glial cells (oRGCs) in the subventricular zone (SVZ). After the neurogenic stages, the radial scaffold detaches from the apical surface and vRGCs become gliogenic, generating astrocytes, or transform into ependymal cells. Tangential migration of interneurons is observed in the MZ, intermediate zone (IZ) and SVZ. Neocortical projection neurons mature into cortical projection neurons (CPNs), which show layer- and subtype-specific morphology and axonal projection patterns. Adapted from Kwan et al. (2012). Obtained from Molnár et al., 2020[186].

In vitro brain research has developed to differentiate brain cell types (e.g., adult-like neurons) from pluripotent stem cells of patients to mainly study neurodegenerative disorders[204–207]. A variety of *in vitro* neuronal models have showed results involving electrical activity, impaired synapses, cell death, cell susceptibility to stressors

compared against cell lines from healthy donors[204–207]. However, the lack these processes in *in vitro* generated cells arguably recapitulate features of the human brain potentially due to incomplete neuronal differentiation and/or uncontrolled differentiation of subpopulations of brain cells.

In vitro generation of 3D brain organoids supposes an advance in disease modelling. To study brain development, 3D brain organoids potentially due to their shared similarities in the protein expression profile with the human brain and/or the formation of brain regions with similar morphology and cell distribution[208–212], have replaced the use of other 3D systems such as organotypic cultures. Nevertheless, the production of 3D organoids is variable even when using a single donor cell line[213,214]. Thus, highlighting the importance of defined 2D *in vitro* neuronal cultures. Although *in vitro* characterization of neuronal cells has been broadly studied using various methods of isolation, differentiation, and cellular sources[215–218], cortical neuronal progenitors, both human fetal and hiPSC-derived cells, have been poorly characterized at the subtyping level. Most of the research conducted on cluster neuronal progenitor populations, either from 2D or 3D systems, has been based on the presence/absence of conventional markers of undifferentiated progenitors and immature neurons e.g. Pax6, Tbr2, Nestin[184,219,220]. Thus, examining the presence/absence of conventional markers of the early brain and markers to distinguish major types of brain cells in *in vitro* neuronal populations requires in-depth analysis to elucidate the potential presence of subclasses of progenitors.

Furthermore, energy metabolism plays a crucial role in brain development[221] and, in the adult brain, coordinated utilisation of macro and micronutrients suggests the need of specific energetic processes to support cellular differentiation and functionality[52,222–226]. Research has showed several differences within subtypes of

early cortical neuronal progenitors based on both their protein expression profiles and their cellular metabolism[227].

Neuronal progenitor cells at different stages of proliferation and differentiation exhibit specific activation and shifts between the main cellular metabolic pathways (glycolysis, glucose and fatty acid oxidation)[55,228–230]. The shift from cytosolic glucose metabolism to mitochondrial glucose oxidation and the activation of fatty acid oxidation are thought to signal for differentiation of quiescent neuronal progenitors to proliferative neuronal progenitors[185,227,231]. To date, few studies have showed *in vitro* physiological characterisation of subtypes of cortical neuronal progenitor cells. This lack of characterization is potentially a contributing factor to the discrepancies reported in the literature regarding *in vitro* modelling of fetal developmental disorders. Thus, in this thesis I hypothesised that the metabolism of different cell types of the developing early fetal brain is distinctively hijacked by neurotropic Zika virus (ZIKV) and underpins the differences in congenital zika syndrome observed over the course of pregnancy[77]. The detailed characterization and physiological subtyping of 2D *in vitro* differentiated neuronal progenitor cells from human induced pluripotent stem cells (hi-NPCs) increases the immense value of current systems and facilitates the discovery of the mechanisms used by ZIKV to disrupt brain homeostasis of different cell types relevant for the correct development at different stages of pregnancy.

3.3 AIMS

Nutritional deprivation and the subsequent energy metabolic dysregulations severely impacts fetal cortical development; a process that requires an orchestrated interaction between different subtypes of neuronal progenitor cells to allow for cell proliferation and differentiation, cell migration, and cortical organization. Various viral infections such as vertical transmission of ZIKV can have devastating effects on the development of the fetal brain. Thus, as hypothesised in this thesis, the metabolic requirements of ZIKV can distinctively stress the metabolic profiling of different cell types present at different ratios during pregnancy underpinning mechanisms for congenital Zika syndrome. This chapter focused on generating a more robust disease model than currently reported in the literature. To this, I performed morphological and physiological characterization of a 2D *in vitro* culture of cortical neuronal progenitor cells differentiated from human induced pluripotent stem cells (hi-NPCs). This facilitated a platform to study specific effects of ZIKV infection on the energy metabolism of different subtypes of neuronal progenitors; potentially the main responsible cell types underpinning the congenital Zika syndrome. This was achieved by the following three aims:

- To determine the extent to which hiPSC-derived neuronal progenitor cells were present during cortical differentiation
- To characterize neuronal subtypes within the pool of hiPSC-derived neuronal progenitor cells obtained during cortical differentiation
- To test the value of measuring the preferential energy metabolic pathway as a tool for the potential distinction of subtypes of hiPSC-derived neuronal progenitor cells based on current literature generated from mouse models

3.4 METHODS

3.4.1 Generation and culture of cortical progenitor cells from hiPSC

hiPSC were obtained and maintained as detailed in section 2.2.2.2.1. Cortical neuronal progenitor differentiation was carried out following the protocol set out in section 2.2.2.2.

3.4.2 Culture of cancerous cells

Culture of cancerous cells Vero CCL-81 and U87 astrocytoma cells were carried out following the protocols set out in sections 2.2.1.1 and 2.2.1.2, respectively.

3.4.3 Immunofluorescence analysis of hi-NPCs

Immunostaining of hi-NPCs and confocal imaging of conventional neuronal markers were carried out following the protocol detailed in section 2.4.1.1. Immunostaining and, quantification of conventional neuronal markers and populations of brain cell types, by flow cytometry, were carried out following the protocol stated in section 2.4.1.2

3.4.4 Radioactive metabolic tracing

Intracellular radioactive metabolic tracing of glucose metabolism, glucose oxidation, and oleic acid oxidation were carried out following the protocols set out in section 2.5.1.

3.4.5 Extracellular glucose measurements

Glucose measurements from cell supernatants were carried out following the protocol set out in section 2.5.2.1.

3.4.6 Extracellular lactate measurements

Lactate measurements from cell supernatants were carried out following the protocol set out in section 2.5.2.2.

3.4.7 Statistical analysis

Datasets containing analysis of two independent donors or independent triplicate experiments of one donor cell line were analyzed using mixed-effects model with Šidák correction. Datasets comprising two independent repeats of a donor cell line were analyzed by two-tailed Mann-Whitney U test. Datasets comprising technical repeats against theoretical values were analyzed by two-tailed Wilcoxon-rank test. Datasets containing analysis of independent experiments of three donors' cell lines were processed using Two-way ANOVA with Šidák's multiple comparisons post hoc test. All the statistical tests were performed using GraphPad Prism 9.3.1. A calculated P value less than 0.05 was reported as significantly different.

3.4.8 Figures

Representation schemes were created with BioRender.com. Summary figures were done using GNU Image Manipulation Program (GIMP 2.8.22).

3.5 RESULTS

3.5.1 Morphological characterization of hiPSC derived cortical neuronal progenitors

Differentiation of cortical neuronal progenitors using a 2D adaptation from Shi et al., 2012; Robbins et al., 2018, produces, at different time-points, hi-NPCs with distinct morphology (Figure 3.3A). Based on the time of differentiation, these cells were called early and late hi-NPCs. Early hi-NPCs are rounded and exhibit a large cytoplasm and a large nucleus with few membrane projections (Figure 3.3B) whilst "star-shaped" late hi-NPCs display abundant projections with a small cytoplasm and nucleus (Figure 3.3C). The metabolic activity using the CCK-8 tetrazolium assay showed that early hi-NPCs had faster cellular proliferation after 24 h post-plating compared to late hi-NPCs yet, this was limited, in further time-points, by the available space in the culture plates (data shown in chapter 4; Figure 4.2A).

Morphological characterization by immunofluorescence showed that both early and late hi-NPCs expressed markers of proliferation and neuronal progenitor cells such as p-H3, nestin, Tbr2 and MAP2 (Figure 3.4). Larger screening of markers including for the distinction of neuronal progenitor cells, Ki67, S100B, Nestin, NeuN, Sox2, MAP2, Pax6 and Tbr2, showed no significant differences ($p \geq 0.05$) in the expression of most of the proteins of interest between early and late hi-NPCs (Figure 3.3E). Figure 3.3.D showed an example of the gating strategy used for the screening conducted by flow cytometry.

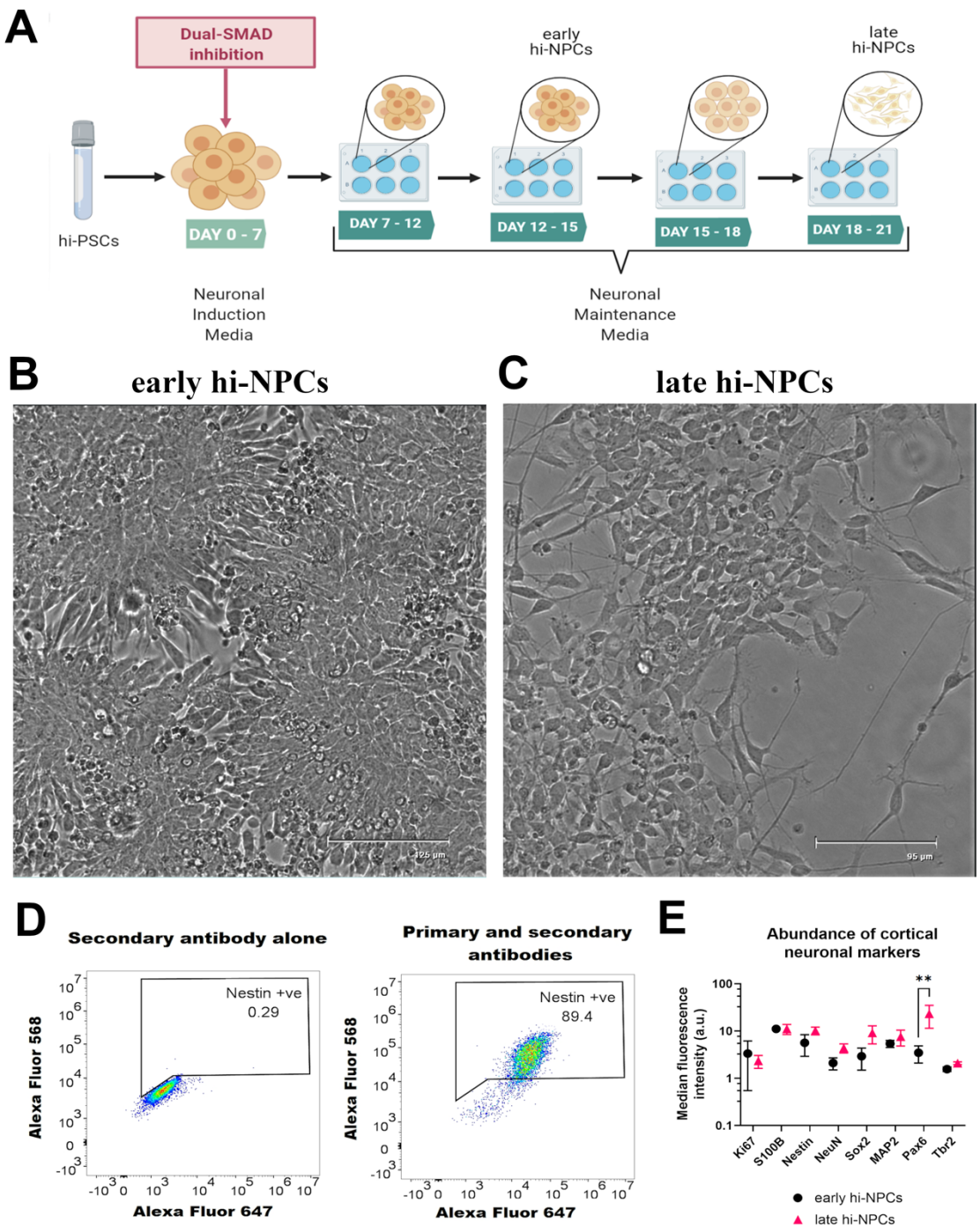


Figure 3.3. Cortical differentiation from hiPSCs produces phenotypically distinct neuronal progenitors (hi-NPCs)

(A) Schematic of 2D differentiation of hiPSCs to cortical neuronal progenitors (hi-NPCs). Brightfield images showing differences in morphology between (B) early hi-NPCs (125 μm) and (C) late hi-NPCs (95 μm). (D) Example of the flow cytometry gating strategy for the detection of conventional early cortical neuronal progenitors in hi-NPCS. (F) Dot plot showing the relative median fluorescence intensity in early and late hi-NPCs of a panel of conventional neuronal markers (Ki67, S100B, Nestin, NeuN, Sox2, MAP2, Pax6 and Tbr2) used to distinguish cortical progenitors. Bars display mean ± SD. n = 1 cortical differentiation of two independent donors' cell lines each conducted in four replicates. Significance was calculated by a mixed-effects model with Šidák correction. Significance is shown when $^{*}p < 0.05$, $^{**}p < 0.01$, $^{***}p < 0.001$, $^{****}p < 0.0001$.

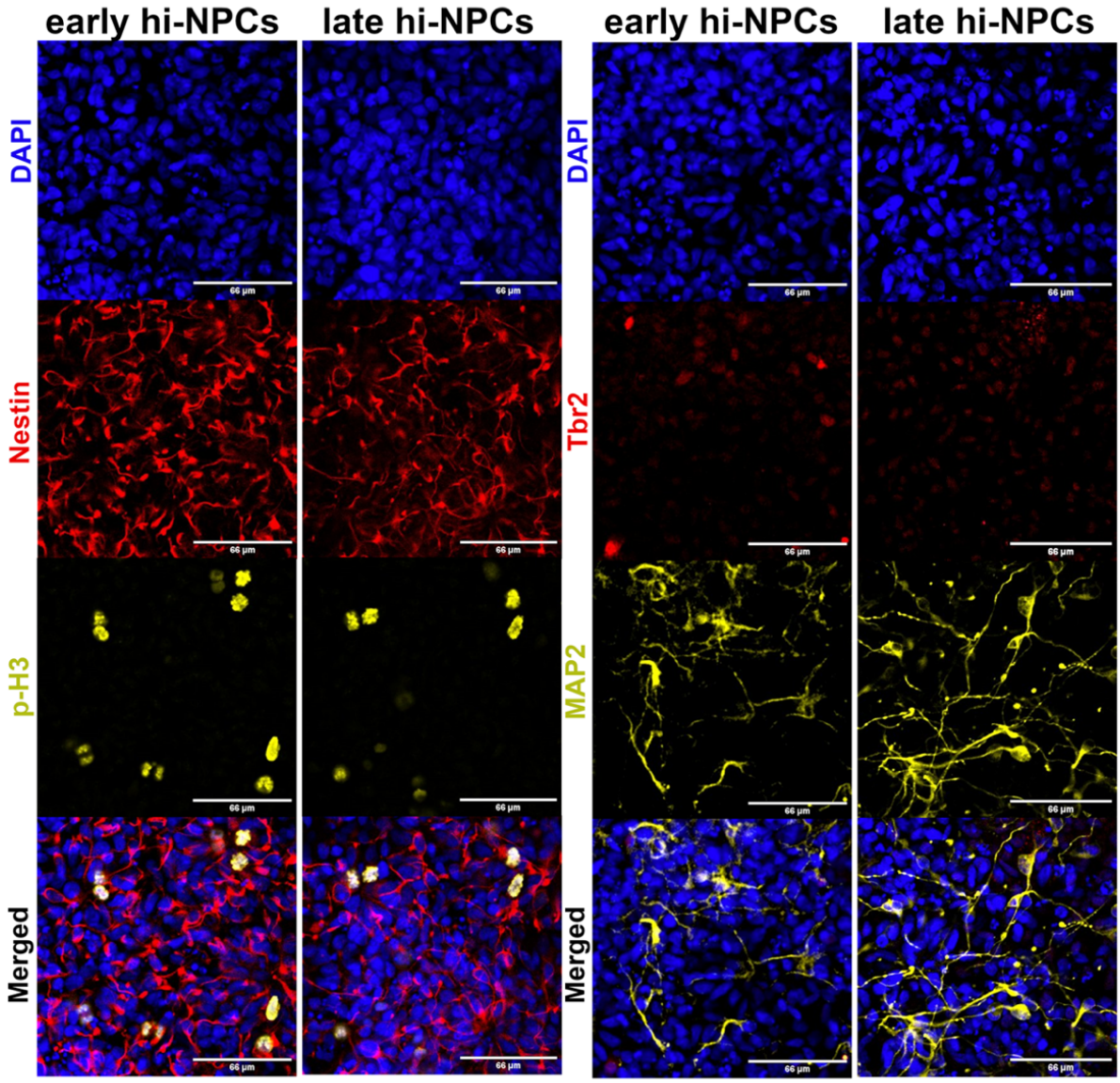


Figure 3.4. Cortical differentiation from hiPSCs produces phenotypically distinct neuronal progenitors (hi-NPCs)
Representative confocal images (10x) of the detection of markers of cellular proliferation phospho-Histone3 (p-H3) and of *in vitro* cortical neuronal progenitors (nestin, Tbr2 and MAP2) in early and late hi-NPCs. Scale bar: 66 µm

3.5.2 Intracellular physiological subtyping of hiPSC derived cortical neuronal progenitors

Characteristics of the *in vitro* culture of hi-NPCs are likely to involve the presence of mixed cell populations. The assessment of subpopulations of brain cell types

between early and late hi-NPCs cultures, done by flow cytometry (Figures 3.5A and 3.5B) . This consisted in two independent immunostainings both conducted in early and late hi-NPCs. The first staining, to quantify hi-NPCs, involved the selection of CD24/CD15 +ve cells after serial selection of CD184 +ve, CD44/CD271 -ve cells (Figure 3.5A). The second staining, to quantify glia, involved the selection of CD44/CD184 +ve cells and, to quantify neurons, CD24 +ve / CD15 -ve cells after serial selection of CD44/CD184 -ve cells). Figure 3.5.C showed the gating strategy used to distinguish subpopulations of brain cells by flow cytometry which did not significantly differ ($p \geq 0.05$) between hi-NPC subtypes (Figure 3.5D).

Cellular metabolism is crucial during differentiation of neuronal progenitor cells[233]. The time post-passage may influence the differentiation of hi-NPCs therefore, I measured their metabolism[A] between 10- and 14-hours post-passage. Cellular adherence occurred at ~5 hours post-passage. Intracellular metabolic tracing using radioactive-labelled substrates showed a significantly lower glycolytic flux ($p = 0.0286$) in late compared to early hi-NPCs (Figure 3.5E) and no differences in the mitochondrial glucose oxidation (Figure 3.5F). The role of lipid metabolism during differentiation of neuronal progenitor cells is arguably as important as that of glucose[185]. The estimation of mitochondrial lipid oxidation was conducted by measuring the oxidation rate of oleic acid (long-chain fatty acid). The oxidation rate of oleic acid was significantly higher in late compared to early hi-NPCs ($p = 0.0286$) (Figure 3 .5G).

[A] This work was done in collaboration with a fellow student from the CMRG group in DPAG-Oxford. Mr. Ujang Purnama conducted the radioactive tracing of glucose and lipid metabolism.

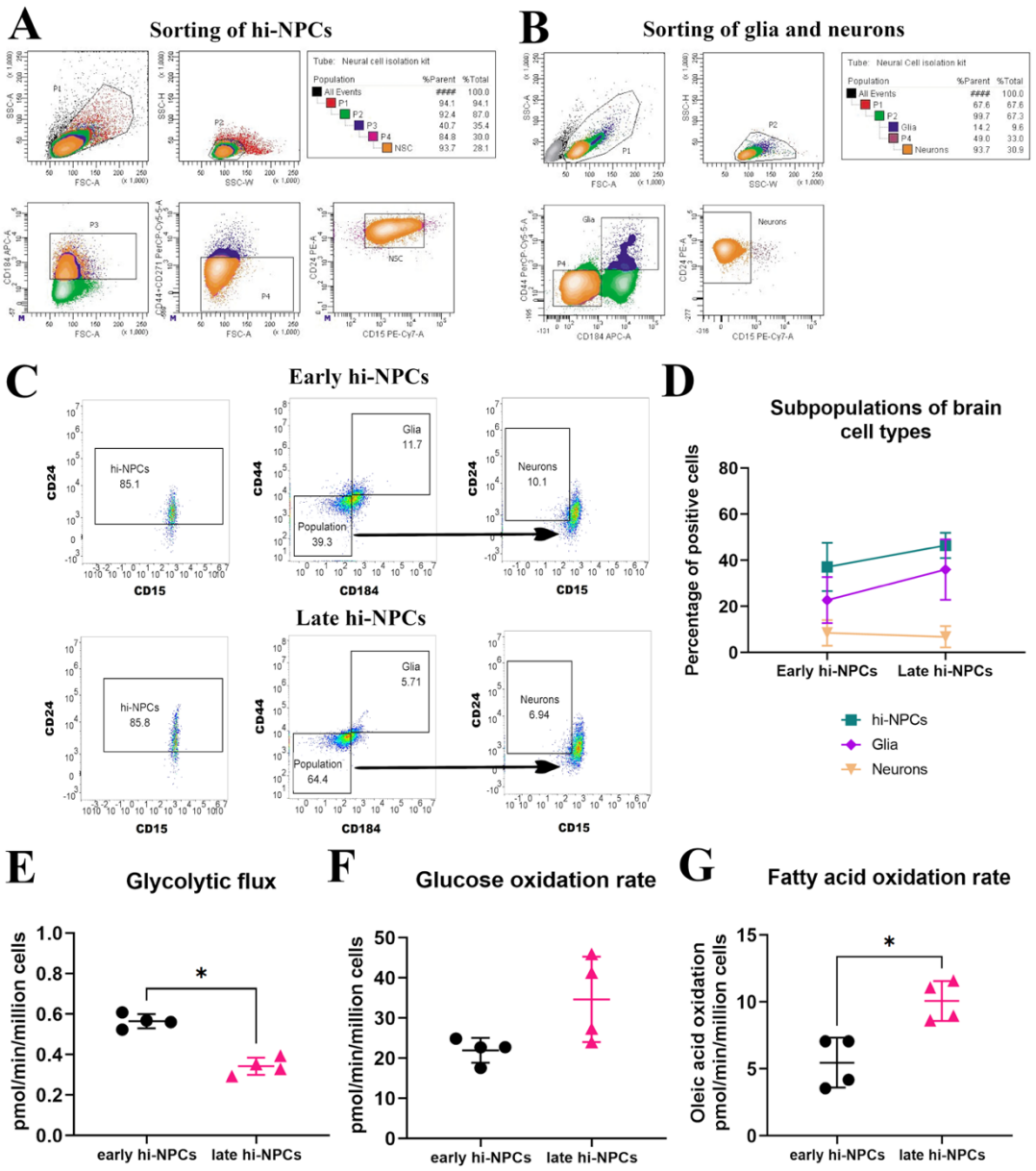


Figure 3.5. Metabolic remodelling distinguishes hi-NPC subtypes

Surface expression of neuronal and non-neuronal markers characterising subpopulations of brain cell types in hi-NPCs produced by 2D differentiation as Illustrated in Figure 3.3A. (A) Gating strategy to sort hi-NPCs and (B) Flow cytometry gating strategy to sort glia and neurons, following manufacturer's procedure. Diagrams obtained from the BD Stemflow™ Technical Data Sheet (Cat No. 562271). (C) Example of gated populations of hi-NPCs, glia, and neurons in early and late hi-NPC. The concentrations of antibodies used for the immunostaining of hi-NPCs followed the manufacturer's procedure. (D) Dot plot showing the percentage summary of brain cell types in early and late hi-NPCs. Bars display mean ± SD. n = 1 cortical differentiation done in triplicates for each of three independent donors' cell lines. Significance was calculated by two-way ANOVA with Šidák's multiple comparisons post hoc test. Intracellular tracing showing the metabolic remodelling of the (E) glycolytic flux, (F) glucose oxidation rate and, (G) fatty acid oxidation rate between early and late hi-NPCs, determined by the rate of radioactive by-products produced after 2-4 h of exposure to radioactive-labelled substrates: glucose and oleic acid. Bars display mean ± SD. n = 2 cortical differentiations each measured at two different time-points, 10 and 14 h post plating, in five replicates for a donor cell line. Significance was calculated by non-parametric two-tailed Mann-Whitney U test. Significance is shown when $^{*}p < 0.05$, $^{**}p < 0.01$, $^{***}p < 0.001$, $^{****}p < 0.0001$.

3.5.3 Extracellular glycolytic capacity as a tool to distinguish hi-NPC subtypes

Periodic evaluation of cellular metabolism during the culture of hi-NPCs may be relevant to demonstrate potential changes induced by Zika virus replication. The cellular metabolism of proliferating cells cultured *in vitro* may be inferred by their glycolytic capacity which is primarily used to fulfil their energetic demands[234]. The glycolytic capacity can be estimated by the extracellular measurements of glucose consumption and lactate release in the culture media.

Due to the large number of samples, a commercial protocol to measure extracellular glucose from the culture media using 1 cm glass cuvettes had to be optimized and thus, a microplate format was adopted (Figure 3.6A). Measurements of glucose from the supernatant of Vero CCL-81 cultures over a time-course experiment showed no significant differences between the conventional and the modified method (Figure 3.6B). Levels of lactate measured by an "*in house*" method based on the absorbance of NADH showed no significant differences in the detection when compared to the theoretical values calculated by the NADH extinction coefficient (Figure 3.6C). Moreover, time-course detection of lactate from the supernatant of cancerous brain cells (U87 astrocytoma), cultured with different levels of glucose, showed the expected kinetics of lactate appearance and disappearance (Figure 3.6D).

Overall, as expected from cells with a higher glycolytic rate (Figure 3.6E), early hi-NPCs, compared to late hi-NPCs, showed a significant increase in the cumulative levels of glucose consumption ($p < 0.0001$) and lactate release ($p = 0.0037$ and $p = 0.0006$, respectively) at 48 h and 72 h (Figure 3.6E). At 72 h post-culture, normalization to cell number showed that early hi-NPCs had a higher glycolytic

capacity represented by a significant increase in the consumption of glucose ($p < 0.0001$) and lactate release ($p = 0.0006$) (Figure 3.6F).

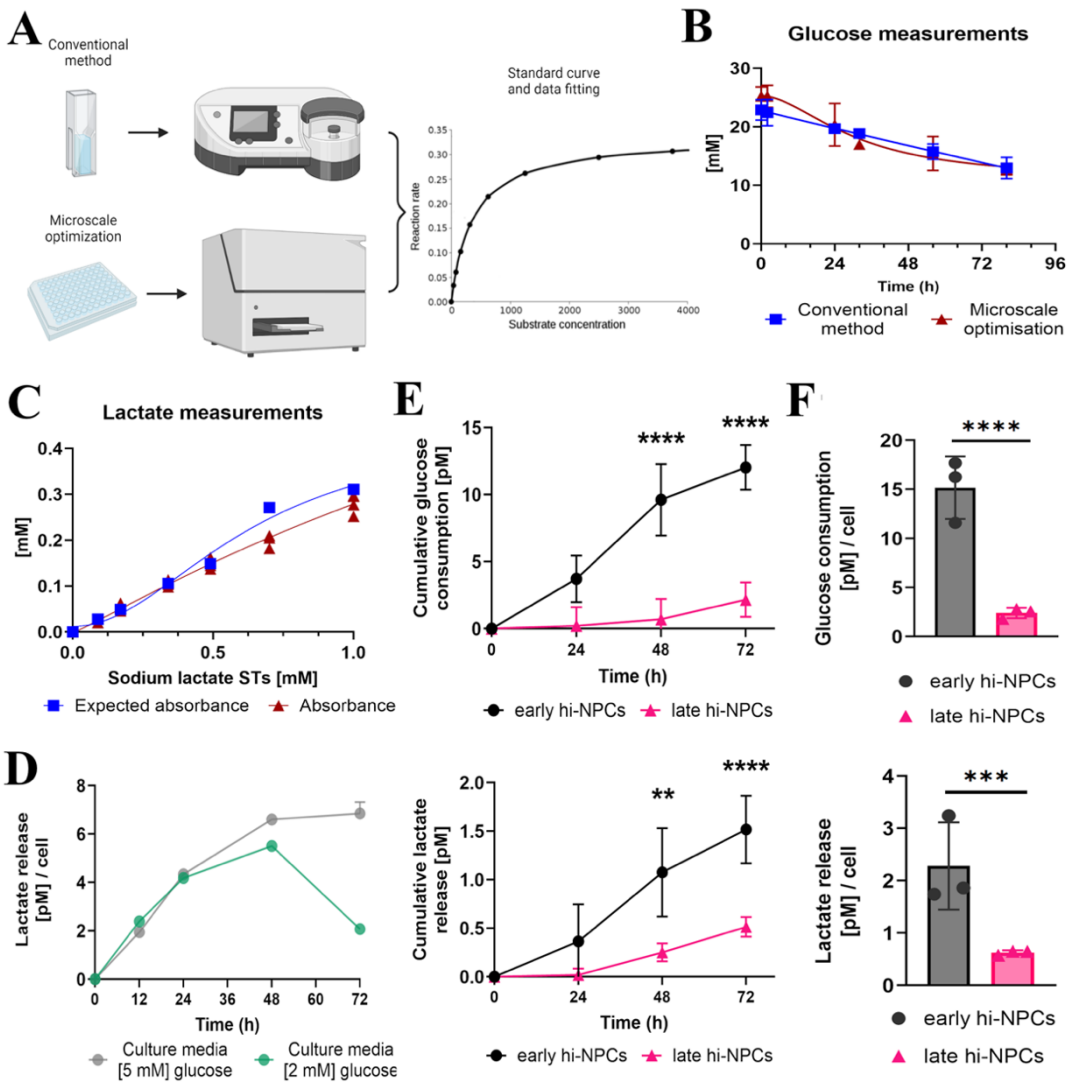


Figure 3.6. Early hi-NPCs exhibit higher glycolytic capacity
(A) Schematic illustration of the conventional method and microscale optimization to measure the presence of glucose in the culture media. (B) Comparison of glucose measurements between the conventional method (1 cm cuvette) and the microscale optimisation (96-well plate). Bars display mean ± SD. n = 3 independent measurements per time-point from supernatants of Vero CCL-81 cultures. Significance was calculated by a mixed-effects model with Šidák correction. (C) Validation of an "*in house*" method to measure extracellular lactate using the absorbance detection of NADH. Dot plot showing n = 4 independent measurements per standard (dark red) compared to the expected absorbance using the NADH extinction coefficient (blue). Significance was calculated by a paired two-tailed Wilcoxon-rank test. (D) Lactate protocol validation using supernatants of U87 astrocytoma cultures with different initial levels of glucose. Bars display mean ± SD. n = 3 independent experiments. (E) Dot plots showing the cumulative glucose consumption (top) and lactate release (bottom) in hi-NPC subtypes cultured over 72 h. (F) Bar graphs displaying the levels of glucose consumption (top) and lactate release (bottom) per hi-NPC subtype at 72 h post-culture. Error bars display mean ± SD. n = 1 cortical differentiation measured in triplicates for three independent donors' cell lines. Significance was calculated by Two-way ANOVA with Šidák's multiple comparisons post hoc test. Significance is shown when $^{*}p < 0.05$, $^{**}p < 0.01$, $^{***}p < 0.001$, $^{****}p < 0.0001$.

3.6 DISCUSSION

3.6.1 Characterization of hi-NPCs for disease modelling

In vitro study of fetal brain development has been conducted using 2D and/or 3D neurospheres or organoid systems differentiated from either fetal or hiPSCs[209,212,235]. However, although these systems accurately mimic the behaviour observed *in vivo*, they have also showed high variability and significantly different responses to stimuli, such as viral infections, between donor cell lines[236]. Thus, I modified an existing 2D protocol, designed for the differentiation of hi-PSC into cortical neuronal progenitors (hi-NPCs)[232] and commonly used to study pathologies involving neurodegenerative processes[204–207]. The developed protocol showed advantages over an existing 2D protocol of similar kind[174] as it comprise a detailed characterization of the neuronal progenitor populations, brain cell populations and, produces a higher yield of cells. The latter, currently representing a limitation of 2D *in vitro* study of the fetal brain when using techniques that require large cell numbers. The production of hi-NPCs showed two morphologically distinct cell populations, obtained at different time-points during differentiation. Both populations expressed generic cellular markers of the neuronal progenitors and proliferation to similar levels as those reported by others[174,232]. Of relevance, the cells obtained at early stages (early hi-NPCS) during the differentiation process, displaying a distinct morphology that involves the presence of a big nucleus to cytoplasm ratio and, rounded shape, have not yet been reported in other 2D culture systems. The lack of reports of these cells may be due to the lower survival rates observed after cryopreservation, the short time before they differentiate or, the potential interest in bulk production of neuronal precursors for final differentiation into adult-like neurons[174,204,206,219]. *In vitro* cultured cells with similar morphology are observed in

3D embryoid bodies. Here, these cells constitute the populations of neuronal precursors selected for further maturation into adult-like neuronal lineages[232]. Hence, as 2D cultures have the advantage of producing a larger homogeneous population when compared to 3D approaches, the characterization and study of these cells — in addition to current validated neuronal precursors (late hi-NPCs) obtained 6-7 days after the appearing of early hi-NPCs — may improve the current *in vitro* study of the different stages of early fetal brain development and the implications of different neuronal cell types in severe disorders such as Zika-induced congenital syndrome. Additional disadvantages of 3D systems compared to 2D systems may include cell differentiation times and different relative abundance of cell subtypes. These disadvantages emphasise the importance to characterize hi-NPCs as potential models to study cell specific mechanisms of fetal brain development in health and disease.

Organoid systems represent a great progress in modelling brain development as they can be induced to produce cells with specific lineage identities[211]. However, the contamination of these 3D cultures by uncharacterized cells[208] differs from both early and late hi-NPC cultures in which I showed a complete differentiation towards brain cells with similar ratios of neuronal progenitors, adult-like neurons, and glial cells in both cultures. Thus, these cultures may provide a platform to study fetal brain development with less variable results. Moreover, as both subtypes of hi-NPCs showed no contamination with uncharacterized cells, the differences between the subtypes are likely to be at the physiological level rather than an artefact of the different culture time spans.

3.6.2 Early and late hi-NPCs recapitulate features of neuronal progenitor subtypes

Cellular metabolism may play a crucial role in supporting neuronal differentiation and to potentially distinguish neuronal subtypes[237]. A sign of metabolic distinctions in subtypes of neuronal progenitors may the presence of glycogen storages in the form of intracellular granules. These granules have been observed in radial glia cells but not in intermediate proliferative progenitors[238] and, although the role of glycogen may influence neurogenesis[239], this short-term energy reserve constitutes a secondary metabolic process of glucose metabolism[239]. Activation and metabolic shift between cytosolic metabolism of glucose and, mitochondrial oxidation of glucose and fatty acids, drive processes which support the generation of the metabolite pool and energy necessary for neuronal differentiation[185,227,230]. Thus, to potentially elucidate early changes that may distinguish neuronal progenitor subtypes *in vitro*, I characterized their metabolism of glucose and fatty acids.

Although early and late hi-NPC cultures are characterized by a mixture of brain cell types, neuronal progenitor cells are present in larger abundance within each culture and at similar percentages between cultures. Based on the results from the metabolic profile in brain rodent and human-derived cells[55,185,227,228,231,233,240], I argued that the potential metabolic differences between these cultures may correspond to the presence of different types of neuronal progenitors. The metabolic differences were a significantly decreased glycolytic flux and a significantly increased fatty acid oxidation in late hi-NPCs and, a significantly increased glycolytic flux and significantly decreased fatty acid oxidation in early hi-NPCs. These suggest that late hi-NPCs metabolically represent cells transitioning between proliferating and intermediate progenitors. In contrast, the metabolic profile of early

hi-NPCs suggests these cells are likely to transition between quiescent radial-glia progenitors and proliferating progenitors.

Although considered a gold-standard methodology to study cellular metabolism, radioactive tracing of glucose and fatty acids requires long lengths of time, high costs and large cultures sizes[234]; with the latter generating difficulties in hi-NPCs studies due to the general low yields of cell production. Furthermore, toxicity of the radioactive tracer prevents paired-measurements during time-course experiments[234,241] that may be required when studying viral replication in hi-NPCs[124,242–244]. To this end, I developed two methods to measure the extracellular levels of glucose and lactate from the supernatant of cell cultures. Both methods were based on the absorbance reading of NADH and showed to be reliable. Moreover, the accuracy of the lactate assay was assessed by the detection of low and high levels of lactate in the culture media of U87 astrocytoma cells. The observed decreased lactate levels at 72 h in the low glucose media may be related to the flexibility of lactate as an energetic substrate in cancer cells when there is low levels of glucose in the media[245–247].

The time-dependent significant increase in the glycolytic capacity of early hi-NPCs compared to late hi-NPCs proved to be sufficient to distinguish the neuronal progenitor subtypes, supporting the importance of metabolism in the subtyping of neuronal progenitor cells[233].

Overall, this chapter shows for the first time the detailed characterization of cells produced at early stages of cortical neuronal progenitor differentiation using a 2D modified protocol of that reported by Shi et al., 2012. The observed differences in cellular metabolism may be attributed to the activation of specific cellular machinery which implies early and late hi-NPCs have distinct cellular profiles which categorize

them as subtypes of neuronal progenitors[248,249]. This supports the hypothesis that shift in metabolism from aerobic glycolysis to mitochondrial oxidation of glucose and, the transition from fatty acid biosynthesis to oxidation are key elements in neuronal differentiation[53,250,251].

3.7 CONCLUSION

The presence of markers of cortical neuronal progenitors in early and late hi-NPCs showed that these cells share neuronal lineage similarities. Thus, the distinct morphologies may not obey to *in vitro* artefacts of partial and/or incomplete neuronal differentiation due to the different times under culture. The similar abundance of different brain cell types in both early and late hi-NPC suggests that their morphological differences are not due to potential contamination by other populations of neuronal and non-neuronal cell types.

Moreover, an *in-house* method for the detection of glucose levels using low volumes of cellular culture' supernatants showed no significant differences when compared to the control method. Similarly, no significant differences were observed in the quantification of lactate levels by an *in-house* method when compared to the theoretical detection values.

Physiological characterization of hi-NPCs showed significant differences in the short- and long-term metabolic profile between early and late hi-NPC cultures. The short-term intracellular metabolic tracing showed that early hi-NPCs had a higher glycolytic capacity and lower mitochondrial oxidation of fatty acids than late hi-NPCs. The results from the glycolytic capacity were corroborated by its long-term extracellular estimation. This suggests that early hi-NPC cultures, may have a pool of neuronal progenitors that are more proliferative and less differentiated than those in late hi-NPC cultures.

To conclude, the 2D differentiation protocol produces, at different stages, cultures containing different subtypes of neuronal progenitor. Thus, the use of these cultures containing subtypes of neuronal progenitor cells will contribute to the research presented in this thesis by facilitating a platform that may be of potential relevance

to elucidate the effects of ZIKV infection in the most relevant cell types during the first trimester of brain development.

Ultimately, this chapter would have benefited from additional techniques to generate a more complete validation of the subpopulations of cells obtained within each culture. For example: measurements of the levels of enzymes involved in the glycolytic and fatty acid oxidation pathway, transcriptional profiling of early and late hi-NPC cultures and, mass-spectrometry of these cultures would have potentially provided a narrower distinction of the subtype of neuronal progenitors I have generated. Other approaches, such as immunostaining of human fetal histological samples, may have also provided a robust *in vitro* platform for the study of brain development in health and disease. Nevertheless, radioactive tracing as the most relevant technique to measure the metabolic flux and the long-term validation by extracellular estimation of the glycolytic capacity of these cells was sufficient to broadly distinguish the two most abundant subpopulations of neuronal progenitors during early development of the brain cortex.

4. ZIKA VIRUS-INDUCED BIRTH DEFECTS DURING FIRST TRIMESTER MAY RESULT FROM THE DIFFERENTIAL METABOLIC DYSFUNCTION INDUCED BY INFECTION OF EARLY VERSUS LATE NEURONAL PROGENITORS

4.1 ABSTRACT

Maternal-fetal transmission allows Zika virus (ZIKV) to populate the fetal brain. Neuronal progenitor (hi-NPC) subtypes, whose relative abundance differs at different stages of fetal brain development, are among the most permissive brain cells to ZIKV infection. I showed in chapter 3 that energy metabolism governs a distinction between cortical neuronal progenitors that may underpin the physiology of different subtypes. Thus, subtype-specific viral hijacking of cellular metabolism to support replication may contribute to distinct damage in the developing fetal brain observed in cases of congenital Zika syndrome. Here, I show that ZIKV replicates differently between each hi-NPC subtype. Also, transcriptional changes in metabolic genes confirmed broad dysregulations which may exacerbate the cellular machinery leading to cell death. Extracellular measurements of glucose and lactate show that ZIKV replication upregulates the glycolytic capacity in hi-NPC subtypes. Analysis using imaging flow cytometry revealed that ZIKV replication alters mitochondria homeostasis in hi-NPC subtypes and dysregulates lipid metabolism in early hi-NPCs. At early stages, ZIKV replication increases lipid droplet abundance and decreases mitochondrial membrane potential and size in early hi-NPCs. At this stage, ZIKV replication decreases mitochondria membrane potential in late hi-

NPCs. Moreover, later stages of ZIKV replication, increase the distribution of lipid droplets in early hi-NPCs whilst decrease the mitochondria size in late hi-NPCs. These findings highlight distinct subtype-specific metabolic alterations during ZIKV infection that may maintain the pool of intracellular metabolites required for sustained replication. Thus, subtype-specific alterations of cellular metabolism and survival may explain the differences in detrimental fetal brain damages over each trimester.

4.2 INTRODUCTION

Maternal-fetal transmission of Zika virus (ZIKV) and its consequences to fetal development have been widely reported[252–254]. ZIKV exhibits tropism for brain cells with a severe impact on the survival of neuronal progenitor cells[75,76,146,255]. Astrocytes, oligodendrocytes and, to a lesser extent, mature neurons are also susceptible to ZIKV[124,146,256–258]. Infection in microglia cells remains unclear[154,259–263]. ZIKV-induced detrimental damage to the fetal brain in new-borns has been correlated with maternal infection during the first trimester of pregnancy. However, when maternal infection occurs during mid and late trimesters, after the accelerated fetal brain expansion has occurred, it correlates with less severe outcomes[264–266]. Thus, whether ZIKV has a higher neurotropism for early progenitors of the forebrain or these progenitors exhibiting higher susceptibility to ZIKV infection is yet to be elucidated. Development of the fetal brain is a rapid process with high energetic demands[56,57,240]. Thus, literature suggesting that ZIKV-related brain abnormalities potentially correlated with nutrient exhaustion highlighted the role of cellular metabolism in the ZIKV-infected fetal brain[36,115,267]. In addition, maternal protein malnutrition in mice resembles some of the brain abnormalities produced by ZIKV infection[36,237] and, aggravates those of the infected subjects[29]. This correlates with surveys showing higher rates of ZIKV-congenital syndrome in populations of Brazil suffering from malnutrition[97,269].

The entry of ZIKV to the brain remains unclear. Studies show potential relevance of tyrosine kinase receptors (AXL) as ubiquitously expressed across cell types susceptible to ZIKV. AXL expression has been reported in susceptible cells including liver, kidney, skin and, brain cells like astrocytes, neuronal progenitors, immature neurons, and oligodendrocytes[148,150,151,270,271]. However, other receptors

might also play a role for viral entry[149,152]. *In vivo* studies demonstrate that overexpressing AXL mice models were obese, diabetic and insulin resistant[272] and *in vitro* studies show alterations of AXL affected the metabolism of glucose in several cell types[273–276]. Thus, AXL receptors potentially involved in the intracellular crosstalk with energy metabolism, particularly that of glucose[272].

The metabolic complexity of the developing brain with (a) the activation of specific energetic pathways at different stages of development and, (b) cellular subtype-dependent preference for alternate energetic pathways [53,233] may underlie specific adaptations during ZIKV replication. To elucidate potential cellular reprogramming in response to ZIKV infection, mitochondria homeostasis, lipid, glucose, and amino-acid metabolism have been studied in different *in vitro* and *in vivo* models[123,277–281]. Data suggesting dysregulation of different energetic pathways by ZIKV infection comprises common features among different ZIKV strains[242,282]. Undoubtedly, these alterations constitute a signature of ZIKV-induced pathogenesis in which glucose dysregulation may play a major role[267,280,283].

In addition, ZIKV, like other flaviviruses, substantially alters the metabolism of lipid droplets, although there is no consensus on whether this alteration is solely required for structural or energetic processes or a combination of both[123,277–279].

Research investigating the role of cellular metabolism during ZIKV-induced cell death of neuronal progenitors remains contradictory. Reports showing alterations in the main metabolic pathways during ZIKV infection largely involve studies of non-human and/or non-neuronal cell types and have produced contradictory findings[123,242,277,282]. Thus, it is necessary to study human neuronal progenitors to elucidate the true extent of metabolic reprogramming of during ZIKV infection.

In this thesis, I hypothesised that the metabolism of different cell types of the developing early fetal brain is distinctively hijacked by neurotropic Zika virus (ZIKV) underpinning the differences in congenital zika syndrome observed over the course of pregnancy[77]. In the previous chapter, I characterized cells produced during 2D *in vitro* cortical differentiation (early and late hi-NPCs) and showed that, based on their metabolic profile, these were different subtypes of neuronal progenitors of the forebrain. Thus, this chapter is designed to investigate to which extent ZIKV productively infects and alters the metabolism of both early and late hi-NPCs with potential implications in the fetal pathogenesis over the pregnancy.

4.3 AIMS

Cellular proliferation and differentiation to support the expansion of the fetal cortical brain during the first trimester of pregnancy is an energy-demanding process. Cells involved in the expansion of the fetal cortical brain are susceptible to infection by ZIKV. As these cells show distinct metabolic profiles, one can assume that metabolic requirements during ZIKV replication might trigger a cell-type specific dysregulation of the energy homeostasis. This differential dysregulation in ZIKV infected early compared to late cortical progenitor cells may explain the diversity of phenotypes observed in new-borns when infection occurs over each trimester of pregnancy. Thus, to study potential differential responses and alterations of susceptible neuronal progenitors under ZIKV infection, it is necessary to use characterized neuronal progenitor subtypes, such as those detailed in chapter 3. To this, I challenged early and late hi-NPCs to ZIKV to address the following five aims:

- To determine the susceptibility of hi-NPC subtypes to ZIKV infection
- To assess the replication, assembly, and release of infectious ZIKV particles in hi-NPC subtypes
- To study the effects of ZIKV replication in the two main energetic pathways of proliferative brain progenitor cells using hi-NPC subtypes
- To study the impact of ZIKV replication in the mitochondria homeostasis of hi-NPC subtypes
- To elucidate potential differences between metabolically distinct hi-NPC subtypes in their reprogramming to ZIKV replication

4.4 METHODS

4.4.1 Culture of cortical progenitor cells from hiPSC

hiPSC were obtained and maintained as detailed in section 2.2.2.2.1. Cortical neuronal progenitor differentiation was carried out following the protocol set out in section 2.2.2.2.

4.4.2 ZIKV challenge in hi-NPC subtypes

hi-NPCs were challenged to culture media containing ZIKV particles. Details of the viral stock can be found in section 2.1.1. Challenge experiments were carried out following the protocols set out in section 2.3.1. Titration of ZIKV by plaque assay was carried out following the protocol set out in section 2.1.2.

4.4.3 Estimation of glycolytic capacity in hi-NPC subtypes

Glycolytic capacity of hi-NPC subtypes ZIKV-challenged, and controls was estimated by readouts of extracellular glucose consumption (section 2.5.2.1) and lactate release (section 2.5.2.2).

4.4.4 Survival of hi-NPCs during ZIKV replication

Cellular survival was measured by metabolic activity CCK-8 assay following the manufacturer's procedure detailed in section 2.5.3. Gross survival was also assessed by nuclear staining as detailed in section 2.4.1.3.

4.4.5 Imaging flow cytometry

Immunostaining and data analysis of mitochondrial membrane potential and lipid droplets in ZIKV-challenged hi-NPC subtypes were conducted following the protocol set out in section 2.4.1.4

4.4.6 Gene expression analysis

RNA extraction and cDNA conversion were done following the procedure detailed in section 2.7.1. qPCR was carried out following the protocol set out in section 2.7.2. Analysis further included the comparisons ZIKV-challenged samples and its respective time-point non-challenged controls.

4.4.7 Immunofluorescence analysis of hi-NPCs

Immunostaining and imaging of neuronal markers in 2D hiPSC-NPC cultures and, mitochondria and lipid droplets in ZIKV-challenged and non-challenged hi-NPC controls were carried out following the protocol set out in section 2.4.1.1.

4.4.8 Statistical analysis

Datasets from single experiments with larger sample size were analyzed by mixed-effects model with Šidák's multiple comparisons test. Datasets containing missing values and/or values of zero after normalization from independent experiments of three donors' cell lines were analyzed using mixed-effects model with Holm-Šidák correction. Datasets comprising one repeat of two donors' cell lines were analyzed by mixed-effects model with Tukey's multiple comparisons test. Datasets containing analysis of independent experiments of three donors' cell lines comprising two groups were processed using Two-way ANOVA with Šidák's multiple comparisons post-hoc test whilst when comprising three or more groups post-hoc were computed using Tukey's multiple comparisons test. All the statistical tests were performed using GraphPad Prism 9.3.1. A calculated P value less than 0.05 was reported as significantly different.

4.4.9 Figures

Representation schemes were created with BioRender.com. Summary figures were done using GNU Image Manipulation Program (GIMP 2.8.22).

4.5 RESULTS

4.5.1 Zika virus (ZIKV) replication in hi-NPC subtypes

To understand the contribution of cellular metabolism to ZIKV infection during the early stages of pregnancy, two neuronal progenitor subtypes (hi-NPCs), characterized in the previous chapter, were challenged with supernatants containing infectious ZIKV particles. Both hi-NPC subtypes showed susceptibility to ZIKV infection with differences in the replication rates (Figure 4.1). RNA quantification showed that late hi-NPCs accumulate significantly more transcripts of ZIKV in a time-dependent manner than early hi-NPC. At 48 h.p.i., late hi-NPCs showed a 1.77-fold increase in intracellular copies of vRNA compared the early hi-NPCs. This further increased to a 1.98-fold change at 72 h.p.i. (Figure 4.1B). Analysis of the intracellular accumulation of the non-structural NS1 and the virion-associated Envelope (Env) viral proteins by flow cytometry revealed greater NS1 levels in late hi-NPCs at 56 h.p.i. ($p = 0.0241$) but no significant differences in Env expression (Figure 4.1C). Infectious virus released by cells was significantly higher in late hi-NPCs at 56 h.p.i. compared to early hi-NPCs (late:early ratio of 2.70), followed by decay productivity at 72 h.p.i. that reaches the levels of that released by early hi-NPCs (Figure 4.1D).

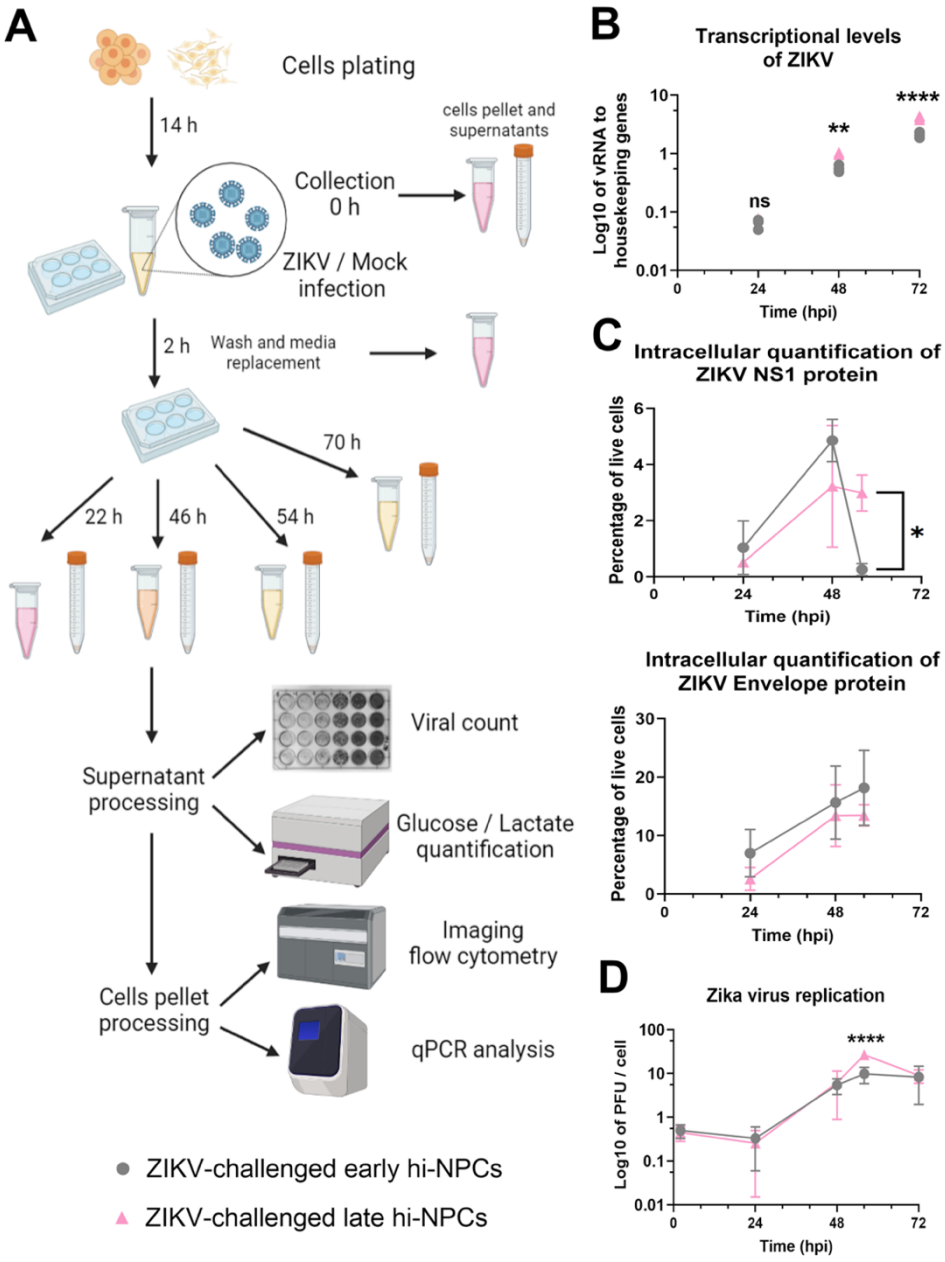


Figure 4.1. Late hi-NPCs exhibit larger accumulation of intracellular non-assembled ZIKV particles

(A) Schematic 2D representation of the protocol conducted to investigate the effects of hi-NPC subtypes exposure to ZIKV. Dot plots showing the intracellular assessment of ZIKV infection in hi-NPC subtypes after exposure to media-containing ZIKV virions for 2 h at 37 °C using an M.O.I. of 1. (B) Transcriptional levels of ZIKV relative to housekeeping genes. qPCR conducted in 4 replicates. Dots displaying the values of each donor cell line. Percentage of live cells containing (C) ZIKV NS1 protein and (D) ZIKV Envelope protein. A minimum of 500 *in focus* cells were analyzed per donor cell line out of 10000 cells recorded. Bars display mean ± SD. n = 1 viral challenge conducted in duplicates of three independent donors' cell lines. Significance was calculated by Two-way ANOVA with Šidák's multiple comparisons post-hoc test. Dot plot showing extracellular release of ZIKV infectious particles normalized per cell number. ZIKV quantification from the supernatants was done by plaque assay. Each sample was conducted in triplicates. Bars display mean ± SD. n = 2 viral challenges conducted in duplicates of three independent donors' cell lines. Significance was calculated by mixed-effects model with Šidák correction. Significance is shown when $^{*}p < 0.05$, $^{**}p < 0.01$, $^{***}p < 0.001$.

4.5.2 ZIKV replication stimulates cytosolic metabolism of glucose in hi-NPC subtypes

Cell viability following ZIKV challenge was assessed using the CCK-8 tetrazolium assay of metabolic activity and revealed significant cell death in both hi-NPC subtypes at later stages of replication ($p \leq 0.0014$) (Figure 4.2A). Further assessment of cell survival by nuclear imaging over 72 h (Supplementary Figures 1 and 2) showed alterations in their size (Figure 4.2B) and morphology (Figure 4.2C). Nuclear size significantly decreased in ZIKV-challenged early hi-NPCs at 24 h.p.i. ($p = 0.0211$) and 48 h.p.i. ($p = 0.036$) and significantly increased in late hi-NPCs at 48 h.pi. and 72 h.p.i. ($p \leq 0.0001$) (Figure 4.2B). Nuclear circularity was only affected at later stages of infection (72 h.p.i.); early hi-NPCs showed a significant increase ($p \leq 0.0001$) whilst late hi-NPCs showed a significant decrease ($p \leq 0.0001$) (Figure 4.2C).

To assess whether these changes in viability were paralleled alterations in the metabolism of glucose, I first quantified the transcripts for key glycolytic genes. Among these genes, HK-1 and GAPDH both showed significant increases in ZIKV-challenged cells compared to non-challenged controls. At 48 h.p.i., ZIKV-challenged early hi-NPCs showed a 1.42-fold increase in the gene expression of HK-1 compared to late hi-NPCs. However, at 72 h.p.i., a 1.26-fold increase was measured in the RNA levels of HK-1 in late hi-NPCs (Figure 4.2D). At this time-point, early hi-NPCs showed a significant increase of 2.64-fold in the RNA levels of GAPDH compared to late hi-NPCs (Figure 4.2D). No significant changes were calculated in the glucose entry receptor GLUT-1 (Figure 4.2D).

These effects were mirrored at the enzyme level, with a significant increase in the overall glucose consumption in early hi-NPCs ($p = 0.0053$) when compared to non-challenged controls at later stages of ZIKV replication (Figure 4.2E). Furthermore, a significantly greater lactate release ($p \leq 0.0101$) was measured for both hi-NPC subtypes (Figure 4.2E). Metabolically distinct hi-NPC subtypes displayed different baseline levels of glycolytic capacity (Figure 4.2E). Thus, glycolytic capacity in ZIKV-challenged hi-NPC subtypes was normalized to their respective controls (Figure 4.2F). Data showed that, at 72 h.p.i., ZIKV challenge significantly increased the glucose consumption ($p = 0.0122$) and lactate release ($p < 0.0001$) in late hi-NPCs compared to early hi-NPCs (Figure 4.2F) with up to 2.31-fold and 2.17-fold changes, respectively.

4.5.3 hi-NPC subtypes challenged to ZIKV exhibit mitochondrial dysregulation

Mitochondrial activity is crucial in hi-NPC subtypes for differentiation[233]. Thus, I examined the characteristics of mitochondrial homeostasis in Env +ve ZIKV-challenged cells, neighbouring cells (Env -ve), and non-challenged controls. Metabolic demands imposed by ZIKV replication significantly decreased the mitochondrial membrane potential in Env +ve early and late hi-NPCs subtypes compared to Env -ve cells ($p = 0.045$ and $p = 0.0151$, respectively) at 24 h.p.i. (Figure 4.3A). Further time-points showed up to 1-fold reduction in the mitochondrial membrane potential of Env -ve cells (Figure 4.3A).

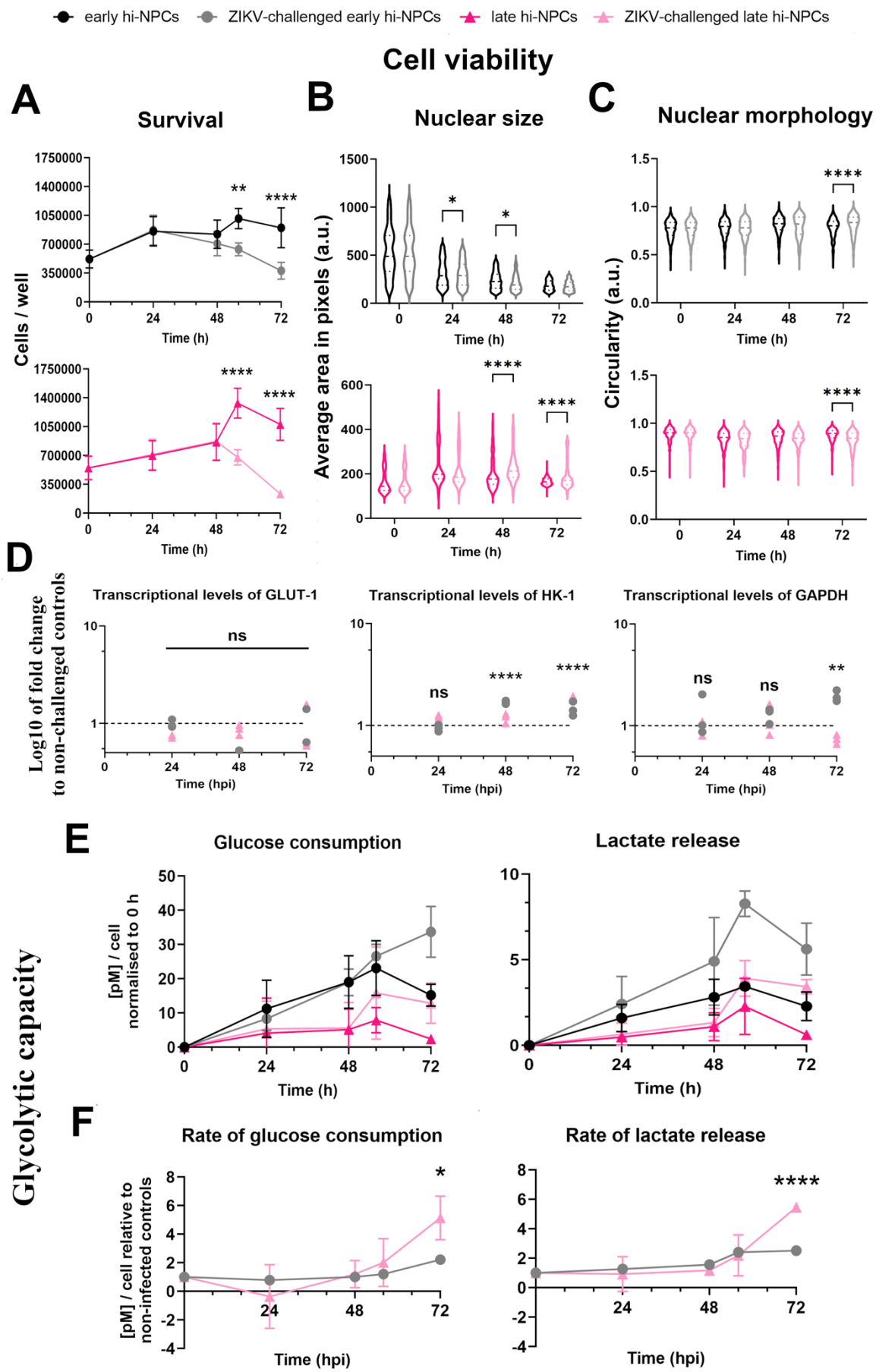

early hi-NPCs
ZIKV-challenged early hi-NPCs
late hi-NPCs
ZIKV-challenged late hi-NPCs
Cell viability
A
Survival
Cells / well
Time (h)
B
Nuclear size
Average area in pixels (a.u.)
Time (h)
C
Nuclear morphology
Circularity (a.u.)
Time (h)
D
Log10 of fold change to non-challenged controls
Transcriptional levels of GLUT-1
Transcriptional levels of HK-1
Transcriptional levels of GAPDH
Time (hpi)
Glycolytic capacity
E
Glucose consumption
[pM] / cell normalised to 0 h
Time (h)
Lactate release
Time (h)
F
Rate of glucose consumption
[pM] / cell relative to non-infected controls
Time (hpi)
Rate of lactate release
Time (hpi)

Figure 4.2. Late hi-NPCs exhibit a larger increase in the glycolytic capacity during ZIKV replication

Cell viability during a 2 h Zika challenge at 37 °C using an M.O.I. of 1 represented by line graphs displaying (A) the bio-reduction capacity of tetrazolium salt in early and late hi-NPCs. Bars display mean ± SD. n = 1 viral challenge conducted in triplicate of one donor cell line. Significance was calculated by mixed-effects model with Holm-Šidák correction. Violin plots displaying the mean value for ≥ 150 nuclei per condition. Quantification of nuclear damage in early and late-NPCs challenged with ZIKV showing (B) nuclear size and (C) nuclear morphology over 72 h. nuclear staining was conducted post-fixation with DAPI and quantification parameters of size and circularity were calculated using ImageJ. Significance was calculated by mixed-effects model with Šidák's multiple comparisons test. The metabolism of glucose was assessed by (D) transcriptional levels of genes relevant in glycolysis in ZIKV-challenged hi-NPCs relative to non-challenged controls. qPCR conducted in 4 replicates. Dots displaying the values of each donor cell line. Significance was calculated by Two-way ANOVA with Šidák's multiple comparisons post-hoc test. Line graphs displaying (E) the calculated glucose consumption and lactate release from ZIKV-challenged and non-challenged hi-NPC subtypes and, (F) the ratio of change compared to their respective non-challenged controls. Bars display mean ± SD. n = 2 viral challenges conducted in duplicates of three independent donors' cell lines. Significance was calculated by mixed-effects model with Holm-Šidák correction. Significance is shown when $^{*}p < 0.05$, $^{**}p < 0.01$, $^{***}p < 0.001$.

Metabolic differences between ZIKV-challenged hi-NPCs and non-challenged controls may be of disease relevance. Here, I showed that parameters of mitochondrial health significantly differ between Env +ve hi-NPCs and non-challenged controls. Env +ve early hi-NPCs showed, at 24 h.p.i., a significant reduction in mitochondrial size ($p = 0.0328$) (Figure 4.3B) and distribution ($p = 0.0251$) (Figure 4.3D). From these cells, a significant reduction in mitochondrial abundance was also observed at 24 h.p.i. ($p = 0.0091$) and 48 h.p.i. ($p = 0.0217$) (Figure 4.3C).

Alterations at 24 h.p.i. in Env +ve late hi-NPCs showed a significant reduction in mitochondrial distribution ($p = 0.0071$) (Figure 4.3D). At 56 h.p.i., mitochondrial size ($p = 0.0047$) (Figure 4.3B) and abundance ($p = 0.002$) in these cells were significantly reduced (Figure 4.3C). Single-cell imaging using defined mitochondria areas of analysis is illustrated in Figure 4.3E. The validation of the immunostaining in both hi-NPC subtypes is displayed in Figures 4.3F and 4.3G.

4.5.4 ZIKV replication hijacks the metabolic lipid machinery of hi-NPCs

Lipid metabolism was investigated due to the potential implications in ZIKV assembly. ZIKV-challenged hi-NPC subtypes showed a significant time-dependent increase in genes involved in beta-oxidation ($p \leq 0.002$) and lipid biosynthesis ($p \leq 0.0076$) yet the rates of gene expression increase were different between early and late hi-NPCs.

Isoforms of PDK regulate the homeostasis of glucose and lipid metabolism by decreasing the glucose utilization to promote fat metabolism[284]. The highly abundant isoform of PDK in brain tissue, PDK2, showed a significant increase ($p = 0.0153$) in early hi-NPCs compared to late hi-NPCs exclusively at 72 h.p.i. (Figure 4.4A). The ACADM gene, essential for the synthesis of enzymes required for the oxidation of medium-chain fatty acids[285], showed at 24 h.p.i. a modest yet significant increase in late compared to early hi-NPCs (late:early RNA ratio of 1.27) (Figure 4.4A).

In contrast, at 72 h.p.i., early hi-NPCs showed a significant 1.62-fold change in the levels of ACADM compared to late hi-NPCs (Figure 4.4A). Significant differences in the gene dysregulation by ZIKV were also observed exclusively at 24 h.p.i. in HADHA (late:early RNA ratio of 1.26), a gene essential for the synthesis of multi-enzymes within the mitochondrial trifunctional complex[286] (Figure 4.4.A). Moreover, a significant differential expression of ACACA and FASN were observed in ZIKV-challenged hi-NPC (Figure 4.4B). ACACA, considered to be a primary rate-limiting enzyme for biosynthesis of lipids[287], was 1.64-fold greater in late hi-NPCs only at 24 h.p.i.

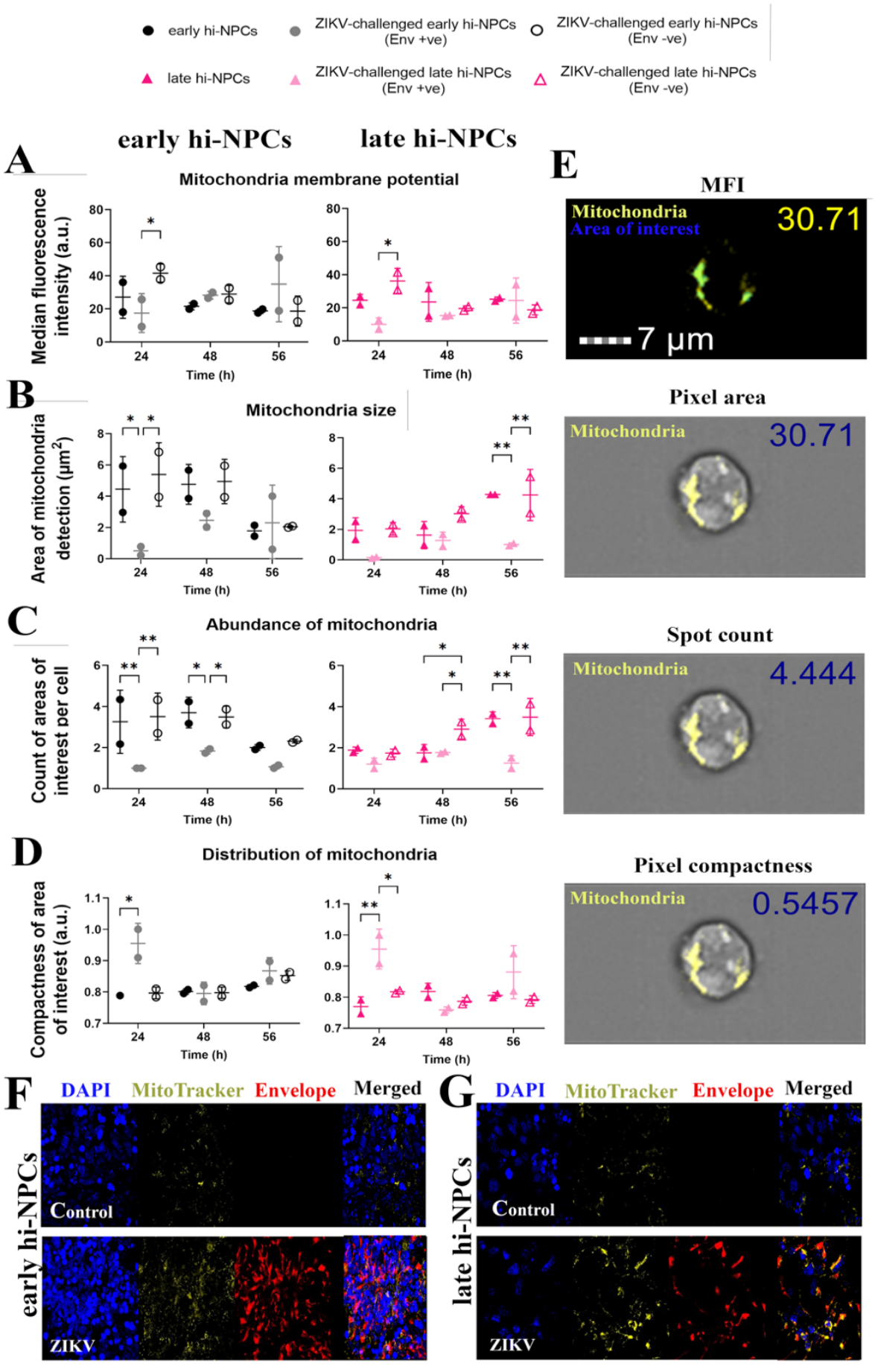

early hi-NPCs
ZIKV-challenged early hi-NPCs (Env +ve)
ZIKV-challenged early hi-NPCs (Env -ve)
late hi-NPCs
ZIKV-challenged late hi-NPCs (Env +ve)
ZIKV-challenged late hi-NPCs (Env -ve)
early hi-NPCs
late hi-NPCs
A
Mitochondria membrane potential
Median fluorescence intensity (a.u.)
Time (h)
B
Mitochondria size
Area of mitochondria detection (μm²)
C
Abundance of mitochondria
Count of areas of interest per cell
D
Distribution of mitochondria
Compactness of area of interest (a.u.)
E
MFI
Mitochondria
Area of interest
30.71
7 μm
Pixel area
Mitochondria
30.71
Spot count
Mitochondria
4.444
Pixel compactness
Mitochondria
0.5457
F
DAPI
MitoTracker
Envelope
Merged
Control
ZIKV
early hi-NPCs
G
late hi-NPCs

Figure 4.3. ZIKV induces hi-NPC subtype-specific mitochondrial stress
Analysis of several characteristics of mitochondria homeostasis in hi-NPC subtypes challenged to media-containing ZIKV for 2 h at 37 °C using an M.O.I. of 1 compared to non-challenged controls. Displayed data compares productively infected hi-NPCs (Env +ve) against challenged non-infected hi-NPCs (Env -ve) and non-challenged control hi-NPCs. Dot plots showing (A) mitochondrial membrane potential by measurements of the median fluorescence intensity of MitoTracker™ Red CMXRos, (B) mitochondria size estimated by the quantification of the total occupied area within the cells, (C) abundance of areas occupied by mitochondria and, (D) distribution of mitochondria determined by the proximity of positive areas within the cells. A minimum of 500 *in focus* cells were analyzed per donor cell line out of 10000 cells recorded. Bars display mean ± SD. n = 1 viral challenge conducted in duplicates of two donors' cell lines. Significance was calculated by mixed-effects model with Tukey's correction. Significance is shown when $^{*}p < 0.05$, $^{**}p < 0.01$, $^{***}p < 0.001$. (E) AMNIS Imaging flow cytometer digital images show representative mitochondria staining (yellow) with different quantified parameters, selected by internally defined mask (blue) in hi-NPC subtypes. (F) Representative confocal images with high magnification (60x) of z-stack projections (15 μm) confirming positive staining of mitochondria (yellow) and ZIKV Envelope protein (red) in hi-NPC subtypes. DAPI staining (blue).

In contrast, the level of transcripts of ACACA at 48 h.p.i., showed a 1.33-fold change in early compared to late hi-NPCs (Figure 4.4.B). Transcriptional levels of FASN, the main biosynthetic enzyme involved in the synthesis of saturated long-chain fatty acids[287], showed similar results at 24 and 48 h.p.i. than those of ACACA. Late hi-NPCs showed a significant 1.43-fold increase compared to early hi-NPCs, exclusively at 24 h.p.i. whilst at 48 h.p.i., opposite results showed a modest 1.12-fold increase early hi-NPCs compared to late hi-NPCs (Figure 4.4.B). Altogether, this data showed that ZIKV alters the transcriptional profile of lipid metabolic genes at different time-points during replication within each hi-NPC subtype. Furthermore, ZIKV exposure did not significantly alter the accumulation of lipid droplets. In early hi-NPCs, exclusively at 56 h.p.i., Env +ve cells exhibited significantly reduced levels of lipid droplets compared to Env -ve cells ($p = 0.0331$) (Figure 4.4C). The data from lipid droplets corresponded to the analysis of the median fluorescence intensity of neutral lipid staining in single cells (Figure 4.4D).

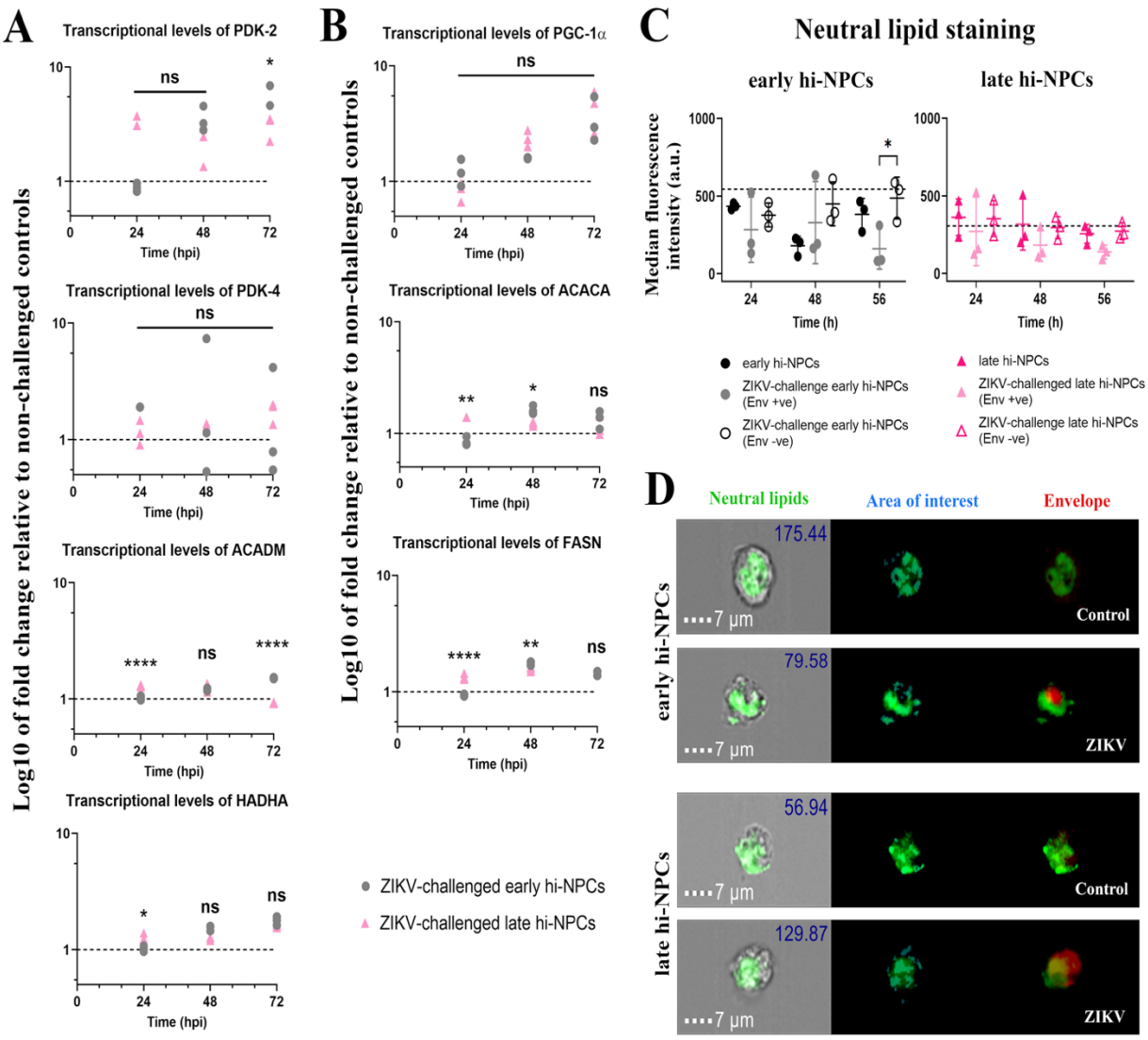


Figure 4.4. ZIKV replication imposes higher demands on the metabolism of lipids in early hi-NPCs

Transcriptional levels of genes relevant in (A) lipid beta-oxidation and, (B) lipid biosynthesis in ZIKV-challenged hi-NPCs relative to non-challenged controls after 2 h exposure to media-containing ZIKV virions at an M.O.I. of 1. qPCR conducted in 4 replicates. Dots displaying the values of each donor cell line. (C) Dot plots showing the quantification of the abundance of lipid droplets in ZIKV challenged Infected: Env +ve and non-infected: Env -ve), and non-challenged hi-NPC controls. Values reflect the median fluorescence intensity (MFI) of CellTracker™ green BODIPY dye. A minimum of 500 *in focus* cells were analyzed per donor cell line out of 10000 cells recorded. Bars display mean ± SD. n = 1 viral challenge conducted in three independent donors' cell lines. Significance was calculated by Two-way ANOVA with Šidák's multiple comparisons post-hoc test. Significance is shown when *p < 0.05, ** p < 0.01, *** p < 0.001. Single cell imaging of lipid droplet content (neutral lipid staining) in ZIKV infected and non-infected hi-NPC subtypes (D) AMNIS Imaging flow cytometer digital images show representative lipid droplet staining (green), selected by internally defined mask (light blue), and ZIKV-Envelope staining (red).

4.5.5 Metabolism of lipid droplets is important for early stages of replication of ZIKV in early hi-NPCs

Early Env +ve hi-NPCs exhibited a significantly higher area occupied by lipid droplets ($p \leq 0.0242$) compared to Env -ve and non-challenged control cells, followed by a time-dependent reduction (Figure 4.5A). No significant differences after 24 h.p.i. were found between conditions with Env -ve and controls reflecting minor changes in the size of the area occupied by lipid droplets during the 72 hours of culture (Figure 4.5A). Data corresponding to the abundance of lipid droplets showed similar results with a significant increase ($p \leq 0.0189$) in early Env +ve hi-NPCs compared to Env -ve and non-challenged controls (Figure 4.5B). Late hi-NPCs showed no alterations during ZIKV replication (Figures 4.5A and 4.5B). Distribution of the area occupied by lipid droplets showed a time-dependent increase in Env +ve hi-NPCs with significant differences at 56 h.p.i. observed exclusively between early Env +ve and Env -ve hi-NPCs (Figure 4.5C). These data showed dysregulation of lipid droplets metabolism at early stages of ZIKV replication exclusively in early hi-NPCs with no significant differences in the ratio of changes between ZIKV-challenged hi-NPC subtypes. Single-cell imaging using define lipid droplets areas of analysis is illustrated in Figures 4.5D and 4.5E. Figures 4.5F and 4.5G show the validation of the immunostaining in both hi-NPC subtypes.

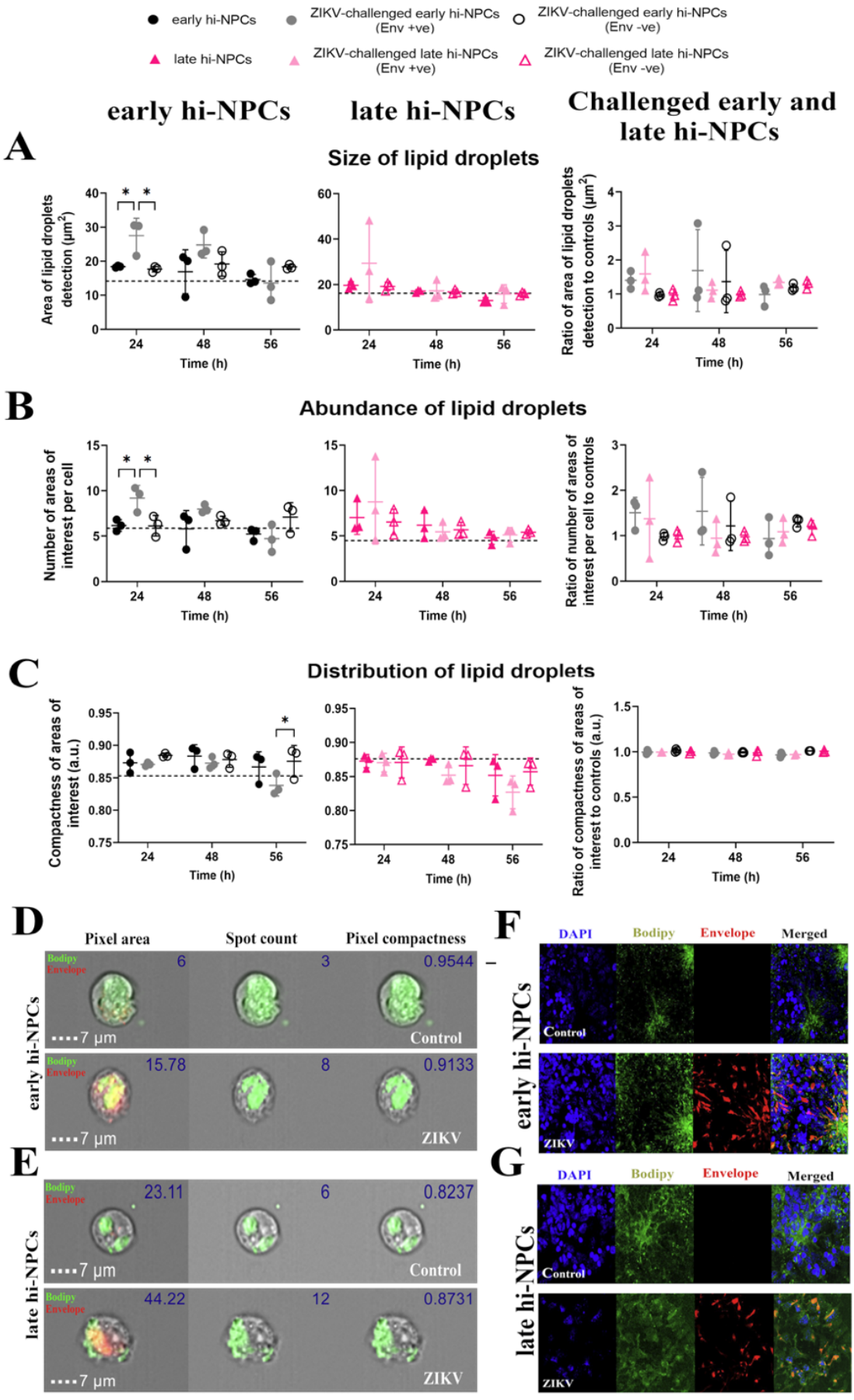

early hi-NPCs
ZIKV-challenged early hi-NPCs (Env +ve)
ZIKV-challenged early hi-NPCs (Env -ve)
late hi-NPCs
ZIKV-challenged late hi-NPCs (Env +ve)
ZIKV-challenged late hi-NPCs (Env -ve)
early hi-NPCs
late hi-NPCs
Challenged early and late hi-NPCs
A
Size of lipid droplets
Area of lipid droplets detection (µm²)
Ratio of area of lipid droplets detection to controls (µm²)
Time (h)
B
Abundance of lipid droplets
Number of areas of interest per cell
Ratio of number of areas of interest per cell to controls
C
Distribution of lipid droplets
Compactness of areas of interest (a.u.)
Ratio of compactness of areas of interest to controls (a.u.)
D
Pixel area
Spot count
Pixel compactness
Bodipy
Envelope
6
3
0.9544
7 µm
Control
15.78
8
0.9133
ZIKV
early hi-NPCs
E
23.11
6
0.8237
44.22
12
0.8731
late hi-NPCs
F
DAPI
Bodipy
Envelope
Merged
Control
ZIKV
G

Figure 4.5. Infected early hi-NPCs accumulate lipid droplets during early stages of ZIKV replication

Analysis of several characteristics of the lipid droplets in hi-NPC subtypes challenged to media-containing ZIKV for 2 h at 37 °C using an M.O.I. of 1 compared to non-challenged controls. Displayed data compares productively infected hi-NPCs (Env +ve) against challenged non-infected hi-NPCs (Env -ve) and non-challenged control hi-NPCs. Dot plots showing (A) lipid droplet sizes estimated by the quantification of the total occupied area within the cells, (B) abundance of areas occupied by lipid droplets and, (C) distribution of lipid droplets determined by the proximity of positive areas within the cells. Graphs showing (left) the quantification by hi-NPC subtypes and (right) the ratio of change of each hi-NPC subtype relative to their respective non-challenge controls. A minimum of 500 *in focus* cells were analyzed per donor cell line out of 10000 cells recorded. Bars display mean ± SD. n = 1 viral challenge conducted in three independent donors' cell lines. Significance was calculated by Two-way ANOVA with Šidák's multiple comparisons post-hoc test. Significance is shown when $^{*}p < 0.05$, $^{**}p < 0.01$, $^{***}p < 0.001$. Single cell imaging of lipid droplet content (Bodipy staining) in ZIKV infected and non-infected hi-NPC subtypes. (D-E) AMNIS Imaging flow cytometer digital images show representative lipid droplet staining (green) and ZIKV-Envelope staining (red) in hi-NPC subtypes. (F-G) Representative confocal images with high magnification (60x) of z-stack projections (15 μm) confirming positive staining of lipid droplets (green) and ZIKV Envelope protein (red) in challenged and non-challenged hi-NPC subtypes. DAPI staining (blue).

4.6 DISCUSSION

4.6.1 Differences in ZIKV replication and its consequence for glucose metabolism in neuronal progenitor subtypes

Analysis of ZIKV replication in brain cell types reflects larger susceptibility and significantly higher infection of neuronal progenitors and astrocytes compared to adult neurons and microglia[255,256,259]. In agreement with current literature, the quantification of infectious virions released from early and late hi-NPCs to ZIKV showed they were productively infected. A significant accumulation of viral RNA in late hi-NPCs together with significant accumulation of intracellular NS1 viral proteins suggested a larger replication than in early hi-NPCs. However, this needs further evaluation with other techniques (e.g., western blot) as NS1 had lower percentage of detection. At 56 h.p.i., a higher encapsidating of the increased viral RNA and protein was translated into a higher release of ZIKV virions. These results are the first to show infection and replication rates of ZIKV among subtypes of neuronal progenitors as means to understand the neurotropism of ZIKV.

Exposure of hi-NPC subtypes to ZIKV showed significant loss of cell viability after 48 h.p.i., as reported elsewhere[75,76,253,255]. Accelerated loss of cell viability of both early and late hi-NPCs may explain the significant decrease of cortical mass observed in new-borns infected during the first trimester of pregnancy where these cells are expected to start neurogenesis. The loss of cell viability was corroborated by nuclear staining[288] at later time-points of ZIKV replication. In late hi-NPCs, a significant increase in nuclear size potentially correlates with a significant reduction in circularity. This, as showed by other groups[289,290], may suggest the visualization of viral perinuclear replication centres (white arrows, Supplementary Figure 2). In early hi-NPCs, significant reduction in nuclear size and increased nuclear circularity

may be related to cellular shrinkage and apoptosis[147,291,292]. The differences in nuclear damage may suggest that early hi-NPCs (proliferating progenitors) suffer from chromatin condensation and cell death producing a lower yield of ZIKV to infect neighbouring cells. On the other hand, late hi-NPCs (intermediate progenitors) have tolerance to ZIKV infection and, despite cell death, clear formation of viral reservoirs may suggest an advantage for ZIKV replication and spread in the developing brain. *In vitro* passages may inflict mutations promoting gain/loss of infectivity among ZIKV strains[293], which may in turn exhibit differential impact on cellular metabolism during replication. Thus, I used a low passage pathogenic African strain U-1962 (MP1751) to study the potential energetic requirements in neuronal progenitors[294,295]. ZIKV infection imposed a transcriptional upregulation of genes involved in glycolysis in hi-NPC subtypes yet to a lesser extent in more mature, late hi-NPCs. The lack of changes observed in the expression profile of the glucose receptor GLUT-1 may be due to saturated expression as cell culture was done under hyperglycaemic media conditions. Reports from human kidney cells in which exogenous elevation of the level of glucose in culture decreases ZIKV replication[296] emphasize the importance of accurate cellular models and culture conditions. Increased glucose consumption over the course of ZIKV replication agrees with reports using a diversity of human and non-human cell lines[242,267,282,283], highlighting the importance of cytosolic processing of glucose during ZIKV replication.

Increased glycolysis serves several cellular processes. A significant increase of lactate production by hi-NPCs suggests that elevated glucose metabolism supports anaerobic energetic demands during ZIKV replication, as observed by other groups[236,242,283,297]. Higher activation of glycolysis in late hi-NPCs, the subtype with lower baseline levels of glycolytic capacity, may suggest that ZIKV requires by-

products of glycolysis to support additional processes such as redox clearance and nucleotide production[236], and/or to signal cell survival-related pathways necessary for efficient viral replication[107,236,244,267,283]. Meanwhile, lower increments in early hi-NPCs may obey to sequestration of the existing cellular pool.

4.6.2 Alterations of mitochondrial homeostasis during ZIKV infection

Mitochondria role in the orchestration of metabolic pathways is likely to be manipulated by stressors such as ZIKV. Results from qPCR analysis showed higher expression of genes involved in beta-oxidation of fatty acids at early time-points in early hi-NPCs whilst at later time-points in late hi-NPCs. These results agree with those from ZIKV infection in human monocytes and drosophila. ZIKV infection has showed to increase the transcription of genes related to oxidative phosphorylation in human monocytes and drosophila cells[154,298], with further increase in genes involved in the electron transport chain and ATP production only in human monocytes[154]. In addition, research have showed increments in the TCA cycle in ZIKV-infected human fibroblasts[282] and larger ROS production in iPSC-derived astrocytes[124]. This may also suggest and increased fatty acid beta-oxidation. However, results from mice models of ZIKV pathology showing decreases in the TCA cycle, oxidative phosphorylation, and cytosolic levels of NAD^+[242,244], may suggest a decreased beta-oxidation of fatty acids.

Early and late hi-NPCs showed remodelling of the transcriptional machinery by changes in the expression profile of relevant genes. Early hi-NPCs transitioned from increased beta-oxidation at early time-points to increased lipid biosynthesis whilst late hi-NPCs showed opposing patterns. This potentially highlights constant alterations at the transcriptional level during ZIKV infection. Thus, the controversy

in the results between *in vitro* and *in vivo* models may obey to the screening time-point. Nevertheless, it may also obey to major intrinsic differences between *in vitro* and *in vivo* systems.

The results from ZIKV-challenged hi-NPC subtypes showed that infected cells (Env +ve) have dysregulated mitochondrial homeostasis in the form of reduced size and number when compared to Env -ve and non-challenged controls. Interestingly, mitochondrial dysregulation showed to be time-dependent between hi-NPC subtypes. This could be potentially explained by the specific metabolic characteristics of early and late hi-NPCs. Reduced distribution of mitochondria was found in the two subtypes of hi-NPC exclusively at the initial time-point when exponential viral replication did not occur potentially suggesting adaptative mechanisms to ZIKV replication. Our results from mitochondria size agree with data from ZIKV-infected human neuronal stem cells[299] but disagree with several other human cell models of naïve proliferating cells in which increased mitochondria size, mitochondria elongation, swelling, and fractioning are features of dysfunctionality and reduced network during ZIKV infection[242,258,299–301]. My results were obtained from live non-apoptotic single cells containing viral Env protein. Thus, potentially generating some of the discrepancies found with the results from other groups.

Oxygen consumption is crucial for mitochondrial activity. ZIKV infected human trophoblasts, placental stromal cells, and iPSC-derived astrocytes have showed decreased oxygen consumption rate compared to controls[124,300], potentially suggesting a reduction in mitochondrial membrane potential. Herein, I showed reduced mitochondrial membrane potential in Env +ve compared to Env -ve hi-NPCs but not to non-infected controls. These findings are different to those in ZIKV-infected human neuronal stem cells, human retinal and human hepatoma cells[301] in

which ZIKV-infected cells had higher mitochondrial membrane potential. However, current findings have failed to show whether the mitochondrial changes were in infected or in non-infected neighbouring cells.

Moreover, mitochondrial depolarization may underpin impaired mitochondrial function which may in turn induce mitophagy[302]. Thus, our results on mitochondrial depolarization in ZIKV-infected cells potentially correlate with reports from mice models showing increased mitophagy genes and mitophagy[107,303]. However, our results exposed limitations as the differences were exclusively observed against non-infected challenged cells but not to non-challenged controls.

Altogether, these results showed that there were minimum changes in mitochondrial membrane potential. In addition, these results highlight for the first time that potential ZIKV-induced mitochondrial stress differs between neuronal progenitor subtypes. Furthermore, mitochondrial dysregulation observed in infected but not in neighbouring cells at specific time-points during viral replication highlights the importance of time-course mitochondrial tracing to better understand the role of energy metabolism in the pathogenesis of ZIKV.

4.6.3 Neuronal progenitor subtype-specific reprogramming of lipid metabolism in response to ZIKV infection

Metabolism of lipids is crucial for cellular function. Low oxygen consumption induced by ZIKV was hypothesized by others to be related to low rates of fatty acid beta-oxidation[124,300]. Thus, I tested whether a change in lipid metabolism during ZIKV infection might contribute to the mitochondrial dysregulation showed above.

Research have showed that ZIKV infection alters the metabolism of lipids in a specific fashion, reflecting the flexibility of lipid rearrangement. This agrees with my

findings, previously discussed, on significant transcriptional upregulation in genes involved in lipid metabolism, both beta-oxidation of fatty acids and lipid biosynthesis in ZIKV-infected hi-NPCs. Other results that are in agreement with my findings involve, in mosquito cells and human fetal microglia cells, an increase in a global panel of lipids at 24 h.p.i. with further decrease at 48 h.p.i.[260]. In human trophoblasts, placental stromal cells, among other cellular models, a lipid rearrangement during ZIKV including increases in the levels of phospholipids, di, and tri-acyl glycerol[257,300]. In *Drosophila* models, ZIKV infection increased the transcriptional levels of ether lipid synthesis genes[298] whilst in mice, the infection showed to increase cholesterol metabolism[244].

Research showing that the manipulation of the intracellular lipid content in ZIKV-permissive cells alters ZIKV replication[145,304], and that blockade of sphingolipid synthesis and diacylglycerol transferase significantly decreases it[145,244], corroborated the importance of lipid metabolism in the pathogenesis of ZIKV.

Moreover, time-dependent decrease in *de novo* lipid biosynthesis followed by decreased lipidomic content during ZIKV infection showed by others[145,244,305] may be related to lipid utilization and exhaustation[306]. This may also be inferred from our results in late hi-NPCs showing an increased transcriptional upregulation of lipid biosynthesis, at early stages, followed by an increased in beta-oxidation genes. Nevertheless, as I showed neuronal subtype-specific patterns in the transcriptional modulation of lipid metabolism, opposing findings may be a result of core cellular properties.

Lipid droplets are multifunctional organelles that comprise aggregates of several types of lipids[120–122] that can be exploited by ZIKV to support its replication[277]. Yet, the role of lipid droplets during ZIKV infection remains unclear. There are reports

that show an increase, potentially due to immune responses to ZIKV infection, as observed by similar patterns produced by UV-irradiated conditional media[300], as well as those showing a decrease[301]. Lipid droplets can differ depending on the concentration of lipids[121], thus, I examined their number and size during ZIKV infection. My results showed differential effects in the lipid droplet content between neuronal progenitor subtypes and that changes in lipid droplet homeostasis were exclusive to ZIKV-infected early hi-NPCs. These time-course changes (initial increase followed by a decrease) in the lipid droplet homeostasis, have also been showed by others[307]. Thus, potentially reflecting the dynamics of lipid droplets during sustained ZIKV infection.

Moreover, the significant increase in the lipid droplet abundance in Env +ve compared with Env -ve cells at 24 h.p.i. are in contradiction with the findings from a study of a similar kind in placental stromal cells that showed significant increases in lipid droplets in Env -ve cells[300]. Besides differences in cell type characteristics, as discussed in the results from mitochondrial dysregulation, analysis performed exclusively in non-apoptotic ZIKV-infected live cells may underlie differences in the findings. Discrepancies in the detection of lipid droplets may also be due to our quantification done by area instead of single droplet count.

Furthermore, the role of specific ZIKV viral proteins in the dysregulation of lipid metabolism, as reported in cancer models[145,308], was not studied due to the lack of transfection of NS4 protein in hi-NPC subtypes (data not shown)[B]. For the full procedure please refer to section 2.9.

[B] This work was done in collaboration with a fellow student from the Sanyal's lab. Ms. Sophie Van-Leur designed the transfection experiment and prepared the required solutions.

4.7 CONCLUSION

ZIKV productively infects neuronal progenitor subtypes and exhibits subtype-specific replication rates which are related to a differential pattern of nuclear damage causing loss of cell viability. Although a straightforward explanation for ZIKV-induced microcephaly in new-borns infected during the first trimester would be a faster loss of cell viability of early neuronal progenitors, my results showed that both early and late hi-NPC have similar rates of cell death. However, as intermediate progenitors (late hi-NPCs) are originated from radial-glial like progenitors (early hi-NPCs), there are different ways in which my results correlate to the pathogenesis of congenital Zika syndrome: a) death of early progenitors reduces the pool of intermediate progenitors required for the correct cortical expansion and, b) efficient replication of ZIKV facilitates the transmission and infection of other cell types as observed in post-mortem brains.

Analysis of the main cellular metabolic pathways of neuronal progenitor subtypes reflected dysregulations due to ZIKV replication. These were reflected in the global cellular transcriptional profile by upregulating genes involved in the metabolism of glucose and, lipid beta-oxidation and biosynthesis. A significant time-dependent increase in the glycolytic capacity, a common feature among hi-NPC subtypes, established a primary role of cytosolic processing of glucose towards lactate production to sustain ZIKV replication.

Moreover, ZIKV dysregulation on mitochondrial homeostasis was observed exclusively in productively infected hi-NPCs. Mitochondrial dysregulation included the alteration of their membrane potential, size, and abundance. However, these dysregulations were exclusive to each neuronal subtype and were not sustained during infection but observed at single time-points. Similar results were obtained

when analysing lipid droplets. Their metabolism was exclusively affected in early hi-NPCs at early stages of replication by significantly increasing their size and number. Overall, these data suggest a primary role of energy metabolism of neuronal progenitors in the pathogenesis of ZIKV in the fetal brain and revealed differences in the metabolic stress and cellular damage between neuronal progenitor subtypes challenged to ZIKV (Figure 4.6). Thus, as native immunity can modulate cellular metabolism, this chapter would have benefitted from the analysis of the metabolic changes in hi-NPC subtypes after exposure to e.g., other neurotropic viruses and/or dsRNA, which mimics viral replication. This exposure may elucidate whether the metabolic alterations are directly dependent on ZIKV replication or if they are a consequence of the native immune detection of ZIKV. However, as it remains of controversy whether cortical neuronal progenitors possess active native immune responses, in my next chapter I will approach whether the reported metabolic dysregulations are a direct consequence of ZIKV replication using yolk-sac derived macrophages instead of neuronal precursors.

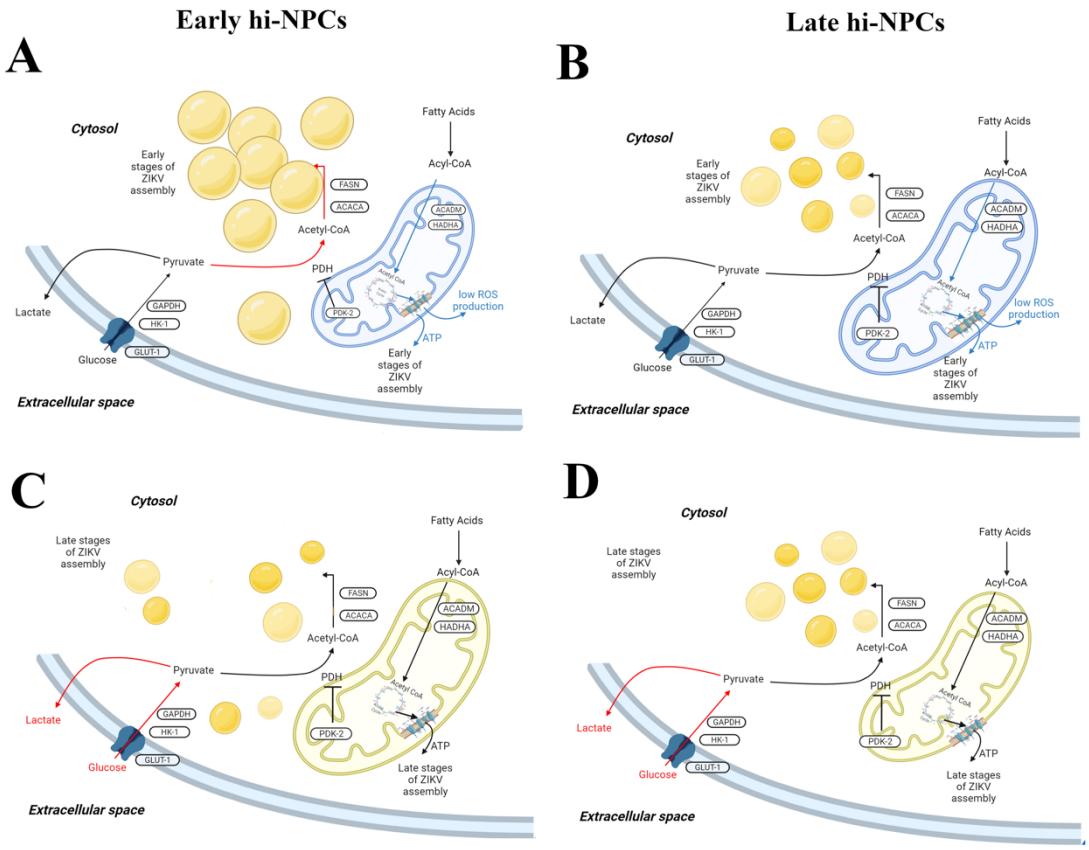


Figure 4.6. Overall metabolic alterations in ZIKV-infected neuronal progenitor subtypes

Schematic representation of the metabolic dysregulation in early and late hi-NPCs in response to ZIKV infection. (A) Increased number and area occupied by lipid droplets with reduced mitochondria membrane potential and size in early hi-NPCs during early stages of ZIKV replication. (B) Normal abundance of lipid droplets, normal mitochondria size and reduced membrane potential in late hi-NPCs during early stages of ZIKV replication. (C) Normal abundance of lipid droplets with larger distribution and increased glycolytic capacity in early hi-NPCs during late stages of ZIKV replication. (D) Normal abundance of lipid droplets, reduced mitochondria size and increased glycolytic capacity in late hi-NPCs during late stages of ZIKV-replication. Black arrows representing normal levels. Red arrows highlighting increased pathways. Light blue representing low mitochondrial activity with light yellow representing normal levels. Lipid droplet abundance and mitochondria size are represented within each figure. Pathways including some of the relevant metabolic genes analyzed as part of the glycolytic, fatty acid oxidative and fatty acid biosynthesis pathways analyzed during ZIKV challenges in early and late hi-NPCs.

5. IMMUNE-METABOLISM OF MACROPHAGES PREVENTS ZIKV INFECTION AND FACILITATES THE DISSEMINATION OF VIRIONS IN THE FETAL BRAIN

5.1 ABSTRACT

How ZIKV populates and infects the fetal brain causing detrimental damage remains unclear. At this stage, yolk-sac-derived macrophages populate the early brain and interact with neuronal progenitors to orchestrate normal brain development. Yolk-sac derived macrophages constitute the only phagocytes of the brain to act against pathogens. Thus, their role in surveillance is highly regulated with responses to insults involving metabolic and immune reprogramming. Current *in vitro* models of the fetal brain are based on the differentiation of iPSC-derived brain cells using culture media likely to contain supplements with immunosuppressant properties which can mask the real cellular immune interactions against pathogens. In this chapter, I studied a) the infectivity capacity of ZIKV in yolk-sac-like macrophages (hiPSC-MPh), b) the impact of ZIKV productive infection in hiPSC-MPh as a route of dissemination to early hi-NPCs and, c) the impact of ZIKV infection on the cytosolic glycolysis in hiPSC-MPh. To do this, I efficiently completed a 2D *in vitro* differentiation of early neuronal progenitors (early hi-NPCs) in a serum-free, defined-source culture media and developed a 2D *in vitro* coculture of early hi-NPCs and hiPSC-MPh. I showed that ZIKV productively infects hiPSC-MPh at low levels yet, these levels are sufficient for the dissemination of virions to early hi-NPCs. Thus, highlighting a route of maternal-fetal transmission of ZIKV in the early fetal brain. In addition, the indirect study of the role of glucose metabolism by the infection

of immune metabolic compromised hiPSC-MPh showed to significantly alter their susceptibility to infection. This supported the results obtained in chapter 4 and highlighted a major role of increased cytosolic glucose processing in the sustained replication of ZIKV. Lastly, I emphasise that the results from the coculture system and glucose metabolism should be repeated for reproducibility purposes.

5.2 INTRODUCTION

ZIKV represented a serious threat to populations in the tropical regions[97,309], due to its marked neurotropism[252,253]. As highlighted in previous chapters, the neurotropism of ZIKV is reflected in the infection of a variety of brain cells, from neuronal progenitors to mature neurons[124,154,236,256,259,261]. ZIKV-induced detrimental fetal brain damage such as fetal microcephaly[75,244,253,256], is driven by, but not limited to, the infection and induced cell death of neuronal progenitors[124,154,236,256].

The epidemic caused by ZIKV in 2016 still requires attention as the potential outcomes on brain health in children infected during late pregnancy, with no clear brain abnormalities as new-borns, may yet to be seen[310–312]. ZIKV infection shows dysregulation of metabolism in the infected cells whether that of glucose, amino-acids, lipids or their combination[36,123,242,279,280]. Viral-induced metabolic dysregulation potentially damage neurons and prevents them from developing circuits later in life that translate into neuropsychiatric conditions[311,313,314] which features emerge during adolescence and adulthood[315,316]. This is the case for other neurotropic viruses[317]. Thus, understanding the mechanisms of ZIKV-mediated metabolic hijacking may signify means for potential therapies.

The precise route of entry for ZIKV to infect the fetal brain remains unclear yet there are several potential mechanisms of vertical maternal-fetal transmission[77,78,313,318] (Figure 5.1) which underlie serious threats for both the mother and the developing fetus[319,320].

Fetal development involves stages of rapid cell division, growth, and cellular crosstalk to support the development of several populations that rise to form the different organs[237,321,322].

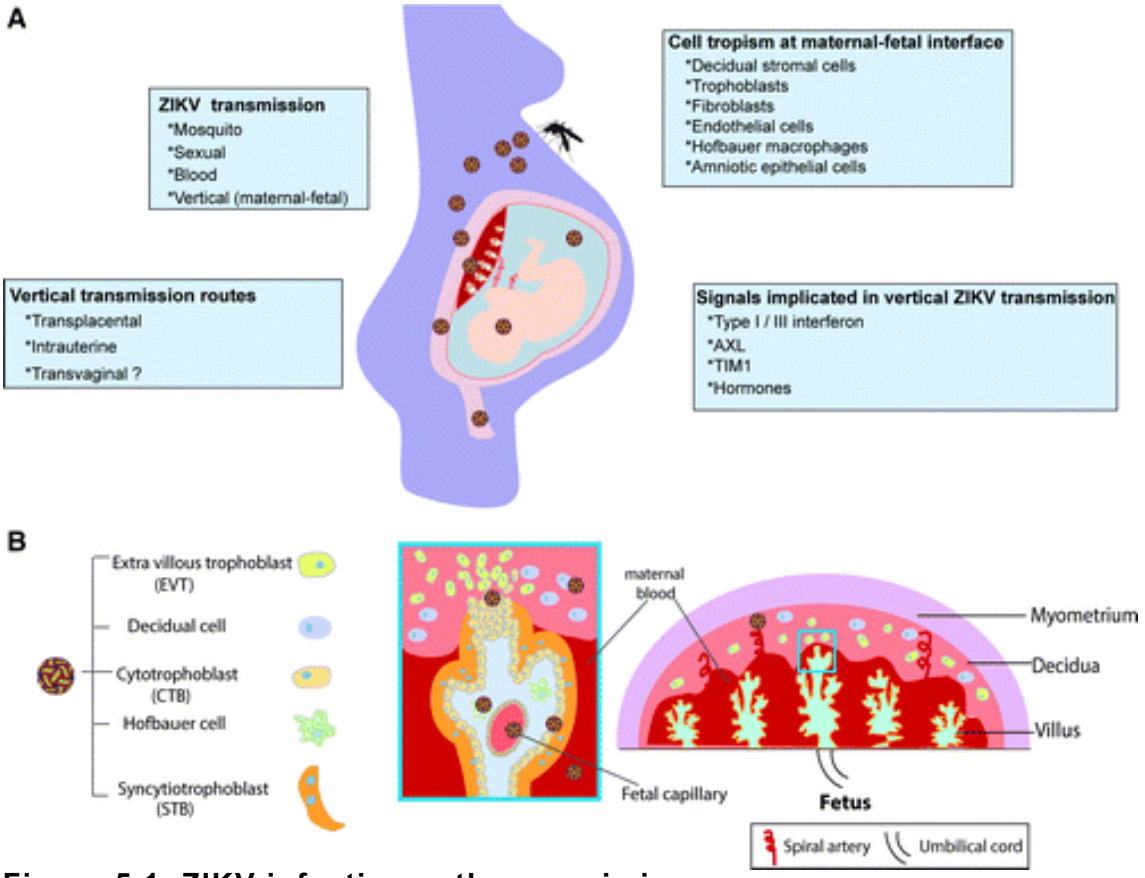


Figure 5.1. ZIKV infection pathogenesis in pregnancy
(A) Summary of routes of ZIKV transmission in a pregnant woman and the cells and signals implicated in transmission. (B) Structure of human placenta and sites of ZIKV infection. In the human placenta, there exist fetal-derived chorionic villi (*blue box*), which are tree-like projections lined with 2 layers of trophoblasts and bathed in maternal blood. Villous trophoblasts comprise 2 layers: the STBs and CTBs. The CTBs are highly proliferative and form a monolayer of polarized cells that eventually differentiate via cell–cell fusion into STBs. STBs form a surface covered by a dense network of branched microvilli that are bathed in maternal blood, mediate nutrient and gas exchange between mother and fetus. Fetal-derived macrophages, known as Hofbauer cells, are found in the intervillous spaces. A subset of trophoblasts, termed EVTs, migrates from the chorionic villi, invades into the uterine wall, and remodels maternal spiral arteries to facilitate blood supply of the placental unit. In addition to the EVTs, the decidual compartment also includes maternal immune cells (eg, decidual macrophages, decidual natural killer cells) and stromal cells. CTBs, cytotrophoblasts; EVTs, extravillous cytotrophoblasts; STBs, syncytiotrophoblasts; ZIKV, Zika virus. Obtained from Cao et al., 2017[77].

The first circulating cells in the developing embryo, upon establishment of the maternal-fetal blood circulation, are yolk-sac-derived macrophages[323–325]. Some of these cells migrate and populate the embryonic brain[326,327]. Macrophages populating the parenchyma of the brain differentiate into specific tissue-resident cells termed microglia[324–326,328]. Macrophages populating the non-parenchyma

areas of the brain are known as central nervous system-associated macrophages[325,328–330] (Figure 5.2). Current *in vitro* models of the fetal brain recapitulate the crosstalk of non-fetal-like macrophages and neuronal progenitors. Nevertheless, some protocols for monoculture provide the tools to successfully differentiate macrophages, among the different types, into those that exhibit the distinctive signatures of brain microglia[331–333].

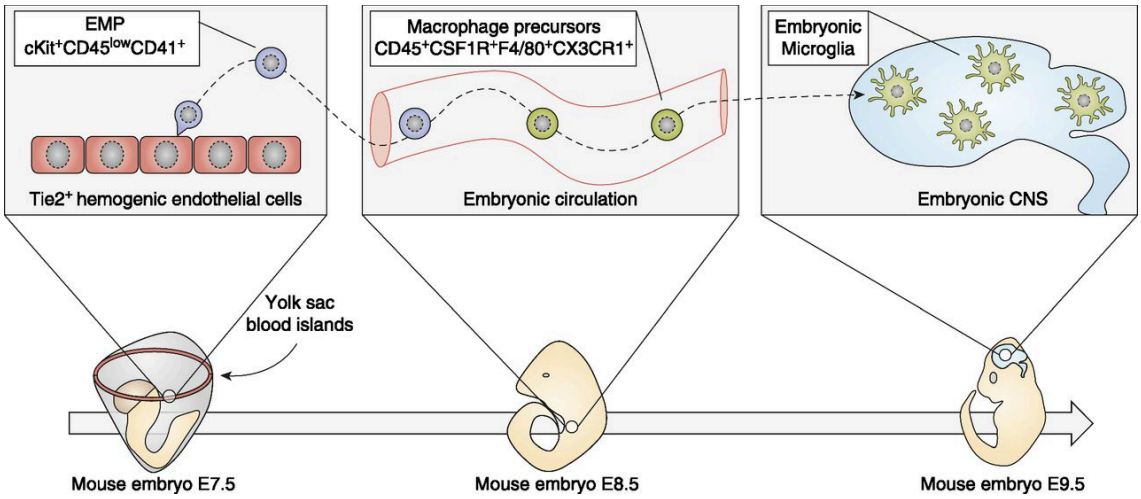


Figure 5.2. Key steps in the development of embryonic microglia
Erythromyeloid precursor cells (EMPs), generated during embryonic primitive haematopoiesis, provide the first cohort of macrophages to the developing embryo. EMPs appear in the blood at E8.5 and complete their differentiation into macrophage precursors. Macrophage precursors invade the brain between E9.5 and ~E14.5 and differentiate into microglia. Obtained from Brioschi et al., 2020[334].

The media used to differentiate these cells include the use of serum, which composition can change between providers and among batches[335], and/or, in the case of serum-free media, they may contain molecules with immunosuppressant properties[173,331,335–337]. This potentially alters the responses of macrophages to external insults[173]. Previous work from my laboratory showed a methodology for the differentiation of macrophages with shared molecular signatures to those of the human yolk-sac-derived tissue-resident macrophages[338,339]. These features are retained when cultured in a serum-free defined-source culture media[173].

In vitro models show susceptibility of macrophages to ZIKV infection measured as the levels of viral RNA and/or protein over time. Of interest, differential susceptibility to infection may depend on the macrophage type[154,173,259–263]. Thus, infected brain-populating macrophages may be responsible for the maternal-fetal transmission of ZIKV (Figure 5.1) and the severe fetal damage during early pregnancy[77].

Glycolysis plays a major role in immune cells as it may provide the fuel for their responses to pathogens[157,340,341] and, polarization in activated macrophages requires an increase in the glycolytic capacity[158,159,342,343]. Interferon- and non-interferon-mediated immune responses reflect the crosstalk of cellular metabolism and native immunity, and the capacity of immune reprogramming of glycolysis[160,344–346]. To date, few studies have shown broad alterations of cellular metabolism in ZIKV-infected macrophages[154,259,260] yet, its implication in the replication processes remains unclear.

In this thesis, I hypothesised that the metabolism of different cell types of the developing early fetal brain is distinctively hijacked by neurotropic Zika virus (ZIKV) underpinning the differences in congenital zika syndrome observed over the course of pregnancy[77]. I've showed in chapter 4 that a common feature of ZIKV infection among hi-NPC subtypes was the significant increment in the cytosolic glycolysis. Thus, the study of energy metabolism particularly that of glycolysis in yolk-sac macrophages (hiPSC-MPh) may reveal the metabolic requirements involved in the sustained replication of ZIKV in the cells of the early fetal brain. To do this, chapter 5 will study the susceptibility of hiPSC-MPh to be productively infected as a potential route of entry to the developing brain. This chapter will also study the effects of ZIKV productive infection in the glycolytic capacity of hiPSC-MPh.

5.3 AIMS

Potential mechanisms of ZIKV infection in several brain cell types, including radial glial cells and proliferating neuronal progenitors, have been reported. However, how the potential metabolic reprogramming in yolk-sac-derived macrophages (hiPSC-MPh) — the immune cells of the developing brain — may facilitate sustained infection by ZIKV is yet to be elucidated. Potential permissibility to infection of these cells highlights a potential route for the maternal-fetal transmission of ZIKV and would potentially reveal common metabolic dysregulations across different brain cell types which may have implications as potential therapeutic targets. I previously showed that, in hi-NPCs, ZIKV significantly dysregulates the metabolism of glucose. Thus, to test whether alterations in the metabolism of glucose of the hiPSC-MPh support ZIKV replication facilitating the dissemination in the fetal brain, it is necessary to model ZIKV infection using cells with fetal phenotypes. To this, I used early hi-NPCs and tissue-resident-like macrophages to address the following five aims:

- To test whether a defined-source, serum-free culture media supports the differentiation of early hi-NPCs
- To develop a stable coculture that models the early fetal brain
- To elucidate the susceptibility of hiPSC-MPh to ZIKV infection
- To assess whether hiPSC-MPh disseminate ZIKV virions to early hi-NPCs as a model of ZIKV transmission to the early fetal brain
- To study the impact of ZIKV infection in the metabolism of glucose of wild-type and immune metabolic compromised hiPSC-MPh

5.4 METHODS

5.4.1 Generation and culture of early hi-NPCs and hiPSC-MPh

hiPSC were obtained and maintained as detailed in section 2.2.2.2.1. Differentiation of hi-NPCs and hiPSC-MPh from hi-PSC were carried out following the protocols set out in sections 2.2.2.2 and 2.2.2.3, respectively.

5.4.2 Development of coculture models of the fetal brain

Coculture models of the fetal brain were performed following the protocols set out in section 2.2.4. For cocultures using hi-NPCs and tissue-resident-like macrophage precursors, the protocol set out in section 2.2.4.1 was followed. The coculture using hi-NPCs and hiPSC-MPh was done following the protocol set out in section 2.2.4.2.

5.4.3 Immunofluorescence analysis of hi-NPCs

Immunostaining and confocal imaging of neuronal markers, populations of brain cell types and, mitochondria and lipid droplets in ZIKV-challenged and non-challenged hi-NPC controls were carried out following the protocol set out in section 2.4.1.1. Protocol for immunostaining and data acquisition using flow cytometry is detailed in the section 2.4.1.2

5.4.4 Immunostaining of hiPSC-derived 3D cortical brain organoids

Immunostaining of cortical neuronal markers in sections of 3D cortical brain organoids and whole organoids for confocal imaging were carried out following the protocols set out in section 2.4.2.

5.4.5 Survival of hi-NPCs differentiated in different culture media

Cellular survival was measured by metabolic activity CCK-8 assay following the manufacturer's procedure detailed in section 2.5.3.

5.4.6 Radioactive metabolic tracing

Intracellular radioactive metabolic tracing of glucose metabolism, glucose oxidation, and oleic acid oxidation were carried out following the protocols set out in section 2.5.1.

5.4.7 Extracellular glucose measurements

Glucose measurements from cell supernatants were carried out following the protocol set out in section 2.5.2.1.

5.4.8 Extracellular lactate measurements

Lactate measurements from cell supernatants were carried out following the protocol set out in section 2.5.2.2.

5.4.9 Thermostability of ZIKV

Thermostability of infectious ZIKV was assessed following the protocol set out in section 2.1.6. Virus infectivity was measured following the protocol 2.1.3.

5.4.10 ZIKV challenge experiments

Cellular mono and coculture models were challenged with culture media containing ZIKV particles. Challenge experiments were carried out following the protocols set out in the sections 2.3.1 and 2.3.2, respectively. Details of the viral stock in section 2.1.1.

5.4.11 Quantification of ZIKV titres

Titration of ZIKV infectious particles by plaque assay were carried out following the protocol set out in section 2.1.2. Microtitration of ZIKV by focus forming unit assay was carried out following the protocol set out in section 2.1.3.

5.4.12 Statistical analysis

Viral quantification from experiments involving a single time-point including both plaque assay and foci forming unit assay readouts were analyzed using unpaired t-test and one-way ANOVA with Tukey's multiple comparisons test, respectively. Datasets containing analysis of two independent donors or independent triplicate experiments of one donor cell line were analyzed using mixed-effects model with Šidák's correction and Šidák's multiple comparisons test, respectively. Datasets containing analysis of three independent donors' cell lines were analyzed using Two-way ANOVA with Šidák's multiple comparisons test. Datasets representing the radioactive measurements of cellular metabolism were analyzed by non-parametric Kruskal-Wallis with Dunn's multiple comparisons test. Datasets from extracellular glucose and lactate from hiNPCs were analyzed by Two-way ANOVA with Tukey's multiple comparisons test whilst those datasets from hiPSC-MPh were analyzed by mixed-effects model with Šidák's multiple comparisons test. Production of infectious ZIKV from cocultures was calculated by mixed-effects model with Tukey's multiple comparisons test. All the statistical tests were performed using GraphPad Prism 9.3.1. A calculated P value less than 0.05 was reported as significantly different.

5.4.13 Figures

Representation schemes were created with BioRender.com. Summary figures were done using GNU Image Manipulation Program (GIMP 2.8.22).

5.5 RESULTS

5.5.1 An advancement in the *in vitro* modelling of the early fetal brain

To better study the metabolic interactions of cells challenged with ZIKV, I differentiated hi-NPCs using a defined-source, serum-free culture medium. Early hi-NPCs cultured under the condition previously described showed a significant increase in cell survival at 48 h ($p = 0.0035$) and 72 h ($p = 0.009$) (Figure 5.3A) compared to early hi-NPCs cultured under conventional commercial neuronal media (N2:B27). However, late hi-NPCs cultured in the defined-source media showed a significant decrease in cell survival post-thawing at 24 h ($p = 0.0101$), 48 h ($p = 0.0003$) and, 72 h ($p = 0.0161$) (Figure 5.3A). Early and late hi-NPCs differentiated in the defined-source media showed no significant differences in the expression levels of cortical neuronal markers compared to N2:B27 differentiated cells (Figure 5.3B). Confocal imaging confirmed the immunostaining of cortical neuronal markers (Figure 5.3D). *In vitro* culture of early and late hi-NPCs using the defined-source media did not produce differences in the levels of subpopulations of brain cell types (Figure 5.3C). Furthermore, assessment of cellular metabolism[A] showed that, exclusively, early hi-NPCs cultured in the defined-source media have a significantly lower ($p = 0.014$) glycolytic rate compared to early hi-NPCs differentiated in N2:B27 media (Figure 5.3E). The differentiation of hi-NPCs in the two different culture media showed no differences in the cellular rate of glucose and oleic acid oxidation (Figure 5.3E). The glycolytic capacity showed that, at 72 h, early hi-NPCs cultured in the defined-source media have a significantly higher glucose consumption than those cultured in N2:B27 ($p = 0.0207$) (Figure 5.3F).

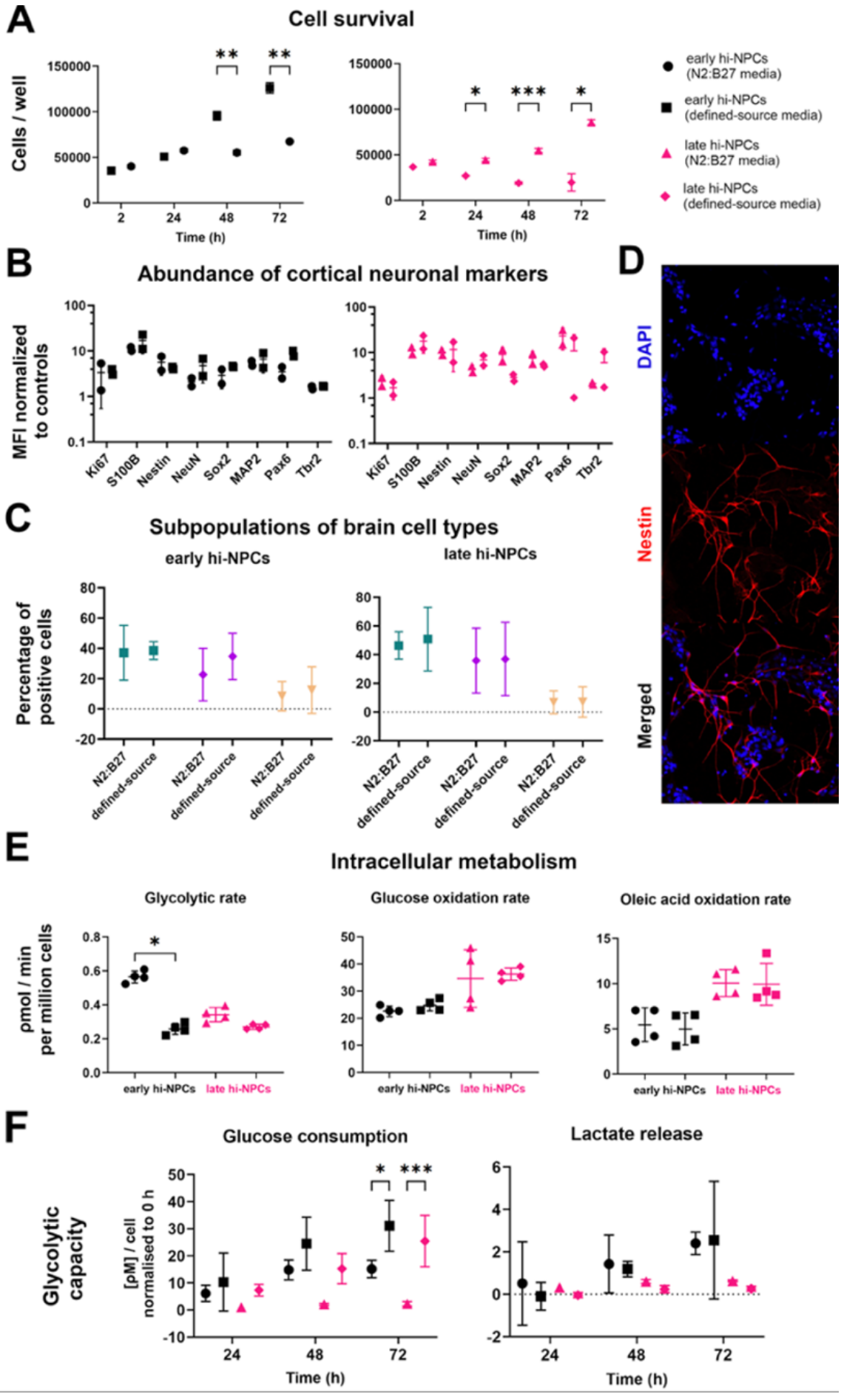

A
Cell survival
Cells / well
Time (h)
early hi-NPCs (N2:B27 media)
early hi-NPCs (defined-source media)
late hi-NPCs (N2:B27 media)
late hi-NPCs (defined-source media)
B
Abundance of cortical neuronal markers
MFI normalized to controls
Ki67
S100B
Nestin
NeuN
Sox2
MAP2
Pax6
Tbr2
C
Subpopulations of brain cell types
early hi-NPCs
late hi-NPCs
Percentage of positive cells
N2:B27
defined-source
D
DAPI
Nestin
Merged
E
Intracellular metabolism
Glycolytic rate
Glucose oxidation rate
Oleic acid oxidation rate
pmol / min per million cells
F
Glucose consumption
Lactate release
Glycolytic capacity
[pM] / cell normalised to 0 h

Figure 5.3. A defined-source, serum-free culture media supports the differentiation of hi-NPC subtypes

Summary of the similarity and differences between early and late hi-NPCs under different culture media conditions. (A) Cell viability over time represented by dot plots showing the bio-reduction capacity of CCK-8 tetrazolium salt. Bars display mean ± SD. n = 1 experiment conducted in triplicate of one donor cell line. Significance was calculated by mixed-effects model with Šidák's multiple comparisons test. (B) Dot plots showing the relative median fluorescence intensity in early and late hi-NPCs of a panel of conventional neuronal markers (Ki67, S100B, Nestin, NeuN, Sox2, MAP2, Pax6 and Tbr2) used to distinguish cortical progenitors. Bars display mean ± SD. n = 1 cortical differentiation of two independent donors' cell lines each conducted in 4 replicates. Significance was calculated by a mixed-effects model with Šidák correction. (C) Dot plots showing the percentage summary of brain cell types present in the cultures of early and late hi-NPCs. Bars display mean ± SD. n = 1 cortical differentiation done in triplicates for each of 3 independent donors' cell lines. Significance was calculated by Two-way ANOVA with Šidák's multiple comparisons post hoc test. (D) Confocal imaging showing an example of the expression of conventional markers of early cortical neuronal progenitors (nestin) in early hi-NPCs cultured in a defined-source, serum-free media. (E) Dot plots showing the metabolic remodelling of the glycolytic flux, glucose oxidation rate and, fatty acid oxidation rate between measured by intracellular tracing of the radioactive by-products formed after 2 and 4 h after culture in media containing radioactive metabolites glucose and oleic acid. Bars display mean ± SD. n = 2 cortical differentiations each measured at two different time-points, 10 and 14 h post plating, in 5 replicates for a donor cell line. Significance was calculated by non-parametric Kruskal-Wallis with Dunn's multiple comparisons test. (F) Dot plots showing the glycolytic capacity expressed as glucose consumption and lactate release. Bars display mean ± SD. n = 1 cortical differentiation done in duplicate for each of 3 independent donors' cell lines. Significance was calculated by Two-way ANOVA with Tukey's multiple comparisons test. Significance is shown when $^{*}p < 0.05$, $^{**}p < 0.01$, $^{***}p < 0.001$, $^{***}p < 0.0001$.

At the same time-point, late hi-NPCs cultured in the defined-source media have a significantly lower glucose consumption than those in N2:B27 ($p < 0.0001$) (Figure 5.3F). No significant differences in the lactate release of early and late hi-NPCs in the different media conditions were calculated at any time-point over the 72 h of culture (Figure 5.3F). Furthermore, the differentiation of hi-NPCs was assessed by the culture of 3D cortical brain organoids. Organoids cultured in the defined-source media following the Lancaster protocol[210] without the use of non-defined commercial supplements were compared to those cultured in the conventional media, comprising a modification of the N2:B27[C].

[C] This work was done in conjunction with a former collaborator of the James lab and fellow students from the Molnár lab. I collaborated with Dr. Paul Kirk Reardon during the culture of brain organoids. Ms. Daria Iakovleva and Ms. Auguste Valdisiute assisted with the sample collection and, the staining and imaging of sectioned brain organoids, respectively.

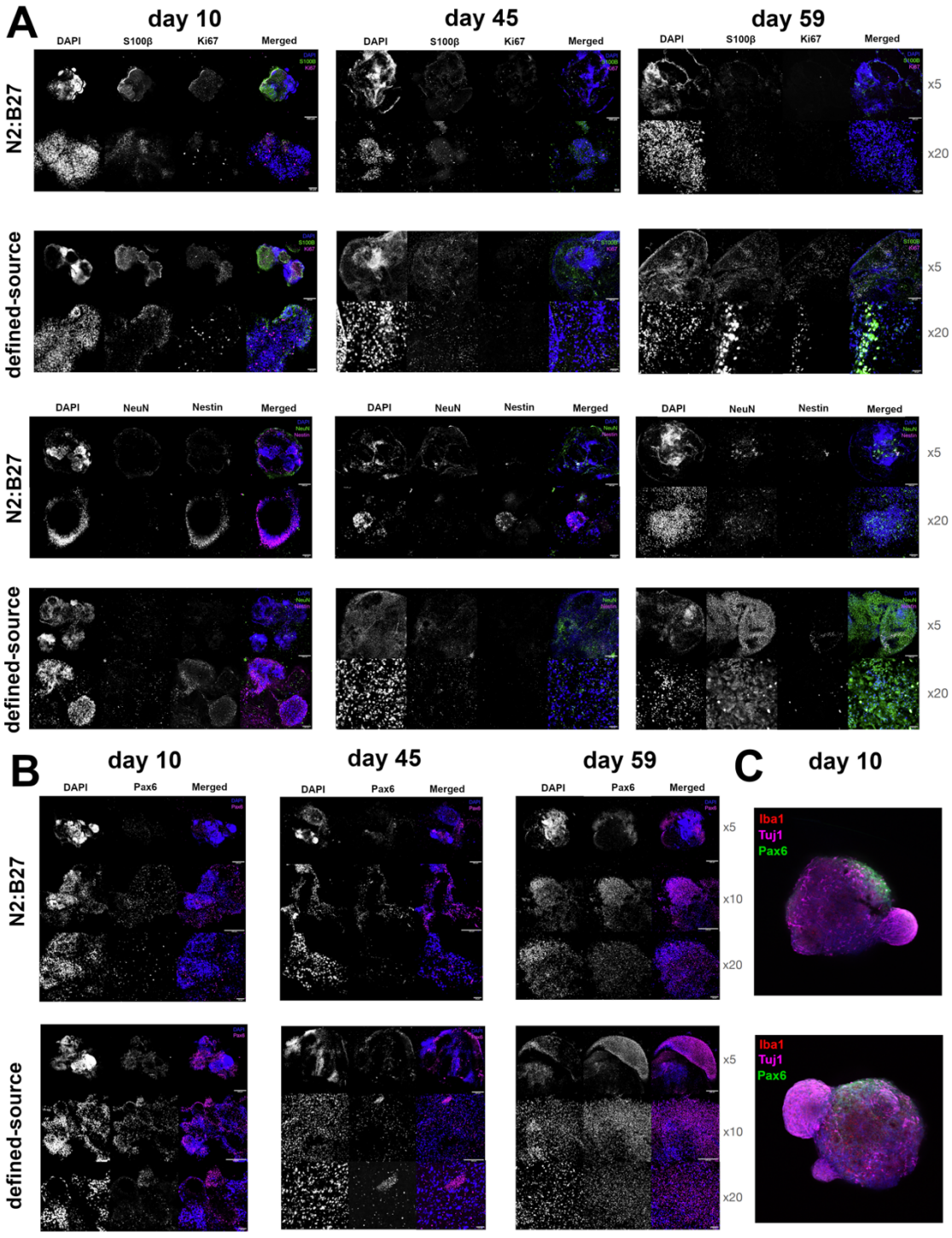


Figure 5.4. Differentiation of hiPSC-derived cortical brain organoids using a defined-source, serum-free culture media

Confocal imaging showing different early cortical brain markers in hiPSC-derived cortical brain organoids at different length of culture under different culture media conditions. (A) 5 µm cryosection slices co-stained with non-cross-reactive antibodies. (B) 5 µm cryosection slices stained with the primary marker of cortical neuronal progenitors (Pax6). (C) Whole organoid staining at 10 days post-differentiation showing the morphology and presence of early brain markers.

Cortical brain organoids showed the presence of neuronal progenitor and cellular proliferation markers over 59 days post-culture (Figure 5.4A). Also, both conditions showed Pax6 +ve cells (Figure 5.4B). The relative abundance of positive cells was not assessed for validation purposes. The brain organoids did not show clear morphological differences nor disruption of cellular organization upon differentiation (Figure 5.4C).

Tissue-resident-like macrophages, and their precursors, previously reported by our group[173], were cocultured with early hi-NPCs differentiated in defined-source culture media. To this, I tested three experimental conditions. The first one, consisting of pre-plated early hi-NPCs, showed a survival length of 72 h post-coculture (Figure 5.5A). The second one, consisting of simultaneously plated macrophage precursors and early showed survival of over 72 h like the third condition consisting of pre-plated macrophage precursors (Figure 5.5A).

The second coculture condition showed populations with distinct morphology (Figure 5.5B). In this coculture, flow cytometry screening of brain cell types, conducted on day four, showed two distinct populations both containing neuronal progenitors and microglia-like cells at similar ratios (Figure 5.5C). The third coculture condition showed a more homogenous cellular distribution (Figure 5.5D). Flow cytometry screening in this coculture, performed on day seven, showed the presence of neuronal precursors and non-neuronal cells including microglia (Figure 5.5E).

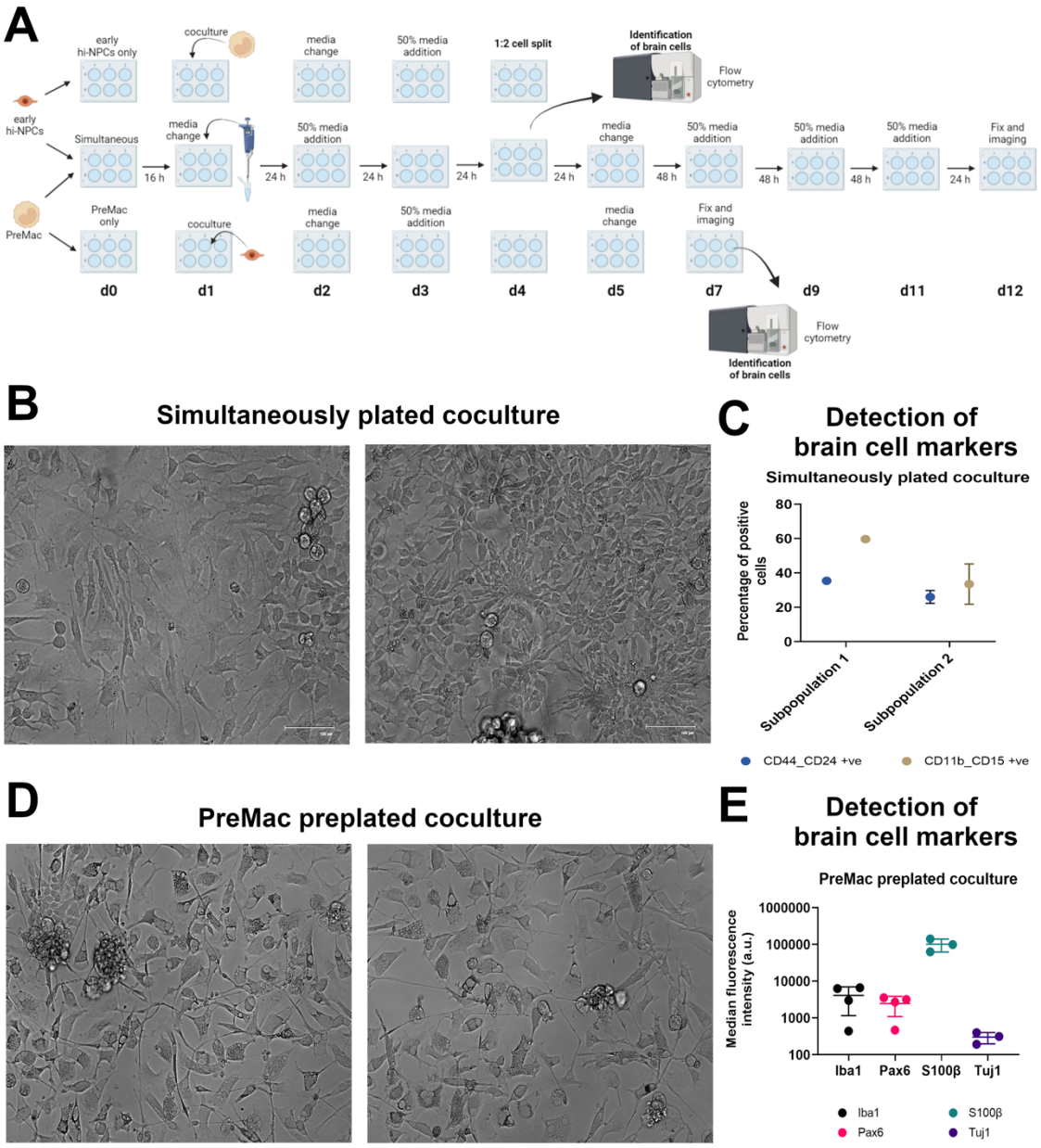


Figure 5.5. Long-term coculture of proliferative neuronal and tissue-resident-like macrophage precursors as a model of the early fetal brain
(A) Schematic representation of the 2D coculture set-up of early hi-NPCs and tissue-macrophage-precursors (PreMac) and the different screening time-points. Coculture condition generated by pre-plated PreMacs showing the coexistence of different types of brain cells by brightfield images (B) and flow cytometry (C). Bars display mean ± SD. N = 1 coculture experiment conducted in duplicate each analyzed in triplicates by flow cytometry. Coculture condition generated by simultaneous plating of PreMacs and early hi-NPCs showing the coexistence of different types of brain cells by brightfield images (D). I Dot plots showing the identification of two subpopulation of cells within the coculture by flow cytometry. Dots showing positive staining for neuronal precursors (blue) and microglia cells (brown). Bars display mean ± SD. N = 1 coculture experiment conducted in duplicate each analyzed in triplicates by flow cytometry. Significance was calculated by a mixed-effects model with Šidák's multiple comparisons test. Significance is shown when $^{*}p < 0.05$, $^{**}p < 0.01$, $^{***}p < 0.001$, $^{***}p < 0.0001$.

5.5.2 Tissue-resident macrophages are a route for ZIKV to enter the fetal developing brain

Plaque assay as a gold-standard method to quantify viruses[173] efficiently counts ZIKV. However, the requirements for large culture volumes impose challenges for *in vitro* disease modelling using cocultures containing early hi-NPCs due to the low cell production. To challenge tissue-resident-like macrophages and coculture systems with ZIKV I first tested a miniaturization approach. Miniaturized plaque assay using a 96-well format plate (Supplementary Figure 3B) showed a significantly lower count of ZIKV titers compared to the assay conducted in a 24-well format ($p = 0.0146$) (Supplementary Figure 3A and 3B).

As an alternative approach, I tested an alternative antibody fluorescence-based assay that requires low culture volumes, termed focus-forming unit (FFU). I identified the accurate dilution of the anti-ZIKV detection antibody 4G2 (1:25 dilution) by the staining of ZIKV-infected Vero CCL-81 cells with two alternate standard doses of virus that were calculated to produce 50 FFU (Supplementary Figure 3C) or 100 FFU (Supplementary Figure 3D) per well. Standard dose of 100 FFU was used in further experiments due to its better quantification range. I validated the accuracy of the detection of ZIKV by the calculation of NT50 values (Supplementary Table 1) using neutralizing human ZIKV+ve / SARS-CoV-2-ve sera from patients in Rio de Janeiro[D] (Supplementary Figure 3E). ZIKV neutralization by human ZIKV-ve / SARS-CoV-2+ve sera, showed no neutralization curve

[D] Sera samples were kindly provided by collaborators in Rio de Janeiro, Brazil. UNIVERSITÁRIO CLEMENTINO FRAGA FILHO DA UNIVERSIDADE FEDERAL DO RIO DE JANEIRO / HUCFF-UFRJ

(Supplementary Figure 3E). An example of focus detection in human sera is shown in Supplementary Figure 3F.

Challenge experiments with ZIKV were conducted at 37 °C. Thus, I assessed the viral thermostability. ZIKV infectivity showed a modest significant decrease at 3 h ($p = 0.0337$) yet not at 4 h. Thermal decay at 6 h or more resulted in a significantly decreased infectivity ($p < 0.0001$) of ZIKV virions (Figure 5.6A). I tested three different M.O.I. at three different incubation periods to assess the susceptibility of hiPSC-MPh to ZIKV infection. Incubation for 2 h and 4 h showed viral titers over 72 h post-challenge only when hiPSC-MPh were challenged to an M.O.I. of 1 (Figure 5.6B). Incubation for 6 h showed viral titers over 72 h post-challenge at an M.O.I. of 1 and over 48 h post-challenge at an M.O.I. of 0.1 (Figure 5.6B). The M.O.I. of 0.01 showed no viral titration. Incubation of 4 h and 6 h showed the highest ZIKV titration levels over the 72 h post-challenge (Figure 5.6B). Immunostaining of the envelope protein showed ZIKV productive infection in macrophages but to lower levels (Figure 5.6C).

ZIKV productive infection of fetal macrophages may underlie its propagation in the developing brain. Thus, I modified two of the previously developed coculture conditions (Figure 5.5A) to test this hypothesis. The modification consisted in the use of tissue-resident macrophages instead of their precursors (Figure 5.7A).

In the coculture experiments, ZIKV infection in the macrophage-only control group showed low titres over the 72 h post-challenge, as showed before (Figure 5.6B). These low titres were sufficient to enhance infection in early hi-NPCs when cocultured (Figure 5.7B). At 72 h post-challenge, the pre-plated coculture condition showed a significant increase ($p = 0.0039$) compared to the hiPSC-MPh only

control; to similar levels than challenged early hi-NPCs ($p < 0.0001$) used as a positive control of productive ZIKV infection (Figure 5.7B).

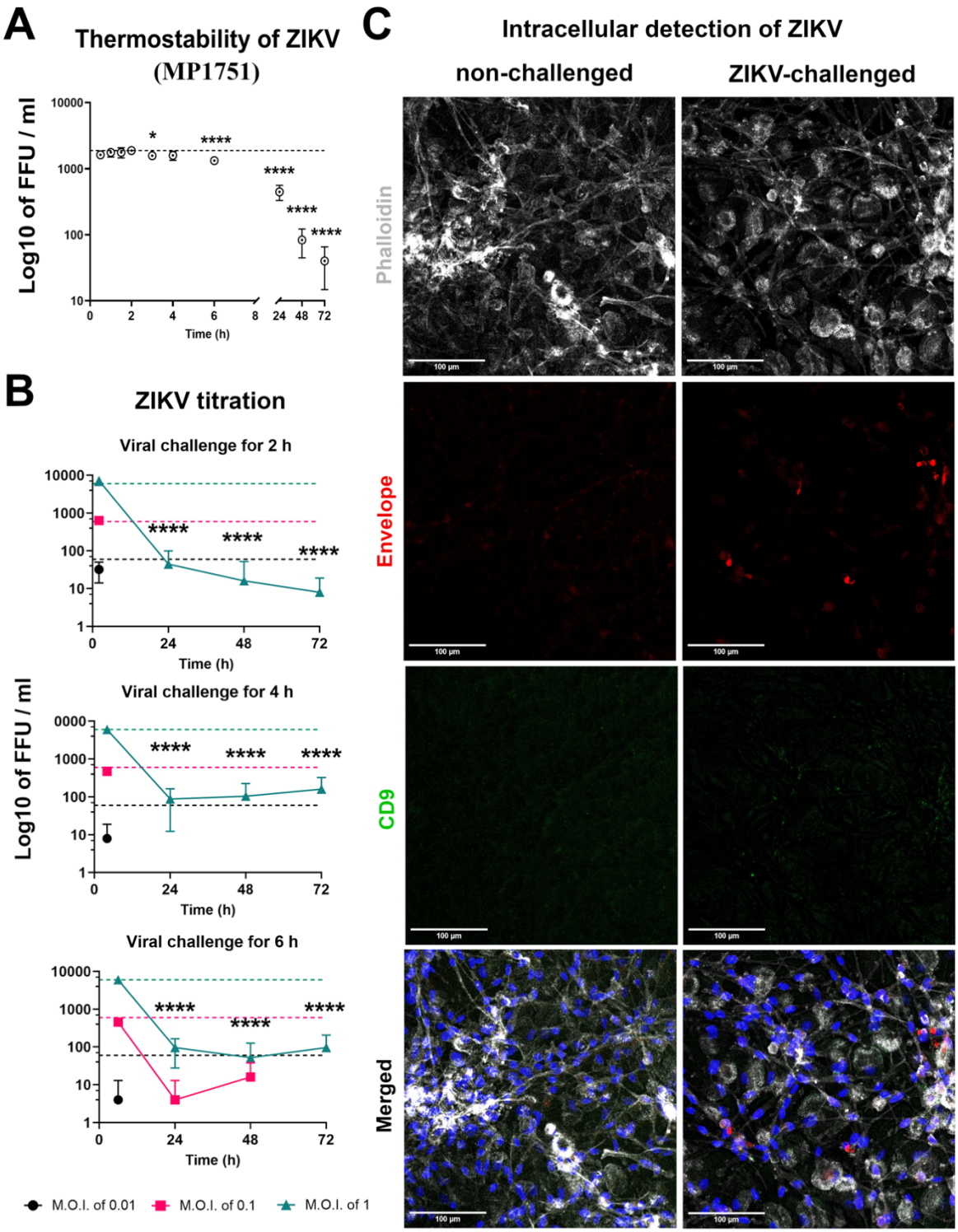


Figure 5.6. ZIKV productively infect tissue-resident-like macrophages at low levels

(A) Dot plot showing the thermostability of Zika virions (MP1751) at 37 °C over 72 h. Bars display mean ± SD. n = 1 experiment using three different viral aliquots of a known stock at each sampled time-point. Each aliquot was microtitrated in duplicate. Significance was calculated by a mixed-effects model with Dunnet's multiple comparisons test. (B) Line graphs displaying the microtitration of ZIKV from the supernatants of tissue-resident-like macrophages challenged with ZIKV for 4 h at different M.O.I. (0.01, 0.1 and, 1) Bars display mean ± SD. n = 1 experiment microtitrated in five replicates per time-point. Significance was calculated by mixed-effects model with Tukey's multiple comparisons test. (C) Confocal imaging of 5 µm Z-stack projections showing the presence of ZIKV-Envelope proteins (red), phalloidin cytoplasmic staining (grey) and, VCC represented by the staining of CD9 (green). Merged images displaying nuclear staining - DAPI (blue). Significance is shown when $^{*}p < 0.05$, $^{**}p < 0.01$, $^{***}p < 0.001$, $^{***}p < 0.0001$.

Macrophage fitness may underlie the susceptibility to ZIKV infection and mechanisms of indirect propagation in the developing brain. Assessment of the glycolytic rate in hiPSC-MPh challenged for 4 hours with ZIKV at an M.O.I. of 1 showed no changes in the glucose consumption and lactate release compared to non-challenged controls (Figure 5.8A). RSAD2, also known as viperin, an immune protein regulated by interferon- and non-interferon- signalling[160–163], decreases cytosolic glucose metabolism through the inhibition of NAD^+-dependent enzyme GAPDH[344]. Data from our group showed significantly higher rates of ZIKV replication ($p < 0.0001$) in RSAD2-CRISPR-KO macrophages compared to controls[E] (Figure 5.8B).

These results showed a primary role of cytosolic glucose metabolism during ZIKV replication. Thus, I tested a potential nutritional intervention using beta hydroxybutyrate (BHB), the main circulating ketone body that acts as an alternative fuel for the brain during starvation and glucose depletion[225] and, that decreases the cytosolic utilization of glucose[347,348].

[E] These results were comparable to those generated by a former post-doctoral researcher at James lab. Dr. Kourosh Ebrahimi generated the hiPSC-CRISPR-KO lines of RSAD2 I used for the differentiation of macrophages and ZIKV infection experiments.

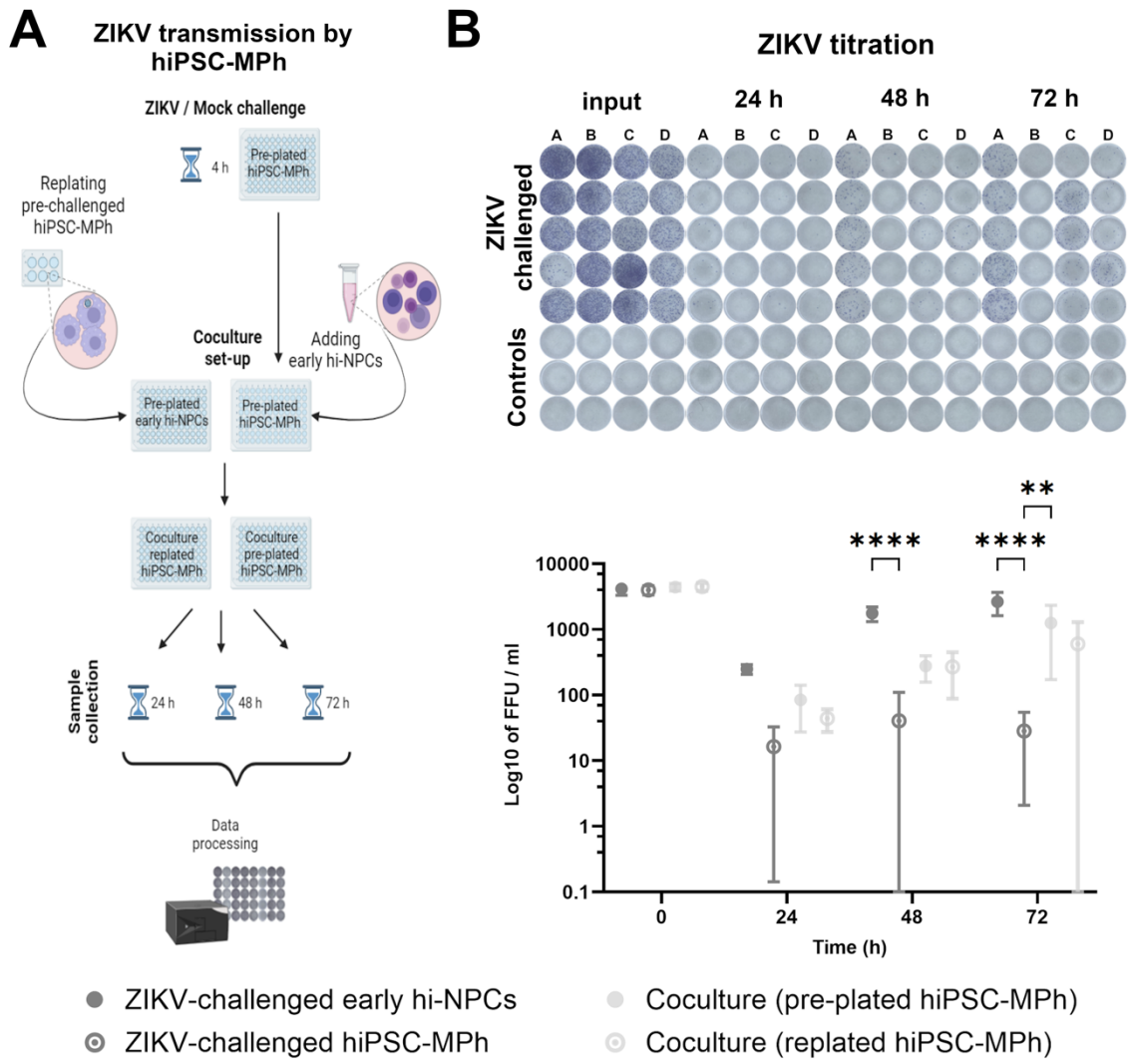


Figure 5.7. Macrophages disseminate ZIKV in the fetal brain
(A) Schematic representation of the modification of the 2D coculture set-up for disease-modelling of the ZIKV infection in the fetal brain by tissue-resident-like macrophages. Macrophages, mock or challenged for 4 h with media-containing ZIKV (M.O.I. of 1), were either lifted or maintained in the culture plates for coculture with early hi-NPCs. ZIKV was washed out before exposure to hi-NPCs. A positive control for ZIKV replication was conducted by challenging hi-NPCs to ZIKV for 4 h at 37 °C using an M.O.I. of 1. (B) Image showing the ZIKV foci forming units (FFU) per experimental condition at different time-points. Line graph showing the FFU quantification. Dot plot displaying mean ± SD. n = 1 coculture experiment conducted in five replicates. Significance was calculated by mixed-effects model with Tukey's multiple comparisons test. Significance is shown when $^{*}p < 0.05$, $^{**}p < 0.01$, $^{***}p < 0.001$, $^{***}p < 0.0001$.

To do this, I adapted U87 astrocytoma cells to serum-free conditions using an "*in house*" media culture that resembles the levels of nutrients of the adult CSF supplemented with BHB (Supplementary Figure 4A). U87 cells, permissive to ZIKV

infection[150], share similarities with early hi-NPCs in the cytosolic processing of glucose. However, their cancerous characteristics facilitated their adaptation to nutrients *in vitro*. There were no significant differences in the ZIKV production (Supplementary Figure 4B) and, analysis of BHB from cellular supernatants showed that U87 astrocytoma cells do not metabolized BHB (Supplementary Figure 4C).

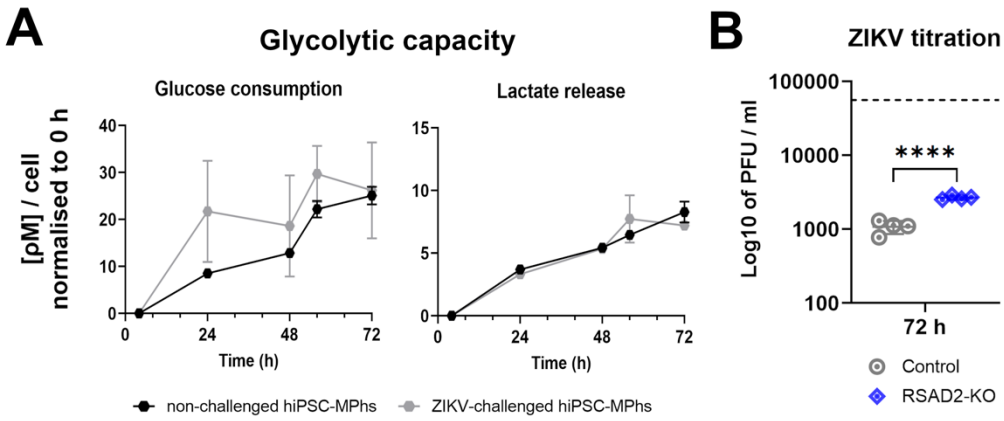


Figure 5.8. Cytosolic metabolism of glucose facilitates ZIKV infection in hiPSC-MPh

(A) Line graphs showing the glycolytic capacity of ZIKV-challenged and non-challenged tissue-resident-like macrophages. For challenge experiments, cells were incubated for 4 h at 37 °C with media-containing ZIKV at an M.O.I. of 1. ZIKV Bars display mean ± SD. n = 1 experiment using two donors' cell lines each measured in duplicate. Significance was calculated by mixed-effects model with Šidák's multiple comparisons test. (B) Dot plot showing the ZIKV titres by plaque assay from supernatants of controls and RSAD2-CRISPR-KO tissue-resident-like macrophages challenged with ZIKV for 72 h at an M.O.I. of 0.05. Bars displaying mean ± SD. n = 4 independent experiments using a single donor cell line per cell type each analyzed in triplicates. Significance was calculated by unpaired t-test with Welch's correction. Significance is shown when $^{*}p < 0.05$, $^{**}p < 0.01$, $^{***}p < 0.001$, $^{***}p < 0.0001$.

5.6 DISCUSSION

5.6.1 *In vitro* modelling of the developing early fetal brain

Current 2D coculture models of the brain do not integrate cells with the characteristics of those present during the embryonic development[54,349,350]. Previous results from our group highlight the importance of *in vitro* culture of fetal-like macrophages using a serum-free defined-source media[173]. Thus, to study ZIKV pathogenesis in the context of the infection of the early fetal brain, I first attempted to differentiate hi-NPCs in a culture media of similar composition.

Current protocols for the differentiation of hi-NPCs require the use of non-defined commercial culture media supplements, even those that study neuronal behaviour in physiological-like culture media[351]. Herein, I showed, for the first time, the efficient differentiation of hi-NCPs using a non-physiological defined-source media. These cells shared similar physiological and anatomical features to those cultured in N2:B27 commercial neuronal media. However, increased survival of early hi-NPCs and a reduction in viability post-thawing of late hi-NPCs compared to those cultured in N2:B27 may suggest that the defined-source culture media supports the differentiation of cells with immature phenotypes. To produce late hi-NPCs the replating of single-cell suspensions is required. hi-NPCs cultured in the defined-source culture media showed greater adherence to those in N2:B27. Thus, the loss of viability post-thawing of late hi-NPCs in the defined-source culture media may potentially be due to stress during the detachment process before freezing. Results from other *in vitro* neuronal systems have showed the requirement of supplements for optimal cellular survival[352,353]. Thus, these may be needed for late hi-NPCs differentiated in a defined-source culture.

Metabolic measurements in these cells showed a significantly lower glycolytic rate in early hi-NPCs, at early time-points post-plating, compared to N2:B27 cultured early hi-NPCs. This may involve a lower glycolytic enzymatic machinery or longer times, post-plating, for the activation of the main metabolic pathway in early hi-NPCs. Moreover, significantly increased long-term glucose consumption but no differences in lactate release in defined-source cultured hi-NPC subtypes may suggest that these cells require cytosolic glucose metabolism for other cellular processes than energy production by glycolysis.

The differentiation of early neuronal precursor cells using a defined-source culture media supported the generation of 3D cortical brain organoids that contained positive markers for neuronal and non-neuronal cells, similar to those produced by the conventional protocol[209,210]. Thus, confirming the correct *in vitro* differentiation of neuronal precursors.

Current models of the early fetal brain are based on 3D systems. These systems show large variability potentially due to differences in intrinsically developed and/or survival of externally cocultured microglia cells[354–356]. Thus, the coculture of early hi-NPCs and fetal-like macrophages may signify an improvement over current 3D models as it will facilitate the study of microglia-neuronal progenitor interactions using controlled cell-to-cell ratios. In addition, the development of the coculture in a serum-free defined-source culture media may reveal novel immune responses when stressing the system with neurotropic pathogens such as ZIKV. I showed that early hi-NPCs and fetal-like macrophages differentiated in a defined-source media would coexist under different coculture conditions. Reports showing the presence of microglia cells alter the definitive differentiation of neuronal progenitors[355,357,358]. This agrees with the findings of low levels of neuronal progenitors and higher levels

of immature astrocytes. However, this needs further repeats for reproducibility purposes.

5.6.2 Brain populating macrophages as a route for ZIKV dissemination in the early fetal brain

To study ZIKV infection in hiPSC-MPhs, the concentration of the virus and the length of exposure may be of relevance. The thermostability of ZIKV has been showed by others to decay after ~5 hours at 37 °C[261–263]. These findings agree with our thermostability data, calculated by FFU assay, showing a sustained decay after 6 h. Exposure of macrophages to ZIKV virions at 4 h and 6 h showed, mainly at an M.O.I. of 1, low levels of viral release over 72 h, this correlates with the low rates of ZIKV infection in hiPSC-MPhs detected by immunostaining of Env +ve cells. When exposing hiPSC-MPh to low M.O.I. there was almost to no output ZIKV. Although these results contradict those in the literature showing high infection rates in human adult microglia and both, kidney and testis macrophages[154,260,261], they agree with the findings from human placental macrophages, fetal microglia, and monocyte-derived macrophages[259,262,263].

Different than our approach using an early passage pathogenic ZIKV strain with low number of mutations, the challenges of ZIKV to macrophages have been done using pathogenic Asian lineage variants[359]. Due to similarities in the incubation times and temperature, differences in the macrophage susceptibility to ZIKV infection are likely to be due to *in vitro* artefacts potentially causing macrophage polarization and/or to the intrinsic differences between types of macrophages.

As a route of maternal-fetal ZIKV transmission, I tested whether the low levels of infection in hiPSC-MPh may be sufficient to disseminate ZIKV in early hi-NPCs. The results from two different coculture approaches showed that ZIKV-infected

macrophages promote the infection of early hi-NPCs. ZIKV growth in the coculture of pre-plated macrophages increases significantly compared to those levels of the directly infected early hi-NPCs. The coculture of replated macrophages showed similar results, yet to a lesser extent.

ZIKV replication kinetics suggest a release of newly formed virions at ~24 h post-challenge[360]. Thus, exponential viral growth observed in the cocultures at 48 and 72 h mainly corresponded to newly formed particles released by early hi-NPCs infected upon virion release from macrophages. In addition, the kinetics of ZIKV and the route of exposure may explain the differences in the titrations between early hi-NPCs and the coculture conditions. Overall, these findings support the growing consensus, derived from studies using human monocyte-derived macrophages[361] and microglia-like cells[362] that the route of ZIKV infection in the early fetal brain is via migratory microglia precursors. However, more repeats are needed to ensure the reliability of these results.

5.6.3 The role of glucose metabolism and immunity during ZIKV infection of tissue-resident-like macrophages

The ability of different types of macrophages to reprogram glycolysis by immune signalling[157,158,343] may underlie mechanisms to resistance to ZIKV infections[261–263]. The metabolism of glucose may also be dysregulated in macrophages during ZIKV infection with evidence of these alterations been exclusively reported at the transcriptional level[154]. Here, I showed no alterations in the glycolytic capacity between ZIKV-challenged and non-challenged hiPSC-MPh. This may correspond to the analysis of the extracellular glycolytic capacity based on the extracellular glucose consumption and lactate release of the entire ZIKV-challenged population from which only a small percentage was infected.

The native immune responses of macrophages combat viral infections and promote cell survival[160,161,163]. A greater ZIKV release from challenged RSAD2-CRISPR-KO macrophages, compared to wild-type controls, potentially suggest a more severe impact in the dissemination of virions in the early brain. To this, the evaluation of viral entry and cell survival in these KO cells should be done. Immune-metabolic interplay mediated by RSAD2 may also require further exploration as it will potentially reveal metabolic controls required for efficient ZIKV replication and/or to promote cell survival. This may be transferable to high susceptible cells, such as neuronal progenitors, underlying therapeutic potentials.

Nutritional therapies may correct some of the outcomes in disorders caused by deprivation/exacerbation of the cellular glycolytic capacity[36,348]. Thus, I tested whether ketone bodies, a known substrate for the brain and capable of being preferentially metabolized over glucose by some brain cells[36], may impact the replication of ZIKV. As adaptation of hi-NPCs to physiological-like media culture imposes several challenges, I used U87 astrocytoma cells. The cancerous nature of these cells suggests them having similar characteristics to early hi-NPCs. However, the assessment of ketone bodies for therapeutic potential for ZIKV infection was inconclusive as the U87 astrocytoma cells failed to metabolize the most blood-circulating ketone body (β-HB). This is in agreement with findings reported elsewhere in other types of cancerous cells[363]. Thus, further investigation in the role of cytosolic glucose metabolism for nutritional therapeutics in ZIKV infection may require the adaptation of relevant cell types to *in vitro* physiological-like culture conditions and/or the use of glucose analogues that block glycolysis such as 2-Deoxy-D-glucose.

5.7 CONCLUSION

A defined-source culture medium supports the 2D differentiation of early hi-NPCs, yet more investigation is required to achieve an efficient survival post-thawing of late hi-NPCs. Moreover, the similarities between 3D cortical brain organoids produced under defined compared to non-defined culture media may suggest a step forward in the *in vitro* production of neuronal precursors. In addition, these cells facilitated the coculture with yolk-sac-like macrophages (hiPSC-MPh) under defined media culture which does not contain immunosuppressants for the study of ZIKV infection and dissemination.

ZIKV productively infects hiPSC-MPh but at low levels, potentially unveiling strong mechanisms to prevent ZIKV infection. Nevertheless, these low levels were sufficient to enhance infection in early hi-NPCs suggesting yolk-sac macrophages may be a route of ZIKV infection in the early fetal brain.

Furthermore, as this research hypothesises that differential dysregulations of energy metabolism induced by ZIKV may underpin the distinct outcomes across different trimesters of pregnancy, I investigated the importance of cytosolic glucose metabolism in ZIKV-challenged macrophages. No significant changes in the glycolytic capacity were estimated from extracellular measurements potentially due to low levels of infection obtained over 72 h. However, ZIKV infectivity was significantly increased in immunocompromised RSAD2-CRISPR-KO hiPSC-MPh. These cells are characterized by lacking the inhibition of NAD^+ dependent enzymes such as GAPDH which will in turn facilitate an increased glycolysis upon interferon signalling during pathogen recognition. Thus, the study of glucose metabolism in ZIKV-infected hiPSC-MPh may highlight key elements that prevent ZIKV replication providing potential therapeutics.

Altogether, these results may suggest the importance of immune regulation of cellular metabolism to prevent ZIKV infection in macrophages and its role in the dissemination in the early fetal brain (Figure 5.9). However, due to the disruptions caused by the COVID-19 pandemic, there was not sufficient time to complete this research. Thus, this chapter would benefit from several experimental repeats to corroborate the data on infection and dissemination of ZIKV by hiPSC-MPh. Also, the use of different techniques may be required to measure glucose metabolism exclusively in infected cells as, different than neuronal progenitors, the glucose consumption rate of these cells is significantly lower. Thus, extracellular measurements of the pool of cells challenged with ZIKV may not be sufficient to quantify potential differences in energy metabolism, particularly when exhibiting low levels of infection. Lastly, the study of the glycolytic capacity in RSAD2-CRISPR-KO hiPSC-MPh and drug inhibition of GAPDH in wild-type hiPSC-MPh may be required to elucidate the role of glycolysis in supporting sustained ZIKV replication.

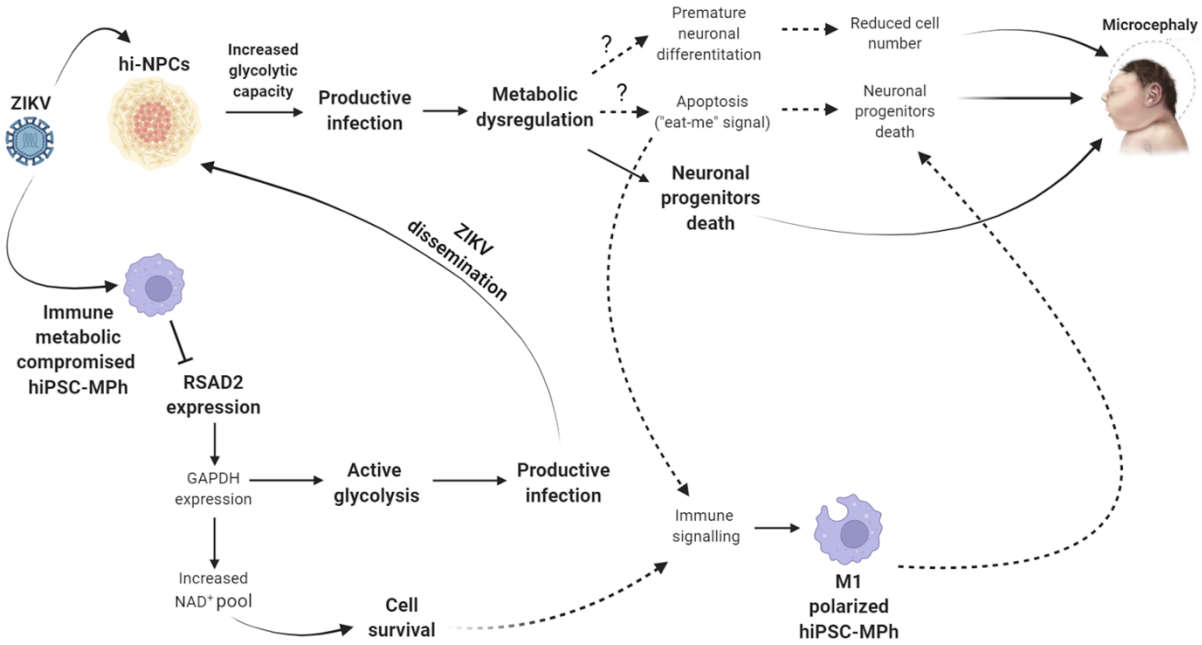


Figure 5.9. Immune-metabolic control in macrophages may highlight mechanisms of ZIKV dissemination causing microcephaly in new-borns
Schematic representation of ZIKV-mediated microcephaly considering the interplay between yolk-sac macrophages (hiPSC-MPh) and neuronal progenitor cells (hi-NPCs) and, the potential role of RSAD2-mediated immune metabolic control in hiPSC-MPh as a route of ZIKV entry into the developing early fetal brain. Dotted lines highlighting potential secondary mechanisms derived from hiPSC-MPh activation and hi-NPCs responses to ZIKV infection contributing to the detrimental phenotypes in new-borns infected during the first trimester of pregnancy.

6. GENERAL DISCUSSION

The gradual activation of mitochondrial metabolism in neuronal cells and the utilization of cytosolic metabolism by non-neuronal cells is not just important for energetic balance[27,28,224,225,240,29,30,37,42,45,49,222,223] but for cellular differentiation during fetal brain development[43,50,53,57,221,231,233,240]. During early stages of pregnancy, ZIKV infection results in either abortions or detrimental pathologies in new-borns such as microcephaly and eye abnormalities[22,67,82,86,91,95,101,264,265]. These features, greatly reported in regions of poverty and malnutrition, highlight a potential role of nutrient metabolism in the pathogenesis of ZIKV[23,268].

There are no current interventions to either prevent ZIKV infection nor to reduce its severe fetal outcomes[66,309,364]. Therapeutics primarily target the viral entry in permissive cells yet, as several receptors may mediate ZIKV entry[148–153,271], blocking ZIKV infection remains a difficult task. Thus, nutritional therapeutics may overcome this issue and provide a platform to ameliorate the outcomes of ZIKV infection by the alteration of metabolites needed for viral assembly.

As there are limited *in vitro* human studies of fetal brain development[70,211,213,220,333], ZIKV research that highlights metabolic requirements[71,242,244,260,282,300,305] that can be targeted by nutritional interventions[36,74] may need validation using characterized relevant cell models, such as human iPSC-derived cells.

This thesis consisted of an *in vitro* investigation of the main metabolic pathways required for optimal ZIKV replication which may underpin cell-type specific energy dysregulations that contribute to the differences in congenital zika syndrome observed over the course of pregnancy[77]. I aimed to achieve this by investigating

potential dysregulations across different metabolic pathways during ZIKV replication in relevant human induced pluripotent stem cell (hiPSC) models of the cells present at early stages of fetal brain development (radial-glial-like progenitors, intermediate progenitors, and yolk-sac-like macrophages). In addition, after revealing a potential regulatory metabolite among the commonly dysregulated energetic pathway in these different cell types, I aimed to test compounds for potential nutritional therapeutics by the activation of secondary energy metabolic pathways which may not provide the by-products required for optimal ZIKV replication but promote cell survival. To do this, the present research was designed as follows:

1. Characterization of hiPSC-derived neuronal progenitors (hi-NPCs) and subtypes produced during cortical differentiation
2. Analysis of the main metabolic pathways utilised by hi-NPCs that can be hijacked by ZIKV for its optimal replication
3. Study of the susceptibility of yolk-sac-like macrophages (hiPSC-MPh) to ZIKV productive infection and their capacity to dissemination virions into the developing fetal brain
4. Investigating the role of a commonly altered metabolic pathway in ZIKV-infected hi-NPCs in the susceptibility of hiPSC-MPh to ZIKV infection
5. Determining the therapeutic potential of nutritional intervention by the exposure of cellular cultures to metabolites that diminish/block the availability of ZIKV-required metabolic intermediates

6.1 *In vitro* hiPSC neuronal differentiation produce subtypes of cortical neuronal progenitors

Fetal brain development requires sensitive and precise regulation of cellular division and differentiation[194,237,321,322]. The gradual activation of certain metabolic pathways involving an increased mitochondrial metabolism may constitute a transition during neuronal differentiation[53,231,233]. This highlights a potential role of energy metabolism in the distinction of brain cell types and subtypes[29,54,55,185,233].

In vitro differentiation of adult-like neurons and astrocytes from hiPSC requires the maturation of neuronal progenitors[207,220,351]. However, as maturation processes involve, for example, the use of inhibitors of neuronal progenitors such as DAPT[174,205,232], the characterization of these progenitors is limited. The validation of the differentiation of neuronal progenitors from hiPSC (hi-NPCs), among different protocols, includes the detection of neuronal and non-neuronal markers[174,205,232]. This may not be sufficient to distinguish neuronal progenitor subtypes and brain cell types. To investigate this further, chapter 3 characterized the preferred metabolic pathways in hi-NPCs at different stages during differentiation aiming to distinguish subtypes of neuronal progenitors; expected to be produced by the different times under culture. The differentiation of hi-NPCs displayed, at different times under culture, two morphologically distinct groups. At early stages, in agreement with 2D and 3D cultures, cultured hi-NPCs exhibit the presence of neuronal progenitors within rosette-like structures. At later stages, the appearance of neuronal-like projections may indicate neuronal maturation[184,210,211,218,220,318]. The latter was potentially induced by the steps of cellular dissociation and low-density during re-plating. A first approach to characterize these cells by the presence/absence of

neuronal markers showed similar expression profiles. To assess whether this may be due to *in vitro* contamination with non-neuronal and/or undifferentiated cells due to the different lengths of time under culture, I identified the percentages of neuronal and non-neuronal cells within each culture. As the similarities recorded between stages of differentiation of hi-NPCs did not correlate with their distinct morphology, I then studied their energy metabolism. Chapter 3 showed differences in the rate of utilization of the main metabolic pathways in early neuronal progenitors. The higher cytosolic metabolism of glucose and lower mitochondrial fatty acid oxidation, compared to data shown by others[185,227,233], suggested that early hi-NPCs are more proliferative and less differentiated than late hi-NPCs.

Potential maturation of hi-NPCs during their time under culture may alter their subtyping. Thus, chapter 3 lastly assessed the long-term physiology of these cells and showed a clear difference in the rate of glucose consumption and lactate release yet, not in the overall glycolytic capacity, suggesting that subtype differences over the course of three days may be related to different cell cycle lengths.

The main findings of chapter 3 can be summarized as:

1. The 2D hiPSC cortical neuronal differentiation protocol produces neuronal progenitors (hi-NPCs) that differ morphologically and physiologically.
2. At early stages, the hi-NPCs utilize cytosolic glucose metabolism as their main energy source suggesting they are less differentiated (radial-glia-like progenitors)
3. Differences in the rate of lactate glycolysis between hi-NPC subtypes (metabolic distinction) was shown over three days

4. *In vitro* energy metabolism facilitates the subtyping of hi-NPCs before changes in protein expression profiles are detected

6.2 Increased glycolytic capacity is imposed during ZIKV optimal replication

The pathogenesis of ZIKV became of worldwide interest due the fetal neurotropism observed during outbreaks in Brazil in 2016[16,82,91,97,362], followed by an extensive distribution of the virus across the Americas[91,95,264,269,362]. ZIKV-induced damage to the fetal brain significantly decreases when maternal infection occurs during late pregnancy[36,78,256,264]. The cells present during embryonic and early fetal brain (neuronal progenitors and yolk-sac macrophages) use specific energy metabolic pathways during development[36,43,56,194,237,240]. Thus, the energetic requirements imposed during viral replication potentially underlie the severe outcomes of ZIKV infection during early pregnancy[36,115,280]. To investigate this further, chapter 4 examined the susceptibility of metabolically distinct hi-NPC subtypes to ZIKV productive infection and the potential alterations on their main energy metabolic pathways (lactate glycolysis, lipid beta-oxidation and, lipid biosynthesis) as a consequence of the ZIKV replication.

hi-NPC subtypes showed differences in the assembly of ZIKV virions. Early hi-NPCs had lower assembly rates at one time-point during replication that may be correlated to availably of intracellular pool due to activated mechanisms to promote cell survival. During infection, intracellular accumulation of ZIKV transcripts was significantly larger in late hi-NPCs. This failed to prove that potential detrimental consequences of ZIKV infection during the first trimester is due to a distinct ZIKV neurotropism and dysregulation in early, but not late, neuronal progenitors.

However, similarities in cell death between progenitor subtypes may highlight those detrimental fetal consequences that may be an artefact of a lower pool of radial-glial-like progenitors capable of producing intermediate progenitors and further neuronal lineages. To this, transcriptional profiling of infected early hi-NPCs may be necessary to examine whether differentiation pathways are dysregulated. Moreover, significantly greater release of ZIKV virions by intermediate progenitors (late hi-NPCs) may be responsible for the viral dissemination to other brain cell types during later stages of brain development. In addition, chapter 4 showed a significant increase in the glycolytic capacity in infected late hi-NPCs compared to early hi-NPCs. I showed in chapter 3 that late hi-NPCs are characterized by mitochondrial utilization of glucose which potentially highlights the capacity of ZIKV to reprogram host cellular metabolism. The metabolic profile of late hi-NPCs suggests that a potentially increased intracellular pool of metabolites in infected cells, produced via increased glycolysis, may contain metabolites less required for cell survival that can be available for viral replication. This may correlate with the greater assembly of ZIKV virions and could in turn reveal potential nutritional therapeutics.

The dysregulation of cellular metabolism by ZIKV involves a global change in cellular transcription and expression[145,154,305,308]. To this end, chapter 4 revealed the upregulation of genes involved in energy metabolism with differences between hi-NPC subtypes. The transcriptional dysregulation of lipid metabolism was exclusively translated into the accumulation of lipid droplets, at early time points during infection, in early hi-NPCs. Despite these changes, chapter 4 found no major alterations in mitochondrial homeostasis in either hi-NPC subtype.

The main findings of chapter 4 can be summarized as:

1. The assembly and release of ZIKV differs between hi-NPC subtypes
2. ZIKV reprograms the transcriptional profile of energy metabolism in hi-NPC subtypes
3. A common metabolic dysregulation across ZIKV-infected hi-NPC subtypes is the significant increase in the glycolytic capacity
4. ZIKV infection promotes a greater increment of the glycolytic capacity in neuronal progenitors with basal lower rates of lactate glycolysis (late hi-NPCs)
5. Early stages of ZIKV infection dysregulates the metabolism of lipid droplets in radial-glia-like hi-NPCs (early hi-NPCs) but not in intermediate-like progenitors (late hi-NPCs)
6. Mitochondrial dysregulation in ZIKV-infected hi-NPCs reflect subtype-specific and time-point-specific changes that are not sustained during infection

6.3 ZIKV dissemination in the fetal brain is an indirect effect of macrophage immune-metabolic control of glycolysis

Yolk-sac derived macrophages populate the developing brain prior to neurogenesis; during the transition between embryonic and fetal life[131,323–325,327,334,357,358]. Once in the brain, these cells become the tissue-resident immune cells termed microglia and constitute the main defence against pathogens[323,329,330,334,362]. These cells may serve as a route of maternal-fetal transmission for ZIKV virus[36,73,77,78,95,97,262]. Thus, chapter 5 investigated the susceptibility of tissue-resident macrophages (hiPSC-MPh) to ZIKV infection and their contribution to viral dissemination to hi-NPCs.

In vitro research of fetal brain development require improvements including, yet not limited to, a) controlled microglia to neuronal progenitor ratios, not met in 3D organoid systems[209,211,355,356] and, b) cellular culture in physiologically relevant conditions. Chapter 5 showed for the first time the differentiation of hi-NPCs in a defined-source serum-free culture media condition. Although hyperglycaemic and not physiological, this media reflected an improvement in fetal disease modelling as it facilitated the interaction of hi-NPCs and hiPSC-MPh in the absence of immune modulators commonly included in commercial culture media recipes. The efficient production of proliferative radial-glia-like cells (early hi-NPCs) was validated in 2D and 3D cultures.

Chapter 5 showed that a low number of hiPSC-MPh are susceptible to ZIKV productive infection and that this is sufficient to disseminate virions to early hi-NPCs when cocultured. The transfer of virions from infected hiPSC-MPh to early hi-NPCs highlights a route for maternal-fetal transmission.

In addition to ZIKV transmission, Chapter 5 investigated whether the common energy metabolic pathway altered in neuronal progenitor subtypes (glycolysis) contributes to the susceptibility of macrophages to ZIKV productive infection. To do this, chapter 5 showed the estimation of the glycolytic capacity in ZIKV-challenged hiPSC-MPh and assessed the replication rates of ZIKV in an immune-metabolic KO cell line. However, validation of this work requires further repeats that were not done due to the disruption caused by the COVID-19 pandemic.

The glycolytic capacity was not increased in challenged hiPSC-MPh yet, as there were low rates of infection, any potential changes in infected cells may have been masked by the overall levels of glucose utilization by non-infected cells. Thus, to better study the role of glycolysis in immune cells of the early fetal brain chapter 5

showed ZIKV infection rates using immunocompromised hiPSC-MPh. RSAD2 regulates the glycolytic capacity by diminishing glycolysis through the inhibition of the NAD^+-dependent enzyme GAPDH[160,162]. Chapter 5 showed that RSAD2-KO hiPSC-MPh are significantly more susceptible to ZIKV productive infection than wild-type hiPSC-MPh. The inhibition of GAPDH by RSAD2 results in the intracellular accumulation of G3P and supresses the production of downstream glycolytic by-products which may be necessary for the correct assembly of ZIKV yet, this needs further investigation in ZIKV-infected RSAD2-KO hiPSC-MPh.

Altogether, data on potential metabolic alterations of glycolysis from chapter 4 and chapter 5, suggest that manipulation of upstream glycolysis may have therapeutic potentials to reduce ZIKV dissemination and infection. Thus, chapter 5 briefly investigated the therapeutic potential of ketone bodies as their metabolism decreases the cytosolic utilization of glucose[114,347,348]. To do this, supplementation of culture media with ketone bodies such as beta hydroxybutyrate (β-HB) is required under physiological-like levels to avoid media acidification and cell toxicity by the utilization of larger quantities of ester β-HB. As adaptation of relevant hiPSC models to low nutrient cultures, I cultured U87 astrocytoma cells in serum-free conditions using an "*in house*" media that resembled the levels of nutrients of those measured in the adult CSF and supplemented it with β-HB. However, no conclusions were drawn due to β-HB was not metabolized by U87 astrocytoma cells. Thus, further experiments such as: a) the use of other cellular models that metabolize β-HB, b) other routes of administration of β-HB in cell cultures and/or, c) other compounds that modulate glycolysis are required.

The main findings of chapter 5 can be summarized as:

1. Early hi-NPCs are efficiently differentiated in a defined-source serum-free culture media that facilitates their culture with hiPSC-MPh or their precursors to model the fetal brain in 2D
2. hiPSC-MPh are susceptible, at low levels, to ZIKV productive infection which is sufficient to disseminate virions to early hi-NPCs
3. Extracellular estimation of the glycolytic capacity does not show differences between ZIKV-challenged and control hiPSC-MPh potentially due to low levels of infection
4. RSAD2-KO hiPSC-MPh are significantly more susceptible to ZIKV infection than wild-type hiPSC-MPh
5. U87 astrocytoma cells do not metabolize the ketone body Beta-hydroxybutyrate (β-HB)

6.4 Limitations of the current research

The research on ZIKV presented in this thesis exhibits three primary limitations, one of which, the lack of experimental repeats for the investigation of ZIKV infection in hiPSC-MPh, is related to the interruption of this work due to the COVID-19 pandemic. To study the role of cell-type specific metabolic modulation in the susceptibility to ZIKV infection and how this may underpin the different neurodevelopmental consequences observed during each trimester of pregnancy, the use of relevant *in vitro* cell models are required.

The second limitation obeys to the nature of *in vitro* studies which may propose mechanisms of infection and transmission of ZIKV that, despite the use of relevant cell models, may reflect behaviours not observed *in vivo*. This may be related to the

lack of interactions such as systemic flux of nutrients, lack of cell-to-cell crosstalk and/or, the lack of immune signalling after recognition of pathogens compared. In addition, *in vitro* cell culture using non-physiological conditions may not reflect normal cellular biology that further complicate the study of cellular metabolism due to hyperglycaemic culture media that may reprogram cells towards glucose utilization, for example. However, in the case of ZIKV pathology, *in vitro* research may currently be of greater disease relevance as the most common *in vivo* model of the viral pathogenesis comprises immunosuppressed rodents[36,75,102,268,362]. Moreover, the 2D *in vitro* research presented in this thesis highlighted mechanisms of metabolic alterations that are required for ZIKV replication. Thus, this study can be complemented by using less detrimental neurotropic viruses (e.g., West Nile virus) that may potentially reveal the effects of cellular metabolism in congenital Zika syndrome. Another complimentary research can include the use of viruses that highly dysregulate cellular metabolism of non-brain cells (e.g., Dengue virus) to highlight potential similarities that may explain cell exhaustion and death mechanisms. Also, investigating the susceptibility of other brain cell types may be crucial to elucidate whether neuronal progenitors display a larger susceptibility to ZIKV infection that may be responsible for the congenital Zika syndrome whilst also explaining the notorious outcomes (microcephalic brains) when infection occurs during the first trimester of pregnancy, when neuronal progenitors constitute most brain cells. The third limitation of this study comprises the potential complications in translational research. Due to the lack of understanding in maternal-fetal transmission of nutrients[43,183] and energetics during intrauterine fetal brain development, metabolic therapeutics such as nutritional ketosis[47,240,348] may not

reflect similar findings in *in vivo* to those potentially observed in *in vitro* systems. This may be due to differential delivery of metabolites/compounds to the fetus.

General limitations on the methodology used to gather data in this thesis have been highlighted within each result chapter. These limitations, because of the work disruptions during the COVID-19 pandemic are summarised but are not limited to: a) tracing of neutral lipid and mitochondrial homeostasis by using faster yet less accurate techniques. This caused that the data reported in this thesis is based on areas of interest occupied by several of these organelles instead of specific area of organelles; b) broad study of neutral lipid and mitochondrial homeostasis. Although this allowed for a screening on the potential alterations suffered during ZIKV infection, it is not enough to elucidate targets for potential therapeutics and; c) results generated by technical repeats instead of biological repeats. This is due to the lack of time required to differentiate cell types from different donors.

6.5 Conclusion and future work

The ZIKV work presented in this thesis highlighted mechanisms of metabolic hijacking by ZIKV using relevant cellular models of fetal brain development. I showed that cytosolic glucose metabolism plays a major role for optimal ZIKV replication. This result is supported by current literature mainly generated using less-relevant cell types. Moreover, the results from this thesis supported a potential mechanism of ZIKV entry into the developing brain, so far exclusively shown by another group. Lastly, I showed data that suggests that blockade of upstream glycolysis at the level of GAPDH may have implications in reducing ZIKV replication. Thus, highlighting a potential means for nutritional interventions and therapeutics.

Future work to continue the research presented in this thesis may involve a larger validation of the neuronal progenitor subtypes by metabolomic characterization.

Also, the main findings on metabolic alterations in hi-NPCs during ZIKV infection can be explored further by using large screening techniques such as transcriptomics. This may be able to not only elucidate more complete energy metabolic pathways but to infer whether early and late hi-NPCs may be reprogramed to undergo distinct differentiation pathways that may correlate with the lack of progenitors available for fetal cortical expansion when infection occurs during the first trimester. Also, the measurement of key enzymes involved in energy metabolism may suggest a complimentary approach to support the data showed in this thesis. Moreover, measurements such as oxidative phosphorylation and respiration capacity may support the current data obtained on mitochondrial homeostasis. Similarly, the study of the potential dysregulation of lipid subtypes in ZIKV-infected hi-NPCs, may strengthen the findings on lipid droplets by potentially revealing specific lipids necessary for the optimal replication of ZIKV.

To better investigate the importance of glycolysis for ZIKV replication, the metabolic tracing exclusively in ZIKV-infected hiPSC-MPh, as done with lipid droplets and mitochondrial membrane potential in hi-NPCs, is necessary. This metabolic tracing is necessary due to the potential low sensitivity of extracellular estimation of the glycolytic capacity when rescuing low levels of ZIKV infection as in hiPSC-MPh. Lastly, as RSAD2-KO potentially revealed glycolytic targets to supress ZIKV replication, the use of drug inhibitors targeting GAPDH and upper glycolysis may elucidate whether metabolic reprogramming possesses therapeutic potential by the decrease of ZIKV replication or if the resistance to ZIKV infection observed in hiPSC-MPh is solely related to larger native immune responses compared to hi-NPCs.

In the following, I introduce the research I conducted on SARS-CoV-2 as the result of the disruption to my ZIKV work during the COVID-19 pandemic.

7. MACROPHAGES PHAGOCYTIZE SARS-CoV-2 VIRIONS AND DECREASE VIRAL REPLICATION IN INFECTED *IN VITRO* TISSUE MODELS

7.1 ABSTRACT

Tissue-resident macrophages constitute the first line of defence against invading pathogens among different tissues. However, in the lung, in response to detrimental insults (e.g., pollution and pathogens) infiltrating peripheral macrophages (MDM) take over this function and are responsible for triggering inflammatory processes. Thus, MDM play the largest immune role during SARS-CoV-2 infection in the lung yet, it remains unclear whether SARS-CoV-2 can productively infect these cells, as well as lung-resident macrophages, and contribute to the pathogenesis of COVID-19. Here, I show, by viral microtitration, that exposure of ACE2-expressing MDM led to no detectable productive infection. Immunofluorescence imaging (IF) and transmission electron microscopy (TEM) showed that internalized SARS-CoV-2 virions by MDM reside within vesicular compartments. The modest colocalization between SARS-CoV-2 N protein and Rab5 +ve compartments, over 6 h of viral challenge, suggested these compartments were early phagosomes. This was further supported by the lack of colocalization between SARS-CoV-2 N protein and CD81, a marker of vesicle-containing compartments (VCC). These results highlighted that MDM may phagocytize SARS-CoV-2 virions for degradation with

further implications for the viral pathogenesis. I then studied the potential susceptibility of MDM to SARS-CoV-2 indirect infection by their coculture with susceptible Vero CCL-81. The results from this coculture showed that macrophages reduced the replication kinetics of SARS-CoV-2 in Vero cells. To overcome potential recognition of the cancerous nature of Vero cells by MDM, I cocultured tissue-resident-like macrophages (hiPSC-MPh) with Vero cells. I showed that, like MDM, hiPSC-MPh may also phagocytize SARS-CoV-2 virions. This translated into a lack of infection but a delay in the viral replication kinetics when cocultured. Potential macrophage phagocytosis of SARS-CoV-2 virions assessed in a disease-relevant coculture model using hiPSC derived cardiomyocytes (hiPSC-CM) and hiPSC-MPh also showed a significant reduction in the viral output compared to the monoculture of hiPSC-CM. Overall, these results suggest that macrophages are not productively infected by SARS-CoV-2 and that phagolysosome degradation of SARS-CoV-2 may influence the course of the viral pathogenesis by, yet may not be limited to, the delay in the viral replication kinetics and the reduction of virus able to infect susceptible cells.

7.2 INTRODUCTION

Coronaviruses are a group of enveloped single-stranded positive RNA [(+)ssRNA] viruses known for causing from severe to life-threatening symptoms in humans[365]. In the past 20 years, newly emerged viruses of this group, with zoonotic origins, have caused events of global concerns: the severe acute respiratory syndrome coronavirus (SARS-CoV) and the Middle East respiratory syndrome coronavirus (MERS-CoV)[365]. A novel coronavirus, named severe acute respiratory syndrome coronavirus 2 (SARS-CoV-2) causes the ongoing coronavirus disease 2019 (COVID-19) pandemic[366].

The origins of this novel coronavirus remains unclear but genetic analysis suggests SARS-CoV-2 is also likely to be of zoonotic origins[367]. Respiratory droplets are the main form of transmission of coronaviruses. However, reports from early in the COVID-19 pandemic suggest that direct contact with fomites and body fluids containing infectious SARS-CoV-2 virions are also ways of transmission for this novel coronavirus[368,369].

SARS-CoV-2 infection and spread still imposes concerns due to the differences in the vaccine rollouts worldwide, waning of immunity against newly appearing variants and subvariants and, long-lasting natural and/or vaccine-mediated immunity[368]. Upon inhalation, SARS-CoV-2 virions exhibit tropism for the cells of the lower respiratory tract (alveolar type I and type II pneumocytes[370]) and, during sustained infection, virions spread across the body[371]. Although the pathology of the lung in COVID-19 patients exhibits distinct features compared to other viral-induced respiratory diseases[372]; its clinical manifestation includes common symptoms, observed in infections by other respiratory viruses, such as fever, dry cough, dyspnoea, chest pain, fatigue, and myalgia[373,374].

Different organs are susceptible to SARS-CoV-2 direct infection[371]. Among these, the lung, heart and kidney exhibit the largest damage and constitute the main cause of death in severe COVID-19 patients[375–377]. Cardiac injury, observed in ~40% of hospitalized patients, represents the second most relevant feature of the COVID-19 multi-organ failure[378–380]. *In vitro* studies using heart biopsies and human induced pluripotent stem cell derived cardiomyocytes (hiPSC-CM) show that SARS-CoV-2 productively infects cardiomyocytes and drives cellular damage. This damage is presented as cytotoxicity, myocarditis, and impaired electrical and mechanical function[381–383].

The expression of the cellular transmembrane receptor angiotensin-converting enzyme 2 (ACE2) is a common feature among the primary cells of the most susceptible organs[384,385]. ACE2 receptors have vital functions in the lung and the heart[386,387]. The main function of ACE2 is to downregulate the renin-angiotensin system (RAS)[386,388], responsible for the regulation of fluid and salt balance[389,390]. The regulation of RAS prevents ARDS, myocarditis and arrythmias[387]. However, in the context of respiratory infections the affinity of SARS-CoV and SARS-CoV-2 to ACE2 gives this receptor the main role for viral entry, infection and pathogenesis[388,391,392]. Subtle differences between the spike glycoprotein subunits S1 and S2 of the SARS-CoV-2 compared to SARS-CoV[393] underpin its higher affinity of binding to the membrane-bound region of the ACE2 receptor[394–396]. Thus, the relative abundance of ACE2 receptors may correlate with cellular susceptibility to viral entry and subsequent infection[397,398].

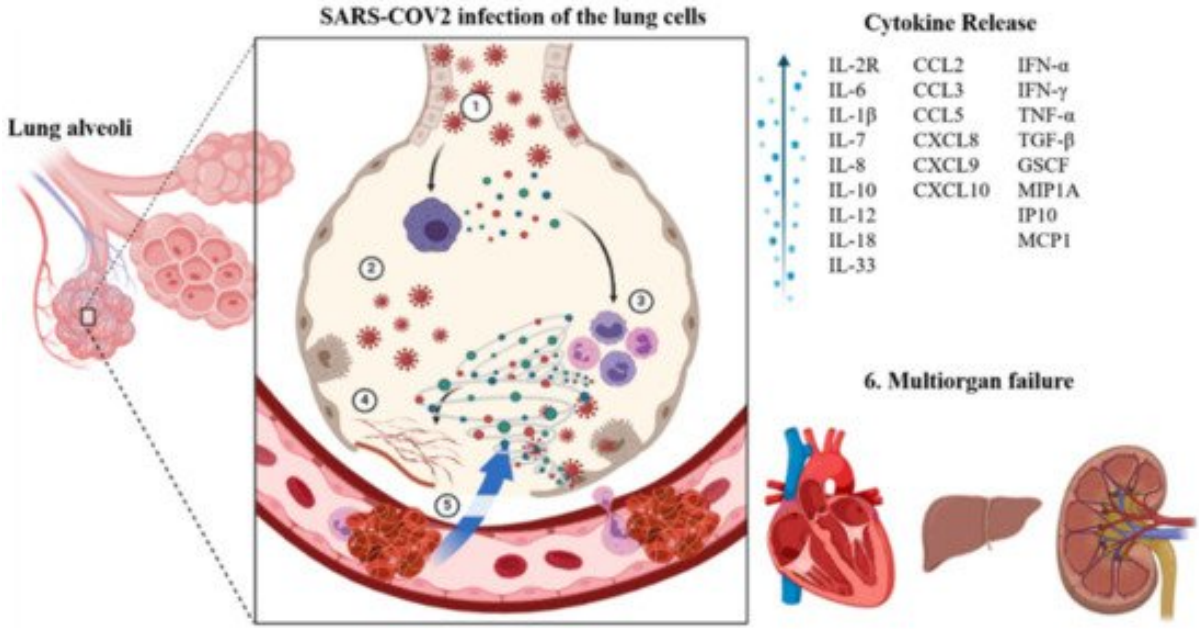


Figure 7.1. SARS-CoV-2 infection of lungs leading to cytokine storm resulting in multi-organ failure

① Lung cells infected by the coronavirus, ② Macrophages recognize the virus and release cytokines, ③ Cytokines attract additional immune cells, such as lymphocytes and monocytes, and they generate more cytokines, causing a storm-like cycle of inflammation that damages lung cells. ④ Damage can also occur because of fibrin production (clot formation) upon macrophage polarization towards tissue repair, ⑤ Blood vessels surrounding the lungs are weakened, allowing fluid to leak into the lung cavities, resulting in respiratory failure, ⑥ Due to the heightened coagulation state, blood that is meant to flow to other organs such as the heart, liver, and kidneys will be obstructed, causing these organs to fail and lead to multiorgan failure. Obtained from Bhalerao *et al.*, 2021[399].

Macrophages constitute the largest resident immune cells in every organ[400]. Although these phagocytes are known as such, their involvement in several processes turn them into essential cells for tissue homeostasis[400,401].

Yolk-sac derived tissue-resident macrophages constitute the immune cells of the lung[400,402]. These cells differentiate into two subpopulations, the alveolar macrophages (AM) and the interstitial macrophages (~30-40% of lung macrophages)[400,401,403], of which AM are the main responders to pathogens due to their higher relative abundance in both the airways and the alveolar space[404]. The

physiology of the lung, as the site for gas exchange, frequently exposes lung cells to pathogens that are not trapped by the mucociliary escalator of the airway epithelia[405]. Thus, AM require highly selective immune mechanisms to preserve tissue homeostasis[406,407]. The main function of AM is to phagocytize particles and the catabolism of surfactants to prevent the collapse of the lung whilst the interstitial macrophages are involved in the antigen-presentation and tissue remodelling and repair[371,400,408]. AM are weak antigen-presenting cells[409–411] that, as known inhibitors of the dendritic cell function[409–411], require the immediate cooperation of infiltrating peripheral macrophages to eliminate pathogens[404,412]. The hyperinflammatory status of invading macrophages and their exacerbated IL-6 release is thought to contribute to the depletion of peripheral NK cells in severe COVID-19 patients[370]. Increased tissue repair function of invading macrophages majorly contributes to the fibrosis in the infected lung[413]. Also, as observed in models of lung inflammation[414], a protective response of peripheral macrophages during SARS-CoV-2 infection involves the replacement of hyperreactive AM and interstitial macrophages[371]. Thus, peripheral macrophages, as a bridge between native and adaptive immunity in the lung, may share a major role with AM during SARS-CoV-2 infection[415–417].

During SARS-CoV-2 infection, the biology of these cells suggest that AM are classically activated (M1 - pro-inflammatory macrophages) whilst interstitial macrophages are alternatively activated (M2 – anti-inflammatory)[371]. The M1 macrophage recognition of SARS-CoV-2 virions triggers the invasion of peripheral immune cells whilst the M2 macrophages release anti-inflammatory cytokines[418]. The invasion of peripheral immune cells is a process that requires the release of proinflammatory signalling by M1 macrophages as well as the presentation of antigens to T cells[140]. This causes a feedback loop of proinflammatory signalling

that, in patients with severe COVID-19, involves pulmonary damage[370,419] and correlates with disease progression[371,420]. Thus, lung and other tissue damage may be due to the exacerbated release of proinflammatory cytokines known as COVID-19 cytokine storm (Figure 7.1). The cytokine storm is defined by increased levels of proinflammatory cytokines in serum, some of them being IL-1, IL-6, IL-12 and IFN- γ, and in plasma, IL-1β, IL-2 and TNF-α, among others[374,421]. Another consequence of the cytokine storm-mediated changes in the lung microenvironment during SARS-CoV-2 infection is COVID-19 pneumonia which accounts for ~5% of the mortality rate among patients[422,423]. This likely occurs by bacterial coinfection facilitated by the damage in the integrity and function of the airway epithelium barrier[424–426]. Further consequences of COVID-19 pneumonia may end, in some patients, with acute respiratory syndrome (ADRS) and septic shock, potentially followed by multi-organ failure[419,427,428].

This suggests that SARS-CoV-2 may be capable of entering and infecting macrophages by efficiently hijacking their immunity and/or using these cells as viral reservoirs[140,429] causing lung and systemic inflammation via cytokine storm (Figure 7.2). Internalized SARS-CoV-2 particles in macrophages have been detected in lung tissue obtained post-mortem from COVID-19 patients[430]. However, this is insufficient to conclude that SARS-CoV-2 infection in macrophages is productive. Some reports conclude that there is SARS-CoV-2 productive infection in ACE2-expressing macrophages[415,431] whilst others show opposing results[417,432–434].

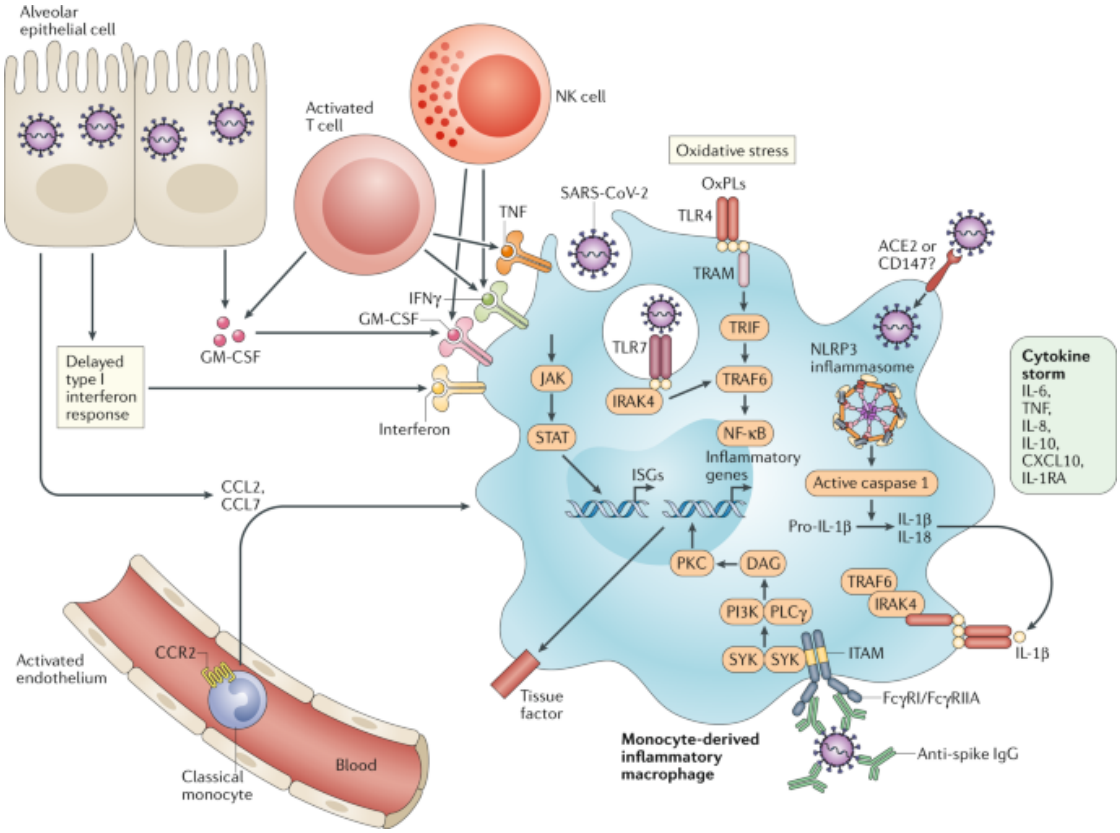


Figure 7.2. Possible pathways contributing to hyperactivation of monocyte-derived macrophages and hyperinflammation in COVID-19

Several mechanisms likely contribute to the hyperactivation of monocyte-derived macrophages that is seen in patients with COVID-19. Delayed production of type I interferon leading to enhanced cytopathic effects and increased sensing of microbial threats promotes the enhanced release of monocyte chemoattractants by alveolar epithelial cells (and likely also by macrophages and stromal cells), leading to sustained recruitment of blood monocytes into the lungs. Monocytes differentiate into pro-inflammatory macrophages though activation of Janus kinase (JAK)–signal transducer and activator of transcription (STAT) pathways. Activated natural killer (NK) cells and T cells further promote the recruitment and activation of monocyte-derived macrophages through the production of granulocyte–macrophage colony-stimulating factor (GM-CSF), tumour necrosis factor (TNF) and interferon-γ (IFNγ). Oxidized phospholipids (OxPLs) accumulate in infected lungs and activate monocyte-derived macrophages through the Toll-like receptor 4 (TLR4)–TRAF6–NF-κB pathway. Virus sensing can trigger TLR7 activation through viral single-stranded RNA recognition. It is possible that type I interferons induce the expression of severe acute respiratory syndrome coronavirus 2 (SARS-CoV-2) entry receptors, enabling the virus to gain access to the cytoplasm of macrophages and to activate the NLRP3 inflammasome, leading to the secretion of mature IL-1β and/or IL-18. IL-1β can amplify activation of monocyte-derived macrophages in an autocrine or paracrine way, but it can also reduce type I interferon production in infected lungs. The engagement of Fcγ receptors (FcγRs) by anti-spike protein IgG immune complexes can contribute to increased inflammatory activation of monocyte-derived macrophages. Activated monocyte-derived macrophages contribute to the COVID-19 cytokine storm by releasing massive amounts of pro-inflammatory cytokines. CCL, CC-chemokine ligand; CXCL10, CXC-chemokine ligand 10; ISG, interferon-stimulated gene; ITAM, immunoreceptor tyrosine-based activation motif; TRAM, TRIF-related adaptor molecule. Obtained from Merad and Martin, 2020[435].

The biology of macrophages in viral pathogenesis underlies anti- and pro-viral mechanisms[162,163,436]. Macrophage encounter with virions promotes their internalization. This can occur by endocytosis, phagocytosis, micropinocytosis or viral-cell membranes fusion[437]. Phagocytosis, as a mechanism to clear virus by pH degradation when virus-containing phagosomes merge with the lysosome (phagolysosome), is considered to be an antiviral mechanism by macrophages[437]. Phagosome formation, after receptor binding to the particle to be ingested, remodels the lipid composition of the membrane and the cytoskeleton[438,439]. Maturation of the phagosome is required to direct phagocytized particles for lysosomal degradation[440]. This process involves sequential fusion and fission interactions to mature early to late endosomes and the further merge with lysosomes[438,440]. The maturation of the phagosome involves the regulation of the membrane fusion between the phagosome and the early endosome. This step is regulated by GTPase Rab5 and precedes the recruitment of other proteins such as Rab7. The loss of Rab5 and retention of Rab7 mediates further maturation by the fusion with late endosomes. The final steps involve the fusion of the mature phagosome with lysosomes and vesicles carrying lysosomal-associated membrane proteins (LAMPs) and proteases[438,440–442]. Throughout this process, the accumulation of V-ATPases is responsible for the acidification of the phagolysosome, by an increased translocation of H^+ into its lumen, and for the degradation of pathogens[443]. Lysosomal hydrolases including cathepsins, proteases, lipases, and lysozymes directly target pathogens structures[444]. Other mechanisms of pathogen degradation by phagolysosomes involve the recruitment of NADPH oxidases that, by the production of ROS and reactive nitrogen species[444], can damage pathogens' nucleic acids, proteins, and lipids[438,440–442,444].

Viral adaptations to counteract anti-viral responses and to avoid degradation by macrophages highlight potential mechanisms of dissemination. Known mechanisms of viral adaptation involve the inhibition of phagosome maturation and fusion[445,446], the escape from the phagosomes into the cytoplasm[445,446] and, the internalization of viral particles within non-degradative compartments termed vesicle-containing compartments (VCC)[447]. VCC comprise markers of plasma membrane and multivesicular bodies[448,449] yet their origins remains unclear[252,447]. Siglec-1, a cell-adhesion molecule known to mediate phagocytosis of sialylated pathogens[450], plays a major role in the formation and function of VCC[447,449,451]. These structures are of high relevance in pandemic viruses such as HIV[437] as it facilitates viral dissemination in restricted tissues such as the brain[451]. Altogether, the macrophage interactions with pathogens highlight several mechanisms that potentially contribute or decrease the pathophysiology of COVID-19. Thus, elucidating the susceptibility of macrophages to SARS-CoV-2 productive infection, primarily of MDM due to their potential role in the COVID-19 disease, is key to better understand the viral pathogenesis in permissive tissues and to potentially decrease the disease severity by targeting early processes during infection.

7.3 AIMS

Phagocytes encounter with ingested SARS-CoV-2 virions, and proinflammatory signalling from infected alveolar type II pneumocytes are expected to occur during the infection of the lung. To date, findings suggest that macrophage responses to SARS-CoV-2 infection cause clinical complications in COVID-19 patients termed cytokine storm. However, whether these cells are susceptible to infection or instead are capable of degrading free SARS-CoV-2 virions to supress the replication kinetics, thus potentially limiting disease progression, remains unclear. To study the susceptibility of macrophage infection to SARS-CoV-2 virions, it is required to mimic their direct and indirect exposure to infectious viral particles. Thus, I differentiated macrophages from (i) monocytes isolated from human peripheral blood (monocyte-derived macrophages - MDM), which represent infiltrating macrophages, and human induced pluripotent stem cells (hiPSC-MPh), which present the characteristics of tissue-resident-like macrophages. These macrophages were challenged with SARS-CoV-2 virions to address the following four aims.

- To determine the permissibility of MDM to SARS-CoV-2 infection by direct cell-free virus exposure
- To study the fate of SARS-CoV-2 virions in MDM
- To study the susceptibility of MDM and hiPSC-MPh to SARS-CoV-2 infection during viral dissemination in non-immune permissive cells (cell-to-cell transfer)
- To assess a role of macrophages in an *in vitro* COVID-19 disease relevant tissue model

7.4 METHODS[F]

7.4.1 Cell culture

hiPSC lines were obtained and maintained as detailed in section 2.2.2.1.1. hiPSC-MPh and hiPSC-CM were differentiated from different donor cell lines as described in section 2.2.2.3 and 2.2.2.4, respectively. Monocytes were isolated from leukocytes cones of different donors as detailed in section 2.2.2.2.1.2 and differentiated into MDM as explained in 2.2.5. Coculture of Vero CCL-81 and macrophages is described in section 2.2.6 and coculture of hiPSC-CM with hiPSC-MPh is described in section 2.2.7.

7.4.2 SARS-CoV-2 challenge

Vero CCL-81, macrophages and hiPSC-CM were challenged with SARS-CoV-2 at an MOI of 0.01 or 2. Challenge experiments in mono and cocultures were carried out following the protocols set out in sections 2.3.3 and 2.3.4, respectively. Details of the viral stocks used for challenge experiments are included in section 2.1.4 and, the quantification method of infectious viral particles is detailed in section 2.1.5.

7.4.3 Survival of cocultured hiPSC-CM with hiPSC-MPh

Cellular survival was measured by metabolic activity CCK-8 assay following the manufacturer's procedure detailed in section 2.5.3.

[F] This work was designed and carried out in collaboration with the Sattentau laboratory. Sample processing and data acquisition both within and outside the Containment Level 3 facility was shared with post-doctoral researcher Dr. Maeva Dupont.

7.4.4 Flow cytometry

Immunostaining in macrophages and experimental controls MDCK and MDCK-ACE2 to detect membrane-bound ACE2 receptor was conducted following the protocol set out in section 2.4.4.

7.4.5 Microscopy

Immunofluorescence analysis of Vero CCL-81 and macrophages was conducted following the protocols in sections 2.4.5.1. Sample processing and TEM image acquisition is detailed in section 2.6.

7.4.6 Imaging Flow Cytometry (ImageStream®)

Immunofluorescence analysis in SARS-CoV-2 challenged macrophages to quantify colocalization between SARS-CoV-2 nucleocapsid protein N and lysosomes was conducted following the protocol set out in section 2.4.5.2.

7.4.7 Statistical analysis

Datasets containing different number of repeats for a single time-point were analyzed using Kruskal-Wallis test. Datasets containing analysis of independent experiments of independent donors' cell lines comprising two groups and, datasets generated to quantify colocalization of probes by microscopy were analyzed using Two-way ANOVA with Holm-Šidák's multiple comparisons post-hoc test. Significance in datasets comprising technical replicates of a single experiment using one donor' cell line over a time-course was calculated by mixed-effects model with Tukey's multiple comparison test. Parameters of contractibility in cardiomyocytes were analyzed by mixed-effects model with Šidák correction.

7.4.8 Figures

Representation schemes were created with BioRender.com. Summary figures were done using GNU Image Manipulation Program (GIMP 2.8.22).

7.5 RESULTS

7.5.1 SARS-CoV-2 does not replicate in MDM

MDM have a main role in the immune response to SARS-CoV-2 infection in the lung[371,404,412]. Thus, I studied their susceptibility to be productively infected. To do this, I first assessed the expression of the entry receptor ACE2 by using an *"in house"* biotinylated construct comprising the receptor-binding C-terminal domain of the spike glycoprotein of SARS-CoV-2 fused to the C region of IgG1 heavy chain (RBD-Fc; details of the synthesizing procedure are available on Deimel et al., 2022 – manuscript under submission). The lack of detection of ACE2, by flow cytometry, in wild-type Madin-Darby canine kidney cells (MDCK) and, the detection in ACE2-transduced MDCK confirmed the specificity of this compound (Figure 7.3A). Titration of the RBD-Fc showed that the ACE2 receptor was expressed in MDM (Figure 7.3A). I then challenged permissive Vero CCL-81 cells and MDM, for 4 h, at an M.O.I. of 2 and tested the culture supernatant for progeny virus of 14 days post-challenge. MDM produced no virus at any time during this period, in contrast to Vero cells, which released progeny virus from 24 h until seven days post-challenge (Figures 7.3B and 7.3D).

Immunostaining of anti-SARS2 nucleocapsid protein (N) showed intracellular SARS-CoV-2 virions in challenged Vero cells and MDM (Figure 7.3C). Productive SARS-CoV-2 infection, evidenced by cytoplasmic distribution of N protein, was observed in Vero cells (Figures 7.3C and 7.4A) whilst in MDM, the N protein was only detected in occasional puncta within the cytoplasm of some cells (Figures 7.3C and 7.4B). The detection of N protein in macrophages faded over three to 14 days post-challenge (Figure 7.4B). These results showed that ACE2-expressing MDM internalized SARS-CoV-2 virions but were unlikely to be productively infected.

Internalization of viruses by macrophages within non-acidic compartments (VCC) may correlate with dissemination to neighbouring cells[378,452,453]. Thus, I studied the intracellular localization of the SARS-CoV-2 in MDM by transmission electron microscopy (TEM). The analysis of TEM sections showed that internalized SARS-CoV-2 virions were clustered within intracellular compartments that separate them from the cytosol (Figure 7.4C). The identification of SARS-CoV-2 was done by the presence of nucleocapsid in virus particles (black arrow heads, Figure 7.4C)[454,455]. TEM analysis of non-challenged macrophages showed empty vesicles (Figure 7.4C).

7.5.2 MDM phagocytize SARS-CoV-2 virions

Degradation of virions within macrophage phagolysosomes would be expected to decrease viral susceptibility[440,442]. To elucidate the fate of internalized virions by MDM, detected by punctate staining (Figures 7.3C and 7.4B), I assessed the nature of these vesicles by IF. The analysis of super-resolution microscopy images of SARS-CoV-2 challenged MDM (Figures 7.5A and 7.5B) showed a modest degree of colocalization/co-occurrence between SARS-CoV-2 N protein and Rab 5+ve compartments (Manders coefficient of 0.5 - 0.7) and a low colocalization/co-occurrence between SARS-CoV-2 N protein and Rab 7+ve compartments (Manders coefficient < 0.5) over the 6 h viral challenge (Figure 7.5C).

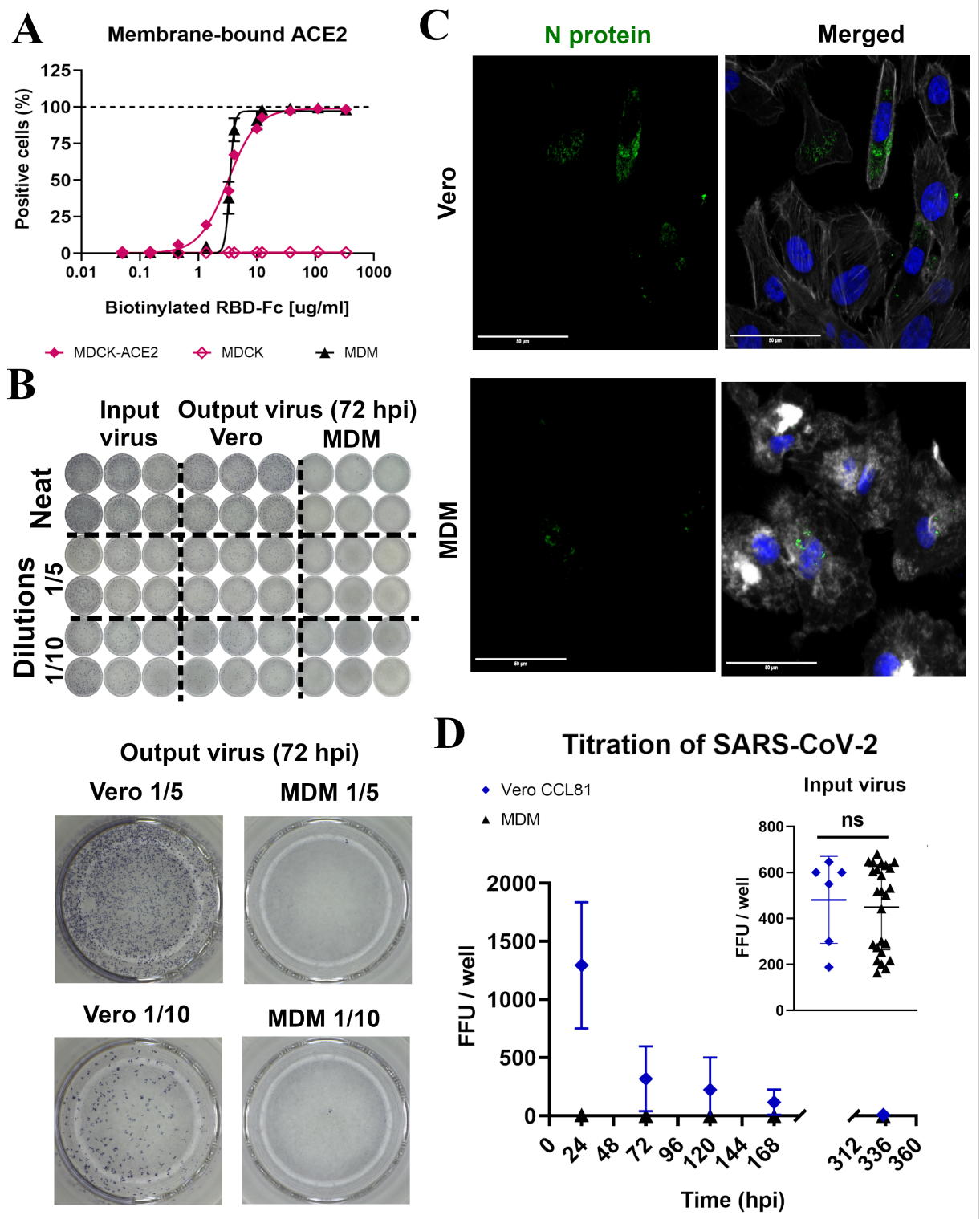

A
Membrane-bound ACE2
Positive cells (%)
125
100
75
50
25
0
0.01
0.1
1
10
100
1000
Biotinylated RBD-Fc [ug/ml]
MDCK-ACE2
MDCK
MDM
B
Input virus
Output virus (72 hpi)
Vero
MDM
Neat
Dilutions
1/5
1/10
Output virus (72 hpi)
Vero 1/5
MDM 1/5
Vero 1/10
MDM 1/10
C
N protein
Merged
Vero
MDM
D
Titration of SARS-CoV-2
Vero CCL81
MDM
Input virus
ns
FFU / well
2000
1500
1000
500
0
0
24
48
72
96
120
144
168
312
336
360
Time (hpi)
800
600
400
200
0

Figure 7.3. SARS-CoV-2 does not productively infect monocyte-derived macrophages

(A) Titration curve of RBD-Fc compound for the detection of the membrane-bound fraction of ACE2 receptors in MDM and control cell lines using flow cytometry. Bars display mean ± SD from n = 3 independent experiments. (B) Example plate of the focus-forming unit (FFU) assay to titrate SARS-CoV-2 virions from the supernatant of challenged cells (top) at an M.O.I. of 2 and, zoom of representative wells to show the presence/absence of foci (bottom). (C) Representative confocal images with high magnification (63x) showing the detection of SARS-CoV-2 N protein (green) in Vero CCL-81 and MDM at 24 h post-challenge (M.O.I. of 2). Merged images display cytoplasm staining of actin filaments (phalloidin - grey) and nuclei (DAPI - blue), scale bar = 50 µm. (D) Dot plots showing a long-term titration of SARS-CoV-2 from cells' supernatants after 4 h challenge. Titration of input virus showing no significant differences between cell types. SARS-CoV-2 quantification was done by the detection of N protein using FFU assay. Bars display mean ± SD. n = 5 independent experiments in Vero and n = 26 independent donors for MDM, each conducted in duplicates. Significance was calculated by Kruskal-Wallis test, $^{*}p < 0.05$, $^{**}p < 0.01$, $^{***}p < 0.001$.

Further analysis by ImageStream® showed, from the 2.56% of cells containing internalized SARS-CoV-2 particles, a 57.2% of colocalization between N protein and lysosomes (Figure 7.5D). In addition, IF analysis showed N protein not to be colocalized with VCC (Figure 7.5E, under quantification). Altogether, these results suggests that upon SARS-CoV-2 encounter, MDM do not store virions in VCC, where it could escape the host immune responses, but instead could degrade the virions inside phagolysosomes.

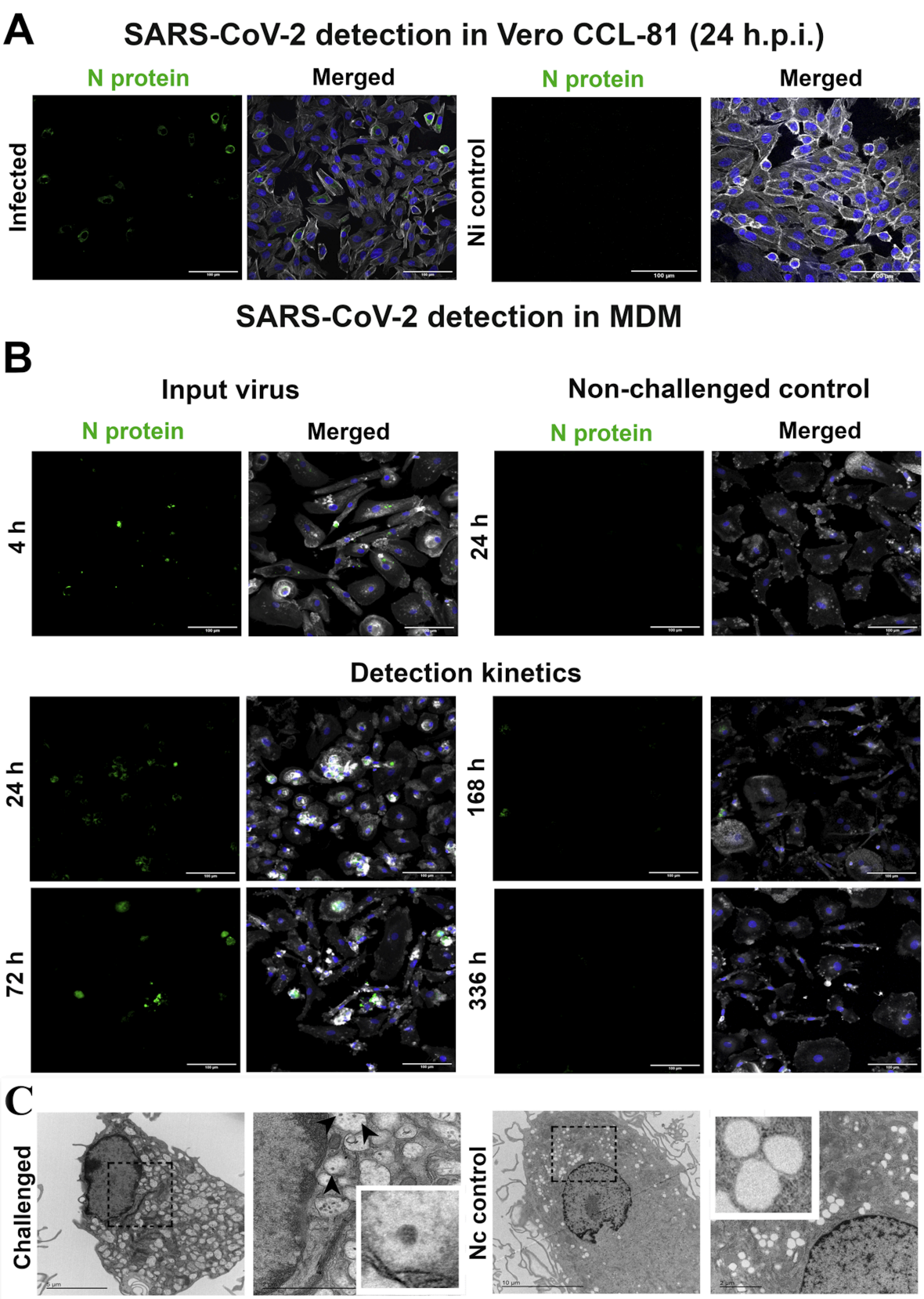

A
SARS-CoV-2 detection in Vero CCL-81 (24 h.p.i.)
N protein
Merged
N protein
Merged
Infected
Ni control
SARS-CoV-2 detection in MDM
B
Input virus
Non-challenged control
N protein
Merged
N protein
Merged
4 h
24 h
Detection kinetics
24 h
168 h
72 h
336 h
C
Challenged
Nc control

Figure 7.4. Detection of macrophage-internalized virions decrease in a time-dependent manner

(A) Representative confocal images with high magnification (20x) showing the detection of SARS-CoV-2 N protein (green) in infected (left panel) and control (right panel) Vero CCL-81. (B) Representative confocal images (20x) showing the detection of SARS-CoV-2 N protein (green) input at 4 h and time-course kinetics over 14 days post-challenge in MDM challenged for 4 h at an M.O.I. of 2. Representative images of mock-challenged macrophages at the top right. Merged images display cytoplasm staining of actin filaments (phalloidin - grey) and nuclei (DAPI - blue). Scale bar = 100 µm. (C) TEM detection of internalized SARS-CoV-2 virions, seen as black dots (nucleocapsid) in MDM challenged for 5 h at an M.O.I. of 2. Black arrow heads pointing at SARS-CoV-2 virions (left) and representative images of non-challenged macrophages showing empty vesicles (right). Black dotted rectangles highlight the zoomed areas (scale bar: 2 µm).

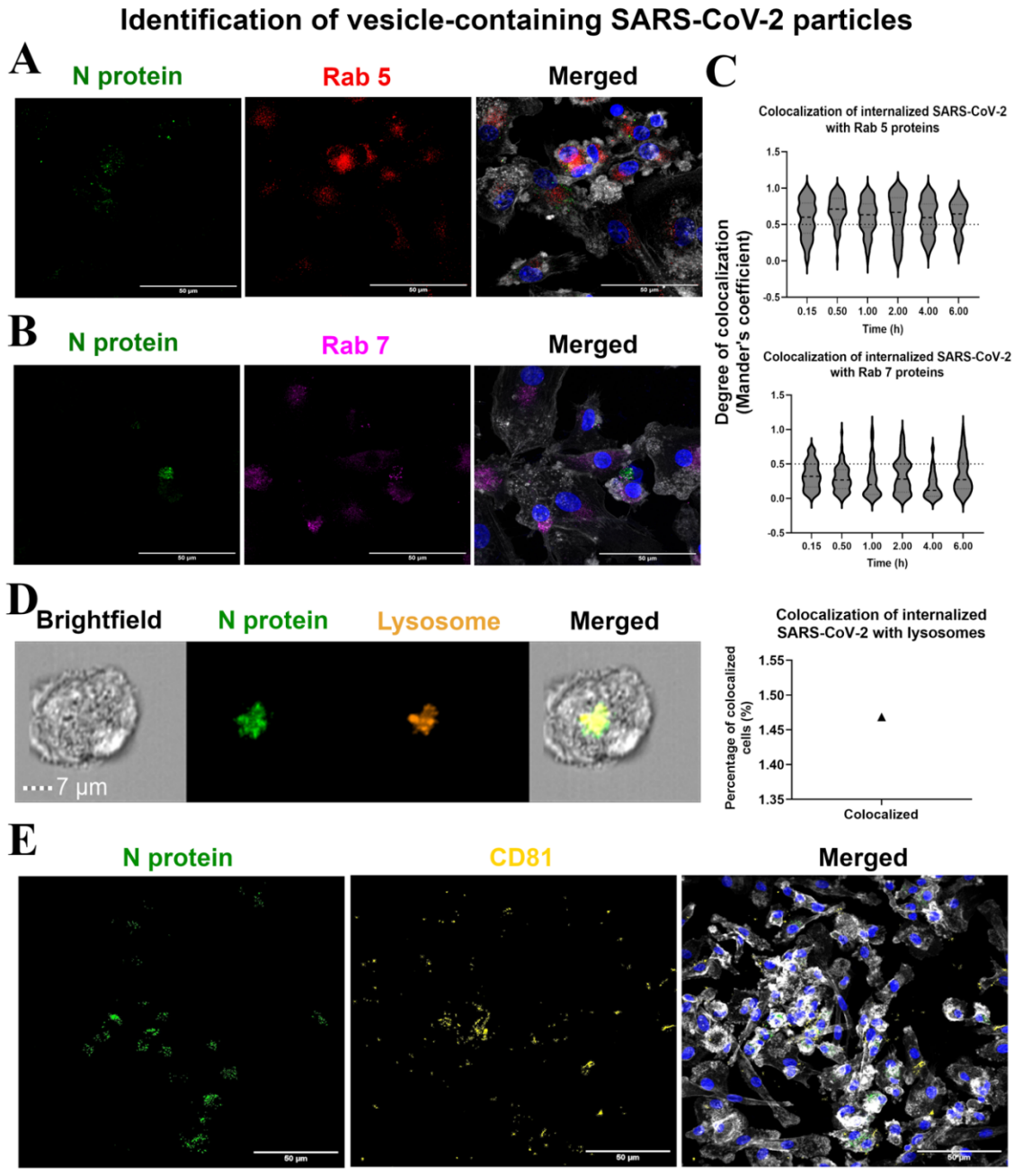


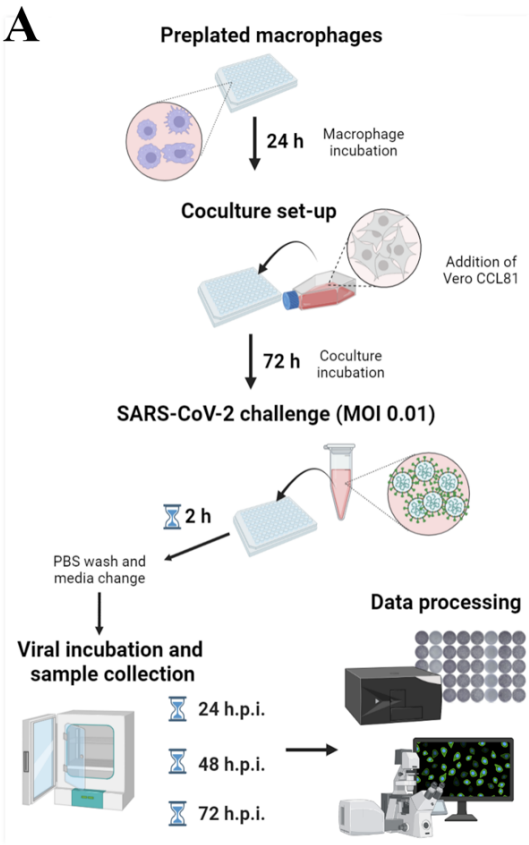
Figure 7.5. Internalized SARS-CoV-2 virions are targeted for phagolysosome degradation

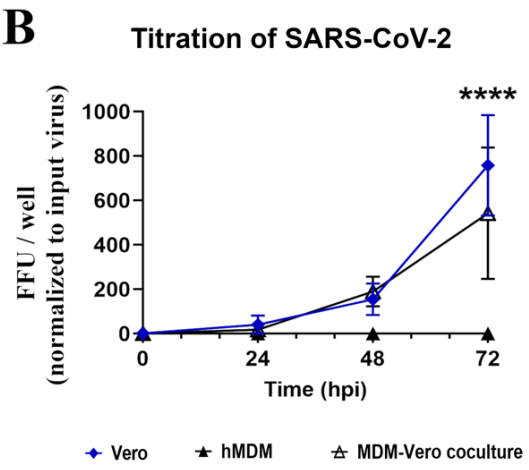
(A-B) Representative super-resolution images (63x), z-stack projections of ~30 μm depth, of MDM 4 h post-challenge with SARS-CoV-2 at an M.O.I. of 2. Images show the immunostaining of SARS-CoV-2 N protein (green), Rab 5+ve compartments (red), Rab 7 +ve compartments (magenta), cytoplasm staining of actin filaments (phalloidin - grey) and nuclei (DAPI - blue). Scale bar = 50 μm. (C) Summary quantification of Mander's coefficient used to measure the occurrence of SARS-CoV-2 in Rab 5 (left) and Rab 7 (right) compartment within macrophages. Violin plots displaying the mean ± SD of no less than 100 SARS-CoV-2 containing cells per time-point per condition, measured in 3 independent donors/experiments. Dotted lines highlight the threshold of low correlation measured by a Mander's coefficient of 0.5. Statistical significance was calculated using a Two-way ANOVA with Holm-Šidák's multiple comparisons post-hoc test, * $p < 0.05$, ** $p < 0.01$, *** $p < 0.001$. (D) Example of data acquisition by ImageStream® used to calculate the percentage colocalization (right) between SARS-CoV-2 N protein and lysosomes. Dot plot showing the percentage of colocalization. (E) Representative images (40x) of VCC staining showing z-stack projections of ~30 μm depth. Images show the immunostaining of SARS-CoV-2 N protein (green) and CD81 (yellow). Merged image display staining of actin filaments (phalloidin - grey) and nuclei (DAPI - blue). Scale bar = 50 μm. (C)

7.5.3 Indirect exposure of macrophages to SARS-CoV-2 virions does not alter their susceptibility to be productively infected

During SARS-CoV-2 infection in tissues macrophages are exposed to SARS-CoV-2 not only by cell-free virions, but also by direct contact with infected cells (cell-to-cell transfer)[456], I cocultured Vero cells with MDM (Figure 7.6A). Infection of mono and coculture systems, at an M.O.I. of 0.01, showed an exponential increase in the replication kinetics of SARS-CoV-2 over 72 h and, the presence of macrophages resulted in a significantly lower viral output in Vero cells (Figure 7.6B). Significant viral reduction in the coculture of MDM was observed at 72 h.p.i. ($p < 0.001$) (Figure 7.6B). Immunostaining of the cocultures showed SARS-CoV-2 N protein staining exclusively in Vero cells (Figures 7.6C).

Macrophages are highly responsive to cancerous cells from which MDM constitute the detrimental tumour-associated macrophages (TAMs)[457,458]. Thus, to discard potential recognition of the cancerous nature of Vero cells by MDM, I cocultured Vero cells with tissue-resident-like macrophages (hiPSC-MPh).


A
Preplated macrophages
24 h
Macrophage incubation
Coculture set-up
Addition of Vero CCL81
72 h
Coculture incubation
SARS-CoV-2 challenge (MOI 0.01)
2 h
PBS wash and media change
Viral incubation and sample collection
24 h.p.i.
48 h.p.i.
72 h.p.i.
Data processing


B
Titration of SARS-CoV-2
****
FFU / well (normalized to input virus)
1000
800
600
400
200
0
0
24
48
72
Time (hpi)
Vero
hMDM
MDM-Vero coculture

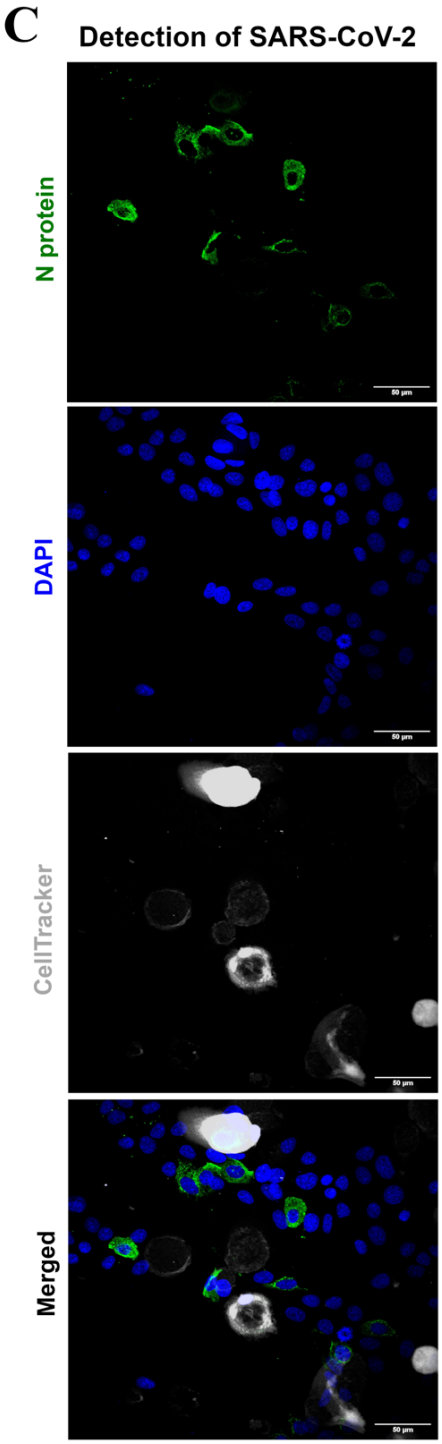

C
Detection of SARS-CoV-2
N protein
DAPI
CellTracker
Merged

Figure 7.6. Macrophages are not permissive to SARS-CoV-2 infection under coculture conditions with susceptible Vero cells
(A) Schematic 2D representation of the Vero CCL-81 and macrophage coculture set-up to investigate the effects of cell-to-cell transfer of SARS-CoV-2 to macrophages. (B) Line graphs showing the replication kinetics of SARS-CoV-2 in mono and cocultures using MDM. SARS-CoV-2 exposure in mono and cocultures was done by a 2 h incubation at 37 °C with media-containing virions at an M.O.I. of 0.01. SARS-CoV-2 quantification was done by detection of SARS-CoV-2 N protein using the FFU assay. Bars display mean ± SD. n = 4 independent experiments in Vero and n=18 independent donors for MDM, each conducted in duplicates. Statistical significance was calculated by Two-way ANOVA with Holm-Šidák's multiple comparisons post-hoc test, * $p < 0.05$, ** $p < 0.01$, *** $p < 0.001$. (C) Representative confocal images (40x) showing the detection of SARS-CoV-2 N protein (green), nuclei (DAPI - blue) and macrophages (gray) in the coculture of MDM. MDM were pre-stained with CellTracker™ prior coculture. Scale bar = 50 µm.

I showed that hiPSC-MPh expressed ACE2 receptors (Figure 7.7A) and that, like MDM, internalized SARS-CoV-2 virions reside within intracellular compartments (Figure 7.7B and black arrowhead in Figure 7.7C). TEM sections showed empty vesicles and vesicles containing particles of different characteristics than the SARS-CoV-2 particles in non-challenge controls (white arrowhead, Figure 7.7C).

Imagestream® analysis showed that, after viral exposure over 6 h, 29.7% of hiPSC-MPh internalized SARS-CoV-2. These cells showed a 69.3% colocalization between lysosomes and SARS-CoV-2 N protein (Figure 7.7D). The coculture of hiPSC-MPh reduced the kinetics of SARS-CoV-2 replication at 48 h.p.i ($p = 0.0195$) and 72 h.p.i. ($p = 0.0096$) (Figure 7.7E) and, by immunostaining of SARS-CoV-2 N protein, showed infection to be exclusively in Vero cells (Figure 7.7F). At 24 h.p.i., these cocultures showed the formation of cell aggregates which were not observed in the Vero monoculture until 72 h.p.i. (Figure 7.8B). Altogether, these data suggest that macrophages, both tissue-resident-like and infiltrating, do not become productively infected through the cell-to-cell transfer route and that these cells may decrease the SARS-CoV-2 infection in susceptible cells.

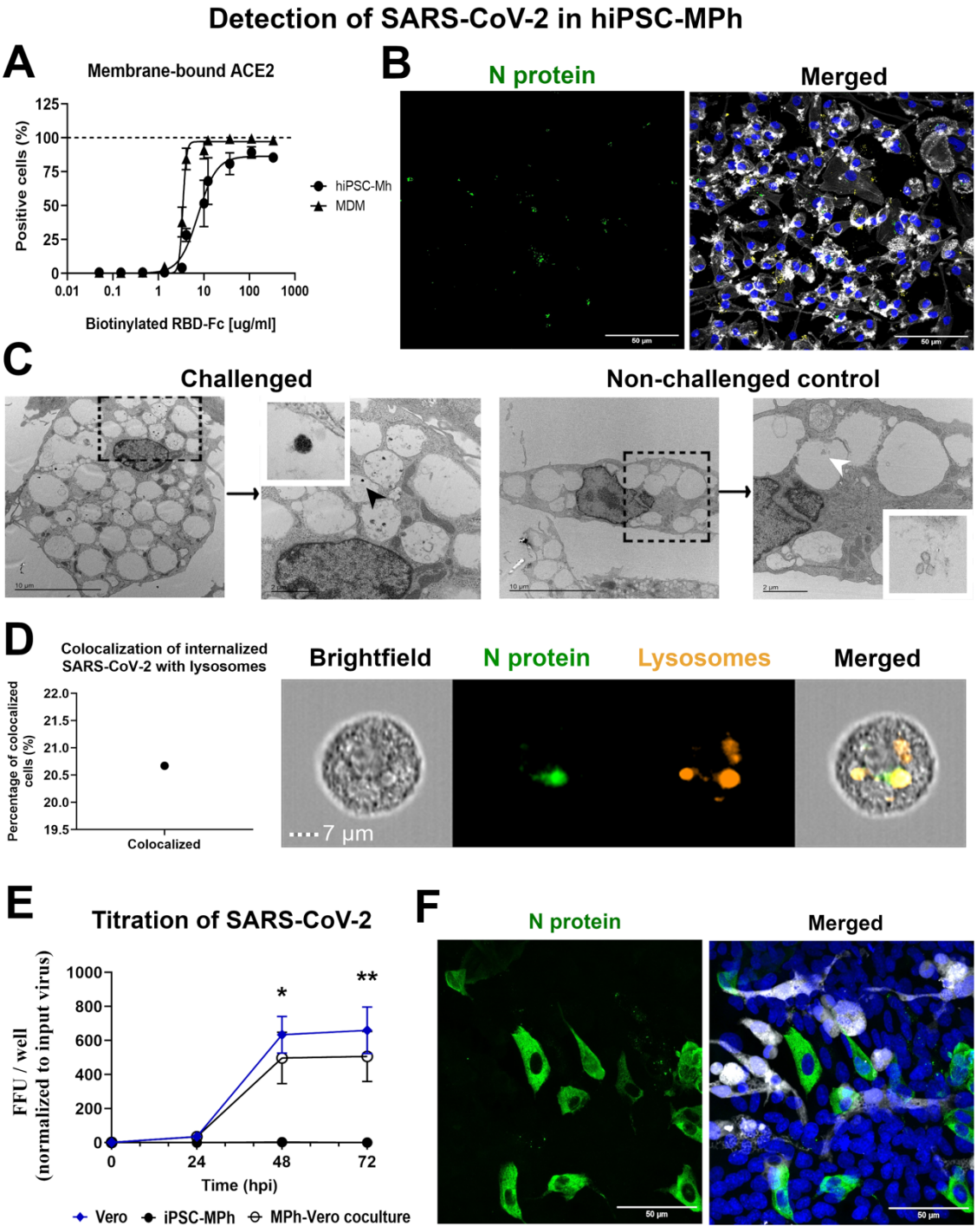

Detection of SARS-CoV-2 in hiPSC-MPh
A
Membrane-bound ACE2
Positive cells (%)
125
100
75
50
25
0
0.01
0.1
1
10
100
1000
Biotinylated RBD-Fc [ug/ml]
hiPSC-Mh
MDM
B
N protein
Merged
50 µm
C
Challenged
Non-challenged control
10 µm
2 µm
D
Colocalization of internalized SARS-CoV-2 with lysosomes
Percentage of colocalized cells (%)
22.0
21.5
21.0
20.5
20.0
19.5
Colocalized
Brightfield
N protein
Lysosomes
Merged
7 µm
E
Titration of SARS-CoV-2
FFU / well (normalized to input virus)
1000
800
600
400
200
0
0
24
48
72
Time (hpi)
*
**
Vero
iPSC-MPh
MPh-Vero coculture
F
N protein
Merged
50 µm

Figure 7.7. SARS-CoV-2 virions are internalized by hiPSC-MPh
(A) Titration curve of RBD-Fc compound for the detection of the membrane-bound fraction of ACE2 receptors in macrophage types using flow cytometry. Bars display mean ± SD from n = 3 independent experiments. (B) Representative confocal images (40x) showing the detection of SARS-CoV-2 N protein (green) in hiPSC-MPh challenged for 4 h at an M.O.I. of 2. Merged image display cytoplasm staining of actin filaments (phalloidin - grey) and nuclei (DAPI - blue). Scale bar = 50 µm. (C) TEM detection of internalized SARS-CoV-2 virions, seen as black dots (nucleocapsid) in hiPSC-MPh challenged for 5 h at an M.O.I. of 2. Black arrow heads pointing at SARS-CoV-2 virions (left) and representative images of non-challenged hiPSC-MPh showing empty vesicles (right). White arrowhead highlighting particles of different characteristics than SARS-CoV-2 virions in non-challenged hiPSC-MPh. Black dotted rectangles highlight the zoomed areas (scale bar: 2 µm). (D) Dot plot showing the percentage of colocalized SARS-CoV-2 N protein and lysosomes in hiPSC-MPh (left). Example of data acquisition by ImageStream® to calculate the percentage colocalization (right). (E) Line graphs showing the replication kinetics of SARS-CoV-2 in mono and cocultures using hiPSC-MPh. SARS-CoV-2 exposure for coculture experiments was done by a 2 h incubation at 37 °C with media-containing virions at an M.O.I. of 0.01. SARS-CoV-2 quantification was done by detection of SARS-CoV-2 N protein using the FFU assay. Bars display mean ± SD. n = 4 independent experiments in Vero and n = 4 independent experiments of one donor' cell line for hiPSC-MPh, each conducted in duplicates. Statistical significance was calculated by Two-way ANOVA with Holm-Šidák's multiple comparisons post-hoc test, * $p < 0.05$, ** $p < 0.01$, *** $p < 0.001$. (F) Representative confocal images (40x) showing the detection of SARS-CoV-2 N protein (green) in the coculture of hiPSC-MPh. hiPSC-MPh were stained post-fixation with macrophage-specific-calcium-binding protein Iba-1 (grey) and DAPI (nuclei - blue). Scale bar = 50 µm.

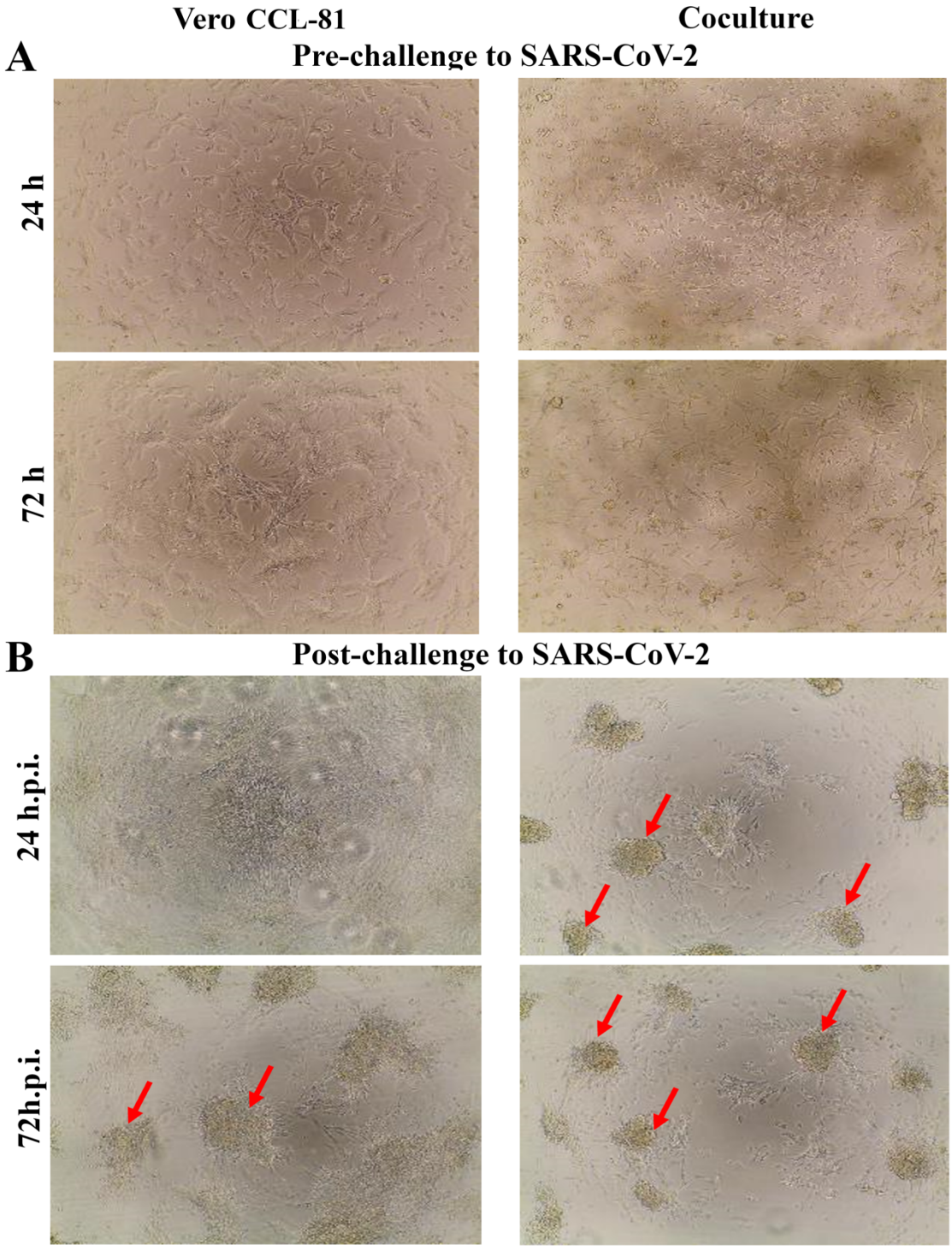


Figure 7.8. Macrophage interactions with Vero CCL-81 show cellular aggregation

Example brightfield images of Vero CCL-81 mono and cocultured with hiPSC-MPh. (A) Vero cell growth in mono and coculture conditions over 72 h. (B) Development of mono and coculture conditions over 72 h post SARS-CoV-2 challenge at an M.O.I of 0.01 for 2 h at 37 °C. Red arrows showing cellular aggregates.

7.5.4 hiPSC-MPh reduce the infection of SARS-CoV-2 in cardiomyocytes

The second most affected organ in severe COVID-19 patients is the heart[378–380]. Thus, to study the role of macrophages in an *in vitro* disease relevant tissue model, I cocultured hiPSC-CM and hiPSC-CM (Figure 7.9A)[G]. I showed the susceptibility of hiPSC-CM to SARS-CoV-2 productive infection using three SARS-CoV-2 variants available in the laboratory at the time of this research (Figure 7.9F). I then cocultured hiPSC-CM and hiPSC-MPh (Figure 7.9A) and showed coculture stability over 120 h. During this time, the cellular survival, estimated by metabolic activity, showed no significant differences compared to the hiPSC-CM monoculture (Figure 7.9B). The integration of hiPSC-MPh within the monolayer of hiPSC-CM (Figure 7.9C) did not significantly alter the cardiomyocyte functions.

The cardiomyocyte functions comprised the measurements of muscle motion represented as contraction duration, contraction amplitude, time to peak, peak amplitude, peak-to-peak time, and relaxation time (Figure 7.9D). Like in Vero cocultures, the presence of macrophages significantly reduced the viral output in hiPSC-CM at 48 and 72 h.p.i ($p = 0.0074$) (Figure 7.9G). These data suggest a potential beneficial role of tissue-resident macrophages by the decrease of SARS-CoV-2 infection in the heart.

[G] The induction for the differentiation of hiPSC-CM was provided by the Carr's group (Department of Physiology, Anatomy and Genetics – DPAG, Oxford). The protocol for the differentiation of these cells has been reported elsewhere[175]. For the initial culture experiments, cells were kindly provided by members of this group.

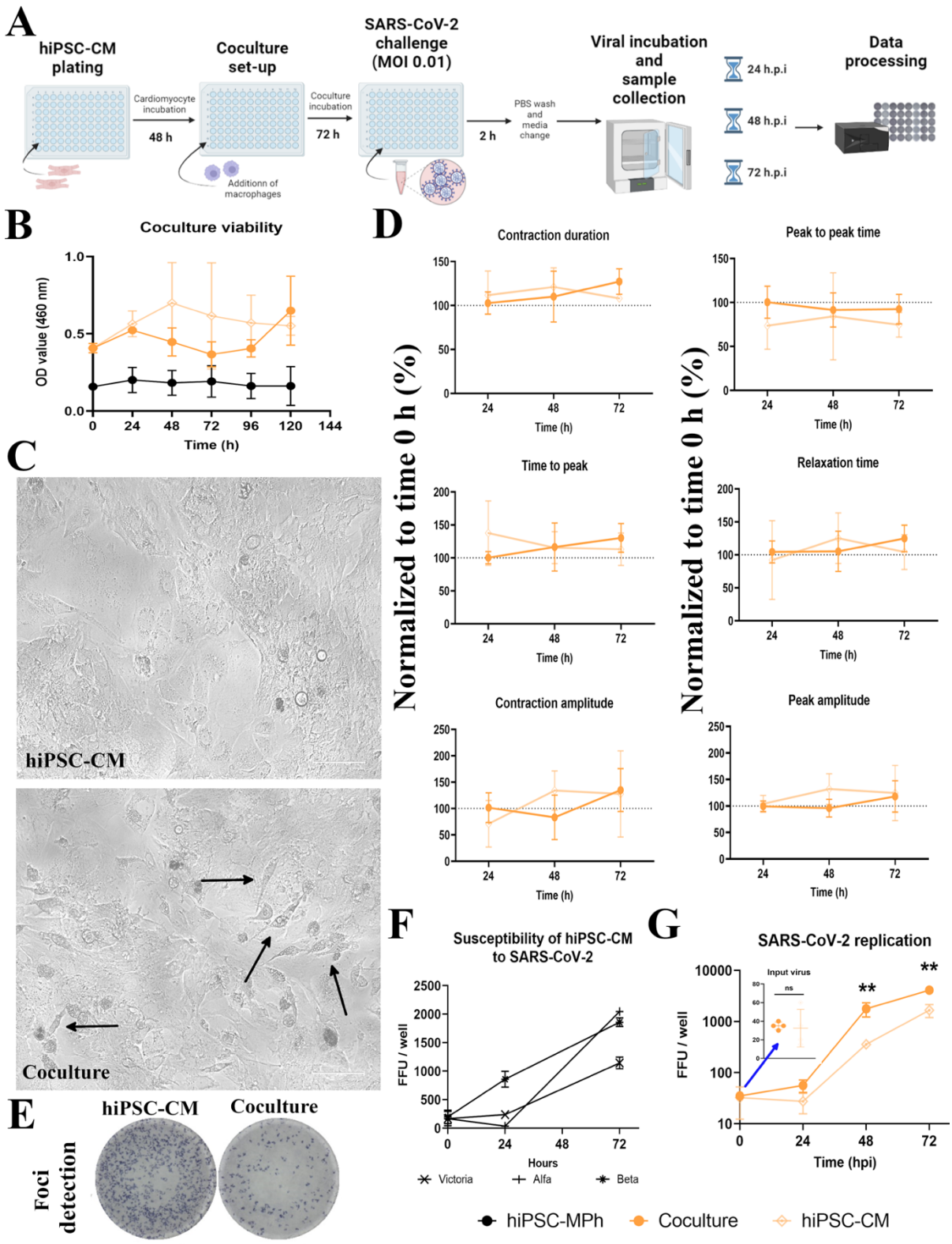

A
hiPSC-CM plating
Cardiomyocyte incubation
48 h
Coculture set-up
Additionn of macrophages
Coculture incubation
72 h
SARS-CoV-2 challenge (MOI 0.01)
2 h
PBS wash and media change
Viral incubation and sample collection
24 h.p.i
48 h.p.i
72 h.p.i
Data processing
B
Coculture viability
OD value (460 nm)
Time (h)
C
hiPSC-CM
Coculture
D
Contraction duration
Peak to peak time
Time to peak
Relaxation time
Contraction amplitude
Peak amplitude
Normalized to time 0 h (%)
Time (h)
E
hiPSC-CM
Coculture
Foci detection
F
Susceptibility of hiPSC-CM to SARS-CoV-2
FFU / well
Hours
Victoria
Alfa
Beta
G
SARS-CoV-2 replication
Input virus
ns
**
FFU / well
Time (hpi)
hiPSC-MPh
Coculture
hiPSC-CM

Figure 7.9. SARS-CoV-2 infected hiPSC-derived cardiomyocytes do not represent a route for cell-to-cell transfer of virions to macrophages
(A) Schematic 2D representation of the protocol conducted to study the cell-to-cell transfer route between infected hiPSC-CM and hiPSC-MPh. When challenged, cocultures and monocultures were exposed to media-containing SARS-CoV-2 for 2 h at 37 °C using an M.O.I. of 0.01. (B) Line graphs showing survival of mono and cocultures over 120 h. Measurements were done using CCK-8 viability assay following the manufacturer's protocol. Bars show mean ± SD. n = 3 independent cocultures, each conducted in quadruplicates using one donor cell line for hiPSC-CM and an independent donor cell line for hiPSC-MPh. Statistical significance was calculated by mixed-effects model with Tukey's multiple comparisons test. (C) Brightfield images showing examples of the integration of hiPSC-MPh (black arrows) within the monolayer of hiPSC-CM. Scale bar = 100 µm. (D) Line graphs showing several parameters of *in vitro* cardiomyocyte function over 72 h of coculture compared to those in monoculture. Bars display mean ± SD. n = 1 independent coculture conducted in duplicate using one donor cell line for hiPSC-CM and an independent donor cell line for hiPSC-MPh. Four videos were recorded per condition, at each time-point, for the quantification of each parameter. Significance was calculated by mixed-effects model with Šidák correction. (E) Zoom of representative wells to show the presence of foci titrated from the supernatants of SARS-CoV-2 infected hiPSC-CM mono and coculture. (F) Line graph showing susceptibility of hiPSC-CM monocultures to different variants of SARS-CoV-2 (MOI 0.05). Bars display mean ± SD. n = 1 independent infection conducted in quadruplicates. (G) Line graph showing the replication kinetics of SARS-CoV-2 in hiPSC-CM mono and coculture over 72 h. blue arrow highlighting the input virus in both conditions. Bars show mean ± SD. n = 1 independent coculture using one donor cell line for hiPSC-CM and an independent donor cell line for hiPSC-MPh. Infection was conducted in quadruplicates. Statistical significance was calculated by mixed-effects model with Tukey's multiple comparisons test. Significance in the input virus was calculated by Kruskal-Wallis test, * $p < 0.05$, ** $p < 0.01$, *** $p < 0.001$.

7.6 DISCUSSION

7.6.1 Macrophages internalize SARS-CoV-2 virions

Current efforts to overcome the COVID-19 pandemic are focused on the development of compounds and vaccines that reduce infectivity and/or decrease the high transmissibility of SARS-CoV-2[1,369,399,427]. To this, understanding the role of lung phagocytes during SARS-CoV-2 infection and spread is crucial to prevent potential negative scenarios such as antibody dependent enhancement against newly appearing variants and subvariants. Thus, chapter 7 focused on elucidating whether SARS-CoV-2 productively infects macrophages or whether macrophages are capable of degrading circulating virions. To do this, I analyzed productive infection in these cells via direct (cell-free) and indirect exposure (cell-to-cell transfer); these methods represent two alternatives for SARS-CoV-2 infection.

Using an *"in house"* biotinylated RBD-Fc compound, I confirmed that ACE2, the main entry receptor for SARS-CoV-2[459], was expressed in both infiltrating monocyte-derived macrophages (MDM) and tissue-resident-like macrophages (hiPSC-MPh), in agreement with other reports[371,415,420,431,434]. The analysis of cell supernatants showed viral production from Vero CCL-81 cells but not from ACE2-expressing macrophages after challenge with SARS-CoV-2 at an M.O.I. of 2. Immunofluorescence analysis confirmed that macrophages contained a cytoplasmic punctate distribution of SARS-CoV-2 N protein (Figures 7.3B and 7.5B), in contrast to the diffused cytoplasmic distribution of N protein in productively infected Vero cells (Figure 7.3A). This is consistent with immunohistology analysis of lung tissue of COVID-19 patients, which shows different distribution patterns of SARS-CoV-2 proteins in macrophages compared to infected pneumocytes[430]. Thus, suggesting macrophages are not productively infected by SARS-CoV-2 cell-

free exposure which is in agreement with findings of *in vitro* macrophage challenges reported elsewhere[433,434,460] but contradict those which are based on intracellular viral RNA analysis[432]. These discrepancies may be due to the differences between viral RNA and protein detection. Viral RNA detection does not accurately distinguish between internalized, degraded or newly produced viral particles[417], thus, quantification of newly assembled viruses, by methods such as FFU, are required to elucidate SARS-CoV-2 productive infection in macrophages.

7.6.2 Macrophage degradation of internalized SARS-CoV-2 virions

As macrophages potentially degrade internalized SARS-CoV-2 virions, I studied the localization of internalized particles by imaging techniques. In contrast to the identification of SARS-CoV-2 particles in infected Vero cells reported elsewhere[454,461], I observed by TEM that internalized viral particles in macrophages reside within intracellular compartments and not throughout the cytosol (Figures 7.3C and 7.6C). This detection resembled that reported in dendritic cells[420]. I then showed, in agreement with data from MDMs reported elsewhere[420], that the compartments containing SARS-CoV-2 particles are not VCC but phagolysosomes. In MDM, the modest colocalization I found between N protein and Rab5 +ve compartments has been recently reported to occur in *in vitro* M1 alveolar macrophages[416]. However, as the modest colocalization was calculated over the 6 h of viral exposure, I also measured the colocalization with Rab7 +ve compartments and lysosomes as an indication of late endosome formation and phagolysosome degradation. There was low colocalization with Rab7+ve compartments and, when analyzed the lysosomes, only half of the internalized virions showed colocalization. This can be explained by potential prevention in the maturation of early phagosomes by SARS-CoV-2 virions. This process is observed in HIV-1 and

porcine respiratory virus[445,446]. Hence, to elucidate this process, future work may involve the study of proteasomal degradation as a potential pathway for the clearance of SARS-CoV-2 virions that may have escaped from early endosomes.

7.6.3 Macrophages decrease the spread of SARS-CoV-2 virions with implications during infection in susceptible tissues

Exposure of macrophages to SARS-CoV-2 also occurs within the infected microenvironment during their interaction with susceptible cells. This may facilitate macrophage infection by changes in their polarization and/or by uptake of infected cells[371,436,437,447,462]. In other viruses, such as HIV, the latter increases the infection rates in macrophages between 100 and 1000 times and facilitates the spread across different tissues[436,463]. To test whether a similar phenomenon occurs with SARS-CoV-2, I challenged susceptible Vero CCL-81 cells cocultured with either MDM or hiPSC-MPh. Due to the role of MDM in cancer, as the main source of tumour-associated macrophages (TAMs)[457,458,464], and the nature of Vero cells, the coculture of Vero cells with hiPSC-MPh was crucial to discard potential artefacts related to macrophage cancer recognition that is independent of the presence of SARS-CoV-2. Immunostaining of SARS-CoV-2 N protein in cocultured cells showed that macrophages were not infected by cell-to-cell transfer. Similar findings have been recently reported in a coculture of HEK293-ACE2 and MDM[420]. To observe the exponential kinetics of viral replication in mono and cocultures, cells were challenged to an M.O.I. of 0.01 (Figure 7.6B). Macrophage coculture significantly reduced the output of infectious virus compared to control, challenged Vero monocultures. Other coculture systems have shown similar results[465,466] and it has been speculated that this reduction is a result of macrophage infiltration and phagocytosis mechanisms[466].

It was observed that the cocultures showed cellular aggregation at earlier times post-infection than the Vero monocultures (Figure 7.7B). This could be explained by a potential reactivity of macrophages to secreted molecules from cancerous Vero cells[464,467]. Potential cellular phagocytosis, independent of SARS-CoV-2 virions, that may correlate with the lower viral production observed in cocultures will need further investigation. To overcome this potential issue and to study disease relevant tissue models, I cocultured hiPSC-derived cardiomyocytes (hiPSC-CM) and hiPSC-MPh which showed to be stable for over 120 h. Stability of coculture systems using cells differentiated from hiPSC has been reported elsewhere[184,332,349,378]. hiPSC-MPh also reduced the replication of SARS-CoV-2 when cocultured with hiPSC-CM. This is in agreement with research reported elsewhere[378,382,466].

Overall, these results suggest that macrophages are not susceptible to SARS-CoV-2 productive infection yet, the relevance of these cells in the pathogenesis of SARS-CoV-2 may be by either the degradation of circulating virions or the phagocytosis of productively infected cells. Future steps in understanding the role of macrophages within the SARS-CoV-2 infected tissue may require the coculture of susceptible non-immune cells with both hiPSC-MPh and MDM.

7.7 CONCLUSION

ACE2-expressing infiltrating macrophages (MDM) show abortive infection by SARS-CoV-2. Measurement of viral replication and release over two weeks and the peculiar punctate detection of virions seen by immunofluorescence (IF), showed that, in contrast to susceptible Vero cells, macrophages do not release new virions. Transmission electron microscopy sections of these cells show limited distribution of internalized virions within intracellular compartments. The modest colocalization of SARS-CoV-2 N protein and Rab 5+ve compartments suggests that macrophage uptake of viral particles occurs via phagocytosis. Low colocalization of SARS-CoV-2 N protein and Rab7 +ve compartments and, the low percentage of infected macrophages containing colocalized SARS-CoV-2 N protein and lysosomes suggest that: a) phagosome degradation may occur after 6 h post-challenge or, b) the virus is able to decrease or inhibit phagosome maturation. Similar results obtained in tissue-resident-like macrophages (hiPSC-MPh) suggest that both macrophage types are not directly infected by SARS-CoV-2 virions with potential implications in the progression of the COVID-19 disease.

SARS-CoV-2 exposure of coculture systems comprised of susceptible cells and MDM or hiPSC-MPh show a significant reduction in the viral replication compared to susceptible monocultures. In addition, IF analysis of the challenged cocultures suggest that macrophages are integrated to the sites of infected Vero cells but do not show signs of infection. Overall, these data suggest that tissue-resident and infiltrating macrophages a) phagocytize SARS-CoV-2 virions, b) are not susceptible to SARS-CoV-2 direct or indirect infection and, c) have a protective role in SARS-CoV-2 infected tissues by the reduction of the viral load and/or viral replication rates, thus preventing infection in neighbouring susceptible cells.

7.7.1 Limitations of the current research

The research on SARS-CoV-2 presented in this thesis showed similar *in vitro* limitations to those mentioned above for the ZIKV work. In addition, other limitations of this work were the restricted working times, access to certain facilities and, the legally approved methods for conducting the SARS-CoV-2 work outside the containment level 3 facility as this research was conducted handling “live viruses”. In addition, the lack of repeats in the cardiomyocyte coculture was due to cells being provided by collaborators. As observed in the ZIKV research, due to super resolution microscopy potentially revealing in more detail cytosolic compartment distributions; I used this method for the colocalization analysis with proteins of the superfamily of Rabs. I conducted the colocalization with lysosomes by imaging flow cytometry due to time constrains. Lastly, another potential limitation is the background detection of SARS-CoV-2 by the staining of N protein using an RBD-Fc. However, this compound showed better affinity and lower background levels than commercial antibodies tested during early stages of the pandemic.

7.7.2 Summary and future work

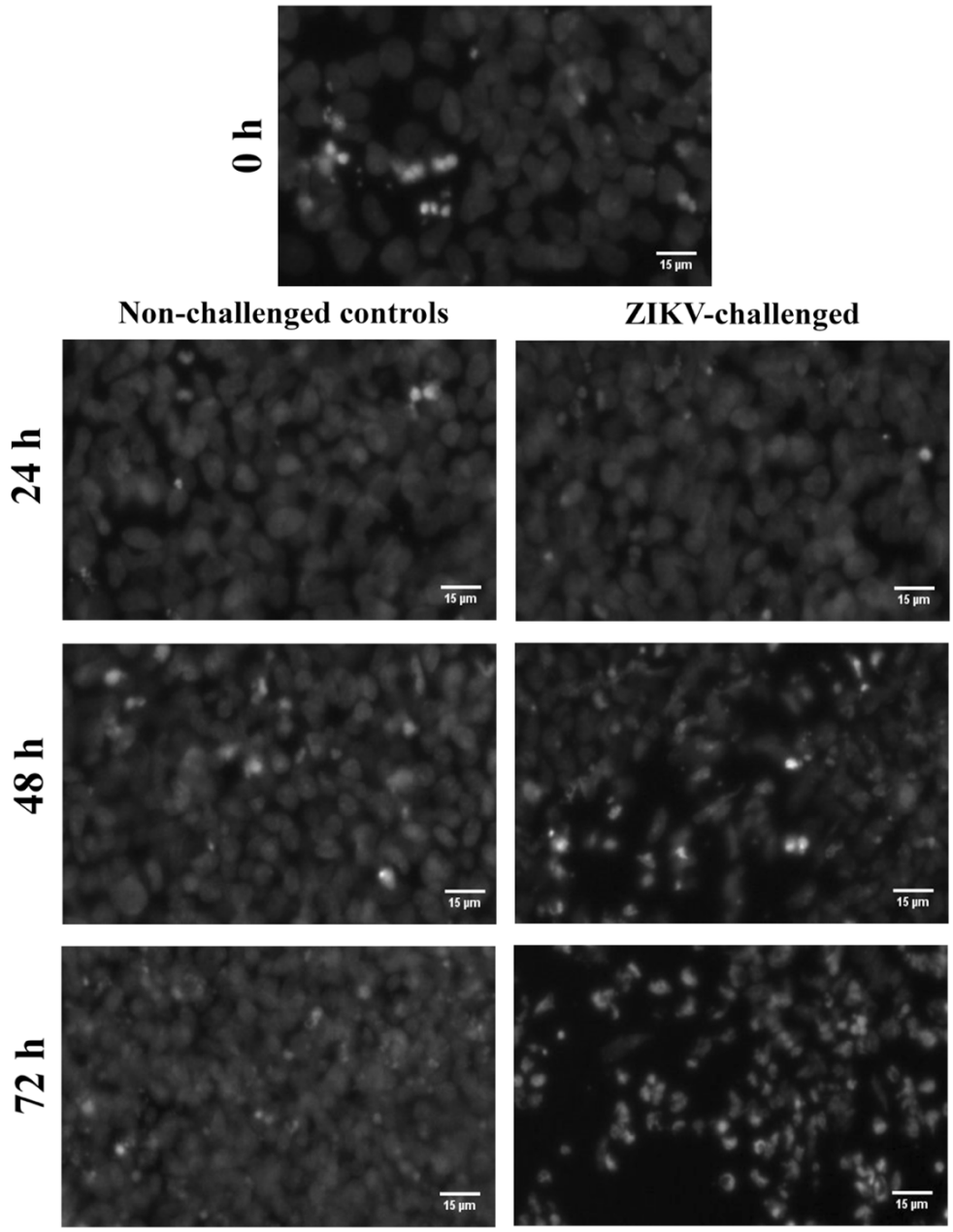
The SARS-CoV-2 work presented in this thesis consisted of a detailed analysis of the controversial fate of SARS-CoV-2 virions in macrophages. This work revealed the phagolysosome degradation of SARS-CoV-2 virions by tissue-resident-like and peripheral macrophages and its implication in reducing viral replication within susceptible cells. Future work to improve this research may focus on generating similar data in hiPSC-MPh and MDM to elucidate whether distinct populations of macrophages may show differences in the processing to SARS-CoV-2 virions. Also, as one can speculate that due to low colocalization with Rab 7 +ve compartments

and lysosomes, some virions may be capable of delaying the maturation of the phagolysosomes, this work can benefit from investigations on whether SARS-CoV-2 virions — which potentially escape from early endosomes — are targeted for proteasomal degradation as a mechanism of viral clearance. Also, approaches such as drug inhibition of lysosome acidification (e.g., hydroxychloroquine) can be used to confirm whether macrophages degrade virions by this mechanism. Measurements of cytokines relevant in the cytokine storm (e.g., IL-6) can support the work in the coculture systems to better understand the pathogenesis of SARS-CoV-2. Lastly, more repeats of the SARS-CoV-2 challenges in the cardiomyocyte coculture are required and the translation of this to a coculture involving pneumocytes may reveal a broader role of macrophages across susceptible tissues highly affected in severe COVID-19 patients.

8. ADDITIONAL MATERIALS

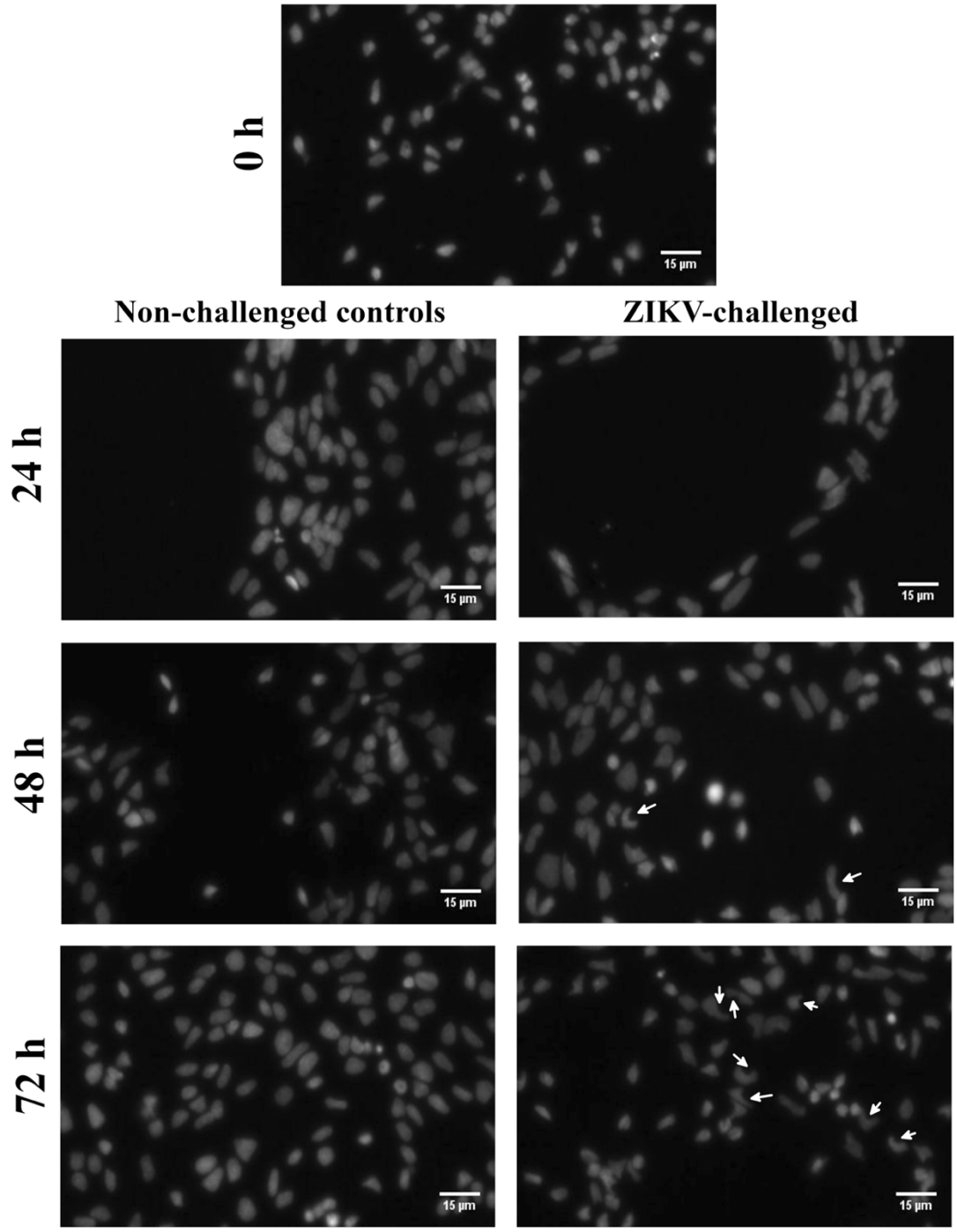
8.1 FIGURES

8.1.1 Nuclear staining in early hi-NPCs



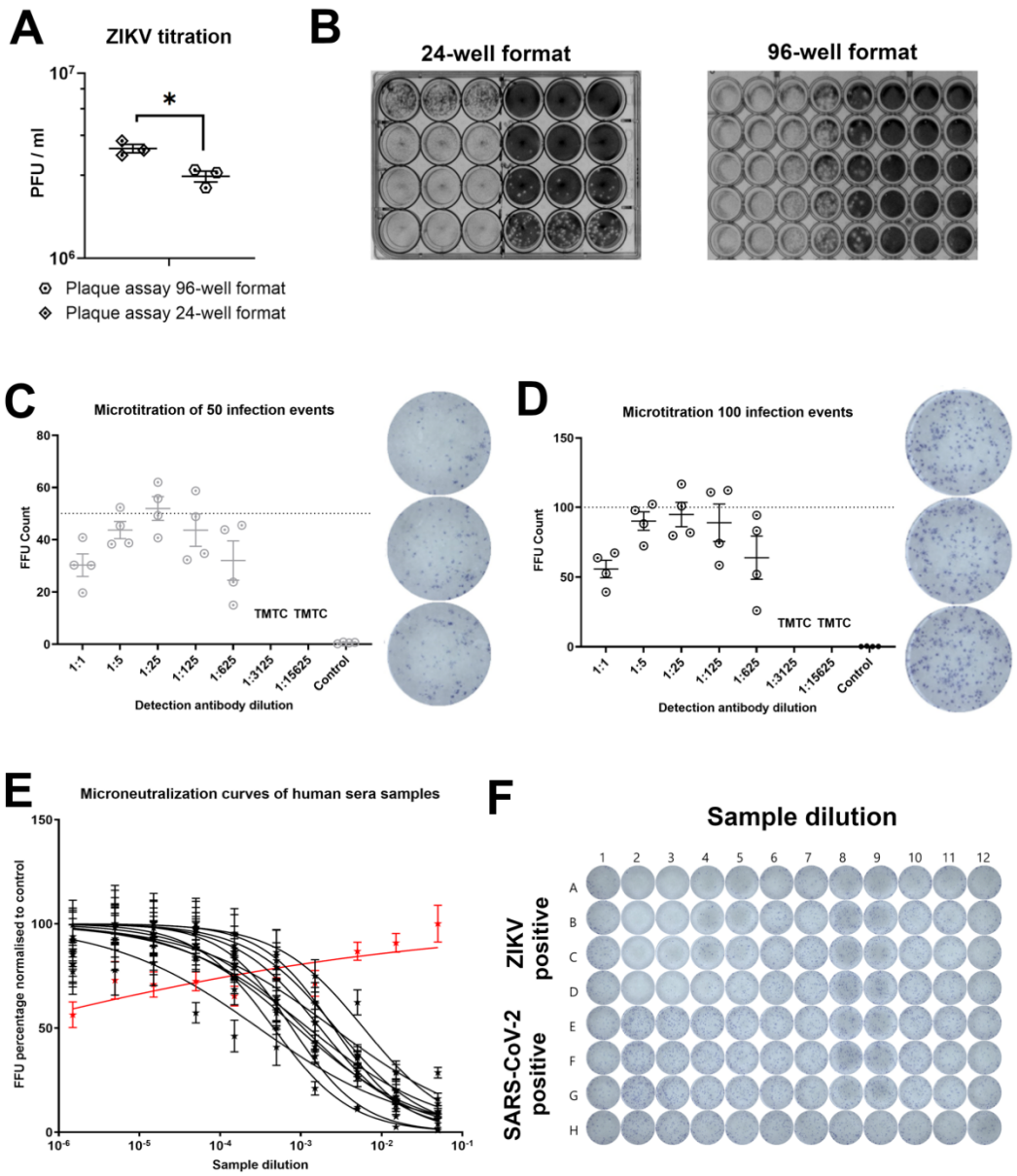
Supplementary Figure 1. ZIKV infection causes nuclear damage in early hi-NPCs
Imaging (40x) of the nuclei of early hi-NPCs challenged to ZIKV over the course of 72 hours and the respective non-challenged controls. Nuclei were stained with DAPI.

8.1.2 Nuclear staining in late hi-NPCs



Supplementary Figure 2. ZIKV show perinuclear replication sites in infected late hi-NPCs
Imaging (40x) of the nuclei of late hi-NPCs challenged to ZIKV over the course of 72 hours and the respective non-challenged controls. Nuclei were stained with DAPI. White arrows highlighting potential sites of viral factories.

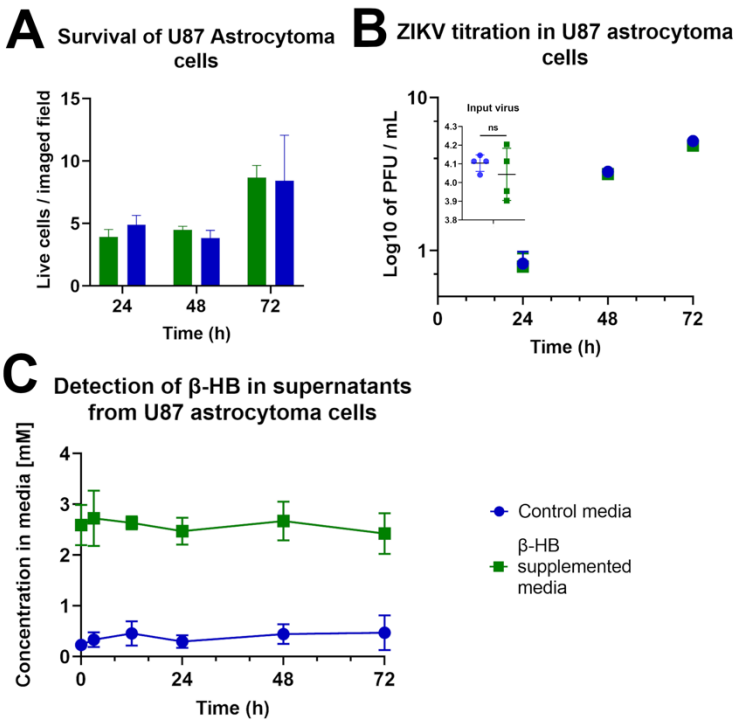
8.1.3 Development of a microtitration assay for the quantification of ZIKV



Supplementary Figure 3. Human ZIKV seropositive samples validate a large-scale high-throughput method for the quantification of ZIKV

(A) Dot plots showing the differences in the detection between the plaque assay developed in a 24-well versus a 96-well format. Bars display mean ± SD. n = 3 independent experiments conducted in triplicates and five replicates per experiment (24-well and 96-well, respectively). Significance was calculated by unpaired t-test. (B) Illustrative images showing the plaque formation in both well plate formats. Dot plots showing the quantification of Zika virions by foci forming unit assay using 4G2 as primary detection antibody. Based on the plaque assay an estimated count of 50 FFU (C) and 100 FFU (D). Bars display mean ± SD. n = 4 independent experiments each conducted in four replicates. Significance was calculated by one-way ANOVA with Tukey's multiple comparisons test. (E) Microneutralization the EC50 curves of human ZIKV+ve/SARS-CoV-2-ve (black) and SARS-CoV-2 +ve/ZIKV-ve (red) sera samples. Bars display mean ± SD. n = 1 experiment conducted in four replicates per dilution. (F) Example of a microtitration plate showing the foci forming units. Significance is shown when $^{*}p < 0.05$, $^{**}p < 0.01$, $^{***}p < 0.001$.

8.1.4 Ketone bodies as potential nutritional therapeutics for ZIKV pathology



Supplementary Figure 4. U87 astrocytoma cells do not uptake ketone body beta-hydroxybutyrate (BHB)

Figure showing U87 astrocytoma cells cultured in a media with composition similar to the human adult CSF with and without supplementation of beta-hydroxybutyrate (BHB). (A) Bar graphs showing cell survival. (B) Dot plots showing the production of ZIKV by U87 astrocytoma cells. Inset showing the input virus per mL). Cells were challenged for 2 h at 37 °C using an M.O.I. of 1. Line graphs showing the detection of BHB from the supernatant of U87 astrocytoma cells. Bars displaying mean ± SD. n = 4 independent experiments each analyzed in duplicates. Significance was calculated by mixed-effects model with Šidák's multiple comparisons test. Significance is shown when $^{*}p < 0.05$, $^{**}p < 0.01$, $^{***}p < 0.001$, $^{***}p < 0.0001$.

8.2 TABLES

Supplementary Table 1.

	Sample 1	Sample 2	Sample 3	Sample 4	Sample 5	Sample 6
R squared	0.6863	0.7735	0.7421	0.9012	0.8050	0.8566
95% CI	-0.8151 to -0.3625	-1.258 to -0.5400	-1.471 to -0.5193	-0.7358 to -0.4827	-0.9445 to -0.4770	-0.5843 to -0.3795
Hill slope	-0.5362	-0.8040	-0.8341	-0.5927	-0.6595	-0.4705
	Sample 7	**Sample 8**	**Sample 9**	**Sample 10**	**Sample 11**	**Sample 12**
R squared	0.6977	0.9209	0.6751	0.9353	0.7925	0.3925
95% CI	-1.366 to -0.5053	-1.248 to -0.6973	-0.7320 to -0.3402	-1.289 to -0.7912	-1.533 to -0.6562	0.09305 to 0.2381
Hill slope	-0.8156	-0.9100	-0.4983	-0.9978	-0.9785	0.1611

Summary NT50 values of human ZIKV +ve / ZIKV -ve sera samples
Summary of the NT50 values in terms of correlation coefficients (R squared), confidence intervals (95% CI) and, Hill slope calculations between ZIKV+ve and ZIKV-ve sera samples.

8.3 SCIENTIFIC CONTRIBUTIONS DURING MY DPHIL

Year 2022

ADRIANA TOMIC, DONAL T. SKELLY, ANE OGBE, DANIEL O'CONNOR, MATTHEW PACE, EMILY ADLAND, FRANCES ALEXANDER, MOHAMMAD ALI, KIRK ALLOTT, M. AZIM ANSARI, SANDRA BELIJ-RAMMERSTORFER, SAGIDA BIBI, LUKE BLACKWELL, ANTHONY BROWN, HELEN BROWN, BREEZE CAVELL, ELIZABETH A. CLUTTERBUCK, THUSHAN DE SILVA, DAVID EYRE, SHEILA LUMLEY, AMY FLAXMAN, JAMES GRIST, CARL-PHILIPP HACKSTEIN, RACHEL HALKERSTON, ADAM C. HARDING, JENNIFER HILL, TIM JAMES, CECILIA JAY, SÍLE A. JOHNSON, BARBARA KRONSTEINER, YOLANDA LIE, ALINE LINDER, STEPHANIE LONGET, SPYRIDOULA MARINOU, PHILIPPA C. MATTHEWS, JACK MELLORS, CHRISTOS PETROPOULOS, PATPONG RONGKARD, CYNTHIA SEDIK, LAURA SILVA-REYES, HOLLY SMITH, LISA STOCKDALE, STEPHEN TAYLOR, STEPHEN THOMAS, TIMOTHY TIPOE, LANCE TURTLE, VINICIUS ADRIANO VIEIRA, TERRI WRIN, LIZZIE STAFFORD, HIBATULLAH ABUELGASIM, AHMED ALHUSSNI, CAROLINA V. ARANCIBIA-CÁRCAMO, MARTYNA BORAK, JOSEPH CUTTERIDGE, ALEXANDRA DEEKS, LUCY DENLY, STAVROS DIMITRIADIS, SHAYAN FASSIH, THOMAS FOORD, THOMAS FORDWOH, JENNIFER HOLMES, BRYN HORSINGTON, SVEN KERNEIS, DAVID KIM, KATY LILLIE, SHEILA LUMLEY, JORDAN MORROW, DENISE O'DONNELL, THOMAS G. RITTER, BEATRICE SIMMONS, ADAN TAYLOR, SARAH R. THOMAS, YOLANDA WARREN, ADAM J. R. WATSON, ESME WEEKS, ROBERT WILSON, REBECCA YOUNG, CHRISTOPHER J. A. DUNCAN, SHONA C. MOORE, REBECCA PAYNE, ALEX RICHTER, SARAH ROWLAND-JONES, ALEXANDER J. MENTZER, MARK PHILIP CASSAR, TAO DONG, ANASTASIA FRIES, **JAVIER GILBERT-JARAMILLO**, LING-PEI HO, JULIAN C. KNIGHT, STEFAN NEUBAUER, YANCHUN PENG, NAYIA PETOUSI, BETTY RAMAN, NICK P. TALBOT, ANDREW J. POLLARD, TERESA LAMBE, CHRIS P. CONLON, KATIE JEFFERY, SIMON TRAVIS, PHILIP GOULDER, JOHN FRATER, ALEX J. MENTZER, LIZZIE STAFFORD, MILES W. CARROLL, WILLIAM S. JAMES, PAUL KLENERMAN, ELEANOR BARNES, CHRISTINA DOLD & SUSANNA J. DUNACHIE, 2022. Divergent trajectories of antiviral memory after SARS-CoV-2 infection. Nature Communications **13,** 1251.

ANGYAL, A., LONGET, S., MOORE, S.C., PAYNE, R.P., HARDING, A., TIPTON, T., RONGKARD, P., ALI, M., HERING, L.M., MEARDON, N., AUSTIN, J., BROWN, R., SKELLY, D., GILLSON, N., DOBSON, S.L., CROSS,

A., SANDHAR, G., KILBY, J.A., TYERMAN, J.K., NICOLS, A.R., SPEGAROVA, J.S., MEHTA, H., HORNSBY, H., WHITHAM, R., CONLON, C.P., JEFFERY, K., GOULDER, P., FRATER, J., DOLD, C., PACE, M., OGBE, A., BROWN, H., ANSARI, M.A., ADLAND, E., BROWN, A., CHAND, M., SHIELDS, A., MATTHEWS, P.C., HOPKINS, S., HALL, V., JAMES, W., ROWLAND-JONES, S.L., KLENERMAN, P., DUNACHIE, S., RICHTER, A., DUNCAN, C.J.A., BARNES, E., CARROLL, M., TURTLE, L., DE SILVA, T.I., WATSON, A., ALHUSSNI, A., NICOLS, A., DEEKS, A., WEBB-BRIDGES, A., JÄMSÉN, A., CHAWLA, A., DUNCAN, C., CONLON, C., O'DONNELL, D., WEEKS, E., ABUELGASIM, H., XIAO, H., SPEGAROVA, J., HOLMES, J., HAWORTH, J., TYERMAN, J., KILBY, J., CUTTERIDGE, J., LILLIE, K., ROMANIUK, L., DENLY, L., HERING, L., ANSARI, M.A., KASANYINGA, M., MATTHEWS, P., PAYNE, R., WILSON, R., ROWLAND-JONES, S., THOMAS, S., MOORE, S., GARDINER, S., TUCKER, S., DOBSON, S., ADLOU, S., DE SILVA, T., LAWRIE, A., SMITH, N., TURTON, H., ZAWIA, A., BAYLEY, M., FAIRMAN, A., HARRINGTON, K., KIRK, R., MARSH, L., WATSON, L., WOOD, S., DIFFEY, B., JONES, C., LETT, L., PLATT, G., SUBRAMANIAM, K., WOOTTON, D., PAYNE, B., HAMBLETON, S., KELLY, S., MARSTON, J., POOLAN, S., TURNER, D., HANIFFA, M., STEPHENSON, E., ADELE, S., AKHTER, H.D., CHINNAKANNAN, S., DE LARA, C., DONNISON, T., HACKSTEIN, C.-., LEE, L., LIM, N., MALONE, T., PHILLIPS, E., RAMAMURTHY, N., ROBINSON, N., SAMPSON, O., EYRE, D., SIMMONS, B., STAFFORD, L., MENTZER, A., AMINI, A., ARANCIBIA-CÁRCAMO, C., PROVINE, N., TRAVIS, S., DIMITRIADIS, S., JOHNSON, S., FOULKES, S., KHAWAM, J., WELLINGTON, E., **GILBERT-JARAMILLO, J.,** KNIGHT, M., DUPONT, M., HORNER, E., THAVENTHIRAN, J. and CHALK, J., 2022. T-cell and antibody responses to first BNT162b2 vaccine dose in previously infected and SARS-CoV-2-naive UK health-care workers: a multicentre prospective cohort study. The Lancet Microbe, 3(1), pp. e21-e31.

HUANG, K.-.A., ZHOU, D., TAN, T.K., CHEN, C., DUYVESTEYN, H.M.E., ZHAO, Y., GINN, H.M., QIN, L., RIJAL, P., SCHIMANSKI, L., DONAT, R., HARDING, A., **GILBERT-JARAMILLO, J**., JAMES, W., TREE, J.A., BUTTIGIEG, K., CARROLL, M., CHARLTON, S., LIEN, C.-., LIN, M.-., CHEN, C.-., CHENG, S.-., CHEN, X., LIN, T.-., FRY, E.E., REN, J., MA, C., TOWNSEND, A.R. and STUART, D.I., 2022. Structures and therapeutic potential of anti-RBD human monoclonal antibodies against SARS-CoV-2. Theranostics, 27(1), pp. 1-17.

QIANG, M., MA, P., LI, Y., LIU, H., HARDING, A., MIN, C., WANG, F., LIU, L., YUAN, M., JI, Q., TAO, P., SHI, X., LI, Z., LI, T., WANG, X., ZHANG, Y., WU, N.C., LEE, C.-.D., ZHU, X., **GILBERT-JARAMILLO, J**., ZHANG, C., SAXENA, A., HUANG, X., WANG, H., JAMES, W., DWEK, R.A., WILSON, I.A., YANG, G. and LERNER, R.A., 2022. Neutralizing Antibodies to SARS-CoV-2 Selected

from a Human Antibody Library Constructed Decades Ago. Advanced Science, 9(1),.

Year 2021

SKELLY, D.T., HARDING, A.C., **GILBERT-JARAMILLO, J**., KNIGHT, M.L., LONGET, S., BROWN, A., ADELE, S., ADLAND, E., BROWN, H., CHINNAKANNAN, S., DONNISON, T., ALI, M., RONGKARD, P., PACE, M., ZACHAROPOULOU, P., ROBINSON, N., CSALA, A., DE LARA, C., HUTCHINGS, C.L., MEHTA, H., LEE, L.N., EDMANS, M., HACKSTEIN, C.-., PHALORA, P., LI, W., PHILLIPS, E., MALONE, T., OGBE, A., JAY, C., TIPOE, T., TIPTON, T., STAFFORD, L., MENTZER, A.J., JOHNSON, S.A., AMINI, A., MARJOT, T., DIMITRIADIS, S., SIMMONS, B., DEEKS, A., KERNEIS, S., ABUELGASIM, H., WILSON, R., THOMAS, S.R., WATSON, A., ALHUSSNI, A., CUTTERIDGE, J., WEEKS, E., DENLY, L., LILLIE, K., HOLMES, J., MATTHEWS, P.C., O'DONNELL, D., TAN, T.K., SCHIMANSKI, L., HUANG, K.-.A., RIJAL, P., TURTLE, L., DE SILVA, T., RICHTER, A., DUNCAN, C.J.A., PAYNE, R.P., MOORE, S.C., KNIGHT, J.C., CASSAR, M.P., RAMAN, B., NEUBAUER, S., FRIES, A., TALBOT, N.P., PETOUSI, N., HO, L.-., PENG, Y., DONG, T., CAMARA, S., MARINOU, S., LINDER, A., ADLOU, S., KASANYINGA, M., BRIDGES-WEBB, A., HILL, J., SILVA-REYES, L., BLACKWELL, L., FRATER, J., GOULDER, P., CONLON, C.P., JEFFERY, K., DOLD, C., POLLARD, A.J., SIGAL, A., DE OLIVEIRA, T., TOWNSEND, A.R., KLENERMAN, P., DUNACHIE, S.J., BARNES, E., CARROLL, M.W. and JAMES, W.S., 2021. Two doses of SARS-CoV-2 vaccination induce robust immune responses to emerging SARS-CoV-2 variants of concern. Nature Communications, 12(1).

VAUGHAN-JACKSON, A., STODOLAK, S., EBRAHIMI, K.H., BROWNE, C., REARDON, P.K., PIRES, E., **GILBERT-JARAMILLO, J.,** COWLEY, S.A. and JAMES, W.S., 2021. Differentiation of human induced pluripotent stem cells to authentic macrophages using a defined, serum-free, open-source medium. Stem Cell Reports, 16(7), pp. 1735-1748.

CHAUVEAU, L., BRIDGEMAN, A., TAN, T.K., BEVERIDGE, R., FROST, J.N., RIJAL, P., PEDROZA-PACHECO, I., PARTRIDGE, T., **GILBERT-JARAMILLO, J**., KNIGHT, M.L., LIU, X., RUSSELL, R.A., BORROW, P., DRAKESMITH, H., TOWNSEND, A.R. and REHWINKEL, J., 2021. Inclusion of cGAMP within virus-like particle vaccines enhances their immunogenicity. EMBO reports, 22(8).

PAYNE, R.P., LONGET, S., AUSTIN, J.A., SKELLY, D.T., DEJNIRATTISAI, W., ADELE, S., MEARDON, N., FAUSTINI, S., AL-TAEI, S., MOORE, S.C.,

TIPTON, T., HERING, L.M., ANGYAL, A., BROWN, R., NICOLS, A.R., GILLSON, N., DOBSON, S.L., AMINI, A., SUPASA, P., CROSS, A., BRIDGES-WEBB, A., REYES, L.S., LINDER, A., SANDHAR, G., KILBY, J.A., TYERMAN, J.K., ALTMANN, T., HORNSBY, H., WHITHAM, R., PHILLIPS, E., MALONE, T., HARGREAVES, A., SHIELDS, A., SAEI, A., FOULKES, S., STAFFORD, L., JOHNSON, S., WOOTTON, D.G., CONLON, C.P., JEFFERY, K., MATTHEWS, P.C., FRATER, J., DEEKS, A.S., POLLARD, A.J., BROWN, A., ROWLAND-JONES, S.L., MONGKOLSAPAYA, J., BARNES, E., HOPKINS, S., HALL, V., DOLD, C., DUNCAN, C.J.A., RICHTER, A., CARROLL, M., SCREATON, G., DE SILVA, T.I., TURTLE, L., KLENERMAN, P., DUNACHIE, S., ABUELGASIM, H., ADLAND, E., ADLOU, S., AKTHER, H.D., ALHUSSNI, A., ALI, M., ANSARI, M.A., ARANCIBIA-CÁRCAMO, C.V., BAYLEY, M., BROWN, H., CHALK, J., CHAND, M., CHAWLA, A., CHINNAKANNAN, S., CUTTERIDGE, J., DE LARA, C., DENLY, L., DIFFEY, B., DIMITRIADIS, S., DRAKE, T.M., DONNISON, T., DUPONT, M., EYRE, D., FAIRMAN, A., GARDINER, S., **GILBERT-JARMILLO, J**., GOULDER, P., HACKSTEIN, C.-., HAMBLETON, S., HANIFFA, M., HAWORTH, J., HOLMES, J., HORNER, E., JÄMSÉN, A., JONES, C., KASANYINGA, M., KELLY, S., KIRK, R., KNIGHT, M.L., LAWRIE, A., LEE, L., LETT, L., LILLIE, K., LIM, N., MEHTA, H., MENTZER, A.J., O'DONNELL, D., OGBE, A., PACE, M., PAYNE, B.A.I., PLATT, G., POOLAN, S., PROVINE, N., RAMAMURTHY, N., ROBINSON, N., ROMANIUK, L., RONGKARD, P., SAMPSON, O.L., SIMMONS, B., SPEGAROVA, J.S., STEPHENSON, E., SUBRAMANIAM, K., THAVENTHIRAN, J., THOMAS, S., TRAVIS, S., TUCKER, S., TURTON, H., WATSON, A., WATSON, L., WEEKS, E., WILSON, R., WOOD, S., WRIGHT, R., XIAO, H. and ZAWIA, A.A.T., 2021. Immunogenicity of standard and extended dosing intervals of BNT162b2 mRNA vaccine. Cell, 184(23), pp. 5699-5714.e11.

DEJNIRATTISAI, W., ZHOU, D., GINN, H.M., DUYVESTEYN, H.M.E., SUPASA, P., CASE, J.B., ZHAO, Y., WALTER, T.S., MENTZER, A.J., LIU, C., WANG, B., PAESEN, G.C., SLON-CAMPOS, J., LÓPEZ-CAMACHO, C., KAFAI, N.M., BAILEY, A.L., CHEN, R.E., YING, B., THOMPSON, C., BOLTON, J., FYFE, A., GUPTA, S., TAN, T.K., **GILBERT-JARAMILLO, J.**, JAMES, W., KNIGHT, M., CARROLL, M.W., SKELLY, D., DOLD, C., PENG, Y., LEVIN, R., DONG, T., POLLARD, A.J., KNIGHT, J.C., KLENERMAN, P., TEMPERTON, N., HALL, D.R., WILLIAMS, M.A., PATERSON, N.G., BERTRAM, F.K.R., SIEBERT, C.A., CLARE, D.K., HOWE, A., RADECKE, J., SONG, Y., TOWNSEND, A.R., HUANG, K.-.A., FRY, E.E., MONGKOLSAPAYA, J., DIAMOND, M.S., REN, J., STUART, D.I. and SCREATON, G.R., 2021. The antigenic anatomy of SARS-CoV-2 receptor binding domain. Cell, 184(8), pp. 2183-2200.e22.

EBRAHIMI, K.H., **GILBERT-JARAMILLO, J**., JAMES, W.S. and MCCULLAGH, J.S.O., 2021. Interferon-stimulated gene products as regulators of central carbon metabolism. FEBS Journal, 288(12), pp. 3715-3726.

HUANG, K.-.A., TAN, T.K., CHEN, T.-., HUANG, C.-., HARVEY, R., HUSSAIN, S., CHEN, C.-., HARDING, A., **GILBERT-JARAMILLO, J**., LIU, X., KNIGHT, M., SCHIMANSKI, L., SHIH, S.-., LIN, Y.-., CHENG, C.-., CHENG, S.-., HUANG, Y.-., LIN, T.-., JAN, J.-., MA, C., JAMES, W., DANIELS, R.S., MCCAULEY, J.W., RIJAL, P. and TOWNSEND, A.R., 2021. Breadth and function of antibody response to acute SARS-CoV-2 infection in humans. PLoS Pathogens, 17(2),.

Year 2020

HUO, J., LE BAS, A., RUZA, R.R., DUYVESTEYN, H.M.E., MIKOLAJEK, H., MALINAUSKAS, T., TAN, T.K., RIJAL, P., DUMOUX, M., WARD, P.N., REN, J., ZHOU, D., HARRISON, P.J., WECKENER, M., CLARE, D.K., VOGIRALA, V.K., RADECKE, J., MOYNIÉ, L., ZHAO, Y., **GILBERT-JARAMILLO, J**., KNIGHT, M.L., TREE, J.A., BUTTIGIEG, K.R., COOMBES, N., ELMORE, M.J., CARROLL, M.W., CARRIQUE, L., SHAH, P.N.M., JAMES, W., TOWNSEND, A.R., STUART, D.I., OWENS, R.J. and NAISMITH, J.H., 2020. Neutralizing nanobodies bind SARS-CoV-2 spike RBD and block interaction with ACE2. Nature Structural and Molecular Biology, 27(9), pp. 846-854.

NORWITZ, N.G., **JARAMILLO, J.G**., CLARKE, K. and SOTO, A., 2020. Ketotherapeutics for neurodegenerative diseases.

MATTHEWS, P.C., ANDERSSON, M.I., ARANCIBIA-CARCAMO, C.V., AUCKLAND, K., BAILLIE, J.K., BARNES, E., BENEKE, T., BIBI, S., BROOKS, T., CARROLL, M., CROOK, D., DINGLE, K., DOLD, C., DOWNS, L.O., DUNN, L., EYRE, D.W., **GILBERT JARAMILLO, J**., HARVALA, H., HOOSDALLY, S., IJAZ, S., JAMES, T., JAMES, W., JEFFERY, K., JUSTICE, A., KLENERMAN, P., KNIGHT, J.C., KNIGHT, M., LIU, X., LUMLEY, S.F., MCNAUGHTON, A.L., MENTZER, A.J., MONGKOLSAPAYA, J., OAKLEY, S., OLIVEIRA, M.S., PETO, T., PLOEG, R.J., RATCLIFF, J., ROBBINS, M.J., ROBERTS, D.J., RUDKIN, J., RUSSELL, R.A., SCREATON, G., SEMPLE, M.G., SKELLY, D., SIMMONDS, P., STOESSER, N., TURTLE, L., WAREING, S. and ZAMBON, M., 2020. SARS-CoV-2 RNA detected in blood products from patients with COVID-19 is not associated with infectious virus. Wellcome Open Research, 5.

MIAO, X., LUO, Y., HUANG, X., LEE, S.M.Y., YUAN, Z., TANG, Y., CHEN, L., WANG, C., WU, F., XU, Y., JIANG, W., GAO, W., SONG, X., YAN, Y., PANG,

T., CHEN, C., ZOU, Y., FU, W., WAN, L., **GILBERT-JARAMILLO, J.,** KNIGHT, M., TAN, T.K., RIJAL, P., TOWNSEND, A., SUN, J., LIU, X., JAMES, W., TSUN, A. and XU, Y., 2020. A novel biparatopic hybrid antibody-ACE2 fusion that blocks SARS-CoV-2 infection: implications for therapy. mAbs, 12(1).

ZHOU, D., DUYVESTEYN, H.M.E., CHEN, C.-., HUANG, C.-., CHEN, T.-., SHIH, S.-., LIN, Y.-., CHENG, C.-., CHENG, S.-., HUANG, Y.-., LIN, T.-., MA, C., HUO, J., CARRIQUE, L., MALINAUSKAS, T., RUZA, R.R., SHAH, P.N.M., TAN, T.K., RIJAL, P., DONAT, R.F., GODWIN, K., BUTTIGIEG, K.R., TREE, J.A., RADECKE, J., PATERSON, N.G., SUPASA, P., MONGKOLSAPAYA, J., SCREATON, G.R., CARROLL, M.W., **GILBERT-JARAMILLO, J**., KNIGHT, M.L., JAMES, W., OWENS, R.J., NAISMITH, J.H., TOWNSEND, A.R., FRY, E.E., ZHAO, Y., REN, J., STUART, D.I. and HUANG, K.-.A., 2020. Structural basis for the neutralization of SARS-CoV-2 by an antibody from a convalescent patient. Nature Structural and Molecular Biology, 27(10), pp. 950-958.

Year 2019

GILBERT-JARAMILLO, J., GARCEZ, P., JAMES, W., MOLNÁR, Z. and CLARKE, K., 2019. The potential contribution of impaired brain glucose metabolism to congenital Zika syndrome. Journal of anatomy, 235(3), pp. 468-480.

PALMER, C.M., **GILBERT-JARAMILLO, J**. and WESTMAN, E.C., 2019. The ketogenic diet and remission of psychotic symptoms in schizophrenia: Two case studies. Schizophrenia research, 208, pp. 439-440.

PÓLIT-ARAGUNDI, M.R., DOMÍNGUEZ-BROWN, N.A., ÁLVAREZ-CÓRDOVA, L.R., ALFONSO-MIELES, H.I., GUERRERO-HARO, J.J., VALDEVILA-FIGUEIRA, J., **GILBERT-JARAMILLO, J.A.** and POVEDA-LOOR, C., 2019. Somatotype and body composition of drug addicts admitted into a dishabituation program. Revista Espanola de Nutricion Comunitaria, 25(2), pp. 48-53.

8.4 FOOTNOTES

[A] This work was done in collaboration with a fellow student from the CMRG group in DPAG-Oxford. Mr. Ujang Purnama conducted the radioactive tracing of glucose and lipid metabolism.

[B] This work was done in collaboration with a fellow student from the Sanyal's lab. Ms. Sophie Van-Leur designed the transfection experiment and prepared the required solutions.

[C] This work was done in conjunction with a former collaborator of the James lab and fellow students from the Molnár lab. I collaborated with Dr. Paul Kirk Reardon during the culture of brain organoids. Ms. Daria Iakovleva and Ms. Auguste Valdisiute assisted with the collection and, the staining and imaging of sectioned brain organoids, respectively.

[D] Sera samples were kindly provided by collaborators in Rio de Janeiro, Brazil. UNIVERSITÁRIO CLEMENTINO FRAGA FILHO DA UNIVERSIDADE FEDERAL DO RIO DE JANEIRO / HUCFF-UFRJ

[E] These results were comparable to those generated by a former post-doctoral researcher at James lab. Dr. Kourosh Ebrahimi generated the hiPSC-CRISPR-KO lines of RSAD2 I used for the differentiation of macrophages and ZIKV infection experiments.

[F] This work was designed and carried out in collaboration with the Sattentau laboratory. Sample processing and data acquisition both within and outside the Containment Level 3 facility was shared with post-doctoral researcher Dr. Maeva Dupont.

[G] The induction for the differentiation of hiPSC-CM was provided by the Carr's group (Department of Physiology, Anatomy and Genetics – DPAG, Oxford). The protocol for the differentiation of these cells has been reported elsewhere[175]. For the initial culture experiments, cells were kindly provided by members of this group.

9. BIBLIOGRAPHY

1. Folegatti PM, Ewer KJ, Aley PK, et al. Safety and immunogenicity of the ChAdOx1 nCoV-19 vaccine against SARS-CoV-2: a preliminary report of a phase 1/2, single-blind, randomised controlled trial. *Lancet*. 2020;396(10249):467-478. doi:10.1016/S0140-6736(20)31604-4
2. Zhou D, Duyvesteyn HME, Chen C-P, et al. Structural basis for the neutralization of SARS-CoV-2 by an antibody from a convalescent patient. *Nat Struct Mol Biol*. Published online July 31, 2020. doi:10.1038/s41594-020-0480-y
3. Huo J, Le Bas A, Ruza RR, et al. Neutralizing nanobodies bind SARS-CoV-2 spike RBD and block interaction with ACE2. *Nat Struct Mol Biol*. Published online July 13, 2020. doi:10.1038/s41594-020-0469-6
4. Miao X, Luo Y, Huang X, et al. A novel biparatopic hybrid antibody-ACE2 fusion that blocks SARS-CoV-2 infection: implications for therapy. *MAbs*. 2020;12(1):1804241. doi:10.1080/19420862.2020.1804241
5. Andersson MI, Arancibia-Carcamo C V., Auckland K, et al. SARS-CoV-2 RNA detected in blood products from patients with COVID-19 is not associated with infectious virus. *Wellcome Open Res*. 2020;5:181. doi:10.12688/wellcomeopenres.16002.1
6. Huang KYA, Zhou D, Tan TK, et al. Structures and therapeutic potential of anti-RBD human monoclonal antibodies against SARS-CoV-2. *Theranostics*. 2022;27(1):1-17. doi:10.7150/THNO.65563
7. Chauveau L, Bridgeman A, Tan TK, et al. Inclusion of cGAMP within virus-like particle vaccines enhances their immunogenicity. *EMBO Rep*. 2021;22(8):e52447. doi:10.15252/EMBR.202152447
8. Dejnirattisai W, Zhou D, Ginn HM, et al. The antigenic anatomy of SARS-CoV-2 receptor binding domain. *Cell*. 2021;184(8):2183-2200.e22. doi:10.1016/J.CELL.2021.02.032/ATTACHMENT/4DE65DC1-1C0E-4A7E-9F07-E5915CEB2AD3/MMC1.PDF
9. Huang KYA, Tan TK, Chen TH, et al. Breadth and function of antibody response to acute SARS-CoV-2 infection in humans. *PLOS Pathog*. 2021;17(2):e1009352. doi:10.1371/JOURNAL.PPAT.1009352
10. Payne RP, Longet S, Austin JA, et al. Immunogenicity of standard and extended dosing intervals of BNT162b2 mRNA vaccine. *Cell*. 2021;184(23):5699-5714.e11. doi:10.1016/J.CELL.2021.10.011/ATTACHMENT/5FFE31AD-402D-408E-9E4B-A4F4BE933A25/MMC1.PDF
11. Qiang M, Ma P, Li Y, et al. Neutralizing Antibodies to SARS-CoV-2 Selected from a Human Antibody Library Constructed Decades Ago. *Adv Sci*. 2022;9(1):2102181. doi:10.1002/ADVS.202102181
12. Skelly DT, Harding AC, Gilbert-Jaramillo J, et al. Two doses of SARS-CoV-2 vaccination induce robust immune responses to emerging SARS-CoV-2 variants of concern. *Nat Commun 2021 121*. 2021;12(1):1-12. doi:10.1038/s41467-021-25167-5
13. Angyal A, Longet S, Moore SC, et al. T-cell and antibody responses to first BNT162b2 vaccine dose in previously infected and SARS-CoV-2-naive UK health-care workers: a multicentre prospective cohort study. *The Lancet Microbe*. 2022;3(1):e21-e31. doi:10.1016/S2666-5247(21)00275-5
14. Vasilakis N, Weaver SC. Flavivirus transmission focusing on Zika. *Curr Opin Virol*. 2017;22:30-35. doi:10.1016/j.coviro.2016.11.007
15. GW D, SF K, AJ H. Zika virus. I. Isolations and serological specificity. *Trans R Soc Trop Med Hyg*. 1952;46(5):509-520. doi:10.1016/0035-9203(52)90042-4

16. Platt DJ, Miner JJ. Consequences of congenital Zika virus infection. *Curr Opin Virol*. 2017;27:1. doi:10.1016/J.COVIRO.2017.09.005
17. Wen Z, Song H, Ming GL. How does Zika virus cause microcephaly? *Genes Dev*. 2017;31(9):849. doi:10.1101/GAD.298216.117
18. Dang J, Tiwari SK, Lichinchi G, et al. Zika Virus Depletes Neural Progenitors in Human Cerebral Organoids through Activation of the Innate Immune Receptor TLR3. *Cell Stem Cell*. 2016;19(2):258-265. doi:10.1016/j.stem.2016.04.014
19. Gomes E. Zika virus and microcephaly: A review of the molecular interactions Dermatophytes Transcription Factors and Cell signalling View project. doi:10.15761/IMM.1000392
20. Christian KM, Song H, Ming G. Pathophysiology and Mechanisms of Zika Virus Infection in the Nervous System. *Annu Rev Neurosci*. 2019;42(1):249-269. doi:10.1146/annurev-neuro-080317-062231
21. Duffy MR, Chen T-H, Hancock WT, et al. Zika virus outbreak on Yap Island, Federated States of Micronesia. *N Engl J Med*. 2009;360(24):2536-2543. doi:10.1056/NEJMOA0805715
22. Cauchemez S, Besnard M, Bompard P, et al. Association between Zika virus and microcephaly in French Polynesia, 2013-15: a retrospective study. *Lancet (London, England)*. 2016;387(10033):2125-2132. doi:10.1016/S0140-6736(16)00651-6
23. Kleber de Oliveira W, Cortez-Escalante J, De Oliveira WTGH, et al. Increase in Reported Prevalence of Microcephaly in Infants Born to Women Living in Areas with Confirmed Zika Virus Transmission During the First Trimester of Pregnancy - Brazil, 2015. *MMWR Morb Mortal Wkly Rep*. 2016;65(9):242-247. doi:10.15585/MMWR.MM6509E2
24. Pacheco O, Beltrán M, Nelson CA, et al. Zika Virus Disease in Colombia - Preliminary Report. *N Engl J Med*. 2020;383(6):e44. doi:10.1056/NEJMOA1604037
25. Faheem M, Naseer MI, Rasool M, et al. Molecular genetics of human primary microcephaly: an overview. *BMC Med Genomics*. 2015;8(Suppl 1):S4. doi:10.1186/1755-8794-8-S1-S4
26. Woods CG. Human microcephaly. *Curr Opin Neurobiol*. 2004;14(1):112-117. doi:10.1016/J.CONB.2004.01.003
27. Dienel GA, Hertz L. Glucose and lactate metabolism during brain activation. *J Neurosci Res*. 2001;66(5):824-838. doi:10.1002/JNR.10079
28. Owen OE, Morgan AP, Kemp HG, Sullivan JM, Herrera MG, Cahill GF. Brain Metabolism during Fasting. *J Clin Invest*. 1967;46(10):1589. doi:10.1172/JCI105650
29. Hofmann K, Rodriguez-Rodriguez R, Gaebler A, Casals N, Scheller A, Kuerschner L. Astrocytes and oligodendrocytes in grey and white matter regions of the brain metabolize fatty acids. *Sci Rep*. 2017;7(1). doi:10.1038/S41598-017-11103-5
30. Falkowska A, Gutowska I, Goschorska M, Nowacki P, Chlubek D, Baranowska-Bosiacka I. Energy Metabolism of the Brain, Including the Cooperation between Astrocytes and Neurons, Especially in the Context of Glycogen Metabolism. *Int J Mol Sci*. 2015;16(11):25959. doi:10.3390/IJMS161125939
31. Barbeito-Andrés J, Schuler-Faccini L, Garcez PP. Why is congenital Zika syndrome asymmetrically distributed among human populations? Riley S, ed. *PLOS Biol*. 2018;16(8):e2006592. doi:10.1371/journal.pbio.2006592
32. Olagnier D, Muscolini M, Coyne CB, Diamond MS, Hiscott J. Mechanisms of Zika Virus Infection and Neuropathogenesis. *DNA Cell Biol*. 2016;35(8):367-372. doi:10.1089/dna.2016.3404
33. Alliot F, Godin I, Pessac B. Microglia derive from progenitors, originating from the yolk sac, and which proliferate in the brain. *Dev Brain Res*. 1999;117(2):145-152. doi:10.1016/S0165-3806(99)00113-3
34. Gomez Perdiguero E, Klapproth K, Schulz C, et al. Tissue-resident macrophages originate from yolk-sac-derived erythro-myeloid progenitors. *Nature*. 2015;518(7540):547-551. doi:10.1038/nature13989

35. Molnár Z, Clowry GJ, Šestan N, et al. New insights into the development of the human cerebral cortex. *J Anat*. 2019;235(3):432-451. doi:10.1111/joa.13055
36. Gilbert-Jaramillo J, Garcez P, James W, Molnár Z, Clarke K. The potential contribution of impaired brain glucose metabolism to congenital Zika syndrome. *J Anat*. 2019;235(3):468-480. Accessed January 23, 2022. https://onlinelibrary.wiley.com/doi/full/10.1111/joa.12959
37. Schönfeld P, Reiser G. Why does brain metabolism not favor burning of fatty acids to provide energy? - Reflections on disadvantages of the use of free fatty acids as fuel for brain. *J Cereb Blood Flow Metab*. 2013;33(10):1493. doi:10.1038/JCBFM.2013.128
38. Tracey TJ, Steyn FJ, Wolvetang EJ, Ngo ST. Neuronal Lipid Metabolism: Multiple Pathways Driving Functional Outcomes in Health and Disease. *Front Mol Neurosci*. 2018;11. doi:10.3389/FNMOL.2018.00010
39. Itoh Y, Esaki T, Shimoji K, et al. Dichloroacetate effects on glucose and lactate oxidation by neurons and astroglia in vitro and on glucose utilization by brain in vivo. *Proc Natl Acad Sci U S A*. 2003;100(8):4879. doi:10.1073/PNAS.0831078100
40. Herrero-Mendez A, Almeida A, Fernández E, Maestre C, Moncada S, Bolaños JP. The bioenergetic and antioxidant status of neurons is controlled by continuous degradation of a key glycolytic enzyme by APC/C-Cdh1. *Nat Cell Biol*. 2009;11(6):747-752. doi:10.1038/NCB1881
41. Maher F, Davies-Hill TM, Lysko PG, Henneberry RC, Simpson IA. Expression of two glucose transporters, GLUT1 and GLUT3, in cultured cerebellar neurons: Evidence for neuron-specific expression of GLUT3. *Mol Cell Neurosci*. 1991;2(4):351-360. doi:10.1016/1044-7431(91)90066-W
42. Jurcovicova J. Glucose transport in brain - effect of inflammation. *Endocr Regul*. 2014;48(1):35-48. doi:10.4149/ENDO_2014_01_35
43. Hay WW, Jr. Placental-Fetal Glucose Exchange and Fetal Glucose Metabolism. *Trans Am Clin Climatol Assoc*. 2006;117:321. Accessed March 4, 2022. /pmc/articles/PMC1500912/
44. Camandola S, Mattson MP. Focus: Metabolism: Brain metabolism in health, aging, and neurodegeneration. *EMBO J*. 2017;36(11):1474. doi:10.15252/EMBJ.201695810
45. Schousboe A, Scafidi S, Bak LK, Waagepetersen HS, McKenna MC. Glutamate Metabolism in the Brain Focusing on Astrocytes. *Adv Neurobiol*. 2014;11:13. doi:10.1007/978-3-319-08894-5_2
46. Pellerin L, Magistretti PJ. Glutamate uptake into astrocytes stimulates aerobic glycolysis: a mechanism coupling neuronal activity to glucose utilization. *Proc Natl Acad Sci U S A*. 1994;91(22):10625. doi:10.1073/PNAS.91.22.10625
47. Grabacka M, Pierzchalska M, Dean M, Reiss K. Regulation of Ketone Body Metabolism and the Role of PPARα. *Int J Mol Sci*. 2016;17(12). doi:10.3390/IJMS17122093
48. Magistretti PJ, Pellerin L. Cellular mechanisms of brain energy metabolism and their relevance to functional brain imaging. *Philos Trans R Soc Lond B Biol Sci*. 1999;354(1387):1155-1163. doi:10.1098/RSTB.1999.0471
49. Thevenet J, De Marchi U, Domingo JS, et al. Medium-chain fatty acids inhibit mitochondrial metabolism in astrocytes promoting astrocyte-neuron lactate and ketone body shuttle systems. *FASEB J*. 2016;30(5):1913-1926. doi:10.1096/FJ.201500182
50. Bougneres PF, Lemmel C, Ferre P, Bier DM. Ketone body transport in the human neonate and infant. *J Clin Invest*. 1986;77(1):42. doi:10.1172/JCI112299
51. Cotter DG, D'Avignon DA, Wentz AE, Weber ML, Crawford PA. Obligate Role for Ketone Body Oxidation in Neonatal Metabolic Homeostasis. *J Biol Chem*. 2011;286(9):6902. doi:10.1074/JBC.M110.192369
52. Blomqvist G, Stone-Elander S, Halldin C, et al. Positron emission tomographic measurements of cerebral glucose utilization using [1-11C]D-glucose. *J Cereb*

Blood Flow Metab. 1990;10(4):467-483. doi:10.1038/JCBFM.1990.89
53. Agostini M, Romeo F, Inoue S, et al. Metabolic reprogramming during neuronal differentiation. *Cell Death Differ 2016 239*. 2016;23(9):1502-1514. doi:10.1038/cdd.2016.36
54. Ioannou MS, Liu Z, Lippincott-Schwartz J. A Neuron-Glia Co-culture System for Studying Intercellular Lipid Transport. *Curr Protoc Cell Biol*. 2019;84(1). doi:10.1002/CPCB.95
55. Maffezzini C, Calvo-Garrido J, Wredenberg A, Freyer C. Metabolic regulation of neurodifferentiation in the adult brain. *Cell Mol Life Sci 2020 7713*. 2020;77(13):2483-2496. doi:10.1007/S00018-019-03430-9
56. Kuzawa CW, Chugani HT, Grossman LI, et al. Metabolic costs and evolutionary implications of human brain development. *Proc Natl Acad Sci U S A*. 2014;111(36):13010-13015. doi:10.1073/PNAS.1323099111/-/DCSUPPLEMENTAL
57. Vannucci RC, Vannucci SJ. Glucose metabolism in the developing brain. *Semin Perinatol*. 2000;24(2):107-115. doi:10.1053/SP.2000.6361
58. Knobloch M, Jessberger S. Metabolism and neurogenesis. *Curr Opin Neurobiol*. 2017;42:45-52. doi:10.1016/j.conb.2016.11.006
59. Knobloch M. The Role of Lipid Metabolism for Neural Stem Cell Regulation. *Brain Plast*. 2017;3(1):61-71. doi:10.3233/bpl-160035
60. Knobloch M, Pilz GA, Ghesquière B, et al. A Fatty Acid Oxidation-Dependent Metabolic Shift Regulates Adult Neural Stem Cell Activity. *Cell Rep*. 2017;20(9):2144-2155. doi:10.1016/j.celrep.2017.08.029
61. Kok RD, Van Den Bergh AJ, Heerschap A, Nijland R, Van Den Berg PP. Transactions of the twenty-first annual meeting of the society for maternal-fetal medicine: Metabolic information from the human fetal brain obtained with proton magnetic resonance spectroscopy. In: *American Journal of Obstetrics and Gynecology*. Vol 185. Mosby Inc.; 2001:1011-1015. doi:10.1067/mob.2001.117677
62. Rambold AS, Pearce EL. Mitochondrial Dynamics at the Interface of Immune Cell Metabolism and Function. *Trends Immunol*. 2018;39(1):6-18. doi:10.1016/j.it.2017.08.006
63. Schiller M, Ben-Shaanan TL, Rolls A. Neuronal regulation of immunity: why, how and where? *Nat Rev Immunol*. 2020;21(1):20-36. doi:10.1038/s41577-020-0387-1
64. Hayes EB. Zika virus outside Africa. *Emerg Infect Dis*. 2009;15(9):1347-1350. doi:10.3201/EID1509.090442
65. Chen LH, Hamer DH. Zika Virus: Rapid Spread in the Western Hemisphere. *Ann Intern Med*. 2016;164(9):613-615. doi:10.7326/M16-0150
66. Rabaan AA, Bazzi AM, Al-Ahmed SH, Al-Ghaith MH, Al-Tawfiq JA. Overview of Zika infection, epidemiology, transmission and control measures. *J Infect Public Health*. 2017;10(2):141-149. doi:10.1016/J.JIPH.2016.05.007
67. El Costa H, Gouilly J, Mansuy JM, et al. ZIKA virus reveals broad tissue and cell tropism during the first trimester of pregnancy. *Sci Rep*. 2016;6. doi:10.1038/SREP35296
68. Garcez PP, Loiola EC, Da Costa RM, et al. Zika virus impairs growth in human neurospheres and brain organoids. *Science*. 2016;352(6287):816-818. doi:10.1126/SCIENCE.AAF6116
69. Petersen E, Wilson ME, Touch S, et al. Rapid Spread of Zika Virus in The Americas--Implications for Public Health Preparedness for Mass Gatherings at the 2016 Brazil Olympic Games. *Int J Infect Dis*. 2016;44:11-15. doi:10.1016/J.IJID.2016.02.001
70. Qian X, Nguyen HN, Song MM, et al. Brain Region-specific Organoids using Mini-bioreactors for Modeling ZIKV Exposure. *Cell*. 2016;165(5):1238. doi:10.1016/J.CELL.2016.04.032
71. Souza BSF, Sampaio GLA, Pereira CS, et al. Zika virus infection induces mitosis abnormalities and apoptotic cell death of human neural progenitor cells. *Sci Rep*.

2016;6. doi:10.1038/SREP39775
72. Tang H, Hammack C, Ogden SC, et al. Zika Virus Infects Human Cortical Neural Precursors and Attenuates Their Growth. *Cell Stem Cell*. 2016;18(5):587. doi:10.1016/J.STEM.2016.02.016
73. Bhatnagar J, Rabeneck DB, Martines RB, et al. Zika Virus RNA Replication and Persistence in Brain and Placental Tissue. *Emerg Infect Dis*. 2017;23(3):405. doi:10.3201/EID2303.161499
74. Li C, Deng YQ, Wang S, et al. 25-Hydroxycholesterol Protects Host against Zika Virus Infection and Its Associated Microcephaly in a Mouse Model. *Immunity*. 2017;46(3):446. doi:10.1016/J.IMMUNI.2017.02.012
75. Zhang N, Zhang N, Qin CF, Liu X, Shi L, Xu Z. Zika Virus Disrupts Neural Progenitor Development and Leads to Microcephaly in Mice. *Cell Stem Cell*. 2016;19(1):120-126. doi:10.1016/J.STEM.2016.04.017
76. Wu KY, Zuo GL, Li XF, et al. Vertical transmission of Zika virus targeting the radial glial cells affects cortex development of offspring mice. *Cell Res*. 2016;26(6):645-654. doi:10.1038/CR.2016.58
77. Cao B, Diamond MS, Mysorekar IU. Maternal-fetal transmission of zika virus: Routes and signals for infection. *J Interf Cytokine Res*. 2017;37(7):287-294. doi:10.1089/JIR.2017.0011/ASSET/IMAGES/LARGE/FIGURE1.JPEG
78. Nguyen SM, Antony KM, Dudley DM, et al. Highly efficient maternal-fetal Zika virus transmission in pregnant rhesus macaques. *PLOS Pathog*. 2017;13(5):e1006378. doi:10.1371/JOURNAL.PPAT.1006378
79. Brault JB, Khou C, Basset J, et al. Comparative Analysis Between Flaviviruses Reveals Specific Neural Stem Cell Tropism for Zika Virus in the Mouse Developing Neocortex. *EBioMedicine*. 2016;10:71. doi:10.1016/J.EBIOM.2016.07.018
80. Miner JJ, Diamond MS. Zika virus pathogenesis and tissue tropism. *Cell Host Microbe*. 2017;21(2):134. doi:10.1016/J.CHOM.2017.01.004
81. Ming G li, Tang H, Song H. Advances in Zika Virus Research: Stem Cell Models, Challenges and Opportunities. *Cell Stem Cell*. 2016;19(6):690. doi:10.1016/J.STEM.2016.11.014
82. Martines RB, Bhatnagar J, de Oliveira Ramos AM, et al. Pathology of congenital Zika syndrome in Brazil: a case series. *Lancet (London, England)*. 2016;388(10047):898-904. doi:10.1016/S0140-6736(16)30883-2
83. Zhang F, Hammack C, Ogden SC, et al. Molecular signatures associated with ZIKV exposure in human cortical neural progenitors. *Nucleic Acids Res*. 2016;44(18):8610. doi:10.1093/NAR/GKW765
84. Hughes BW, Addanki KC, Sriskanda AN, McLean E, Bagasra O. Infectivity of Immature Neurons to Zika Virus: A Link to Congenital Zika Syndrome. *EBioMedicine*. 2016;10:65. doi:10.1016/J.EBIOM.2016.06.026
85. Araujo AQC, Silva MTT, Araujo APQC. Zika virus-associated neurological disorders: a review. *Brain*. 2016;139(Pt 8):2122-2130. doi:10.1093/BRAIN/AWW158
86. Mlakar J, Korva M, Tul N, et al. Zika Virus Associated with Microcephaly. *N Engl J Med*. 2016;374(10):951-958. doi:10.1056/NEJMOA1600651
87. Sarno M, Sacramento GA, Khouri R, et al. Zika Virus Infection and Stillbirths: A Case of Hydrops Fetalis, Hydranencephaly and Fetal Demise. *PLoS Negl Trop Dis*. 2016;10(2). doi:10.1371/JOURNAL.PNTD.0004517
88. Merfeld E, Ben-Avi L, Kennon M, Cerveny KL. Potential mechanisms of Zika-linked microcephaly. *Wiley Interdiscip Rev Dev Biol*. 2017;6(4):273. doi:10.1002/WDEV.273
89. Adachi Y, Mochida G, Walsh C, Barkovich J. Posterior Fossa in Primary Microcephaly: Relationships between Forebrain and Mid-Hindbrain Size in 110 Patients. *Neuropediatrics*. 2014;45(2):93. doi:10.1055/S-0033-1360483
90. Azevedo FAC, Carvalho LRB, Grinberg LT, et al. Equal numbers of neuronal and nonneuronal cells make the human brain an isometrically scaled-up primate brain.

J Comp Neurol. 2009;513(5):532-541. doi:10.1002/CNE.21974
91. Lin HZ, Tambyah PA, Yong EL, Biswas A, Chan SY. A review of Zika virus infections in pregnancy and implications for antenatal care in Singapore. *Singapore Med J*. 2017;58(4):171. doi:10.11622/SMEDJ.2017026
92. Heymann DL, Hodgson A, Sall AA, et al. Zika virus and microcephaly: why is this situation a PHEIC? *Lancet (London, England)*. 2016;387(10020):719. doi:10.1016/S0140-6736(16)00320-2
93. Krow-Lucal ER, de Andrade MR, Cananéa JNA, et al. Association and birth prevalence of microcephaly attributable to Zika virus infection among infants in Paraíba, Brazil, in 2015-16: a case-control study. *Lancet Child Adolesc Heal*. 2018;2(3):205-213. doi:10.1016/S2352-4642(18)30020-8
94. Colón-González FJ, Peres CA, Steiner São Bernardo C, Hunter PR, Lake IR. After the epidemic: Zika virus projections for Latin America and the Caribbean. *PLoS Negl Trop Dis*. 2017;11(11). doi:10.1371/JOURNAL.PNTD.0006007
95. Honein MA, Dawson AL, Petersen EE, et al. Birth Defects Among Fetuses and Infants of US Women With Evidence of Possible Zika Virus Infection During Pregnancy. *JAMA*. 2017;317(1):59-68. doi:10.1001/JAMA.2016.19006
96. Rick A-M, Domek G, Cunningham M, et al. Baseline microcephaly prevalence in rural Guatemala: implications for neonatal screening for congenital Zika virus infection. *Lancet Glob Heal*. 2017;5:S16. doi:10.1016/S2214-109X(17)30123-7
97. Barbeito-Andrés J, Schuler-Faccini L, Garcez PP. Why is congenital Zika syndrome asymmetrically distributed among human populations? 2018;16(8):e2006592. doi:10.1371/JOURNAL.PBIO.2006592
98. Devhare P, Meyer K, Steele R, Ray RB, Ray R. Zika virus infection dysregulates human neural stem cell growth and inhibits differentiation into neuroprogenitor cells. *Cell Death Dis*. 2017;8(10):e3106. doi:10.1038/CDDIS.2017.517
99. Garcez PP, Nascimento JM, De Vasconcelos JM, et al. Zika virus disrupts molecular fingerprinting of human neurospheres. *Sci Rep*. 2017;7. doi:10.1038/SREP40780
100. Jampol LM, Goldstein DA. Zika Virus Infection and the Eye. *JAMA Ophthalmol*. 2016;134(5):535-536. doi:10.1001/JAMAOPHTHALMOL.2016.0284
101. De Paula Freitas B, De Oliveira Dias JR, Prazeres J, et al. Ocular Findings in Infants With Microcephaly Associated With Presumed Zika Virus Congenital Infection in Salvador, Brazil. *JAMA Ophthalmol*. 2016;134(5):529. doi:10.1001/JAMAOPHTHALMOL.2016.0267
102. Garcez PP, Stolp HB, Sravanam S, et al. Zika virus impairs the development of blood vessels in a mouse model of congenital infection. *Sci Rep*. 2018;8(1):12774. doi:10.1038/S41598-018-31149-3
103. Fernandez MP, Parra Saad E, Ospina Martinez M, et al. Ocular Histopathologic Features of Congenital Zika Syndrome. *JAMA Ophthalmol*. 2017;135(11):1163. doi:10.1001/JAMAOPHTHALMOL.2017.3595
104. Yu Y, Clippinger AJ, Alwine JC. Viral affects on metabolism: changes in glucose and glutamine utilization during human cytomegalovirus infection. *Trends Microbiol*. 2011;19(7):360. doi:10.1016/J.TIM.2011.04.002
105. Yu Y, Maguire TG, Alwine JC. Human Cytomegalovirus Activates Glucose Transporter 4 Expression To Increase Glucose Uptake during Infection. *J Virol*. 2011;85(4):1573. doi:10.1128/JVI.01967-10
106. Savidis G, McDougall WM, Meraner P, et al. Identification of Zika Virus and Dengue Virus Dependency Factors using Functional Genomics. *Cell Rep*. 2016;16(1):232-246. doi:10.1016/J.CELREP.2016.06.028
107. Tiwari SK, Dang JW, Lin N, Qin Y, Wang S, Rana TM. Zika virus depletes neural stem cells and evades selective autophagy by suppressing the Fanconi anemia protein FANCC. *EMBO Rep*. 2020;21(12):e49183. doi:10.15252/EMBR.201949183
108. Samsa MM, Mondotte JA, Iglesias NG, et al. Dengue Virus Capsid Protein Usurps Lipid Droplets for Viral Particle Formation. *PLoS Pathog*. 2009;5(10):1000632.

doi:10.1371/JOURNAL.PPAT.1000632
109. Tongluan N, Ramphan S, Wintachai P, et al. Involvement of fatty acid synthase in dengue virus infection. *Virol J*. 2017;14(1). doi:10.1186/S12985-017-0685-9
110. Lee YR, Kuo SH, Lin CY, et al. Dengue virus-induced ER stress is required for autophagy activation, viral replication, and pathogenesis both in vitro and in vivo. *Sci Rep*. 2018;8(1). doi:10.1038/S41598-017-18909-3
111. McLean JE, Wudzinska A, Datan E, Quaglino D, Zakeri Z. Flavivirus NS4A-induced Autophagy Protects Cells against Death and Enhances Virus Replication. *J Biol Chem*. 2011;286(25):22147. doi:10.1074/JBC.M110.192500
112. Heaton NS, Randall G. Dengue Virus and Autophagy. *Viruses*. 2011;3(8):1332. doi:10.3390/V3081332
113. Heaton NS, Randall G. Dengue virus induced autophagy regulates lipid metabolism. *Cell Host Microbe*. 2010;8(5):422. doi:10.1016/J.CHOM.2010.10.006
114. Vidali S, Aminzadeh S, Lambert B, et al. Mitochondria: The ketogenic diet--A metabolism-based therapy. *Int J Biochem Cell Biol*. 2015;63:55-59. doi:10.1016/J.BIOCEL.2015.01.022
115. Blonz ER. Zika virus and GLUT1. *Lancet Infect Dis*. 2016;16(6):642. doi:10.1016/S1473-3099(16)30062-7
116. De La Cadena SG, Hernández-Fonseca K, Camacho-Arroyo I, Massieu L. Glucose deprivation induces reticulum stress by the PERK pathway and caspase-7- and calpain-mediated caspase-12 activation. *Apoptosis*. 2014;19(3):414-427. doi:10.1007/S10495-013-0930-7
117. Liu Z, Zhou T, Ziegler AC, Dimitrion P, Zuo L. Oxidative Stress in Neurodegenerative Diseases: From Molecular Mechanisms to Clinical Applications. *Oxid Med Cell Longev*. 2017;2017. doi:10.1155/2017/2525967
118. Rossignol DA, Frye RE. Mitochondrial dysfunction in autism spectrum disorders: a systematic review and meta-analysis. *Mol Psychiatry*. 2012;17(3):290. doi:10.1038/MP.2010.136
119. Liu L, Zhang K, Sandoval H, et al. Glial Lipid Droplets and ROS Induced by Mitochondrial Defects Promote Neurodegeneration. *Cell*. 2015;160(0):177. doi:10.1016/J.CELL.2014.12.019
120. Thiam AR, Farese R V., Walther TC. The biophysics and cell biology of lipid droplets. *Nat Rev Mol Cell Biol 2013 1412*. 2013;14(12):775-786. doi:10.1038/nrm3699
121. Olzmann JA, Carvalho P. Dynamics and functions of lipid droplets. *Nat Rev Mol Cell Biol 2018 203*. 2018;20(3):137-155. doi:10.1038/s41580-018-0085-z
122. Hashemi HF, Goodman JM. The life cycle of lipid droplets. *Curr Opin Cell Biol*. 2015;33:119-124. doi:10.1016/J.CEB.2015.02.002
123. Martín-Acebes MA, Oya NJ de, Saiz JC. Lipid Metabolism as a Source of Druggable Targets for Antiviral Discovery against Zika and Other Flaviviruses. *Pharmaceuticals*. 2019;12(2). doi:10.3390/PH12020097
124. Ledur PF, Karmirian K, Pedrosa C da SG, et al. Zika virus infection leads to mitochondrial failure, oxidative stress and DNA damage in human iPSC-derived astrocytes. *Sci Reports 2020 101*. 2020;10(1):1-14. doi:10.1038/s41598-020-57914-x
125. Ross C, Boroviak TE. Origin and function of the yolk sac in primate embryogenesis. *Nat Commun*. 2020;11(1):1-14. doi:10.1038/s41467-020-17575-w
126. Rezaie P, Male D. Mesoglia & microglia--a historical review of the concept of mononuclear phagocytes within the central nervous system. *J Hist Neurosci*. 2002;11(4):325-374. doi:10.1076/JHIN.11.4.325.8531
127. Migliaccio G, Migliaccio AR, Petti S, et al. Human embryonic hemopoiesis. Kinetics of progenitors and precursors underlying the yolk sac----liver transition. *J Clin Invest*. 1986;78(1):51-60. doi:10.1172/JCI112572
128. Silbereis JC, Pochareddy S, Zhu Y, Li M, Sestan N. The Cellular and Molecular Landscapes of the Developing Human Central Nervous System. *Neuron*.

2016;89(2):248. doi:10.1016/J.NEURON.2015.12.008
129. Robbins JR, Bakardjiev AI. Pathogens and the placental fortress. *Curr Opin Microbiol*. 2012;15(1):36-43. doi:10.1016/j.mib.2011.11.006
130. Zeldovich VB, Clausen CH, Bradford E, et al. Placental Syncytium Forms a Biophysical Barrier against Pathogen Invasion. Wessels MR, ed. *PLoS Pathog*. 2013;9(12):e1003821. doi:10.1371/journal.ppat.1003821
131. Gomez-Nicola D, Menassa DA. Microglial Dynamics During Human Brain Development. *Microglial Dyn Dur Hum Brain Dev Front Immunol*. 2018;9:1014. doi:10.3389/fimmu.2018.01014
132. Dutta K, Mishra MK, Nazmi A, Kumawat KL, Basu A. Minocycline differentially modulates macrophage mediated peripheral immune response following Japanese encephalitis virus infection. *Immunobiology*. 2010;215(11):884-893. doi:10.1016/J.IMBIO.2009.12.003
133. Wilkinson J, Radkowski M, Eschbacher JM, Laskus T. Activation of brain macrophages/microglia cells in hepatitis C infection. *Gut*. 2010;59(10):1394-1400. doi:10.1136/GUT.2009.199356
134. Stevenson E V., Collins-McMillen D, Kim JH, Cieply SJ, Bentz GL, Yurochko AD. HCMV reprogramming of infected monocyte survival and differentiation: a Goldilocks phenomenon. *Viruses*. 2014;6(2):782-807. doi:10.3390/V6020782
135. Herbein G, Varin A. The macrophage in HIV-1 infection: from activation to deactivation? *Retrovirology*. 2010;7. doi:10.1186/1742-4690-7-33
136. Fischer-Smith T, Rappaport J. Evolving paradigms in the pathogenesis of HIV-1-associated dementia. *Expert Rev Mol Med*. 2005;7(27). doi:10.1017/S1462399405010239
137. Analysis of human immunodeficiency virus type 1 gp160 sequences from a patient with HIV dementia: evidence for monocyte trafficking into brain - PubMed. Accessed March 7, 2022. https://pubmed.ncbi.nlm.nih.gov/10871768/
138. Clatch RJ, Miller SD, Metzner R, Dal Canto MC, Lipton HL. Monocytes/macrophages isolated from the mouse central nervous system contain infectious Theiler's murine encephalomyelitis virus (TMEV). *Virology*. 1990;176(1):244-254. doi:10.1016/0042-6822(90)90249-Q
139. Gazzolo L, Moscovici C, Moscovici MG. Persistence of avian oncoviruses in chicken macrophages. *Infect Immun*. 1979;23(2):294-297. doi:10.1128/IAI.23.2.294-297.1979
140. Nikitina E, Larionova I, Choinzonov E, Kzhyshkowska J. Molecular Sciences Monocytes and Macrophages as Viral Targets and Reservoirs. Published online 2018. doi:10.3390/ijms19092821
141. Quicke KM, Bowen JR, Johnson EL, et al. Zika Virus Infects Human Placental Macrophages. *Cell Host Microbe*. 2016;20(1):83-90. doi:10.1016/J.CHOM.2016.05.015
142. Thorley JA, McKeating JA, Rappoport JZ. Mechanisms of viral entry: sneaking in the front door. *Protoplasma 2010 2441*. 2010;244(1):15-24. doi:10.1007/S00709-010-0152-6
143. Grove J, Marsh M. The cell biology of receptor-mediated virus entry. *J Cell Biol*. 2011;195(7):1071-1082. doi:10.1083/JCB.201108131
144. Shang J, Wan Y, Luo C, et al. Cell entry mechanisms of SARS-CoV-2. *Proc Natl Acad Sci U S A*. 2020;117(21). doi:10.1073/PNAS.2003138117
145. Leier HC, Weinstein JB, Kyle JE, et al. A global lipid map defines a network essential for Zika virus replication. *Nat Commun 2020 111*. 2020;11(1):1-15. doi:10.1038/s41467-020-17433-9
146. Brault JB, Khou C, Basset J, et al. Comparative Analysis Between Flaviviruses Reveals Specific Neural Stem Cell Tropism for Zika Virus in the Mouse Developing Neocortex. *EBioMedicine*. 2016;10:71-76. doi:10.1016/J.EBIOM.2016.07.018
147. Anfasa F, Goeijenbier M, Widagdo W, et al. Zika virus infection induces elevation of tissue factor production and apoptosis on human umbilical vein endothelial cells.

Front Microbiol. 2019;10(APR):817. doi:10.3389/FMICB.2019.00817/BIBTEX
148. Nowakowski TJ, Pollen AA, Di Lullo E, Sandoval-Espinosa C, Bershteyn M, Kriegstein AR. Expression Analysis Highlights AXL as a Candidate Zika Virus Entry Receptor in Neural Stem Cells. *Cell Stem Cell*. 2016;18(5):591-596. doi:10.1016/J.STEM.2016.03.012
149. Wells MF, Salick MR, Wiskow O, et al. Genetic Ablation of AXL Does Not Protect Human Neural Progenitor Cells and Cerebral Organoids from Zika Virus Infection. *Cell Stem Cell*. 2016;19(6):703-708. doi:10.1016/J.STEM.2016.11.011
150. Chen J, Yang YF, Yang Y, et al. AXL promotes Zika virus infection in astrocytes by antagonizing type I interferon signalling. *Nat Microbiol 2017 33*. 2018;3(3):302-309. doi:10.1038/s41564-017-0092-4
151. Richard AS, Shim BS, Kwon YC, et al. AXL-dependent infection of human fetal endothelial cells distinguishes Zika virus from other pathogenic flaviviruses. *Proc Natl Acad Sci U S A*. 2017;114(8):2024-2029. doi:10.1073/PNAS.1620558114/-/DCSUPPLEMENTAL
152. Wang Z-Y, Wang Z, Zhen Z-D, et al. Axl is not an indispensable factor for Zika virus infection in mice. doi:10.1099/jgv.0.000886
153. Agrelli A, de Moura RR, Crovella S, Brandão LAC. ZIKA virus entry mechanisms in human cells. *Infect Genet Evol*. 2019;69:22-29. doi:10.1016/J.MEEGID.2019.01.018
154. Tiwari SK, Dang J, Qin Y, Lichinchi G, Bansal V, Rana TM. Zika virus infection reprograms global transcription of host cells to allow sustained infection. *Emerg Microbes Infect*. 2017;6(4). doi:10.1038/EMI.2017.9/SUPPL_FILE/TEMI_A_12040201_SM0007.XLS
155. Nathan CF, Prendergast TJ, Wiebe ME, et al. Activation of human macrophages. Comparison of other cytokines with interferon-gamma. *J Exp Med*. 1984;160(2):600-605. doi:10.1084/JEM.160.2.600
156. Katholnig K, Linke M, Pham H, Hengstschläger M, Weichhart T. Immune responses of macrophages and dendritic cells regulated by mTOR signalling. *Biochem Soc Trans*. 2013;41(4):927-933. doi:10.1042/BST20130032
157. Ghesquière B, Wong BW, Kuchnio A, Carmeliet P. Metabolism of stromal and immune cells in health and disease. *Nat 2014 5117508*. 2014;511(7508):167-176. doi:10.1038/nature13312
158. Galván-Peña S, O'Neill LAJ. Metabolic reprogramming in macrophage polarization. *Front Immunol*. 2014;5(AUG):420. doi:10.3389/FIMMU.2014.00420/BIBTEX
159. Wang T, Liu H, Lian G, Zhang SY, Wang X, Jiang C. HIF1 α -Induced Glycolysis Metabolism Is Essential to the Activation of Inflammatory Macrophages. *Mediators Inflamm*. 2017;2017. doi:10.1155/2017/9029327
160. Honarmand Ebrahimi K, Vowles J, Browne C, McCullagh J, James WS. ddhCTP produced by the radical-SAM activity of RSAD2 (viperin) inhibits the NAD+-dependent activity of enzymes to modulate metabolism. *FEBS Lett*. 2020;594(10):1631-1644. doi:10.1002/1873-3468.13778
161. Ebrahimi KH, Howie D, Rowbotham JS, McCullagh J, Armstrong FA, James WS. Viperin, through its radical-SAM activity, depletes cellular nucleotide pools and interferes with mitochondrial metabolism to inhibit viral replication. *FEBS Lett*. 2020;594(10):1624-1630. doi:10.1002/1873-3468.13761
162. Helbig KJ, Beard MR. The Role of Viperin in the Innate Antiviral Response. *J Mol Biol*. 2014;426(6):1210-1219. doi:10.1016/J.JMB.2013.10.019
163. Ebrahimi KH. A unifying view of the broad-spectrum antiviral activity of RSAD2 (viperin) based on its radical-SAM chemistry. *Metallomics*. 2018;10(4):539-552. doi:10.1039/C7MT00341B
164. Virus Pathogen Database and Analysis Resource (ViPR) - Flaviviridae - Flavivirus Zika virus Strain MP1751. Accessed March 24, 2022. https://www.viprbrc.org/brc/viprStrainDetails.spg?strainName=MP1751&decorator=flavi

165. Virus Collection: 1308258v Zika virus. Accessed March 24, 2022. https://www.culturecollections.org.uk/products/viruses/detail.jsp?refId=1308258v&collection=ncpv
166. Caly L, Druce J, Roberts J, et al. Isolation and rapid sharing of the 2019 novel coronavirus (SARS-CoV-2) from the first patient diagnosed with COVID-19 in Australia. *Med J Aust*. 2020;212(10):459-462. doi:10.5694/MJA2.50569
167. Preliminary genomic characterisation of an emergent SARS-CoV-2 lineage in the UK defined by a novel set of spike mutations - SARS-CoV-2 coronavirus / nCoV-2019 Genomic Epidemiology - Virological. Accessed March 14, 2022. https://virological.org/t/preliminary-genomic-characterisation-of-an-emergent-sars-cov-2-lineage-in-the-uk-defined-by-a-novel-set-of-spike-mutations/563
168. Cele S, Gazy I, Jackson L, et al. Escape of SARS-CoV-2 501Y.V2 from neutralization by convalescent plasma. doi:10.1038/s41586-021
169. Fernandes HJRHJR, Hartfield EMEM, Christian HCHC, et al. ER Stress and Autophagic Perturbations Lead to Elevated Extracellular α-Synuclein in GBA-N370S Parkinson's iPSC-Derived Dopamine Neurons. 2016;6(3):342-356. Accessed March 14, 2022. https://pubmed.ncbi.nlm.nih.gov/26905200/
170. Beers J, Gulbranson DR, George N, et al. Passaging and colony expansion of human pluripotent stem cells by enzyme-free dissociation in chemically defined culture conditions. *Nat Protoc*. 2012;7(11):2029-2040. doi:10.1038/nprot.2012.130
171. Haenseler W, Sansom SN, Buchrieser J, et al. A Highly Efficient Human Pluripotent Stem Cell Microglia Model Displays a Neuronal-Co-culture-Specific Expression Profile and Inflammatory Response. *Stem Cell Reports*. 2017;8(6):1727-1742. doi:10.1016/j.stemcr.2017.05.017
172. Morrison M, Klein C, Clemann N, et al. StemBANCC: Governing Access to Material and Data in a Large Stem Cell Research Consortium. *Stem Cell Rev*. 2015;11(5):681. doi:10.1007/S12015-015-9599-3
173. Vaughan-Jackson A, Stodolak S, Ebrahimi KH, et al. Differentiation of human induced pluripotent stem cells to authentic macrophages using a defined, serum-free, open-source medium. *Stem Cell Reports*. 2021;16(7):1735-1748. doi:10.1016/J.STEMCR.2021.05.018
174. Robbins JP, Perfect L, Ribe EM, et al. Clusterin Is Required for β-Amyloid Toxicity in Human iPSC-Derived Neurons. *Front Neurosci*. 2018;12. doi:10.3389/fnins.2018.00504
175. Lopez CA, Al-Siddiqi HHAA, Purnama U, et al. Physiological and pharmacological stimulation for in vitro maturation of substrate metabolism in human induced pluripotent stem cell-derived cardiomyocytes. *Sci Reports 2021 111*. 2021;11(1):1-13. doi:10.1038/s41598-021-87186-y
176. Lancaster MA, Renner M, Martin CA, et al. Cerebral organoids model human brain development and microcephaly. *Nat 2013 5017467*. 2013;501(7467):373-379. doi:10.1038/nature12517
177. Board M, Lopez C, van den Bos C, Callaghan R, Clarke K, Carr C. Acetoacetate is a more efficient energy-yielding substrate for human mesenchymal stem cells than glucose and generates fewer reactive oxygen species. *Int J Biochem Cell Biol*. 2017;88:75-83. doi:10.1016/J.BIOCEL.2017.05.007
178. Collins CL, Bode BP, Souba WW, Abcouwer SF. Multiwell 14CO2-capture assay for evaluation of substrate oxidation rates of cells in culture. *Biotechniques*. 1998;24(5):803-808. doi:10.2144/98245ST04
179. Folch J, Lees M, Sloane GH. A SIMPLE METHOD FOR THE ISOLATION AND PURIFICATION OF TOTAL LIPIDES FROM ANIMAL TISSUES*. *J Biol Chem*. 1957;226:497-509. doi:10.1016/S0021-9258(18)64849-5
180. Malandraki-Miller S, Lopez CA, Alonaizan R, et al. Metabolic flux analyses to assess the differentiation of adult cardiac progenitors after fatty acid supplementation. *Stem Cell Res*. 2019;38:101458. doi:10.1016/J.SCR.2019.101458

181. van Meer BJ, Sala L, Tertoolen LGJ, Smith GL, Burton FL, Mummery CL. Quantification of Muscle Contraction In Vitro and In Vivo Using MUSCLEMOTION Software: From Stem Cell-Derived Cardiomyocytes to Zebrafish and Human Hearts. *Curr Protoc Hum Genet*. 2018;99(1). doi:10.1002/CPHG.67
182. Sala L, Van Meer BJ, Tertoolen LGJ, et al. MUSCLEMOTION: A Versatile Open Software Tool to Quantify Cardiomyocyte and Cardiac Muscle Contraction In Vitro and In Vivo. *Circ Res*. 2018;122(3):e5-e16. doi:10.1161/CIRCRESAHA.117.312067
183. Burton GJ, Hempstock J, Jauniaux E. Nutrition of the Human Fetus during the First Trimester—A Review. *Placenta*. 2001;22(SUPPL.1):S70-S77. doi:10.1053/PLAC.2001.0639
184. Otani T, Marchetto MC, Gage FH, Simons BD, Livesey FJ. 2D and 3D Stem Cell Models of Primate Cortical Development Identify Species-Specific Differences in Progenitor Behavior Contributing to Brain Size. *Cell Stem Cell*. 2016;18(4):467-480. doi:10.1016/J.STEM.2016.03.003
185. Knobloch M, Pilz GA, Ghesquière B, et al. A Fatty Acid Oxidation-Dependent Metabolic Shift Regulates Adult Neural Stem Cell Activity. *Cell Rep*. 2017;20(9):2144-2155. doi:10.1016/J.CELREP.2017.08.029
186. Molnár Z, Clowry GJ, Šestan N, et al. New insights into the development of the human cerebral cortex. *J Anat*. 2019;235(3). doi:10.1111/JOA.13055
187. Postiglione MP, Hippenmeyer S. Monitoring neurogenesis in the cerebral cortex: An update. *Future Neurol*. 2014;9(3):323-340. doi:10.2217/FNL.14.18/ASSET/IMAGES/LARGE/FIGURE4.JPEG
188. Goasdoué K, Miller SM, Colditz PB, Björkman ST. Review: The blood-brain barrier; protecting the developing fetal brain. *Placenta*. 2017;54:111-116. doi:10.1016/J.PLACENTA.2016.12.005
189. Engelhardt B. Development of the blood-brain barrier. *Cell Tissue Res*. 2003;314(1):119-129. doi:10.1007/S00441-003-0751-Z/FIGURES/3
190. Engelhardt B, Liebner S. Novel insights into the development and maintenance of the blood-brain barrier. *Cell Tissue Res*. 2014;355(3):687-699. doi:10.1007/S00441-014-1811-2/FIGURES/2
191. Saunders NR, Dziegielewska KM, Møllgård K, Habgood MD. Physiology and molecular biology of barrier mechanisms in the fetal and neonatal brain. *J Physiol*. 2018;596(23):5723-5756. doi:10.1113/JP275376
192. Saunders NR, Dreifuss JJ, Dziegielewska KM, et al. The rights and wrongs of blood-brain barrier permeability studies: A walk through 100 years of history. *Front Neurosci*. 2014;8(DEC):404. doi:10.3389/FNINS.2014.00404/BIBTEX
193. Saunders NR, Daneman R, Dziegielewska KM, Liddelow SA. Transporters of the blood–brain and blood–CSF interfaces in development and in the adult. *Mol Aspects Med*. 2013;34(2-3):742-752. doi:10.1016/J.MAM.2012.11.006
194. Buss C, Entringer S, Wadhwa PD. Fetal programming of brain development: Intrauterine stress and susceptibility to psychopathology. *Sci Signal*. 2012;5(245). doi:10.1126/SCISIGNAL.2003406/SUPPL_FILE/SCISIGNAL_5245PT7.ZIP
195. Johnson MB, Wang PP, Atabay KD, et al. Single-cell analysis reveals transcriptional heterogeneity of neural progenitors in human cortex. *Nat Neurosci 2015 185*. 2015;18(5):637-646. doi:10.1038/nn.3980
196. Kester L, van Oudenaarden A. Single-Cell Transcriptomics Meets Lineage Tracing. *Cell Stem Cell*. 2018;23(2):166-179. doi:10.1016/J.STEM.2018.04.014
197. Ma J, Shen Z, Yu YC, Shi SH. Neural lineage tracing in the mammalian brain. *Curr Opin Neurobiol*. 2018;50:7-16. doi:10.1016/J.CONB.2017.10.013
198. Figueres-Oñate M, Sánchez-González R, López-Mascaraque L. Deciphering neural heterogeneity through cell lineage tracing. *Cell Mol Life Sci 2020 785*. 2020;78(5):1971-1982. doi:10.1007/S00018-020-03689-3
199. Hoerder-Suabedissen A, Molnár Z. Development, evolution and pathology of neocortical subplate neurons. *Nat Rev Neurosci 2015 163*. 2015;16(3):133-146.

doi:10.1038/nrn3915
200. Ramon y Cajal S, Azoulay L. Histologie du systeme nerveux de l'homme et des vertebres. Published online 1955:2v-2v.
201. Jones EG. Microcolumns in the cerebral cortex. *Proc Natl Acad Sci*. 2000;97(10):5019-5021. doi:10.1073/PNAS.97.10.5019
202. Goldman S. Glia as neural progenitor cells. *Trends Neurosci*. 2003;26(11):590-596. doi:10.1016/J.TINS.2003.09.011
203. Casper KB, McCarthy KD. GFAP-positive progenitor cells produce neurons and oligodendrocytes throughout the CNS. *Mol Cell Neurosci*. 2006;31(4):676-684. doi:10.1016/J.MCN.2005.12.006
204. Torrent R, De Angelis Rigotti F, Dell'Era P, Memo M, Raya A, Consiglio A. Using iPS cells toward the understanding of parkinson's disease. *J Clin Med*. 2015;4(4):548-566. doi:10.3390/JCM4040548
205. Liu X, Li F, Stubblefield EA, et al. Direct reprogramming of human fibroblasts into dopaminergic neuron-like cells. *Cell Res*. 2012;22(2):321-332. doi:10.1038/CR.2011.181
206. Falkenburger BH, Saridaki T, Dinter E. Cellular models for Parkinson's disease. *J Neurochem*. Published online October 1, 2016:121-130. doi:10.1111/JNC.13618
207. Nimtz L, Hartmann J, Tigges J, et al. Characterization and application of electrically active neuronal networks established from human induced pluripotent stem cell-derived neural progenitor cells for neurotoxicity evaluation. *Stem Cell Res*. 2020;45:101761. doi:10.1016/J.SCR.2020.101761
208. Di Lullo E, Kriegstein AR. The use of brain organoids to investigate neural development and disease. *Nat Rev Neurosci 2017 1810*. 2017;18(10):573-584. doi:10.1038/nrn.2017.107
209. Nascimento JM, Saia-Cereda VM, Sartore RC, et al. Human Cerebral Organoids and Fetal Brain Tissue Share Proteomic Similarities. *Front Cell Dev Biol*. 2019;7:303. doi:10.3389/FCELL.2019.00303/BIBTEX
210. Lancaster MA, Corsini NS, Wolfinger S, et al. Guided self-organization and cortical plate formation in human brain organoids. *Nat Biotechnol 2017 357*. 2017;35(7):659-666. doi:10.1038/nbt.3906
211. Rehbach K, Fernando MB, Brennand KJ, Tian A, Muffat XJ, Li Y. Studying Human Neurodevelopment and Diseases Using 3D Brain Organoids. *J Neurosci*. 2020;40(6):1186-1193. doi:10.1523/JNEUROSCI.0519-19.2019
212. Luo C, Lancaster MA, Castanon R, Nery JR, Knoblich JA, Ecker JR. Cerebral Organoids Recapitulate Epigenomic Signatures of the Human Fetal Brain. *Cell Rep*. 2016;17(12):3369-3384. doi:10.1016/J.CELREP.2016.12.001
213. Kelava I, Lancaster MA. Dishing out mini-brains: Current progress and future prospects in brain organoid research. *Dev Biol*. 2016;420(2):199-209. doi:10.1016/J.YDBIO.2016.06.037
214. Quadrato G, Arlotta P. Present and future of modeling human brain development in 3D organoids. *Curr Opin Cell Biol*. 2017;49:47-52. doi:10.1016/J.CEB.2017.11.010
215. Chambers SM, Fasano CA, Papapetrou EP, Tomishima M, Sadelain M, Studer L. Highly efficient neural conversion of human ES and iPS cells by dual inhibition of SMAD signaling. *Nat Biotechnol*. 2009;27(3):275-280. doi:10.1038/NBT.1529
216. Takahashi K, Tanabe K, Ohnuki M, et al. Induction of Pluripotent Stem Cells from Adult Human Fibroblasts by Defined Factors. *Cell*. 2007;131(5):861-872. doi:10.1016/J.CELL.2007.11.019
217. Thomson JA. Embryonic stem cell lines derived from human blastocysts. *Science (80-)*. 1998;282(5391):1145-1147. doi:10.1126/SCIENCE.282.5391.1145
218. Rosati J, Ferrari D, Altieri F, et al. Establishment of stable iPS-derived human neural stem cell lines suitable for cell therapies. *Cell Death Dis 2018 910*. 2018;9(10):1-16. doi:10.1038/s41419-018-0990-2
219. Zhou S, Szczesna K, Ochalek A, et al. Neurosphere based differentiation of human IPSC improves astrocyte differentiation. *Stem Cells Int*. 2016;2016.

doi:10.1155/2016/4937689
220. Chandrasekaran A, Avci HX, Ochalek A, et al. Comparison of 2D and 3D neural induction methods for the generation of neural progenitor cells from human induced pluripotent stem cells. *Stem Cell Res*. 2017;25:139-151. doi:10.1016/J.SCR.2017.10.010
221. Cremer JE. Substrate utilization and brain development. *J Cereb Blood Flow Metab*. 1982;2(4):394-407. doi:10.1038/JCBFM.1982.45
222. Chi CP, Roberts EL. Energy Substrates for Neurons during Neural Activity: A Critical Review of the Astrocyte-Neuron Lactate Shuttle Hypothesis. *J Cereb Blood Flow Metab*. 2003;23(11):1263-1281. doi:10.1097/01.WCB.0000081369.51727.6F
223. Dienel GA. Brain lactate metabolism: The discoveries and the controversies. *J Cereb Blood Flow Metab*. 2012;32(7):1107-1138. doi:10.1038/jcbfm.2011.175
224. Amaral AI. Effects of hypoglycaemia on neuronal metabolism in the adult brain: role of alternative substrates to glucose. *J Inherit Metab Dis 2012 364*. 2012;36(4):621-634. doi:10.1007/S10545-012-9553-3
225. Sokoloff L. Metabolism of Ketone Bodies by the Brain. *https://doi.org/101146/annurev.me24020173001415*. 2003;24:271-280. doi:10.1146/ANNUREV.ME.24.020173.001415
226. McKenna MC, Dienel GA, Sonnewald U, Waagepetersen HS, Schousboe A. Energy Metabolism of the Brain. *Basic Neurochem*. Published online January 1, 2012:200-231. doi:10.1016/B978-0-12-374947-5.00011-0
227. Knobloch M, Braun SMG, Zurkirchen L, et al. Metabolic control of adult neural stem cell activity by Fasn-dependent lipogenesis. 493(7431):226-230. Accessed January 8, 2022. https://www.nature.com/articles/nature11689
228. Stoll EA, Makin R, Sweet IR, et al. Neural Stem Cells in the Adult Subventricular Zone Oxidize Fatty Acids to Produce Energy and Support Neurogenic Activity. Published online 2015. doi:10.1002/stem.2042
229. Beckervordersandforth R. Role of mitochondrial metabolism in the control of early lineage progression and aging phenotypes in adult hippocampal neurogenesis. *Neuron*. 2017;93:560-573.e6.
230. Ramosaj M, Madsen S, Maillard V, et al. Lipid droplet availability affects neural stem/progenitor cell metabolism and proliferation. *Nat Commun 2021 121*. 2021;12(1):1-17. doi:10.1038/s41467-021-27365-7
231. Zheng X, Boyer L, Jin M, et al. Metabolic reprogramming during neuronal differentiation from aerobic glycolysis to neuronal oxidative phosphorylation. *Elife*. 2016;5(JUN2016). doi:10.7554/ELIFE.13374
232. Shi Y, Kirwan P, Smith J, Robinson HPC, Livesey FJ. Human cerebral cortex development from pluripotent stem cells to functional excitatory synapses. *Nat Publ Gr*. 2012;15. doi:10.1038/nn.3041
233. Knobloch M, Jessberger S. Metabolism and neurogenesis. *Curr Opin Neurobiol*. 2017;42:45-52. doi:10.1016/J.CONB.2016.11.006
234. Teslaa T, Teitell MA. Techniques to Monitor Glycolysis. *Methods Enzymol*. 2014;542:91. doi:10.1016/B978-0-12-416618-9.00005-4
235. Tamaki S, Eckert K, He D, et al. Engraftment of sorted/expanded human central nervous system stem cells from fetal brain. *J Neurosci Res*. 2002;69(6):976-986. doi:10.1002/JNR.10412
236. McGrath EL, Rossi SL, Gao J, et al. Differential Responses of Human Fetal Brain Neural Stem Cells to Zika Virus Infection. *Stem Cell Reports*. 2017;8(3):715-727. doi:10.1016/J.STEMCR.2017.01.008
237. Wu G, Bazer FW, Cudd TA, Meininger CJ, Spencer TE. Maternal Nutrition and Fetal Development. *J Nutr*. 2004;134(9):2169-2172. doi:10.1093/JN/134.9.2169
238. Götz M, Huttner WB. The cell biology of neurogenesis. *Nat Rev Mol Cell Biol 2005 610*. 2005;6(10):777-788. doi:10.1038/nrm1739
239. Hui SP, Nag TC, Ghosh S. Characterization of Proliferating Neural Progenitors after Spinal Cord Injury in Adult Zebrafish. *PLoS One*. 2015;10(12):e0143595.

doi:10.1371/JOURNAL.PONE.0143595
240. Nutr A, Steiner P. Brain Fuel Utilization in the Developing Brain. *Ann Nutr Metab*. 2019;75(1):8-18. doi:10.1159/000508054
241. Lipscomb JC, Poet TS. In vitro measurements of metabolism for application in pharmacokinetic modeling. *Pharmacol Ther*. 2008;118(1):82-103. doi:10.1016/J.PHARMTHERA.2008.01.006
242. Yau C, Low JZH, Gan ES, et al. Dysregulated metabolism underpins Zika-virus-infection-associated impairment in fetal development. *Cell Rep*. 2021;37(11):110118. doi:10.1016/J.CELREP.2021.110118
243. Huang Y, Lin Q, Huo Z, et al. Inositol-Requiring Enzyme 1α Promotes Zika Virus Infection through Regulation of Stearoyl Coenzyme A Desaturase 1-Mediated Lipid Metabolism. *J Virol*. 2020;94(23). doi:10.1128/JVI.01229-20/ASSET/665EF0CE-4034-4BD2-BC5B-8D624F0FAA64/ASSETS/GRAPHIC/JVI.01229-20-F0007.JPEG
244. Pang H, Jiang Y, Li J, et al. Aberrant NAD+ metabolism underlies Zika virus–induced microcephaly. *Nat Metab 2021 38*. 2021;3(8):1109-1124. doi:10.1038/s42255-021-00437-0
245. Semenza GL. Tumor metabolism: cancer cells give and take lactate. *J Clin Invest*. 2008;118(12):3835-3837. doi:10.1172/JCI37373
246. Goodwin ML, Gladden LB, Nijsten MWN, Jones KB. Lactate and Cancer: Revisiting the Warburg Effect in an Era of Lactate Shuttling. *Front Nutr*. 2015;1:27. doi:10.3389/FNUT.2014.00027/BIBTEX
247. Bonuccelli G, Tsirigos A, Whitaker-Menezes D, et al. Ketones and lactate "fuel" tumor growth and metastasis: Evidence that epithelial cancer cells use oxidative mitochondrial metabolism. *Cell Cycle*. 2010;9(17):3506-3514. doi:10.4161/CC.9.17.12731/SUPPL_FILE/KCCY_A_10912731_SM0001.ZIP
248. Tietjen I, Rihel JM, Cao Y, Koentges G, Zakhary L, Dulac C. Single-Cell Transcriptional Analysis of Neuronal Progenitors. *Neuron*. 2003;38(2):161-175. doi:10.1016/S0896-6273(03)00229-0
249. Daviaud N, Chevalier C, Friedel RH, Zou H. Distinct Vulnerability and Resilience of Human Neuroprogenitor Subtypes in Cerebral Organoid Model of Prenatal Hypoxic Injury. *Front Cell Neurosci*. 2019;13:336. doi:10.3389/FNCEL.2019.00336/BIBTEX
250. Son G, Han J. Roles of mitochondria in neuronal development. *BMB Rep*. 2018;51(11):549. doi:10.5483/BMBREP.2018.51.11.226
251. Bifari F, Dolci S, Bottani E, et al. Complete neural stem cell (NSC) neuronal differentiation requires a branched chain amino acids-induced persistent metabolic shift towards energy metabolism. *Pharmacol Res*. 2020;158:104863. doi:10.1016/J.PHRS.2020.104863
252. Rombi F, Bayliss R, Tuplin A, Yeoh S. The journey of Zika to the developing brain. *Mol Biol Reports 2020 474*. 2020;47(4):3097-3115. doi:10.1007/S11033-020-05349-Y
253. Russo FB, Beltrão-Braga PCB. The impact of Zika virus in the brain. *Biochem Biophys Res Commun*. 2017;492(4):603-607. doi:10.1016/J.BBRC.2017.01.074
254. Krauer F, Riesen M, Reveiz L, et al. Zika Virus Infection as a Cause of Congenital Brain Abnormalities and Guillain–Barré Syndrome: Systematic Review. *PLOS Med*. 2017;14(1):e1002203. doi:10.1371/JOURNAL.PMED.1002203
255. Li H, Saucedo-Cuevas L, Regla-Nava JA, et al. Zika Virus Infects Neural Progenitors in the Adult Mouse Brain and Alters Proliferation. *Cell Stem Cell*. 2016;19(5):593-598. doi:10.1016/J.STEM.2016.08.005
256. Van Den Pol AN, Mao G, Yang Y, Ornaghi S, Davis JN. Zika Virus Targeting in the Developing Brain. *J Neurosci*. 2017;37(8):2161-2175. doi:10.1523/JNEUROSCI.3124-16.2017
257. Dabaja MZ, Lima E de O, de Oliveira DN, et al. Metabolic alterations induced by attenuated Zika virus in glioblastoma cells. *Cell Biosci*. 2018;8(1):1-9. doi:10.1186/S13578-018-0243-1/FIGURES/2
258. Luplertlop N, Suwanmanee S, Muangkaew W, Ampawong S, Kitisin T,

Poovorawan Y. The impact of Zika virus infection on human neuroblastoma (SH-SY5Y) cell line. *J Vector Borne Dis*. 2017;54(3):207. doi:10.4103/0972-9062.217611
259. Lum FM, Low DKS, Fan Y, et al. Zika Virus Infects Human Fetal Brain Microglia and Induces Inflammation. *Clin Infect Dis*. 2017;64(7):914-920. doi:10.1093/CID/CIW878
260. Diop F, Vial T, Ferraris P, et al. Zika virus infection modulates the metabolomic profile of microglial cells. *PLoS One*. 2018;13(10):e0206093. doi:10.1371/JOURNAL.PONE.0206093
261. Yang W, Wu YH, Liu SQ, et al. S100A4+ macrophages facilitate zika virus invasion and persistence in the seminiferous tubules via interferon-gamma mediation. *PLOS Pathog*. 2020;16(12):e1009019. doi:10.1371/JOURNAL.PPAT.1009019
262. Quicke KM, Bowen JR, Johnson EL, et al. Zika Virus Infects Human Placental Macrophages. *Cell Host Microbe*. 2016;20(1):83-90. doi:10.1016/J.CHOM.2016.05.015
263. Yang D, Chu H, Lu G, et al. STAT2-dependent restriction of Zika virus by human macrophages but not dendritic cells. *Emerg Microbes Infect*. 2021;10(1):1024-1037. doi:10.1080/22221751.2021.1929503/SUPPL_FILE/TEMI_A_1929503_SM9966.TIF
264. Zorrilla CD, García García I, García Fragoso L, De La Vega A. Zika Virus Infection in Pregnancy: Maternal, Fetal, and Neonatal Considerations. *J Infect Dis*. 2017;216(Suppl 10):S891. doi:10.1093/INFDIS/JIX448
265. Brasil P, Pereira JP, Moreira ME, et al. Zika Virus Infection in Pregnant Women in Rio de Janeiro. *N Engl J Med*. 2016;375(24):2321. doi:10.1056/NEJMOA1602412
266. de Almeida BL, Giovanetti M, Oliveira JV, et al. Detection and sequencing of Zika virus in normocephalic newborns with congenital Zika infection. *Int J Infect Dis*. 2022;114:128-131. doi:10.1016/J.IJID.2021.10.051
267. Lin SC, Chen MC, Liu S, et al. Phloretin inhibits Zika virus infection by interfering with cellular glucose utilisation. *Int J Antimicrob Agents*. 2019;54(1):80-84. doi:10.1016/J.IJANTIMICAG.2019.03.017
268. Barbeito-Andrés J, Pezzuto P, Higa LM, et al. Congenital Zika syndrome is associated with maternal protein malnutrition. *Sci Adv*. 2020;6(2). doi:10.1126/SCIADV.AAW6284/SUPPL_FILE/AAW6284_TABLE_S5.XLS
269. Ah O. Protein Energy Malnutrition and Susceptibility to Viral Infections as Zika and Influenza Viruses. Published online 2016. doi:10.4172/2155-9600.1000489
270. Jin L, Guo X, Shen C, et al. Salivary factor LTRIN from Aedes aegypti facilitates the transmission of Zika virus by interfering with the lymphotoxin-β receptor. *Nat Immunol 2018 194*. 2018;19(4):342-353. doi:10.1038/s41590-018-0063-9
271. Hamel R, Dejarnac O, Wichit S, et al. Biology of Zika Virus Infection in Human Skin Cells. *J Virol*. 2015;89(17):8880-8896. doi:10.1128/JVI.00354-15/SUPPL_FILE/ZJV999090703SO1.PDF
272. Zhao M, Jung Y, Jiang Z, Svensson KJ. Regulation of Energy Metabolism by Receptor Tyrosine Kinase Ligands. *Front Physiol*. 2020;11:354. doi:10.3389/FPHYS.2020.00354/BIBTEX
273. Cavet ME, Smolock EM, Ozturk OH, et al. Gas6-Axl receptor signaling is regulated by glucose in vascular smooth muscle cells. *Arterioscler Thromb Vasc Biol*. 2008;28(5):886-891. doi:10.1161/ATVBAHA.108.162693
274. Lee CH, Shieh YS, Hsiao FC, et al. High glucose induces human endothelial dysfunction through an Axl-dependent mechanism. *Cardiovasc Diabetol*. 2014;13(1):1-13. doi:10.1186/1475-2840-13-53/FIGURES/8
275. Bansal N, Mishra PJ, Stein M, et al. Axl receptor tyrosine kinase is up-regulated in metformin resistant prostate cancer cells. *Oncotarget*. 2015;6(17):15321-15331. doi:10.18632/ONCOTARGET.4148
276. Cavet ME, Smolock EM, Ozturk OH, et al. Gas6-Axl receptor signaling is regulated

by glucose in vascular smooth muscle cells. *Arterioscler Thromb Vasc Biol*. 2008;28(5):886-891. doi:10.1161/ATVBAHA.108.162693
277. Zhang J, Lan Y, Sanyal S. Modulation of lipid droplet metabolism-A potential target for therapeutic intervention in Flaviviridae Infections. *Front Microbiol*. 2017;8(NOV):2286. doi:10.3389/FMICB.2017.02286/BIBTEX
278. Martín-Acebes MA, Vázquez-Calvo Á, Saiz JC. Lipids and flaviviruses, present and future perspectives for the control of dengue, Zika, and West Nile viruses. *Prog Lipid Res*. 2016;64:123-137. doi:10.1016/J.PLIPRES.2016.09.005
279. Cloherty APM, Olmstead AD, Ribeiro CMS, Jean F. Hijacking of Lipid Droplets by Hepatitis C, Dengue and Zika Viruses—From Viral Protein Moonlighting to Extracellular Release. *Int J Mol Sci*. 2020;21(21):1-18. doi:10.3390/IJMS21217901
280. Rothan HA, Fang S, Mahesh M, Byrareddy SN. Zika Virus and the Metabolism of Neuronal Cells. *Mol Neurobiol*. 2019;56(4):2551-2557. doi:10.1007/S12035-018-1263-X/FIGURES/3
281. Li X, Wu K, Zeng S, et al. Viral Infection Modulates Mitochondrial Function. *Int J Mol Sci*. 2021;22(8). doi:10.3390/IJMS22084260
282. Thaker SK, Chapa T, Garcia G, et al. Differential Metabolic Reprogramming by Zika Virus Promotes Cell Death in Human versus Mosquito Cells. *Cell Metab*. 2019;29(5):1206-1216.e4. doi:10.1016/J.CMET.2019.01.024
283. Singh S, Singh PK, Suhail H, et al. AMP-Activated Protein Kinase Restricts Zika Virus Replication in Endothelial Cells by Potentiating Innate Antiviral Responses and Inhibiting Glycolysis. *J Immunol*. 2020;204(7):1810-1824. doi:10.4049/JIMMUNOL.1901310/-/DCSUPPLEMENTAL
284. Nakai N, Obayashi M, Nagasaki M, et al. The abundance of mRNAs for pyruvate dehydrogenase kinase isoenzymes in brain regions of young and aged rats. *Life Sci*. 2000;68(5):497-503. doi:10.1016/S0024-3205(00)00947-4
285. Grünert SC, Wehrle A, Villavicencio-Lorini P, et al. Medium-chain acyl-CoA dehydrogenase deficiency associated with a novel splice mutation in the ACADM gene missed by newborn screening. *BMC Med Genet*. 2015;16(1):1-9. doi:10.1186/S12881-015-0199-5/FIGURES/5
286. Yang J, Yuan D, Tan X, et al. Analysis of a family with mitochondrial trifunctional protein deficiency caused by HADHA gene mutations. *Mol Med Rep*. 2022;25(2):1-8. doi:10.3892/MMR.2021.12563/HTML
287. Menendez JA, Lupu R. Fatty acid synthase and the lipogenic phenotype in cancer pathogenesis. *Nat Rev Cancer*. 2007;7(10):763-777. doi:10.1038/NRC2222
288. Tarnowski BI, Spinale FG, Nicholson JH. Biotechnic & Histochemistry DAPI as a Useful Stain for Nuclear Quantitation. Published online 1991. doi:10.3109/10520299109109990
289. Caldas LA, Azevedo RC, da Silva JL, de Souza W. Microscopy analysis of Zika virus morphogenesis in mammalian cells. *Sci Reports 2020 101*. 2020;10(1):1-11. doi:10.1038/s41598-020-65409-y
290. Cortese M, Goellner S, Acosta EG, et al. Ultrastructural Characterization of Zika Virus Replication Factories. *Cell Rep*. 2017;18(9):2113-2123. doi:10.1016/J.CELREP.2017.02.014
291. Elmore S. Apoptosis: A Review of Programmed Cell Death. *Toxicol Pathol*. 2007;35(4):495. doi:10.1080/01926230701320337
292. Rogalińska M. Alterations in cell nuclei during apoptosis. *Cell Mol Biol Lett*. 2002;7(4):995-1018. Accessed February 8, 2022. https://europepmc.org/article/med/12511968
293. Duggal NK, McDonald EM, Weger-Lucarelli J, et al. Mutations present in a low-passage Zika virus isolate result in attenuated pathogenesis in mice. *Virology*. 2019;530:19-26. doi:10.1016/J.VIROL.2019.02.004
294. Simonin Y, van Riel D, Van de Perre P, Rockx B, Salinas S. Differential virulence between Asian and African lineages of Zika virus. *PLoS Negl Trop Dis*. 2017;11(9):e0005821. doi:10.1371/JOURNAL.PNTD.0005821

295. Beaver JT, Lelutiu N, Habib R, Skountzou I. Evolution of two major Zika virus lineages: Implications for pathology, immune response, and vaccine development. *Front Immunol*. 2018;9(JUL):1640. doi:10.3389/FIMMU.2018.01640/BIBTEX
296. Reslan A, Haddad JG, Koundi LM, Desprès P, Bascands JL, Gadea G. Zika Virus Growth in Human Kidney Cells Is Restricted by an Elevated Glucose Level. *Int J Mol Sci 2021, Vol 22, Page 2495*. 2021;22(5):2495. doi:10.3390/IJMS22052495
297. He Z, An S, Chen J, et al. Neural progenitor cell pyroptosis contributes to Zika virus-induced brain atrophy and represents a therapeutic target. *Proc Natl Acad Sci U S A*. 2020;117(38):23869-23878. doi:10.1073/PNAS.2007773117/-/DCSUPPLEMENTAL
298. Harsh S, Fu Y, Kenney E, Han Z, Eleftherianos I. Zika virus non-structural protein NS4A restricts eye growth in Drosophila through regulation of JAK/STAT signaling. Published online 2020. doi:10.1242/dmm.040816
299. Yang S, Gorshkov K, Lee EM, et al. Zika Virus-Induced Neuronal Apoptosis via Increased Mitochondrial Fragmentation. *Front Microbiol*. 2020;11. doi:10.3389/FMICB.2020.598203/FULL
300. Chen Q, Gouilly J, Ferrat YJ, et al. Metabolic reprogramming by Zika virus provokes inflammation in human placenta. *Nat Commun 2020 111*. 2020;11(1):1-16. doi:10.1038/s41467-020-16754-z
301. García CC, Vázquez CA, Giovannoni F, et al. Cellular Organelles Reorganization During Zika Virus Infection of Human Cells. *Front Microbiol*. 2020;11:1558. doi:10.3389/FMICB.2020.01558/BIBTEX
302. Twig G, Shirihai OS. The Interplay Between Mitochondrial Dynamics and Mitophagy. *Antioxid Redox Signal*. 2011;14(10):1939. doi:10.1089/ARS.2010.3779
303. Ponia SS, Robertson SJ, McNally KL, et al. Mitophagy antagonism by Zika virus reveals Ajuba as a regulator of PINK1-Parkin signaling, PKR-dependent inflammation, and viral invasion of tissues. *bioRxiv*. Published online January 30, 2021:2021.01.29.428870. doi:10.1101/2021.01.29.428870
304. Jiménez de Oya N, Esler WP, Huard K, et al. Targeting host metabolism by inhibition of acetyl-Coenzyme A carboxylase reduces flavivirus infection in mouse models. *https://doi.org/101080/2222175120191604084*. 2019;8(1):624-636. doi:10.1080/22221751.2019.1604084
305. Melo CFOR, De Oliveira DN, De Oliveira Lima E, et al. A Lipidomics Approach in the Characterization of Zika-Infected Mosquito Cells: Potential Targets for Breaking the Transmission Cycle. *PLoS One*. 2016;11(10):e0164377. doi:10.1371/JOURNAL.PONE.0164377
306. Zhou J, Chi X, Cheng M, et al. Zika virus degrades the ω-3 fatty acid transporter Mfsd2a in brain microvascular endothelial cells and impairs lipid homeostasis. *Sci Adv*. 2019;5(10):7142-7165. doi:10.1126/SCIADV.AAX7142/SUPPL_FILE/AAX7142_SM.PDF
307. Zhang J, Lan Y, Li MY, et al. Flaviviruses Exploit the Lipid Droplet Protein AUP1 to Trigger Lipophagy and Drive Virus Production. *Cell Host Microbe*. 2018;23(6):819-831.e5. doi:10.1016/J.CHOM.2018.05.005/ATTACHMENT/AD40031E-B931-4DFA-91D0-55A3B36F64F6/MMC3.XLSX
308. Coyaud E, Ranadheera C, Cheng D, et al. Global interactomics uncovers extensive organellar targeting by Zika Virus. *Mol Cell Proteomics*. 2018;17(11):2242-2255. doi:10.1074/MCP.TIR118.000800/ATTACHMENT/1B4FC3E6-3159-4BE4-BEAE-6D2D779C17CD/MMC1.ZIP
309. Fauci AS, Morens DM. Zika Virus in the Americas — Yet Another Arbovirus Threat. *N Engl J Med*. 2016;374(7):601-604. doi:10.1056/NEJMP1600297/SUPPL_FILE/NEJMP1600297_DISCLOSURES.PDF
310. Joob B, Wiwanitkit V. Zika virus infection and psychosis. *Brazilian J Psychiatry*. 2018;40(1):113-113. doi:10.1590/1516-4446-2017-2561
311. Tucci V, Moukaddam N, Meadows J, Shah S, Galwankar SC, Bobby Kapur G. The Forgotten Plague: Psychiatric Manifestations of Ebola, Zika, and Emerging

Infectious Diseases. *J Glob Infect Dis*. 2017;9(4):151. doi:10.4103/JGID.JGID_66_17
312. SciELO - Brazil - Zika virus infection and psychosis Zika virus infection and psychosis. Accessed February 24, 2022. https://www.scielo.br/j/rbp/a/XsBHnGP7HTBM5fPZBsnbktD/?lang=en
313. Dinakaran D, Sreeraj VS, Venkatasubramanian G. Dengue and Psychiatry: Manifestations, Mechanisms, and Management Options. *Indian J Psychol Med*. Published online 2021. doi:10.1177/02537176211022571
314. Cheslack-Postava K, Brown AS. Prenatal infection and schizophrenia: A decade of further progress. *Schizophr Res*. Published online May 17, 2021. doi:10.1016/J.SCHRES.2021.05.014
315. Jones HJ, Stergiakouli E, Tansey KE, et al. Phenotypic Manifestation of Genetic Risk for Schizophrenia During Adolescence in the General Population. *JAMA Psychiatry*. 2016;73(3):221-228. doi:10.1001/JAMAPSYCHIATRY.2015.3058
316. Neuropsychiatric disorders of childhood and adolescence. - PsycNET. Accessed February 24, 2022. https://psycnet.apa.org/record/2007-14922-029
317. Walterfang M, Bonnot O, Mocellin R, Velakoulis D. The neuropsychiatry of inborn errors of metabolism. *J Inherit Metab Dis 2013 364*. 2013;36(4):687-702. doi:10.1007/S10545-013-9618-Y
318. Baggiani M, Dell'Anno MT, Pistello M, Conti L, Onorati M. Human Neural Stem Cell Systems to Explore Pathogen-Related Neurodevelopmental and Neurodegenerative Disorders. *Cells*. 2020;9(8). doi:10.3390/CELLS9081893
319. Lee AKY, Henrietta MH, Wong VCW. Mechanisms of Maternal-Fetal Transmission of Hepatitis B Virus. *J Infect Dis*. 1978;138(5):668-671. doi:10.1093/INFDIS/138.5.668
320. Douglas GC, King BF. Maternal-Fetal Transmission of Human Immunodeficiency Virus: A Review of Possible Routes and Cellular Mechanisms of Infection. *Clin Infect Dis*. 1992;15(4):678-691. doi:10.1093/CLIND/15.4.678
321. Waters MJ, Kaye PL. The role of growth hormone in fetal development. *Growth Horm IGF Res*. 2002;12(3):137-146. doi:10.1016/S1096-6374(02)00018-7
322. Meyer G, Schaaps JP, Moreau L, Goffinet AM. Embryonic and Early Fetal Development of the Human Neocortex. *J Neurosci*. 2000;20(5):1858-1868. doi:10.1523/JNEUROSCI.20-05-01858.2000
323. Brioschi S, Zhou Y, Colonna M. Brain Parenchymal and Extraparenchymal Macrophages in Development, Homeostasis, and Disease. *J Immunol*. 2020;204(2):294-305. doi:10.4049/JIMMUNOL.1900821
324. Alliot F, Godin I, Pessac B. Microglia derive from progenitors, originating from the yolk sac, and which proliferate in the brain. *Dev Brain Res*. 1999;117(2):145-152. doi:10.1016/S0165-3806(99)00113-3
325. Utz SG, See P, Mildenberger W, et al. Early Fate Defines Microglia and Non-parenchymal Brain Macrophage Development. *Cell*. 2020;181(3):557-573.e18. doi:10.1016/J.CELL.2020.03.021
326. Wynn TA, Chawla A, Pollard JW. Macrophage biology in development, homeostasis and disease. *Nat 2013 4967446*. 2013;496(7446):445-455. doi:10.1038/nature12034
327. McGrath KE, Frame JM, Palis J. Early hematopoiesis and macrophage development. *Semin Immunol*. 2015;27(6):379-387. doi:10.1016/J.SMIM.2016.03.013
328. Lee E, Eo JC, Lee C, Yu JW. Distinct Features of Brain-Resident Macrophages: Microglia and Non-Parenchymal Brain Macrophages. *Mol Cells*. 2021;44(5):281. doi:10.14348/MOLCELLS.2021.0060
329. Engelhardt B, Vajkoczy P, Weller RO. The movers and shapers in immune privilege of the CNS. *Nat Immunol*. 2017;18(2):123-131. doi:10.1038/NI.3666
330. Kierdorf K, Masuda T, Jordão MJC, Prinz M. Macrophages at CNS interfaces: ontogeny and function in health and disease. *Nat Rev Neurosci*. 2019;20(9):547-

562. doi:10.1038/S41583-019-0201-X
331. Vogel DYS, Glim JE, Stavenuiter AWD, et al. Human macrophage polarization in vitro: Maturation and activation methods compared. *Immunobiology*. 2014;219(9):695-703. doi:10.1016/J.IMBIO.2014.05.002
332. Zhang H, Reilly MP. Human induced pluripotent stem cell?derived macrophages for unraveling human macrophage biology. *Arterioscler Thromb Vasc Biol*. 2017;37(11):2000-2006. doi:10.1161/ATVBAHA.117.309195
333. Lee CZW, Kozaki T, Ginhoux F. Studying tissue macrophages in vitro: are iPSC-derived cells the answer? *Nat Rev Immunol 2018 1811*. 2018;18(11):716-725. doi:10.1038/s41577-018-0054-y
334. Brioschi S, Zhou Y, Colonna M. Brain macrophages in development, homeostasis and disease. *J Immunol*. 2020;204(2):294. doi:10.4049/JIMMUNOL.1900821
335. Rey-Giraud F, Hafner M, Ries CH. In Vitro Generation of Monocyte-Derived Macrophages under Serum-Free Conditions Improves Their Tumor Promoting Functions. *PLoS One*. 2012;7(8):e42656. doi:10.1371/JOURNAL.PONE.0042656
336. Vo Q V., Trenerry C, Rochfort S, Wadeson J, Leyton C, Hughes AB. Synthesis and anti-inflammatory activity of indole glucosinolates. *Bioorg Med Chem*. 2014;22(2):856-864. doi:10.1016/J.BMC.2013.12.003
337. Kreutz M, Krause SW, Hennemann B, Rehm A, Andreesen R. Macrophage heterogeneity and differentiation: defined serum-free culture conditions induce different types of macrophages in vitro. *Res Immunol*. 1992;143(1):107-115. doi:10.1016/0923-2494(92)80087-2
338. Buchrieser J, Oliva-Martin MJ, Moore MD, et al. RIPK1 is a critical modulator of both tonic and TLR-responsive inflammatory and cell death pathways in human macrophage differentiation. *Cell Death Dis*. 2018;9(10). doi:10.1038/S41419-018-1053-4
339. Buchrieser J, James W, Moore MD. Human Induced Pluripotent Stem Cell-Derived Macrophages Share Ontogeny with MYB-Independent Tissue-Resident Macrophages. *Stem Cell Reports*. 2017;8(2):334-345. doi:10.1016/J.STEMCR.2016.12.020
340. Palmer CS, Cherry CL, Sada-Ovalle I, Singh A, Crowe SM. Glucose Metabolism in T Cells and Monocytes: New Perspectives in HIV Pathogenesis. *EBioMedicine*. 2016;6:31-41. doi:10.1016/J.EBIOM.2016.02.012
341. Hollenbaugh JA, Munger J, Kim B. Metabolite profiles of human immunodeficiency virus infected CD4+ T cells and macrophages using LC–MS/MS analysis. *Virology*. 2011;415(2):153-159. doi:10.1016/J.VIROL.2011.04.007
342. Odegaard JI, Chawla A. Alternative macrophage activation and metabolism. *Annu Rev Pathol Mech Dis*. 2011;6:275-297. doi:10.1146/ANNUREV-PATHOL-011110-130138
343. Rodríguez-Prados J-C, Través PG, Cuenca J, et al. Substrate Fate in Activated Macrophages: A Comparison between Innate, Classic, and Alternative Activation. *J Immunol*. 2010;185(1):605-614. doi:10.4049/JIMMUNOL.0901698
344. H. Ebrahimi K, Gilbert jaramillo J, James WS, McCullagh JSO. Interferon-stimulated gene products as regulators of central carbon metabolism. *FEBS J*. Published online November 13, 2020:febs.15625. doi:10.1111/febs.15625
345. Yan S, Kumari M, Xiao H, et al. IRF3 reduces adipose thermogenesis via ISG15-mediated reprogramming of glycolysis. *J Clin Invest*. 2021;131(7). doi:10.1172/JCI144888
346. Xie M, Yu Y, Kang R, et al. PKM2-dependent glycolysis promotes NLRP3 and AIM2 inflammasome activation. *Nat Commun 2016 71*. 2016;7(1):1-13. doi:10.1038/ncomms13280
347. Yellen G. Ketone bodies, glycolysis, and KATP channels in the mechanism of the ketogenic diet. *Epilepsia*. 2008;49(Suppl 8):80. doi:10.1111/J.1528-1167.2008.01843.X
348. Fei Y, Shi R, Song Z, Wu J. Metabolic Control of Epilepsy: A Promising

Therapeutic Target for Epilepsy. *Front Neurol*. 2020;11:1694. doi:10.3389/FNEUR.2020.592514/BIBTEX
349. Viviani B. Preparation and Coculture of Neurons and Glial Cells. *Curr Protoc Cell Biol*. 2006;32(1):2.7.1-2.7.21. doi:10.1002/0471143030.CB0207S32
350. Johnson MA, Weick JP, Pearce RA, Zhang SC. Functional Neural Development from Human Embryonic Stem Cells: Accelerated Synaptic Activity via Astrocyte Coculture. *J Neurosci*. 2007;27(12):3069-3077. doi:10.1523/JNEUROSCI.4562-06.2007
351. Bell S, Hettige NC, Silveira H, et al. Differentiation of Human Induced Pluripotent Stem Cells (iPSCs) into an Effective Model of Forebrain Neural Progenitor Cells and Mature Neurons. *Bio-protocol*. 2019;9(5). doi:10.21769/BIOPROTOC.3188
352. Burnham P, Raiborn C, Varon S. Replacement of Nerve-Growth Factor by Ganglionic Non-Neuronal Cells for the Survival In Vitro of Dissociated Ganglionic Neurons. *Proc Natl Acad Sci*. 1972;69(12):3556-3560. doi:10.1073/PNAS.69.12.3556
353. Roth S, Zhang SJ, Chiu J, Wirth EK, Schweizer U. Development of a serum-free supplement for primary neuron culture reveals the interplay of selenium and vitamin E in neuronal survival. *J Trace Elem Med Biol*. 2010;24(2):130-137. doi:10.1016/J.JTEMB.2010.01.007
354. Song L, Yuan X, Jones Z, et al. Functionalization of Brain Region-specific Spheroids with Isogenic Microglia-like Cells. *Sci Reports 2019 91*. 2019;9(1):1-18. doi:10.1038/s41598-019-47444-6
355. Fagerlund I, Dougalis A, Shakirzyanova A, et al. Microglia Orchestrate Neuronal Activity in Brain Organoids. *SSRN Electron J*. Published online January 29, 2021. doi:10.2139/SSRN.3773789
356. Ormel PR, Vieira de Sá R, van Bodegraven EJ, et al. Microglia innately develop within cerebral organoids. *Nat Commun 2018 91*. 2018;9(1):1-14. doi:10.1038/s41467-018-06684-2
357. Sato K. Effects of Microglia on Neurogenesis. *Glia*. 2015;63(8):1394-1405. doi:10.1002/GLIA.22858
358. Pérez-Rodríguez DR, Blanco-Luquin I, Mendioroz M. The Participation of Microglia in Neurogenesis: A Review. *Brain Sci 2021, Vol 11, Page 658*. 2021;11(5):658. doi:10.3390/BRAINSCI11050658
359. Aubry F, Jacobs S, Darmuzey M, et al. Recent African strains of Zika virus display higher transmissibility and fetal pathogenicity than Asian strains. *Nat Commun 2021 121*. 2021;12(1):1-14. doi:10.1038/s41467-021-21199-z
360. Bernhauerová V, Rezelj V V., Vignuzzi M. Modelling Degradation and Replication Kinetics of the Zika Virus In Vitro Infection. *Viruses*. 2020;12(5). doi:10.3390/V12050547
361. Ayala-Nunez NV, Follain G, Delalande F, et al. Zika virus enhances monocyte adhesion and transmigration favoring viral dissemination to neural cells. *Nat Commun 2019 101*. 2019;10(1):1-16. doi:10.1038/s41467-019-12408-x
362. Mesci P, Macia A, Larock CN, et al. Modeling neuro-immune interactions during Zika virus infection. doi:10.1093/hmg/ddx382
363. Magee BA, Potezny N, Rofe AM, Conyers RAJ. THE INHIBITION OF MALIGNANT CELL GROWTH BY KETONE BODIES. *Aust J Exp Biol Med Sci*. 1979;57(5):529-539. doi:10.1038/ICB.1979.54
364. Xie X, Yang Y, Muruato AE, et al. Understanding zika virus stability and developing a chimeric vaccine through functional analysis. *MBio*. 2017;8(1). doi:10.1128/MBIO.02134-16/ASSET/C7BBDCE7-7895-4730-9CC6-156249BA219B/ASSETS/GRAPHIC/MBO0011731870005.JPEG
365. Gorbalenya AE, Baker SC, Baric RS, et al. The species Severe acute respiratory syndrome-related coronavirus: classifying 2019-nCoV and naming it SARS-CoV-2. *Nat Microbiol 2020 54*. 2020;5(4):536-544. doi:10.1038/s41564-020-0695-z
366. Harapan H, Itoh N, Yufika A, et al. Coronavirus disease 2019 (COVID-19): A

literature review. *J Infect Public Health*. 2020;13(5):667-673. doi:10.1016/J.JIPH.2020.03.019
367. Hu B, Guo H, Zhou P, Shi Z-L. Characteristics of SARS-CoV-2 and COVID-19. doi:10.1038/s41579-020-00459-7
368. Zhou L, Ayeh SK, Chidambaram V, Karakousis PC. Modes of transmission of SARS-CoV-2 and evidence for preventive behavioral interventions. *BMC Infect Dis*. 2021;21(1):496. doi:10.1186/S12879-021-06222-4
369. Seto WH, Tsang D, Yung RWH, et al. Effectiveness of precautions against droplets and contact in prevention of nosocomial transmission of severe acute respiratory syndrome (SARS). *Lancet (London, England)*. 2003;361(9368):1519. doi:10.1016/S0140-6736(03)13168-6
370. Gustine JN, Jones D. Immunopathology of Hyperinflammation in COVID-19. *Am J Pathol*. 2021;191(1). doi:10.1016/J.AJPATH.2020.08.009
371. Abassi Z, Knaney Y, Karram T, Heyman SN. The Lung Macrophage in SARS-CoV-2 Infection: A Friend or a Foe? *Front Immunol*. 2020;11:1312. doi:10.3389/FIMMU.2020.01312/BIBTEX
372. Wang C, Xie J, Zhao L, et al. Alveolar macrophage dysfunction and cytokine storm in the pathogenesis of two severe COVID-19 patients. *EBioMedicine*. 2020;57:102833. doi:10.1016/J.EBIOM.2020.102833
373. Wang D, Hu B, Hu C, et al. Clinical Characteristics of 138 Hospitalized Patients With 2019 NovelCoronavirus–Infected Pneumonia in Wuhan, China. *JAMA*. 2020;323(11):1061. doi:10.1001/JAMA.2020.1585
374. Huang C, Wang Y, Li X, et al. Clinical features of patients infected with 2019 novel coronavirus in Wuhan, China. *Lancet (London, England)*. 2020;395(10223):497. doi:10.1016/S0140-6736(20)30183-5
375. Zheng Y-Y, Ma Y-T, Zhang J-Y, Xie X. COVID-19 and the cardiovascular system. *Nat Rev Cardiol*. doi:10.1038/s41569-020-0360-5
376. Arentz M, Yim E, Klaff L, et al. Characteristics and Outcomes of 21 Critically Ill Patients WithCOVID-19 in Washington State. *JAMA*. 2020;323(16):1612. doi:10.1001/JAMA.2020.4326
377. Perico L, Benigni A, Remuzzi G. Should COVID-19 Concern Nephrologists? Why and to What Extent? The Emerging Impasse of Angiotensin Blockade. *Nephron*. 2020;144(5):213-221. doi:10.1159/000507305
378. Yang L, Han Y, Jaffré F, et al. An Immuno-Cardiac Model for Macrophage-Mediated Inflammation in COVID-19 Hearts. *Circ Res*. Published online June 25, 2021:33-46. doi:10.1161/CIRCRESAHA.121.319060
379. Shi S, Qin M, Shen B, et al. Association of Cardiac Injury With Mortality in Hospitalized Patients With COVID-19 in Wuhan, China. *JAMA Cardiol*. 2020;5(7):802-810. doi:10.1001/JAMACARDIO.2020.0950
380. Ammirati E, Wang DW. SARS-CoV-2 inflames the heart. The importance of awareness of myocardial injury in COVID-19 patients. *Int J Cardiol*. 2020;311:122-123. doi:10.1016/J.IJCARD.2020.03.086
381. Marchiano S, Hsiang TY, Khanna A, et al. SARS-CoV-2 Infects Human Pluripotent Stem Cell-Derived Cardiomyocytes, Impairing Electrical and Mechanical Function. *Stem Cell Reports*. 2021;16(3):478-492. doi:10.1016/J.STEMCR.2021.02.008
382. Bailey AL, Dmytrenko O, Greenberg L, et al. SARS-CoV-2 Infects Human Engineered Heart Tissues and Models COVID-19 Myocarditis. *Basic to Transl Sci*. 2021;6(4):331-345. doi:10.1016/J.JACBTS.2021.01.002
383. Bojkova D, Wagner JUG, Shumliakivska M, et al. SARS-CoV-2 infects and induces cytotoxic effects in human cardiomyocytes. *Cardiovasc Res*. 2020;116(14):2207-2215. doi:10.1093/CVR/CVAA267
384. Clarke NE, Turner AJ. Angiotensin-Converting Enzyme 2: The First Decade. *Int J Hypertens*. 2012;2012:12. doi:10.1155/2012/307315
385. Hamming I, Cooper ME, Haagmans BL, et al. The emerging role of ACE2 in physiology and disease. *J Pathol*. 2007;212(1):1. doi:10.1002/PATH.2162

386. Donoghue M, Hsieh F, Baronas E, et al. *A Novel Angiotensin-Converting Enzyme-Related Carboxypeptidase (ACE2) Converts Angiotensin I to Angiotensin 1-9*.; 2000. http://www.circresaha.org.
387. Lumbers ER, Delforce SJ, Pringle KG, Smith GR. The Lung, the Heart, the Novel Coronavirus, and the Renin-Angiotensin System; The Need for Clinical Trials. *Front Med*. 2020;7:248. doi:10.3389/FMED.2020.00248/BIBTEX
388. Imai Y, Kuba K, Rao S, et al. Angiotensin-converting enzyme 2 protects from severe acute lung failure. *Nature*. 2005;436(7047):112. doi:10.1038/NATURE03712
389. Danilczyk U, Eriksson U, Oudit GY, Penninger JM. Physiological roles of angiotensin-converting enzyme 2. *Cell Mol Life Sci*. 2004;61(21):2714-2719. doi:10.1007/S00018-004-4241-6
390. Boehm M, Nabel EG. Angiotensin-converting enzyme 2--a new cardiac regulator. *N Engl J Med*. 2002;347(22):1795-1797. doi:10.1056/NEJMCIBR022472
391. Pang X, Cui Y, Zhu Y. Recombinant human ACE2: potential therapeutics of SARS-CoV-2 infection and its complication. *Acta Pharmacol Sin 2020 419*. 2020;41(9):1255-1257. doi:10.1038/s41401-020-0430-6
392. Yan R, Zhang Y, Li Y, Xia L, Zhou Q. Structure of dimeric full-length human ACE2 in complex with B0AT1. *bioRxiv*. Published online February 18, 2020:2020.02.17.951848. doi:10.1101/2020.02.17.951848
393. Liu Z, Xiao X, Wei X, et al. Composition and divergence of coronavirus spike proteins and host ACE2 receptors predict potential intermediate hosts of SARS-CoV-2. *J Med Virol*. 2020;92(6):595-601. doi:10.1002/JMV.25726
394. Shang J, Ye G, Shi K, et al. Structural basis of receptor recognition by SARS-CoV-2. *Nature*. doi:10.1038/s41586-020-2179-y
395. Hoffmann M, Kleine-Weber H, Schroeder S, et al. SARS-CoV-2 Cell Entry Depends on ACE2 and TMPRSS2 and Is Blocked by a Clinically Proven Protease Inhibitor. *Cell*. 2020;181(2):271. doi:10.1016/J.CELL.2020.02.052
396. Yan R, Zhang Y, Li Y, Xia L, Guo Y, Zhou Q. Structural basis for the recognition of SARS-CoV-2 by full-length human ACE2. *Science*. 2020;367(6485):1444. doi:10.1126/SCIENCE.ABB2762
397. Hoffmann M, Kleine-Weber H, Schroeder S, et al. SARS-CoV-2 Cell Entry Depends on ACE2 and TMPRSS2 and Is Blocked by a Clinically Proven Protease Inhibitor. *Cell*. 2020;181(2):271-280.e8. doi:10.1016/J.CELL.2020.02.052
398. Perrotta F, Matera MG, Cazzola M, Bianco A. Severe respiratory SARS-CoV2 infection: Does ACE2 receptor matter? *Respir Med*. 2020;168:105996. doi:10.1016/J.RMED.2020.105996
399. Bhalerao A, Raut S, Noorani B, Mancuso S, Cucullo L. Molecular Mechanisms of Multi-Organ Failure in COVID-19 and Potential of Stem Cell Therapy. *Cells 2021, Vol 10, Page 2878*. 2021;10(11):2878. doi:10.3390/CELLS10112878
400. Tan SYS, Krasnow MA. Developmental origin of lung macrophage diversity. *Dev*. 2016;143(8):1318-1327. doi:10.1242/DEV.129122/-/DC1
401. Den Haan JMM, Kraal G. Innate immune functions of macrophage subpopulations in the spleen. *J Innate Immun*. 2012;4(5-6):437-445. doi:10.1159/000335216
402. Hu G, Christman JW. Editorial: Alveolar macrophages in lung inflammation and resolution. *Front Immunol*. 2019;10(SEP):2275. doi:10.3389/FIMMU.2019.02275/BIBTEX
403. Takahashi K, Yamamura F, Naito M. Differentiation, maturation, and proliferation of macrophages in the mouse yolk sac: a light-microscopic, enzyme-cytochemical, immunohistochemical, and ultrastructural study. *J Leukoc Biol*. 1989;45(2):87-96. doi:10.1002/JLB.45.2.87
404. Twigg HL. Macrophages in Innate and Acquired Immunity. *Semin Respir Crit Care Med*. 2004;25(1):21-31. doi:10.1055/S-2004-822302/ID/41
405. Vareille M, Kieninger E, Edwards MR, Regamey N. The Airway Epithelium: Soldier in the Fight against Respiratory Viruses. *Clin Microbiol Rev*. 2011;24(1):210.

doi:10.1128/CMR.00014-10
406. Spiteri MA, Poulter LW. *Characterization of Immune Inducer and Suppressor Macrophages from the Normal Human Lung*. Vol 93. https://academic.oup.com/cei/article/83/1/157/6488601
407. Kradin RL, Liu HW, Van Rooijen N, Springer K, Zhao LH, Leary CP. Pulmonary Immunity to Listeria Is Enhanced by Elimination of Alveolar Macrophages. *https://doi.org/101164/ajrccm15969810117*. 2012;159(6):1967-1974. doi:10.1164/AJRCCM.159.6.9810117
408. Aguzzi A, Barres BA, Bennett ML. Microglia: Scapegoat, Saboteur, or Something Else? doi:10.1126/science.1227901
409. Toews GB, Vial WC, Dunn MM, et al. The accessory cell function of human alveolar macrophages in specific T cell proliferation. *J Immunol*. 1984;132(1).
410. Lipscomb MF, Lyons CR, Nunez G, et al. Human alveolar macrophages: HLA-DR-positive macrophages that are poor stimulators of a primary mixed leukocyte reaction. *J Immunol*. 1986;136(2).
411. Lyons CR, Ball EJ, Toews GB, Weissler JC, Stastny P, Lipscomb MF. Inability of human alveolar macrophages to stimulate resting T cells correlates with decreased antigen-specific T cell-macrophage binding. *J Immunol*. 1986;137(4).
412. Singh Gangwar R, Vinayachandran V, Rengasamy P, et al. Differential contribution of bone marrow-derived infiltrating monocytes and resident macrophages to persistent lung inflammation in chronic air pollution exposure. 2020;10:14348. doi:10.1038/s41598-020-71144-1
413. Wendisch D, Dietrich O, Mari T, et al. SARS-CoV-2 infection triggers profibrotic macrophage responses and lung fibrosis. *Cell*. 2021;184(26):6243. doi:10.1016/J.CELL.2021.11.033
414. Maus UA, Janzen S, Wall G, et al. Resident alveolar macrophages are replaced by recruited monocytes in response to endotoxin-induced lung inflammation. *Am J Respir Cell Mol Biol*. 2006;35(2):227-235. doi:10.1165/RCMB.2005-0241OC
415. Banu N, Panikar SS, Leal LR, Leal AR. Protective role of ACE2 and its downregulation in SARS-CoV-2 infection leading to Macrophage Activation Syndrome: Therapeutic implications. *Life Sci*. 2020;256:117905. doi:10.1016/J.LFS.2020.117905
416. Lv J, Wang Z, Qu Y, et al. Distinct uptake, amplification, and release of SARS-CoV-2 by M1 and M2 alveolar macrophages. *Cell Discov 2021 71*. 2021;7(1):1-12. doi:10.1038/s41421-021-00258-1
417. Grant RA, Morales-Nebreda L, Markov NS, et al. Circuits between infected macrophages and T cells in SARS-CoV-2 pneumonia. *Nat 2021 5907847*. 2021;590(7847):635-641. doi:10.1038/s41586-020-03148-w
418. Hu G, Christman JW. Editorial: Alveolar Macrophages in Lung Inflammation and Resolution. *Alveolar Macrophages Lung Inflamm Resolut Front Immunol*. 2019;10:2275. doi:10.3389/fimmu.2019.02275
419. Chen N, Zhou M, Dong X, et al. Epidemiological and clinical characteristics of 99 cases of 2019 novel coronavirus pneumonia in Wuhan, China: a descriptive study. *Lancet (London, England)*. 2020;395(10223):507. doi:10.1016/S0140-6736(20)30211-7
420. Perez-Zsolt D, Muñoz-Basagoiti J, Rodon J, et al. SARS-CoV-2 interaction with Siglec-1 mediates trans-infection by dendritic cells. *Cell Mol Immunol 2021 1812*. 2021;18(12):2676-2678. doi:10.1038/s41423-021-00794-6
421. Wong CK, Lam CWK, Wu AKL, et al. Plasma inflammatory cytokines and chemokines in severe acute respiratory syndrome. *Clin Exp Immunol*. 2004;136(1):95-103. doi:10.1111/J.1365-2249.2004.02415.X
422. Gattinoni L, Chiumello D, Rossi S. COVID-19 pneumonia: ARDS or not? *Crit Care*. 2020;24(1):1-3. doi:10.1186/S13054-020-02880-Z/FIGURES/1
423. Du RH, Liu LM, Yin W, et al. Hospitalization and critical care of 109 decedents with COVID-19 pneumonia in Wuhan, China. *Ann Am Thorac Soc*. 2020;17(7):839-846.

doi:10.1513/ANNALSATS.202003-225OC/SUPPL_FILE/DISCLOSURES.PDF
424. Wu CP, Adhi F, Highland K. Recognition and management of respiratory co-infection and secondary bacterial pneumonia in patients with COVID-19. *Cleve Clin J Med*. 2020;87(11):659-663. doi:10.3949/CCJM.87A.CCC015
425. Shafran N, Shafran I, Ben-Zvi H, et al. Secondary bacterial infection in COVID-19 patients is a stronger predictor for death compared to influenza patients. *Sci Reports* |. 123AD;11:12703. doi:10.1038/s41598-021-92220-0
426. Feldman C, Anderson R. The role of co-infections and secondary infections in patients with COVID-19. *Pneumonia 2021 131*. 2021;13(1):1-15. doi:10.1186/S41479-021-00083-W
427. Wang W, Xu Y, Gao R, et al. Detection of SARS-CoV-2 in Different Types of Clinical Specimens. *JAMA*. 2020;323(18):1843-1844. doi:10.1001/JAMA.2020.3786
428. Zhou M, Zhang X, Qu J. Coronavirus disease 2019 (COVID-19): a clinical update. *Front Med 2020 142*. 2020;14(2):126-135. doi:10.1007/S11684-020-0767-8
429. Yilla M, Harcourt BH, Hickman CJ, et al. SARS-coronavirus replication in human peripheral monocytes/macrophages. *Virus Res*. 2005;107(1):93. doi:10.1016/J.VIRUSRES.2004.09.004
430. Nicholls JM, Poon LLM, Lee KC, et al. Lung pathology of fatal severe acute respiratory syndrome. *Lancet*. 2003;361(9371):1773-1778. doi:10.1016/S0140-6736(03)13413-7
431. Hu W, Song X, Yu H, Zhao L, Zhao Y, Zhao Y. Further comments on the role of ACE-2 positive macrophages in human lung. *Cytometry*. Published online 2021. doi:10.1002/CYTO.A.24484
432. Cheung CY, Poon LLM, Ng lHY, et al. Cytokine Responses in Severe Acute Respiratory Syndrome Coronavirus-Infected Macrophages In Vitro: Possible Relevance to Pathogenesis. *J Virol*. 2005;79(12):7819-7826. doi:10.1128/JVI.79.12.7819-7826.2005/ASSET/5D65B65C-B125-4D00-A3BB-1835D6B2B29D/ASSETS/GRAPHIC/ZJV0120563950004.JPEG
433. Niles MA, Gogesch P, Kronhart S, et al. Macrophages and Dendritic Cells Are Not the Major Source of Pro-Inflammatory Cytokines Upon SARS-CoV-2 Infection. *Front Immunol*. 2021;12:1984. doi:10.3389/FIMMU.2021.647824/BIBTEX
434. García-Nicolás O, V'kovski P, Zettl F, Zimmer G, Thiel V, Summerfield A. No Evidence for Human Monocyte-Derived Macrophage Infection and Antibody-Mediated Enhancement of SARS-CoV-2 Infection. *Front Cell Infect Microbiol*. 2021;11:248. doi:10.3389/FCIMB.2021.644574/BIBTEX
435. Merad M, Martin JC. Author Correction: Pathological inflammation in patients with COVID-19: a key role for monocytes and macrophages (Nature Reviews Immunology, (2020), 20, 6, (355-362), 10.1038/s41577-020-0331-4). *Nat Rev Immunol*. 2020;20(7):448. doi:10.1038/S41577-020-0353-Y
436. Dupont M, Souriant S, Balboa L, et al. Tuberculosis-associated IFN-I induces Siglec-1 on tunneling nanotubes and favors HIV-1 spread in macrophages. *Elife*. 2020;9. doi:10.7554/ELIFE.52535
437. Hammonds JE, Beeman N, Ding L, et al. Siglec-1 initiates formation of the virus-containing compartment and enhances macrophage-to-T cell transmission of HIV-1. *PLOS Pathog*. 2017;13(1):e1006181. doi:10.1371/JOURNAL.PPAT.1006181
438. Levin R, Grinstein S, Canton J. The life cycle of phagosomes: formation, maturation, and resolution. *Immunol Rev*. 2016;273(1):156-179. doi:10.1111/IMR.12439
439. Levin R, Grinstein S, Schlam D. Phosphoinositides in phagocytosis and macropinocytosis. *Biochim Biophys Acta - Mol Cell Biol Lipids*. 2015;1851(6):805-823. doi:10.1016/J.BBALIP.2014.09.005
440. Uribe-Querol E, Rosales C. Phagocytosis: Our Current Understanding of a Universal Biological Process. *Front Immunol*. 2020;11:1066. doi:10.3389/FIMMU.2020.01066/BIBTEX

441. Fairn GD, Grinstein S. How nascent phagosomes mature to become phagolysosomes. *Trends Immunol*. 2012;33(8):397-405. doi:10.1016/J.IT.2012.03.003
442. Canton J. Phagosome maturation in polarized macrophages. *J Leukoc Biol*. 2014;96(5):729-738. doi:10.1189/JLB.1MR0114-021R
443. Marshansky V, Futai M, Graç Raposo by, Stenmark H. The V-type H+-ATPase in vesicular trafficking: targeting, regulation and function. *Curr Opin Cell Biol*. 2008;20(4):415-426. doi:10.1016/J.CEB.2008.03.015
444. Kinchen JM, Ravichandran KS. Phagosome maturation: going through the acid test. *Nat Rev Mol Cell Biol*. 2008;9(10):781. doi:10.1038/NRM2515
445. Chaudhuri S, McKenna N, Balce DR, Yates RM. Infection of porcine bone marrow-derived macrophages by porcine respiratory and reproductive syndrome virus impairs phagosomal maturation. *J Gen Virol*. 2016;97(3):669-679. doi:10.1099/JGV.0.000384/CITE/REFWORKS
446. Dumas A, Lê-Bury G, Marie-Anaïs F, et al. The HIV-1 protein Vpr impairs phagosome maturation by controlling microtubule-dependent trafficking. *J Cell Biol*. 2015;211(2):359-372. doi:10.1083/JCB.201503124/VIDEO-2
447. Dupont M, Sattentau QJ. Macrophage Cell-Cell Interactions Promoting HIV-1 Infection. doi:10.3390/v12050492
448. Welsch S, Keppler OT, Habermann A, Allespach I, Krijnse-Locker J, Kräusslich HG. HIV-1 Buds Predominantly at the Plasma Membrane of Primary Human Macrophages. *PLoS Pathog*. 2007;3(3). doi:10.1371/JOURNAL.PPAT.0030036
449. Deneka M, Pelchen-Matthews A, Byland R, Ruiz-Mateos E, Marsh M. In macrophages, HIV-1 assembles into an intracellular plasma membrane domain containing the tetraspanins CD81, CD9, and CD53. *J Cell Biol*. 2007;177(2):329. doi:10.1083/JCB.200609050
450. Oliveira JJ, Karrar S, Rainbow DB, et al. The plasma biomarker soluble SIGLEC-1 is associated with the type I interferon transcriptional signature, ethnic background and renal disease in systemic lupus erythematosus. *Arthritis Res Ther*. 2018;20(1):1-13. doi:10.1186/S13075-018-1649-1/FIGURES/5
451. Tan J, Sattentau QJ. The HIV-1-containing macrophage compartment: a perfect cellular niche? *Trends Microbiol*. 2013;21(8):405-412. doi:10.1016/J.TIM.2013.05.001
452. Koenig S, Gendelman HE, Orenstein JM, et al. Detection of AIDS Virus in Macrophages in Brain Tissue from AIDS Patients with Encephalopathy. *Science (80-)*. 1986;233(4768):1089-1093. doi:10.1126/SCIENCE.3016903
453. Park MD. Macrophages: a Trojan horse in COVID-19? *Nat Rev Immunol 2020 206*. 2020;20(6):351-351. doi:10.1038/s41577-020-0317-2
454. Hopfer H, Herzig MC, Gosert R, et al. Hunting coronavirus by transmission electron microscopy – a guide to SARS-CoV-2-associated ultrastructural pathology in COVID-19 tissues. *Histopathology*. 2021;78(3):358-370. doi:10.1111/HIS.14264
455. Bullock HA, Goldsmith CS, Miller SE. Best practices for correctly identifying coronavirus by transmission electron microscopy. *Kidney Int*. 2021;99(4):824-827. doi:10.1016/J.KINT.2021.01.004
456. Dalskov L, Møhlenberg M, Thyrsted J, et al. SARS-CoV-2 evades immune detection in alveolar macrophages. *EMBO Rep*. 2020;21(12):e51252. doi:10.15252/EMBR.202051252
457. Shibutani M, Maeda K, Nagahara H, et al. The peripheral monocyte count is associated with the density of tumor-associated macrophages in the tumor microenvironment of colorectal cancer: A retrospective study. *BMC Cancer*. 2017;17(1):1-7. doi:10.1186/S12885-017-3395-1/FIGURES/4
458. Ostuni R, Kratochvill F, Murray PJ, Natoli G. Macrophages and cancer: from mechanisms to therapeutic implications. *Trends Immunol*. 2015;36(4):229-239. doi:10.1016/J.IT.2015.02.004
459. Hamming I, Timens W, Bulthuis MLC, Lely AT, Navis GJ, van Goor H. Tissue

distribution of ACE2 protein, the functional receptor for SARS coronavirus. A first step in understanding SARS pathogenesis. *J Pathol*. 2004;203(2):631. doi:10.1002/PATH.1570
460. Boumaza A, Gay L, Mezouar S, et al. Monocytes and macrophages, targets of SARS-CoV-2: the clue for Covid-19 immunoparalysis. *bioRxiv*. Published online September 17, 2020:2020.09.17.300996. doi:10.1101/2020.09.17.300996
461. Goldsmith CS, Miller SE, Martines RB, Bullock HA, Zaki SR. Electron microscopy of SARS-CoV-2: a challenging task. *Lancet*. 2020;395(10238):e99. doi:10.1016/S0140-6736(20)31188-0
462. Yazdanpanah F, Hamblin MR, Rezaei N. The immune system and COVID-19: Friend or foe? *Life Sci*. 2020;256:117900. doi:10.1016/J.LFS.2020.117900
463. Iwami S, Takeuchi JS, Nakaoka S, et al. Cell-to-cell infection by HIV contributes over half of virus infection. *Elife*. 2015;4(OCTOBER2015). doi:10.7554/ELIFE.08150
464. Hagemann T, Wilson J, Burke F, et al. Ovarian Cancer Cells Polarize Macrophages Toward A Tumor-Associated Phenotype. *J Immunol*. 2006;176(8):5023-5032. doi:10.4049/JIMMUNOL.176.8.5023
465. Thorne LG, Reuschl A-K, Zuliani-Alvarez L, et al. SARS-CoV-2 sensing by RIG-I and MDA5 links epithelial infection to macrophage inflammation. *EMBO J*. 2021;40(15):e107826. doi:10.15252/EMBJ.2021107826
466. Yang L, Nilsson-Payant BE, Han Y, et al. Cardiomyocytes recruit monocytes upon SARS-CoV-2 infection by secreting CCL2. *Stem Cell Reports*. 2021;16(9):2274-2288. doi:10.1016/J.STEMCR.2021.07.012
467. Miki Y, Ono K, Hata S, Suzuki T, Kumamoto H, Sasano H. The advantages of co-culture over mono cell culture in simulating in vivo environment. *J Steroid Biochem Mol Biol*. 2012;131(3-5):68-75. doi:10.1016/J.JSBMB.2011.12.004